# Development of accurate force fields for a Pareto screening of high-performance metal-organic frameworks

Jelle Wieme

Supervisors: Prof. dr. ir. Veronique Van Speybroeck, Prof. dr. Stefaan Cottenier
Counsellors: Ir. Louis Vanduyfhuys, Dr. ir. Kurt Lejaeghere, Ir. Sven Rogge

Master's dissertation submitted in order to obtain the academic degree of
Master of Science in Engineering Physics

Department of Applied Physics
Chairman: Prof. dr. ir. Christophe Leys

Department of Materials Science and Engineering
Chairman: Prof. dr. ir. Joris Degrieck

Faculty of Engineering and Architecture
Academic year 2014-2015

UNIVERSITEIT
GENT


This work has been performed at the Center for Molecular Modeling.

# Preface

While the deadline keeps getting closer and closer, I often find myself reminiscing about the past five years. After my first year at university, I was convinced that I would like to continue in research. During my years as a bachelor student in engineering physics, the quantum mechanical nature of matter piqued my interest. By taking elective courses on computational physics, I learned that simulations at the nanoscale can give a wealth of information about the physical behavior of a system. This illustrated to me that computational techniques offer the possibility to gain insight in fundamental physics. Twelve months ago, I chose a topic in the field of computational molecular modeling, a burgeoning area of research, in which many opportunities and challenges lie ahead. I hope this work can make a positive contribution.

Foremost, I would like to express my deepest thanks to my supervisor prof. dr. ir. Veronique Van Speybroeck for the positive support throughout the year. Your experience, insights and critical remarks guided me along the way. I am grateful for the opportunity to work on an interesting and relevant topic with a great team of counsellors and to do so for the coming years. I would also like to thank my co-supervisor prof. dr. Stefaan Cottenier for his contributions.

I also want to thank Louis, Kurt and Sven for all the support during these past months. This thesis represents a collaborative effort which, without your aid, would not have been possible. A few lines are not enough to express my gratitude. Thank you Louis, for the help with all theoretical and computational problems, and your dedication to teach me the required skills. Thank you Kurt, for the many suggestions and resolved issues. Despite the number of thesis students under your care and the busy schedule, there was always time to help me. Thank you Sven, for the many hours you spent in improving this work. It was a pleasure to work and share an office with you. I would like to thank you all for your precious time invested in me. I hope that it was not completely wasted from your end and that you learned something from it too.

In addition, a thank you to prof. dr. em. Michel Waroquier for his support and perseverance that lead to one of the major results of this thesis. Thank you, to all other members of the Center for Molecular Modeling (CMM). Although I was only a student, it felt like I was a member of the team. Thank you, Jeroen and Kristof, for the positive work environment in our office and thank you to my fellow thesis students at the CMM. There are a few, but special thanks to Michiel and Sam for

the enjoyable company this year.

And finally, thanks to my parents, my sister and my brother; for the support and patience when needed and the opportunity to personally and academically grow in the best possible circumstances.

Jelle Wieme
May 22, 2015

# Copyright agreement



Jelle Wieme
May 22, 2015

# Development of accurate force fields for a Pareto screening of high-performance metal-organic frameworks

by Jelle Wieme

Supervisors: prof. dr. ir. Veronique Van Speybroeck, prof. dr. Stefaan Cottenier
Counsellors: ir. Louis Vanduyfhuys, dr. ir. Kurt Lejaeghere, ir. Sven Rogge

Master's dissertation submitted in order to obtain the academic degree of
Master of Science in Engineering Physics

Department of Applied Physics
Chairman: prof. dr. ir. Christophe Leys

Department of Materials Science and Engineering
Chairman: prof. dr. ir. Joris Degrieck

Faculty of Engineering and Architecture
Academic year 2014-2015

---

## Overview

This work aims to develop the necessary tools for a high-throughput screening of metal-organic frameworks (MOFs). MOFs form a new class of nanoporous crystalline materials which typically consist of metal oxide clusters connected through organic linkers. The focus lies on the development of accurate all-atom flexible force fields derived from ab initio input, which is generated for model systems representing the inorganic metal node and organic linker. A test set containing different well-known and experimentally characterized MOFs such as MOF-5, MIL-53 and ZIF-8 is considered, illustrating the general applicability of the used methodology. The force fields are validated by comparing structural data for this test set with available experimental and theoretical values. Based on these force fields, thermal and mechanical properties are characterized, where especially the thermal expansion and anisotropic elastic behavior are studied. Finally, the test set of materials is extended by considering different linkers and metal centers for a subset of MOFs, allowing the identification of several useful trends.

## Keywords

Metal-organic frameworks, force fields, thermal expansion, mechanical properties, high-throughput

---

# Development of accurate force fields for a Pareto screening of high-performance metal-organic frameworks

Jelle Wieme

Supervisor(s): Veronique Van Speybroeck, Stefaan Cottenier
Counsellor(s): Louis Vanduyfhuys, Kurt Lejaeghere, Sven Rogge

*Abstract*— **This work aims to develop the necessary tools for a high-throughput screening of metal-organic frameworks (MOFs). MOFs form a new class of nanoporous crystalline materials which typically consist of metal oxide clusters connected through organic linkers. The focus lies on the development of accurate all-atom flexible force fields derived from ab initio input, which is generated for model systems representing the inorganic metal node and organic linker. A test set containing different well-known and experimentally characterized MOFs such as MOF-5, MIL-53 and ZIF-8 is considered, illustrating the general applicability of the used methodology. The force fields are validated by comparing structural data for this test set with available experimental and theoretical values. Based on these force fields, thermal and mechanical properties are characterized, where especially the thermal expansion and anisotropic elastic behavior are studied. Finally, the test set of materials is extended by considering different linkers and metal centers for a subset of MOFs, allowing the identification of several useful trends.**

*Keywords*— **metal-organic frameworks, force fields, thermal expansion, mechanical properties, high-throughput**

## I. Introduction and objectives

COMPUTATIONAL high-throughput methods provide a new tool for materials design, offering the advantage of rapid and efficient materials screening. It is a booming area of materials science, which grows hand-in-hand with the increasing power of supercomputers [1]. High-throughput approaches aim to identify novel promising structures and gain new physical insights such as structure-property relations.

MOFs form a new class of nanoporous crystalline materials which consist of metal oxide clusters connected through organic linkers. First synthesized by Yaghi in 1999 [2], MOFs have since then attracted enormous attention from academia and industry. The number of synthesized structures has increased considerably over the past decade [3], but the number of unexplored combinations remains vast. Because of their modular build-up, they can be combined in various ways, leading to a nearly infinite variety of MOFs. MOFs are therefore particularly attractive for a high-throughput screening. Several efforts have been undertaken to facilitate the large-scale screening of MOFs. The Hypothetical MOF database is a noteworthy initiative [4], where the authors have generated a database of 137 953 MOFs by combining 102 known building blocks in various ways. This database has been the subject of several high-throughput screening studies [5]. However, to date a fully quantum mechanical large-scale screening of MOFs is not feasible due to the high computational cost. Hence, other less accurate, but cheaper, molecular simulation techniques such as force fields need to be considered.

J. Wieme is with the Center for Molecular Modeling, Ghent University (UGent), Gent, Belgium. E-mail: Jelle.Wieme@UGent.be.

Until now, high-throughput searches have mainly focused on gas adsorption and separation of small molecules [5]. To this end, rigid force fields were used, where only the guest-host interactions are described and the intramolecular framework interactions are not considered. However, it has been shown that even properties such as gas diffusivity are underestimated by assuming a rigid model [6]. This is therefore inherently a limited approach and to study thermal, mechanical and dynamical behavior flexible force fields are required. Recently, some groups have started generating all-atom flexible force fields derived from ab initio data [7], [8], which allows a systematic approach that can in principle be applied to hypothetical MOFs as well. In this work, ab initio parametrized force fields are generated with QuickFF [8] (Section II), a software package developed at the Center for Molecular Modeling (CMM).

The force fields were first validated (Section II), with an emphasis on elastic constants and thermal expansion coefficients (Section III). The methodology to calculate these properties was then checked by comparing with literature data. The results are discussed in Section III. Finally, the test set was expanded to various combinations of organic linkers and inorganic metal nodes, for which the most important characteristics were assessed (Section IV).

## II. Development of force fields

### A. Force-field energy expression

For the force fields used in this work, the multidimensional potential energy surface is approximated with the following analytical expression:

$$V^{FF} = \underbrace{V_{bond} + V_{bend} + V_{oopd} + V_{torsion}}_{V^{FF}_{cov}} + \underbrace{V_{EI} + V_{vdW}}_{V^{FF}_{noncov}} \tag{1}$$

The most important parts of this expression are discussed in the following paragraphs.

#### A.1 Covalent interactions

The covalent part of the force field models the interaction between the chemically bonded atoms as a function of the bond

distance (bond), bend angle (bend), out-of-plane distance (oopd) and dihedral angle (torsion). The unknown parameters (force constants, rest values and multiplicities) in the covalent energy expression can be directly estimated with QuickFF [8].

The bond stretches $r_n$ are described using a harmonic potential:

$$V_{bond} = \sum_{n=1}^{N_{bonds}} \frac{K_{r,n}}{2} (r_n - r_{n,0})^2 \quad (2)$$

where $K_{r,n}$ is the force constant and $r_{n,0}$ the rest value of the bond distance. Here, the summation runs over all pairs of neighboring, i.e. chemically bonded, atoms.

The bends are described using a similar term, but now the internal coordinate is the bend angle $\theta_n$ between three neighboring atoms:

$$V_{bend} = \sum_{n=1}^{N_{bends}} \frac{K_{\theta,n}}{2} (\theta_n - \theta_{n,0})^2 \quad (3)$$

The out-of-plane distances $d_n$ are also described using a harmonic potential:

$$V_{oopd} = \sum_{n=1}^{N_{oopd}} \frac{K_{d,n}}{2} (d_n - d_{n,0})^2 \quad (4)$$

This term allows for a more accurate description of planar $sp^2$ and some nonplanar $sp^3$ configurations.

The fourth covalent term is the dihedral energy term. Here, a cosine term is used as a function of the dihedral angle $\phi_n$ between four atoms:

$$V_{torsion} = \sum_{n=1}^{N_{dih}} \frac{K_{\phi,n}}{2} (1 - \cos(m_{\phi,n}(\phi - \phi_0))) \quad (5)$$

with $m_{\phi,n}$ the multiplicity of the dihedral angle.

### A.2 Electrostatic interactions

The electrostatic interaction is modeled with a Coulombic potential between Gaussian charge distributions separated by a distance $r_{ij}$:

$$V_{EI} = \frac{1}{2} \sum_{\substack{i,j=1 \\ (i \neq j)}} \frac{q_i q_j}{4\pi\epsilon_0 r_{ij}} \mathrm{erf}\left(\frac{r_{ij}}{d_{ij}}\right) \quad (6)$$

In this work, Gaussian charge distributions are used with a total charge $q_i$ and radius $d_i$ for atom $i$. The mixed radius of the Gaussian charges, $d_{ij}$, is given by $\sqrt{d_i^2 + d_j^2}$. The atomic charges are derived via an atom-in-molecules scheme newly developed at the CMM: Minimal Basis Iterative Stockholder (MBIS). The radii of the Gaussian charge distribution are determined with the method of Chen and Martinéz [9].

### A.3 van der Waals interactions

The van der Waals interactions are modeled using the MM3 Buckingham potential.

$$V(r) = \epsilon_{ij} \left[ 1.84 \times 10^5 \exp\left(-12 \frac{r}{\sigma_{ij}}\right) - 2.25 \left(\frac{\sigma_{ij}}{r}\right)^6 \right] \quad (7)$$

The two parameters $\sigma_{ij}$ and $\epsilon_{ij}$ present the equilibrium distance and the well depth of the potential respectively. These parameters are typically determined with empirical mixing rules for the interaction between atom $i$ and atom $j$:

$$\sigma_{ij} = \sigma_i + \sigma_j \text{ and } \epsilon_{ij} = \sqrt{\epsilon_i \epsilon_j} \quad (8)$$

These parameters are taken from Ref. [10].

## B. *Cluster model approach*

With QuickFF [8], it is possible to derive force-field parameters from ab initio input on isolated molecules. Since MOFs are crystalline materials, representative cluster models need to be constructed. These cluster models represent the inorganic metal cluster and organic linker. An example for MIL-47 is given in Figure 1, where cluster models for the benzenedicarboxylate (BDC) linker and the 1D V-O metal chains are shown. This cluster model approach has been used previously and can be considered well-established for the design of force fields for MOFs [7], [11]. Moreover, this cluster approach allows to easily construct force fields on a large scale for multiple MOFs by combining force fields from various clusters.

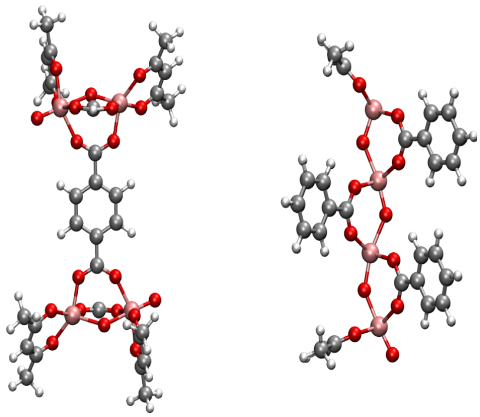

Fig. 1. Model systems for organic linker (left) and inorganic metal chain (right) of MIL-47.

## C. *Validation of the methodology*

To verify our methodology, force fields were developed for well-known and experimentally characterized structures. The test set consisted of MOF-5, MIL-53, MIL-47, HKUST-1, ZIF-8 and DMOF-1. Each structure was studied in detail, with special attention to the reproduction of the structural parameters of the ab initio cluster and the correct prediction of the unit cell shape. In Table I our lattice parameters of the cubic unit cells of MOF-5, ZIF-8 and HKUST-1 are shown and compared with experimental results.

For the flexible MOFs, such as MIL-53(Al) and MIL-47, the van der Waals parameters were fine-tuned. In this way, a better correspondence with experimental and/or theoretical results

TABLE I

LATTICE PARAMETERS OF SOME CUBIC MOFS.

| | MOF-5 [2] | ZIF-8 [12] | HKUST-1 |
|---|---|---|---|
| Exp. [Å] | 25.8 | 17.0 | 26.3 |
| FF [Å] (0 K) | 26.1 | 17.1 | 26.6 |

was obtained. An example is the pressure-induced breathing of MIL-47, which was experimentally observed by Yot *et al.* [14]. With the new ab initio derived force field, transition pressures between the large pore and narrow pore are in good agreement with the experiment. The simulated $PV$-characteristic is shown in Figure 2.

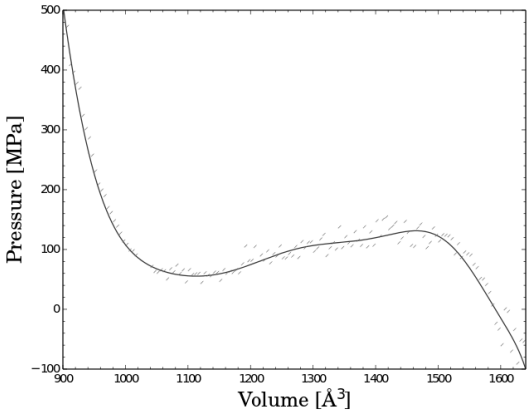


Fig. 2. Simulated volume dependence of the pressure of MIL-47. The crosses represent the simulated data on a volume grid and the solid line is a polynomial fit of order 11.

## III. CALCULATING PROPERTIES ON MOFS

The first step in a large-scale screening is the development of descriptors that can accurately predict the properties under study. These descriptors connect the calculated microscopic parameters to macroscopic materials properties. However, as discussed above, high-throughput investigations of MOFs so far mainly focused on gas adsorption and separation. There is a major lack of data on thermal and mechanical properties of MOFs, which are of interest for industrial use. This work therefore investigated a number of potential descriptors to describe these quantities. One particularly interesting property of MOFs is the framework flexibility [15]. Recently, Ortiz *et al.* [16] proposed the elastic anisotropy as a descriptor to quantify the framework flexibility of MOFs. To be useful in a large-scale screening of MOFs, our force fields must therefore be able to accurately describe the elastic behavior. In this work, it was shown that the anistropic elastic behavior obtained with the force fields at 0 K clearly separates the rigid from the flexible frameworks. However, large deviations were observed for the elastic constants and derived properties compared with ab initio results. In Table II, the ratio of the maximum and minimum Young's modulus $A_E$, the ratio of the maximum and minimum shear modulus $A_G$ and the maximum and minimum linear compressibility $\beta$ are shown for the rigid MOFs ZIF-8 and HKUST-1, and the flexible MOFs MIL-53(Al) and MIL-47 in the large pore. The anisotropy factors $A_E$ and $A_G$, and the ranges of the linear compressibility are clearly much higher for the flexible MOFs.

TABLE II

ANISOTROPIC ELASTIC PROPERTIES OF FLEXIBLE AND RIGID MOFS

| | $A_E$ | $A_G$ | $\beta_{max}$ | $\beta_{min}$ |
|---|---|---|---|---|
| MIL-53(Al) | 285 | 423 | 1836 | -1255 |
| MIL-47 | 57 | 85 | 303 | -201 |
| ZIF-8 | 1 | 1 | 41 | 42 |
| HKUST-1 | 4 | 5 | 24 | 24 |

A large-scale thermal characterization has not yet been performed. In this work, the thermal expansion behavior was studied. The volumetric thermal expansion coefficient at constant pressure is defined by

$$\alpha_V = \frac{1}{V}\frac{\partial V}{\partial T} = \frac{\partial \ln(V)}{\partial T} \tag{9}$$

A comparison with the literature showed that the new force fields tend to overestimate this coefficient. Another interesting result is shown in Figure 3. Here, a temperature-dependent thermal expansion coefficient of DMOF-1 was found at 1 bar by performing $NPT$ molecular dynamics simulations of 10.5 ns. For each temperature, the volumetric thermal expansion coefficient was found with following thermodynamic relation:

$$\alpha_V = \frac{1}{k_B T^2}\left[\frac{\langle HV\rangle_{(N,P,T)}}{\langle V\rangle_{(N,P,T)}} - \langle H\rangle_{(N,P,T)}\right] \tag{10}$$

where $V$ is the volume and $H$ the enthalpy. The black full line, on the other hand, represents the result of a linear fit of $\ln(V)$ versus $T$ over the whole temperature range (see Eq. 9), which in this case corresponds to the high-temperature limit of the thermal expansion coefficient.

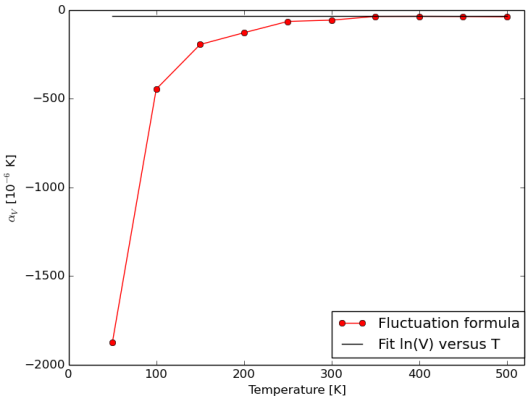


Fig. 3. Temperature dependence of the thermal expansion coefficient of DMOF-1.

## IV. EXTENDING THE SEARCH SPACE

After validating the methodology for deriving force fields and properties of MOFs, the explored set of MOFs was extended.

Inspired by the HMOF database [4], other organic linkers and functional groups were considered for MOF-5, MIL-53 and MIL-47. Furthermore, different metal centra were studied for MIL-53 and HKUST-1. Although only a small group of about hundred materials was studied, some interesting trends were revealed. For instance, the flexible MOFs - MIL-53 and MIL-47 - displayed thermal expansion behavior that was strongly dependent on the organic linker. For the mechanical properties of HKUST-1, it was found that the metal centers have hardly any influence. These two examples illustrate the wealth of information that can be obtained by increasing the search space.

## V. Conclusions

This work aimed to develop the necessary tools for a large-scale screening of MOFs. First, force fields were derived for a test set of well-known and experimentally characterized structures. These structures displayed different molecular and coordination environments. Overall, a good agreement with experimental and other theoretical results was obtained, illustrating the general applicability of the methodology.

In a second step, mechanical and thermal properties were calculated with the derived force fields. There is a major lack of data on these properties, which are, however, very important for the further industrialization of MOFs. The anisotropic elastic behavior was studied and a clear separation between flexible and rigid MOFs was observed. This indicates that derived anisotropic properties can be used as descriptors for framework flexibility. The calculation of the thermal expansion behavior showed that the new force fields tend to overestimate the thermal expansion coefficients. A temperature dependent thermal expansion coefficient was observed for a sufficiently long $NPT$ MD simulation.

The final step of a high-throughput screening, the data analysis, was not addressed in this work and belongs to future work in this area. Herein, the following question needs to be addressed: How to select the best performing materials? Here, one desirable property needs to be traded against another. Several multicriterion analysis methods are available, one of them being a Pareto analysis, which has already been used in materials science [17]. The Pareto-optimal set is the set of solutions that are nondominated, i.e. it is impossible to choose another solution that improves one property without worsening another one. Pareto dominance is often not very discerning, especially when looking at a very large set of materials. A post-Pareto method was recently proposed by Lejaeghere *et al.* [18], which ranks the materials in an intuitive way. It is the intention to use this method in the future to rank the MOFs according to various studied properties.

## Acknowledgments

This work was performed at the Center for Molecular Modeling (CMM), under supervision of ir. Louis Vanduyfhuys, dr. ir. Kurt Lejaeghere, ir. Sven Rogge, prof. dr. ir. Veronique Van Speybroeck and prof. dr. Stefaan Cottenier. I wish to thank them and the colleagues at the CMM for their support and guidance throughout the realization of this thesis. The computational resources and services used were provided by Ghent University (Stevin Supercomputer Infrastructure).

## References

[1] S. Curtarolo, G. L. W. Hart, M. B. Nardelli, N. Mingo, S. Sanvito and O. Levy, *The High-Throughput Highway to Computational Materials Design*, Nature Mater., vol. 12, pp. 191–201, 2013.

[2] H. Li, M. Eddaoudi, M. O'Keeffe and O. M. Yaghi, *Design and Synthesis of an Exceptionally Stable and Highly Porous Metal-Organic Framework*, Nature, vol. 402, pp. 276–279, 1999.

[3] H. Furukawa, K. E. Cordova, M. O'Keeffe and O. M. Yaghi, *The Chemistry and Applications of Metal-Organic Frameworks*, Science, vol. 341, p. 1230444, 2013.

[4] C. E. Wilmer, M. Leaf, C. Y. Lee, O. K. Farha, B. G. Hauser, J. T. Hupp and R. Q. Snurr, *Large-Scale Screening of Hypothetical Metal-Organic Frameworks*, Nature Chem., vol. 4, pp. 83–89, 2012.

[5] Y. J. Colón and R. Q. Snurr, *High-Throughput Computational Screening of Metal-Organic Frameworks*, Chem. Soc. Rev., vol. 43, pp. 5735–5749, 2014.

[6] S. Amirjalayer, M. Tafipolsky and R. Schmid, *Molecular Dynamics Simulation of Benzene Diffusion in MOF-5: Importance of Lattice Dynamics*, Angew. Chem. Int. Ed., vol. 46, pp. 463–466, 2007.

[7] S. Bureekaew, S. Amirjalayer, M. Tafipolsky, C. Spickermann, T. Kanchan Roy and R. Schmid, *MOF-FF - A Flexible First-Principles Derived Force Field for Metal-Organic Frameworks*, Phys. Status Solidi B, vol. 250, pp. 1128–1141, 2013.

[8] L. Vanduyfhuys, S. Vandenbrande, T. Verstraelen, R. Schmid, M. Waroquier and V. Van Speybroeck, *QuickFF: A Program for a Quick and Easy Derivation of Force Fields for Metal-Organic Frameworks from Ab Initio Input*, J. Comput. Chem., vol. 36, pp. 1015–1027, 2015.

[9] J. Chen and T. J. Martinéz, *The Dissociation Catastrophe in Fluctuating-Charge Models and its Implications for the Concept of Atomic Electronegativity*, Advances in the Theory of Atomic and Molecular Systems, pp. 397–415, 2009.

[10] N. L. Allinger, X. Zhou and J. Bergsma, *Molecular Mechanics Parameters*, THEOCHEM, vol. 312, pp. 69–83, 1994.

[11] L. Vanduyfhuys, T. Verstraelen, M. Vandichel, M. Waroquier and V. Van Speybroeck, *Ab Initio Parametrized Force Field for the Flexible Metal-Organic Framework MIL-53(Al)*, J. Chem. Theory Comput., vol. 8, pp. 3217–3231, 2012.

[12] J.-C. Tan, B. Civalleri, C.-C. Lin, L. Valenzano, R. Galvelis, P.-F. Chen, T. D. Bennett, C. Mellot-Draznieks, C. M. Zicovich-Wilson and A. K. Cheetham, *Exceptionally Low Shear Modulus in a Prototypical Imidazole-Based Metal-Organic Framework*, Phys. Rev. Lett., vol. 108, p. 095502, 2012.

[13] V. K. Peterson, Y. Liu, C. M. Brown and C. J. Kepert, *Neutron Powder Diffraction Study of $D_2$ Sorption in $Cu_3$(1,3,5-benzenetricarboxylate)$_2$*, J. Am. Chem. Soc., vol. 128, pp. 15578–15579, 2006.

[14] P. G. Yot, Q. Ma, J. Haines, Q. Yang, A. Ghoufi, T. Devic, C. Serre, V. Dimitriev, G. Férey, C. Zhong and G. Maurin, *Large Breathing of the MOF MIL-47(V(IV)) under Mechanical Pressure: A Joint Experimental-Modelling Exploration*, Chem. Sci., vol. 3, pp. 1100–1104, 2012.

[15] A. Schneemann, V. Bon, I. Schwedler, I. Senkovska, S. Kaskel and R. A. Fischer, *Flexible Metal-Organic Frameworks*, Chem. Soc. Rev., vol. 43, pp. 6062–6096, 2014.

[16] A. U. Ortiz, A. Boutin, A. H. Fuchs and F.-X. Coudert, *Anisotropic Elastic Properties of Flexible Metal-Organic Frameworks: How Soft Are Soft Porous Crystals?*, Phys. Rev. Lett., vol. 109, p. 195502, 2012.

[17] T. Bligaard, G. H. Jóhannesson, A. V. Ruban, H. L. Skriver, K. W. Jacobsen and J. K. Nørskov, *Pareto-Optimal Alloys*, Appl. Phys. Lett., vol. 83, pp. 4527-4529, 2003

[18] K. Lejaeghere, S. Cottenier and V. Van Speybroeck, *Ranking the Stars: A Refined Pareto Approach to Computational Materials Design*, Phys. Rev. Lett., vol. 111, p. 075501, 2013.

# Contents

**Preface** ii

**Copyright agreement** iii

**Overview** iv

**Extended abstract** v

**Table of contents** ix

**List of abbreviations** xi

**1 Introduction** 1

1.1 The necessity for high-throughput computational exploration . . . 1

1.2 Metal-organic frameworks . . . 3

1.3 Scope and structure of this work . . . 5

**2 Force fields** 7

2.1 Overview of the literature . . . 8

2.2 Methodology . . . 12

2.2.1 Force-field energy expression . . . 12

2.2.2 Cluster model approach . . . 14

2.2.3 Covalent interactions with QuickFF . . . 14

2.2.4 Electrostatic interaction . . . 21

2.2.5 van der Waals interaction . . . 27

2.2.6 Computational details . . . 29

2.3 Development of force fields for well-known MOFs . . . 30

2.3.1 MOF-5 . . . 30

2.3.2 MIL-53 . . . 33

2.3.3 MIL-47 . . . 43

2.3.4 HKUST-1 . . . 50

2.3.5 DMOF-1 . . . 58

2.3.6 ZIF-8 . . . 61

**3 Calculating properties on MOFs** **68**
3.1 Introduction . . . 68
3.2 Textural properties . . . 68
3.3 Thermal Properties . . . 70
3.3.1 Heat Capacity . . . 71
3.3.2 Thermal expansion coefficients . . . 77
3.4 Mechanical Properties . . . 86
3.4.1 Definition of the elastic constants . . . 87
3.4.2 Overview of literature . . . 92
3.4.3 Methods to determine the elastic constants . . . 95
3.4.4 Derived characteristics . . . 97
3.4.5 Validation of the methodology . . . 103

**4 Extending the search space** **116**
4.1 The IRMOF series . . . 116
4.2 The MIL-53 family . . . 119
4.3 The MIL-47 family . . . 124
4.4 The HKUST-1 family . . . 126
4.5 Conclusion . . . 127

**5 Conclusion and outlook** **130**

**Bibliography** **133**

# List of abbreviations

| | |
|---|---|
| **ACAC** | Acetylacetone |
| **AI** | Ab initio |
| **AIM** | Atom-In-Molecule |
| **AMBER** | Assisted Model Building with Energy Refinement |
| **ASA** | Accessible surface area |
| **AV** | Accessible volume |
| **B3LYP** | Becke, 3-parameter, Lee-Yang-Parr |
| **BDC** | Benzene-1,4-dicarboxylate |
| **BM** | Birch-Murnaghan |
| **BTC** | 1,3,5-benzenetricarboxylate |
| **BPDC** | 4,4'-biphenyldicarboxylate |
| **CBBDC** | 1,2-cyclobutane-3,6-benzenedicarboxylate |
| **CoRE** | Computation-Ready, Experimental |
| **CCDC** | Cambridge Crystallographic Data Center |
| **CMM** | Center for Molecular Modeling |
| **CVFF** | Consistent Valence Forcefield |
| **DABCO** | 1,4-diazabicylo[2.2.2]octane |
| **DFT** | Density Functional Theory |
| **DFTB** | Density-Functional-based Tight-Binding |
| **DPADC** | diphenyl-acetylene dicarboxylate |
| **DPTZDC** | 3,6-diphenyl-3,6-dihydro-1,2,4,5-tetrazine-dicarboxylate |
| **EIAM** | Elastic Anisotropy Measures |
| **EOS** | Equation of state |
| **ESP** | Electrostatic potential |
| **FF** | Force field |
| **GAFF** | General AMBER force field |
| **GGA** | Generalized gradient approximation |
| **HO** | Harmonic oscillator |
| **HI** | Iterative Hirshfeld |
| **HKUST** | Hong Kong University of Science and Technology |
| **HMOF** | Hypothetical metal-organic framework |
| **HPDC** | 4,5,9,10-tetrahydropyrene-2,7-dicarboxylate |
| **IC** | Internal coordinate |
| **IRMOF** | Isoreticular metal-organic framework |
| **LCD** | Largest cavity diameter |
| **LDA** | Local-density approximation |
| **lp** | Large pore |

| | |
|---|---|
| **MBIS** | Minimal Basis Iterative Stockholder |
| **MD** | Molecular dynamics |
| **MeIM** | 2-methylimidazole |
| **MIL** | Matériaux de l'Institut Lavoisier |
| **MK** | Merz-Kollman |
| **MOF** | Metal-organic framework |
| **MTTK** | Martyna-Tuckerman-Tobias-Klein |
| **NDC** | Napthalene-dicarboxylate |
| **NHC** | Nosé-Hoover chain |
| **NMA** | Normal mode analysis |
| **np** | Narrow pore |
| **NTE** | Negative thermal expansion |
| **PDC** | Pyrene-2,7-dicarboxylate |
| **PES** | Potential energy surface |
| **PIMD** | Path Integral Molecular Dynamics |
| **PLD** | Pore limiting diameter |
| **QM** | Quantum mechanics |
| **QMDFF** | Quantum Mechanically Derived Force Field |
| **RCSR** | Reticular Chemistry Structure Resource |
| **RESP** | Restrained electrostatic potential |
| **RV** | Rose-Vinet |
| **TPDC** | Triphenyl-4,4'-dicarboxylate |
| **UFF** | Universal Force Field |
| **UiO** | Universitetet i Oslo |
| **ZIF** | Zeolitic imidazolate framework |

# Chapter 1

# Introduction

Less than a century after the development of the first computer, computational research has emerged as one of the major branches in science, alongside the older branches of experiment and theory. Rooted in the exponentially increasing computational power, this field of study finds its applications in almost all scientific fields, such as particle physics, medical science, electronic and aerospace engineering, with astonishing results. Recently, some of these results in computational chemistry were awarded the Nobel Prize in Chemistry 2013 for the development of multiscale models for complex chemical systems. This work aims to continue this development by the large-scale characterization of metal-organic frameworks.

## 1.1 The necessity for high-throughput computational exploration

In physics, two different approaches can be distinguished when one is interested in studying the kinematic or dynamic behavior of molecules on the nanoscale. On the one hand, ab initio techniques such as Density Functional Theory (DFT) are used to determine the properties of interest very precisely, with a full quantum mechanical treatment. However, such approaches are computationally very expensive, and can hence only be carried out for limited time and length scales. On the other hand, less reliable approximations exist as well, such as molecular mechanics, which do not incorporate a full quantum mechanical treatment, but are much cheaper. As a consequence, they can be used on much longer time and length scales, which is sometimes necessary to capture long-time or long-range effects. In this work, the gap between both treatments is bridged. Starting from the ab initio treatment of the constituents of a larger stucture, an approximate description of this larger structure is obtained using force fields, which can then be employed on a much larger scale. This computational exploration has also proven to be an indispensable tool in the exploration of new materials, which often have to be tailored for specific needs. For instance, some materials described in this work will allow large volume fluctuations of their nanopores, hence drastically changing their behavior. These transformations are often too fast to study experimentally, but can be captured with molecular mechanics [1]. Furthermore, experimental research is often slow-paced, and prone to practical restrictions such as the accuracy with which some properties can be

measured. A computational first screening of possible materials can reduce the number of possible candidates for a certain application immensely, allowing to focus on the most promising materials in a later stage and hence lower the experimental effort. These high-throughput searches are becoming increasingly popular in the last decade [2].

High-throughput methods have become a new tool that offer the promise of rapid and efficient materials screening. It is an emerging area of materials science that grows hand in hand with the increasing power of supercomputers. In a review article by Curtarolo *et al.* [2], the authors provide examples of succesful high-throughput investigations illustrating the maturity of this new research area, and furthermore highlight the current challenges and opportunities. They define high-throughput as the throughput of data that is way too high to be produced or analyzed by the researcher's direct intervention, and must therefore be performed automatically. They separate the process in three steps:

1. virtual materials growth: thermodynamic and electronic-structure calculations of materials
2. rational materials storage: systematic storage of the information in database repositories
3. materials characterization and selection: data analysis aimed at selecting novel materials or gaining new physical insights

On the one hand, the direct result of a large-scale screening is the detection of new materials with exceptional properties ('selecting novel materials'). Curtarolo *et al.* posit that the most important and challenging part is the identification of a 'descriptor', which connects the calculated microscopic parameters to macroscopic properties of the materials. Afterwards, following question needs to be addressed: How to select the best performing materials? A compromise has to be made, trading one desirable property against another. Multi-objective optimization techniques exist and have been used in other fields of research such as economics. One of them is a Pareto analysis as originally defined by the economist Vilfredo Pareto [3]. This approach extracts the Pareto optimal set, which is the set of solutions that are nondominated, i.e. it is impossible to choose another solution that improves the property making another property worse.

Pareto analyses have been employed in high-throughput materials science previously. Bligaard *et al.* [4] determined a Pareto optimal set of 82 materials from a set of more than 60 000 alloys, with as defining properties the price, the formation energy and the compressibility. Andersson *et al.* [5] used Pareto optimality to select the best solid heterogeneous catalysts. However, Pareto dominance is often not very discerning, especially when looking at a very large set of materials. Several post-Pareto analysis methods therefore try to reduce the number of candidates even further [6–8]. A new post-Pareto method was recently proposed by Lejaeghere *et al.* [9]. This method ranks the materials in an intuitive way, based on the trade-off between two Pareto solutions.

On the other hand, a large-scale screening can detect structure-property relations ('gaining new physical insights'). Identifying them can increase the theoretical understanding of microscopic properties, which leads to the prediction of new and better materials and increases the discovery rate in the long term.

## 1.2 Metal-organic frameworks

Metal-organic frameworks (MOFs) form a new class of nanoporous crystalline materials which typically consist of metal oxide clusters connected through organic linkers. The first MOF, MOF-5, was first synthesized by Yaghi and co-workers in 1999 [10]. In the last two decades, many more MOFs have emerged, such as the IRMOF series [11], the MIL-53 family [12] and the ZIFs [13]. This continuous expansion of the number of synthesized MOFs can partly be explained by the relative ease with which they can be synthesized, especially when compared to other nanoporous materials such as zeolites. The easy synthesis is a result of the building block structure of MOFs, where the many different metal nodes and organic linkers can be combined to form a nearly infinite number of MOFs. Two illustrative examples of these MOFs, for which the building blocks are particularly recognizable, are shown in Figure 1.1.

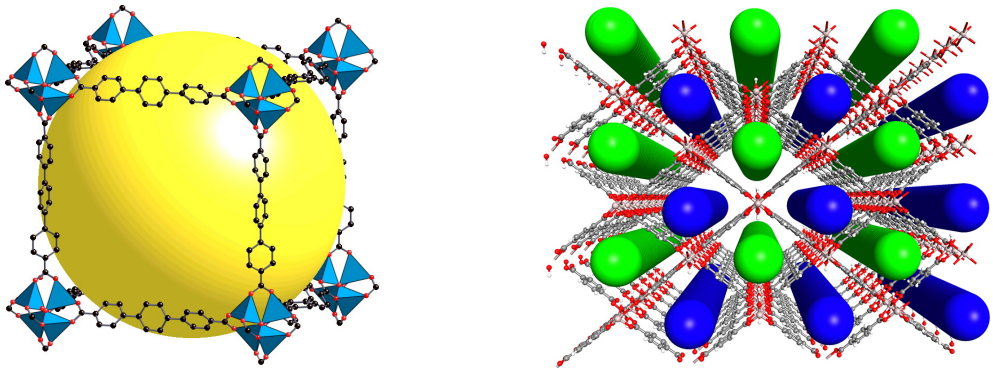

**Figure 1.1:** Examples of metal-organic frameworks: IRMOF-16 (left) and MIL-53 (right). Figures taken from Refs. [11, 14].

In recent years, MOFs have attracted a large interest thanks to their extraordinary properties. MOFs can, for instance, be used for gas separation/storage [15], as a platform for clean energy [16], as a host for nanoparticles [17], as chemical sensors [18], for catalysis [19], for biomedicine [20], and for optical and electronic applications [21]. Moreover, they have shown interesting magnetic properties [22] as well as semiconducting behavior [23]. This nonexhaustive overview of applications illustrates that MOFs are unparallelled in their degree of tunability and structural diversity as well as their range of physical and chemical properties. An especially interesting property, which will be highlighted in this work, is framework flexibility [24–26]. Despite being crystalline - and hence ordered - structures, some MOFs can transform between two stable structures under influence of external stimuli such as guest adsorption or thermal and mechanical impulses. During this process,

denoted as breathing, the pore volume of the MOF can change drastically, as shown in Figure 1.2 for MIL-53(Cr).

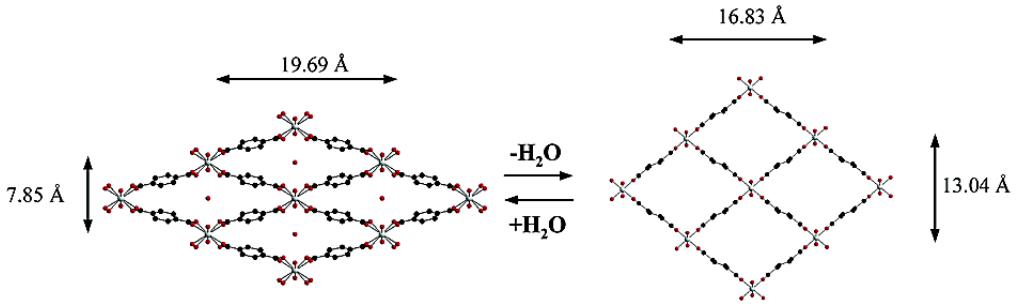


**Figure 1.2:** The breathing behavior of MIL-53(Cr) between the narrow-pore structure (left) and the large-pore structure (right) [12].

MOFs are a class of materials for which a high-throughput search is particularly attractive [27]. The number of synthesized MOFs has increased enormously in the past decade [28], but the number of unexplored combinations remains vast. To start a large-scale computational screening, a database is required. A universal system and database of nomenclature, classification, identification and topological structures was already introduced in 2008 by the Reticular Chemistry Structure Resource (RCSR) [29]. The construction of a database directly for computational screening was discussed by Colón *et al.* in Ref. [27], where they identified two different approaches. In the first approach, a database is constructed by screening availabe structures, such as the ones available in the Cambridge Structural Database [30]. This resulted, for example, in the Computation-Ready, Experimental Metal-organic frameworks (CoRE) database by Chung *et al.* [31] of more than 4 000 structures. The second approach is exemplified by Wilmer *et al.* [32], who developed the Hypothetical Metal-Organic Frameworks database (HMOFs). To this end, they made a library of 102 building blocks, extracted from existing MOFs, combined them in various ways and obtained 137 953 MOFs.

As mentioned in Section 1.1, the generation and storage of a computational database is typically followed by a data analysis stage. Several of such studies are also available for MOFs. Watanabe and Sholl [33] investigated 1 163 MOFs to detect promising materials for $CO_2/N_2$ gas separation via a multiscale computational approach. Fernandez *et al.* [34] developed machine learning tools to select high-performing MOFs for the application of $CO_2$ storage. Their method enables to significantly reduce the computation time for screening large databases. Several high-throughput searches on MOFs have started from the HMOF database. Wilmer *et al.* [32, 35] have studied their database several times, for example. In Ref. [35], the authors searched for important structure-property relations for $CO_2$ separation and storage, while Ref. [32] focused on structure-property relations for $CH_4$ storage. An example of such a structure-property relation detected via the HMOF database, is shown in Figure 1.3. A large-scale structure-property analysis on the HMOF database was also performed by Fernandez *et al.* [36]. They studied the effect of textural properties such as pore size and void fraction on $CH_4$ storage and they proposed models that can predict $CH_4$ storage

based on some geometric parameters. Gomez *et al.* [37] screened the HMOF database to select candidate structures for $H_2$ storage and found that especially paddle wheel MOFs are interesting. A more detailed investigation of $H_2$ storage was made by Colón *et al.* [38]. Using the algorithms of Wilmer *et al.* [32], they generated a more specific database of 18 000 MOFs containing Mg functional groups and subsequently studied $H_2$ uptake and delivery at room temperature. A part of the HMOF database was considered by Gomez *et al.* [39], when investigating the physical limits for $CH_4$ storage and delivery in nanoporous materials. Sikora *et al.* also analyzed the textural properties of the complete database [40] and studied the Xe/Kr separation [41]. These examples illustrate the potential of the HMOF database. The descriptors for gas separation and storage detected from these high-througput screenings are e.g. the number of functional groups, the void fraction and the pore limiting diameter, but new descriptors that predict the stability of MOFs (thermal, chemical or mechanical) would be very useful [27]. The predictors of framework flexibility proposed by Ortiz *et al.* [42] are in that regard interesting quantities to study on a large scale.

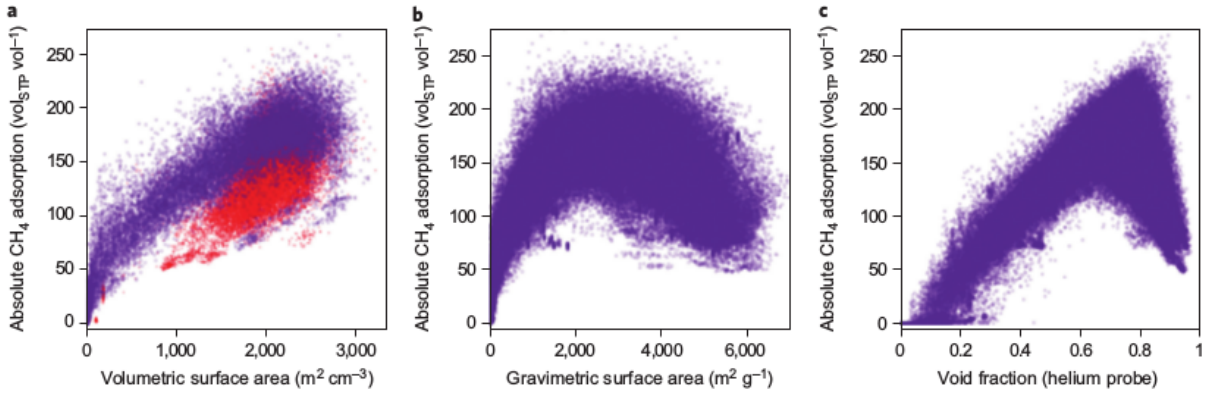


**Figure 1.3:** Some structure-property relations identified by Wilmer *et al.* [32] for $CH_4$ storage from the HMOF database. Purple dots are the elements of the HMOF database, while red dots correspond to HMOFs that have enough space to interpenetrate, but are not interpenetrated. Figure taken from Ref. [32].

## 1.3 Scope and structure of this work

The overall aim of this work is the development of the necessary tools for a high-througput search on MOFs, which could in turn lead to valuable information for experimentalists. According to the definition of Curtarolo *et al.* [2], this work should hence be seen as a first step towards a true high-throughput screening of MOFs. To achieve this goal, several metal centers and organic linkers will be described via ab initio calculations, on which a vast set of force fields will be based to describe different combination of these building blocks. However, unlike earlier work, which mostly focused on gas separation and adsorption properties, this work highlights the thermal and mechanical behavior of these materials. In the former studies, the MOF structure is often kept fixed during a simulation, which is no longer possible in our treatment, where for instance elastic properties will be determined. This flexibility will be shown to pose additional restrictions to our simulations.

The remainder of this thesis is organized as follows. Force-field models are derived for various MOFs with different topology and chemical structure, showing the general applicability of the method in Chapter 2. After explaining the methodology to derive the force fields, a study is made of well-known and experimentally characterized structures. This test set consists of MOF-5, MIL-53, MIL-47, HKUST-1, DMOF-1 and ZIF-8. Subsequently, in Chapter 3 some thermal and mechanical properties are studied and the sensitivity of these properties on the force-field parametrization is discussed. Textural properties are also considered as these properties are a key characteristic of nanoporous materials. To validate the methodology, the obtained properties of existing materials will be compared with published results. In Chapter 4, the set of materials is expanded with hypothetical materials inspired by the building blocks used in the HMOF database. Although a relatively small set was considered, some interesting properties and trends are revealed.

# Chapter 2

# Force fields

Metal-organic frameworks (MOFs) have become a prominent area of research during the past decade. Different combinations of molecular building blocks have been synthesized and characterized experimentally. However, the number of structures that may be proposed is almost unlimited. Therefore, more and more researchers focus on computational MOF research. The idea of a high-throughput material screening is particularly attractive for MOFs as was stated in the previous chapter. The accurate prediction of the properties of MOFs relies on an accurate computational description of hypothetical materials.

The molecular building blocks typically comprise more than ten atoms. The crystallographic unit cell, consisting of a number of these blocks, can contain more than hundred atoms and is considered large. This rules out most highly accurate quantum chemistry methods. Ab initio Density Functional Theory (DFT) calculations can be used for a detailed study of MOFs, but it is computationally expensive. Mostly, the available time scale is restricted due to the large size. Molecular dynamics (MD) are nowadays an indispensable tool for a computational researcher to study e.g. the effect of temperature on lattice dynamics or the breathing behavior in flexible materials, but long ab initio MD simulations are not possible on a large scale. These computational considerations illustrate the restricted range of application of ab initio methods in screening large numbers of MOFs.

A succesful modeling technique for large systems is the use of force fields. This approach completely neglects the electronic structure of materials, which is a significant disadvantage. It is, however, possible to approximate the potential energy surface (PES) as an analytical function of the nuclear coordinates. Neglecting the specific electronic motion results in a low computational cost and as such, larger systems and longer time scales are accessible. The PES describes the potential energy felt by the nuclei. In a system with $N$ atoms, this complex surface is a function of $3N$ Cartesian coordinates, the degrees of freedom of the system. Usually, the force-field energy is expressed in terms of internal coordinates, which represent natural internal degrees of freedom. To develop a force field, one has to identify these internal coordinates, which depend on the Cartesian coordinates of the nuclei. Straightforward choices are the bond distance between chemically bonded atoms and

the angle between two neighboring bonds, but one can also include a four-atom internal coordinate such as a dihedral angle. With each of these internal coordinates corresponds a contribution to the potential energy and the choice of their functional form defines the force field. An accurate force field can only be obtained when the internal degrees of freedom that govern the behavior of the system are correctly identified and described with a suitable potential energy term. A distinction is made between bonded or covalent energy terms and nonbonded or noncovalent energy terms. The covalent terms are related to the presence of chemical bonds, while the noncovalent terms describe the long-range interactions such as electrostatic and dispersion interactions. The potential energy terms contain unknown parameters, which can be determined by fitting the force field to experimentally available data such as bond distances and enthalpies of formation or to ab initio calculations performed on representative systems.

To date, most computational investigations of MOFs have been performed using rigid force fields [33, 43–45]. It can be used to study adsorption isotherms, where only the interactions between the framework and the guests are modeled. The intraframework interactions are not considered and the atoms of the MOF are kept fixed. If one wants to describe dynamical behavior, such as breathing, this approach is not sufficient. It has been shown that dynamic properties such as gas diffusivity are underestimated by assuming a rigid model [46, 47]. Other properties such as the thermal expansion and elastic constants cannot be determined without intraframework interactions as these quantities are strongly dependent on the strength of the chemical bonds, which is described by the covalent energy terms.

In this work, nonpolarizable and nonreactive, but flexible and all-atom force fields are developed and used. An overview of the literature on the development of force fields is given in Section 2.1. The aim is not to provide a complete overview of the force field literature in general, but the focus lies on the development of ab initio derived flexible force fields specifically for MOFs. The methodology used in this work is explained in Section 2.2. Before proceeding to predict material properties of hypothetical materials in the next chapter, one should first validate the force fields on experimentally characterized structures. The generated force fields on well-known MOFs as MOF-5, MIL-53, MIL-47, HKUST-1, DMOF-1 and ZIF-8 are discussed and validated in Section 2.3. MOFs with various network topologies and molecular environments are studied, which illustrates the general applicability of the methodology for constructing the force fields.

## 2.1 Overview of the literature

Several force fields that allow a general approach to molecular mechanics are available in the literature. UFF [48] and DREIDING [49] are examples of such generic force fields. Their philosophy is to derive force-field parameters based on structural information of a large set of simple reference systems, e.g. diatomic molecules, in combination with empirical rules such as Badger's rule or hybridization dependent force constants. These force fields consist of specific potential terms where

the necessary parameters have been defined for most atoms in the periodic table. This leads to lower accuracy, but has the virtue of allowing reasonable predictions to be made for novel combinations of elements. Other, less general, force fields are MM3 [50], AMBER [51] and CVFF [52]. These force fields were fitted to experimental data, specifically to reproduce the properties of a certain class of molecules. MM3 was originally determined for hydrocarbons, while AMBER and CVFF for proteins, but these force fields became very popular and are now often used in different molecular environments. For example, the AMBER force field was extended such that it could be applied to a wider range of molecules (GAFF [53]).

General force-field parameters would ideally be directly applicable to MOFs. However, this is not the case, as the available parameter set for the metals in MOFs is not very accurate. The existing force fields are not capable to accurately reproduce the coordination environment that is present in the inorganic building units. Several authors have used parameters of these general force fields to describe the interactions in the organic linker, while parameters are refitted to describe the inorganic building blocks. Examples are the force fields developed by Greathouse *et al.* (CVFF) [54], Dubbeldam *et al.* (DREIDING, CVFF) [55], Tafipolsky *et al.* (MM3) [56], Salles *et al.* (DREIDING, CVFF) [1], and Hu *et al.* (AMBER) [57].

To solve this problem in a more general way, an extension of UFF [48] was published by Addicoat *et al.* [58]. This is known as UFF4MOF. The authors estimated new parameters for the metal elements Zn, Cu, Ni, Co, Fe, Mn, Cr, V, Ti, Sc, and Al. Also, additional oxygen parameters are provided for a reliable description of the inorganic metal oxide blocks. UFF4MOF does not change the potential energy expression, it merely presents new parameters for these atoms, which were estimated from a fit to geometric reference data. If available, high-quality experimental structures were used, while DFT calculations were performed to obtain missing input data. The extended parameter set was then validated by comparing structural parameters for various MOFs with available theoretical and experimental results. The test set consists of different MOFs such as IRMOFs, paddle wheel MOFs (e.g. HKUST-1) and several elements of the MIL-53 family. The biggest advantage of force fields comprised of parameters from UFF4MOF is the transferability. The authors suggested the use of UFF4MOF for screening MOF structures for selected applications, providing structures for visual analysis or as a starting point for more sophisticated simulations. The computed ground state structures compared reasonably well with previously published results (both experimental and theoretical). Other material properties were not calculated, thus the question remains if accurate results can be obtained with UFF4MOF as the newly derived parameters were explicitly fitted to reproduce structural data. The extended set of parameters is available in Ref. [58] and can directly be used in standard UFF calculations.

Very recently, Bristow, Tiana and Walsh developed BTW-FF [59], an ab initio derived force field with special attention on transferability. The force field should be able to describe different MOFs regardless of metal cluster and organic linker. The used potential energy expression was the same

as the MM3 force field [50]. The newly derived force-field parameters were directly fitted on DFT calculations of periodic MOF structures. Electrostatic interactions were described by Coulomb interactions between point charges, derived from the ab initio electron density using Bader's atom-in-molecules partitioning scheme [60]. A Buckingham potential (see Section 2.2.5) was used to model the dispersion interactions and parameters were taken directly from the original MM3 force field, while the covalent parameters were determined by fitting it to the ab initio optimized crystal structural data. The test set included MOF-5, IRMOF-10, IRMOF-14, UiO-66, UiO-67 and HKUST-1. The fitted parameters are available in the supporting information of Ref. [59]. To validate their work, different properties were calculated such as bulk moduli, thermal expansion coefficients, heat capacities and vibrational frequencies. An overall good agreement is found with the DFT reference data.

The group of Schmid has published several ab initio derived force fields for MOFs. Already in 2007, a force field based on first-principles calculations was derived for MOF-5 [56]. The energy expression and parameters for the organic linker were taken from the MM3 force field [50], but the inorganic building unit was refitted. To this end, they worked with two different cluster models on which they manually fitted different parameters. An improved fitting procedure was proposed in 2009 [61], which included a modified form of the MM3 model with extra cross terms for a better description of the vibrational frequencies. Instead of the MM3 dipole-dipole electrostatic interaction, the typical Coulombic point charge approach was used to model the long-range electrostatic interactions. The atomic charges were derived using the Merz-Kollman Electrostatic Potential fitting method [62]. For the first time a systematic strategy, that allowed to estimate force-field parameters for MOFs from nonperiodic cluster models, was developed. A genetic algorithm was used where the objective function is based on the ab initio equilibrium geometry and Hessian in internal coordinate space. This transformation is not unique due to the redundancy of the set of internal coordinates. The objective function contained weight factors that can manually be adjusted and choosing their value is a non-trivial task. The procedure was validated by performing a vibrational frequency analysis on the nonperiodic cluster model. The ab initio frequencies were compared with the frequencies as predicted by the force field and a good agreement was found. Furthermore, the force field equilibrium geometry also nicely reproduced the DFT equilibrium. These validations proved that the force field PES matched the ab initio PES in the neighborhood of the equilibrium. Finally, MD simulations were carried out to calculate elastic and thermal properties at finite temperatures. These were compared with other theoretical and experimental results, showing a good correspondence. This approach was later also applied on the well-known paddle wheel MOF, HKUST-1 [63]. Here some speficic potential terms were introduced for a better description of the square planar coordination environment of the metal ions. The authors again validated the force field by studying vibrational frequencies, structural parameters and by performing MD simulations to obtain elastic and thermal properties.

Their latest development was the construction of MOF-FF [64]. Here, they decided to abandon

the MM3 energy expression and the MM3 parameters for the organic linkers, and all covalent parameters of the force field were refitted on small nonperiodic cluster models. The electrostatic interaction was described using a Coulombic interaction between Gaussian charge distributions and therefore all interactions could be included, in contrast with other force fields, where often the 1-2 and 1-3 interactions are excluded. After a careful analysis of the van der Waals interactions [65] with special attention for reproducing guest-host interactions in MOF-5, they concluded that the MM3-Buckingham potential provides a better description than the Lennard-Jones potential for the dispersion interactions. The parametrization procedure was still based on the minimization of an objective function, depending on the ab initio equilibrium geometry and Hessian in internal coordinate space, via a genetic algorithm approach. They demonstrated their methodology on experimentally known and well-studied MOFs. To this end, they proposed a number of nonperiodic clusters for the organic linkers and inorganic building blocks. Their test set included among other HKUST-1, MOF-5, UiO-66 and DMOF-1 and the authors reported an excellent reproduction of the ab initio results.

A recent general force-field parametrization protocol was proposed by Grimme [66]. The Quantum Mechanically Derived Force Field (QMDFF) is a black-box procedure based solely on quantum mechanical input data such as the equilibrium structure, ab initio Hessian, atomic partial charges and covalent bond orders. QMDFF aims to reproduce the QM PES, but is not transferable to other systems. The force field is able to describe the dissociation of bonds, but not the formation of new bonds. The method itself was not tested on MOFs, but was benchmarked on different properties such as vibrational frequencies and atomization energies. Some transition metal complexes were studied and showed a good agreement with the ab initio calculations, indicating that QMDFF could in principle be applied to the complex metal clusters in MOFs. The covalent potential terms all have anharmonic contributions, which allow for an accurate description of strong chemical bonds (such as $N_2$), and weak metallic interactions and cross terms are included for neighboring bonds. The bending, inversion and torsional terms are multiplied with damping terms, such that at infinite distances the energy is only described by the bond stretch terms. The most innovating part of the QMDFF energy expression consists of the noncovalent potential terms. This is separated in different contributions such as the Pauli repulsion, electrostatic interaction and London dispersion. The electrostatic interaction is modeled using the standard Coulombic potential between point charges, where the interactions between 1-2 and 1-3 pairs (atoms seperated by one and two covalent bonds) are excluded. The fitting procedure of the unknown parameters is based on a least-square fit of the force field Hessian to the ab initio Hessian. QMDFF provides excellent results on a wide variety of systems as well as for several hard-to-describe properties such as atomization energies. Future work will need to validate the entire QMDFF approach.

A final and most recent general parametrization protocol is QuickFF [67], which was used in this thesis and will be discussed in Section 2.2.3.

## 2.2 Methodology

In this section, the different parts of the force fields and the methodology to derive them are discussed.

### 2.2.1 Force-field energy expression

The multidimensional potential energy surface is approximated with the following analytical expression:

$$V^{FF} = \underbrace{V_{bond} + V_{bend} + V_{oop} + V_{torsion}}_{V^{FF}_{cov}} + \underbrace{V_{EI} + V_{vdW}}_{V^{FF}_{noncov}} \tag{2.1}$$

The covalent part of the force field models the interaction between the chemically bonded atoms as function of the bond distance (bond), bend angle (bend), out-of-plane distance (oopd) and dihedral angle (torsion). The internal degrees of freedom are illustrated in Figure 2.1. The bond stretches are described using a harmonic potential:

$$V_{bond} = \sum_{n=1}^{N_{bonds}} \frac{K_{r,n}}{2} \left(r_n - r_{n,0}\right)^2 \tag{2.2}$$

where $K_{r,n}$ is the force constant and $r_{n,0}$ the rest value. Here, the summation runs over all pairs of neighboring, i.e. chemically bonded, atoms. The internal coordinate in this expression is the bond length $r_n$. The bends are described using a similar term, but now the internal coordinate is the angle between two neighboring bonds:

$$V_{bend} = \sum_{n=1}^{N_{bends}} \frac{K_{\theta,n}}{2} \left(\theta_n - \theta_{n,0}\right)^2 \tag{2.3}$$

The out-of-plane distances are also described using a harmonic potential:

$$V_{oopd} = \sum_{n=1}^{N_{oopd}} \frac{K_{d,n}}{2} \left(d_n - d_{n,0}\right)^2 \tag{2.4}$$

This is a four-atom interaction, where the internal coordinate is the distance between the central atom and the plane determined by its three neighbors. This term allows for a more accurate description of planar $sp^2$ and some nonplanar $sp^3$ configurations. The added value of this term for MIL-53(Al) and a set of organic molecules was shown in Ref. [67].

The fourth covalent term is the dihedral energy term. Here, a cosine term is used as a function of the dihedral angle, including the multiplicity $m_{\phi,n}$ of the dihedral angle.

$$V_{torsion} = \sum_{n=1}^{N_{dih}} \frac{K_{\phi,n}}{2} \left(1 - \cos(m_{\phi,n}(\phi - \phi_0))\right) \tag{2.5}$$

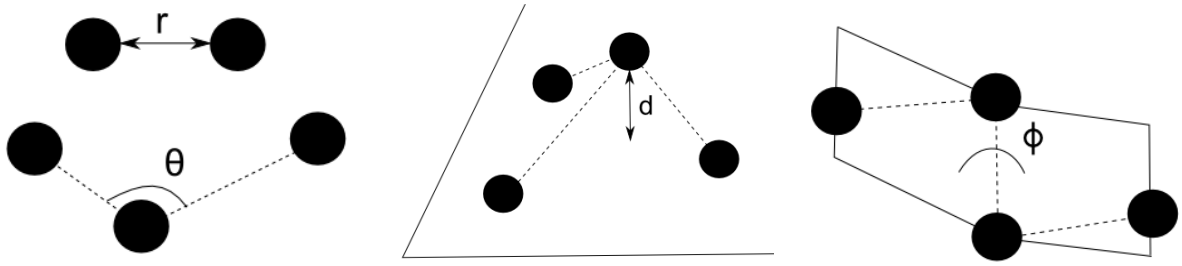


**(a)** Bond stretch and bend angle **(b)** Out-of-plane distance **(c)** Dihedral angle

**Figure 2.1:** Illustration of the different internal coordinates used in the covalent energy expression. The dotted lines represent the chemical bonds between the atoms.

The unknown parameters in all terms (force constants, rest values and multiplicities) in the covalent energy expression can be estimated directly with QuickFF (see Section 2.2.3).

The separation between the covalent and the noncovalent interactions is not strictly defined. In the covalent terms, representing the chemical bonds, there is some electrostatic interaction included. This is certainly the case for ionic bonds where there is a large transfer of electrons between the two atoms.

The electrostatic interaction is modeled with a Coulombic potential between Gaussian charge distributions:

$$V_{EI} = \frac{1}{2} \sum_{\substack{i,j=1 \\ (i \neq j)}} \frac{q_i q_j}{4\pi\epsilon_0 r_{ij}} \mathrm{erf}\left(\frac{r_{ij}}{d_{ij}}\right) \tag{2.6}$$

In this work, Gaussian charge distributions are used with a total charge $q_i$ and radius $d_i$, centered on atom $i$. The mixed radius of the Gaussian charges, $d_{ij}$, is given by $\sqrt{d_i^2 + d_j^2}$. The interaction depends on the distance $r_{ij}$ between the two atoms. The van der Waals part is described using the MM3-Buckingham potential. This term includes Pauli repulsion and dispersion interactions.

$$V(r) = \epsilon_{ij} \left[ 1.84 \times 10^5 \exp\left(-12 \frac{r}{\sigma_{ij}}\right) - 2.25 \left(\frac{\sigma_{ij}}{r}\right)^6 \right] \tag{2.7}$$

The noncovalent interactions are discussed in Sections 2.2.4 and 2.2.5.

Another aspect of a force field are the atom types. Atom types are assigned based on the element and the molecular environment or thus the connectivity. A covalent interaction between different atoms with the same atom types have the same force constant and rest value. Each atom type has a set of nonbonded parameters. This consists of an atomic charge $q_i$, a distribution width $d_i$, a van der Waals radius $\sigma_i$ and a van der Waals interaction strength $\epsilon_i$, which are used to model the noncovalent interactions (see Sections 2.2.4 and 2.2.5).

### 2.2.2 Cluster model approach

To estimate the force-field parameters for the periodic crystal, representative nonperiodic clusters are proposed. This approach is inspired by the composition of a MOF, which is built from metal clusters connected through organic linkers. The model systems represent the inorganic metal cluster and the organic linker. The use of cluster models is considered well-established for the force field development of MOFs. The group of Schmid have used this approach several times [56, 61, 63, 64], but many others have followed their strategy [14, 47, 58, 68]. Moreover, it is exactly this cluster model approach that allows a large-scale screening of MOFs.

An important aspect in a nonperiodic cluster model is the termination. This is required to reduce the effects of an artificial charge or spin introduced by truncating the chemical cluster. Appropriate groups are required to saturate the dangling bonds and different approaches can be found in the literature. An example is the $Li^+$ saturation of oxygen atoms in the models for the organic linkers of the IRMOF series [47, 61]. Their argument is that the ionic radius of $Li^+$ is similar to $Zn^{2+}$, which is bonded in the periodic crystal to the oxygen atoms. Wang *et al.* [69] used proton saturation in their cluster model for ZIF-8. Vanduyhuys *et al.* [14] terminated the inorganic cluster model of MIL-53 along the metal chain with hydrogen atoms. For each family of MOFs other solutions exist and the examples given in the literature are used in this work.

The main disadvantage of the finite clusters is the neglection of long-range interactions. To describe these long-range interactions, the electrostatic interaction (Section 2.2.4) and van der Waals interactions (Section 2.2.5) require a good potential energy expression, which can pose a problem. The use of atomic charges derived from a finite cluster assumes that the finite cluster is able to capture the main features of the electrostatic potential of the periodic system.

Finally, not all force-field parameters derived for the cluster are transferred to the periodic structure. Only those parameters defined for the core region of the cluster model are used. For a reliable estimate, this core region has to be far enough from the termination. In following sections, the atom types of the core region considered in the cluster model are indicated on the figures.

### 2.2.3 Covalent interactions with QuickFF

The covalent part of the ab initio derived force fields are constructed with QuickFF. It is a Python software package developed at the Center for Molecular Modeling (CMM) by Vanduyfhuys *et al.* and details can be found in Ref. [67]. QuickFF is designed to generate accurate force fields for MOFs, although it is applicable on a wide variety of molecular systems. The general idea of the fitting procedure is to reproduce the ab initio (AI) equilibrium geometry and Hessian matrix in Cartesian coordinate space $\mathbf{H}^{AI}$ as accurate as possible. To this end, a four-step method is used, which is briefly discussed here.

A crucial part in the force field, especially for flexible MOFs, are the dihedral force-field parameters. The integer dihedral multiplicities $m_k$ and rest angles $\phi_{0,k}$ are estimated in the first step, based on the ab initio equilibrium geometry. The multiplicity determines the periodicity of the energy term and controls the symmetry of the local topology. An example is the dihedral $O_{ca}$-$C_{ca}$-$C_{pc}$-$C_{ph}$ in the organic linker of MIL-53 (see Figure 2.13) with energy minima at 0° and 180° and thus multiplicity 2. QuickFF tries to describe each dihedral pattern and if no unique multiplicity and rest value are found, the dihedral is neglected. An illustration of the generation procedure of $m_k$ and $\phi_{0,k}$ for dihedrals can be found in the supporting information of Ref. [67].

In the second step, perturbation trajectories are generated on the PES around the equilibrium, which are used to fit the force constants and rest values of the harmonic covalent terms. The internal coordinates considered in this step are the bonds, bends and out-of-plane distances, which are all described by means of a harmonic potential energy term. For each internal coordinate (IC) $q_n$, a trajectory is constructed by slightly perturbing $q_n$ to a value $\tilde{q}_n$ in such a way that the energy change of the system is approximately only dependent on the perturbation $\tilde{q}_n$. As such, the energy change along the trajectory is ascribed entirely to the covalent harmonic term belonging to $q_n$. To obtain such a trajectory, a cost function is defined:

$$\chi_n^s\left(\overrightarrow{R}(\tilde{q}_n)\right) = \frac{1}{2}\sum_{m\neq n}\left[q_m\left(\overrightarrow{R}(\tilde{q}_n)\right) - q_m\left(\overrightarrow{R}_0\right)\right]^2 \tag{2.8}$$

where the summation runs over all ICs apart from the perturbed IC $q_n$. $\overrightarrow{R}$ is the vector with the Cartesian coordinates of the atoms. As only small perturbations are considered, $q_m(\overrightarrow{R})$ can be approximated by a first-order Taylor expansion evaluated at the ab initio equilibrium $\overrightarrow{R}_0$. In this way, the cost function can be rewritten as the product of a strain matrix $\mathbf{S}_n$ and the deviation of the Cartesian coordinates from the equilibrium geometry:

$$\chi_n^s\left(\overrightarrow{R}(\tilde{q}_n)\right) = \frac{1}{2}\left(\overrightarrow{R}(\tilde{q}_n) - \overrightarrow{R}_0\right)^T \cdot \mathbf{S}_n \cdot \left(\overrightarrow{R}(\tilde{q}_n) - \overrightarrow{R}_0\right) \tag{2.9}$$

This strain matrix depends on the uniquely defined derivative of the ICs toward the Cartesian coordinates evaluated at the ab initio equilibrium geometry. After some further manipulations to obtain a better conditioned set of equations (details can be found in the supporting information of Ref. [67]), this cost function is minimized and a minimally strained system under the constraint of the fixed perturbed $\tilde{q}_n$ is found. In this way, the internal coordinate $q_n$ is decoupled as much as possible and by repeating this minimization procedure for different perturbations, a set of Cartesian coordinates $\overrightarrow{R}_n$ is obtained representing the perturbation trajectory of $q_n$. In this work, the QuickFF default of eleven perturbations is used in a range of 0.05 Å for distances and 5° for angles for each bond, bend and out-of-plane distance.

The ab initio total energy along the perturbation trajectory of $q_n$ can be approximated with the ab

initio Cartesian Hessian:

$$V^{AI}\left(\overrightarrow{R}(\tilde{q}_n)\right) \approx V_0^{AI} \; + \; \left[\nabla V^{AI}\right]^T \cdot \left(\overrightarrow{R}(\tilde{q}_n) - \overrightarrow{R}_0\right) \; + \; \frac{1}{2}\left(\overrightarrow{R}(\tilde{q}_n) - \overrightarrow{R}_0\right)^T \cdot \mathbf{H}^{AI} \cdot \left(\overrightarrow{R}(\tilde{q}_n) - \overrightarrow{R}_0\right) \tag{2.10}$$

As the perturbation trajectories are constructed with a strain minimized according to Eq. 2.8, the force-field energy can be approximated as follows:

$$\begin{aligned} V^{FF}\left(\overrightarrow{R}(\tilde{q}_n)\right) &= V_{EI}^{FF}\left(\overrightarrow{R}(\tilde{q}_n)\right) + V_{cov}^{FF}\left(\overrightarrow{R}(\tilde{q}_n)\right) \\ &\approx V_{EI}^{FF}\left(\overrightarrow{R}(\tilde{q}_n)\right) + \frac{K_n}{2}\left(\tilde{q}_n - q_{0,n}\right)^2 + c \end{aligned} \tag{2.11}$$

where it is thus assumed that the change of the covalent energy is only due to the change of the harmonic term corresponding with $q_n$ and where $c$ is a constant. When equating $V^{AI}$ and $V^{FF}$ according to Eqs. 2.10 and 2.11, the only remaining unknowns are the force constant and rest value belonging to the potential energy term of $q_n$. By fitting a parabola to the difference of $V^{AI}$ and $V_{EI}^{FF}$ a direct estimate of these force-field parameters can be found. Note that in Eq. 2.11 not the entire total force field energy expression is used as defined in Eq. 2.1. The van der Waals interactions are neglected here and only the nonbonded electrostatic interactions are used. This is justified as the ab initio calculations have been performed with DFT using the hybrid B3LYP functional. As standard DFT with a regular functional includes little to no dispersion, it would be wrong to subtract the energy related to these interactions and include these effects in the fit. After this step, a first estimate for the force constants and rest values of the harmonic terms is obtained. Force-field parameters of ICs with the same atom types are averaged afterwards. This fitting procedure is designed to minimize correlations among the force-field parameters. However, these perturbation trajectories are not completely decoupled. There is still some contribution from the covalent energy assigned to ICs different from the perturbed IC and this leads to an overestimation of the force constants. This overestimation is corrected for in the third step. No perturbation trajectories are generated for the dihedrals as the aim of this second step is a reliable determination of rest values, which were already determined for dihedrals in the first step.

In the third step, the force constants $\overrightarrow{K}$ are refined for all covalent terms (including the dihedrals) by explicitly fitting the potential energy expression to the ab initio Cartesian Hessian keeping the rest values fixed. This is carried out using following cost function:

$$\chi^H(\overrightarrow{K}) = \sum_{i \leq j}\left(\left[\mathbf{H}^{AI}\right]_{ij} - \frac{\partial^2 V_{EI}^{FF}}{\partial R_i \partial R_j} - \frac{\partial^2 V_{cov}^{FF}}{\partial R_i \partial R_j}(\overrightarrow{K})\right)^2 \tag{2.12}$$

The van der Waals interactions are again neglected. In the fourth step, which is not included in the original QuickFF methodology, the rest values are refined by revisiting the perturbation trajectories from the second step. In contrast to the second step, the whole covalent energy expression is used instead of attributing the energy change entirely to the perturbed IC $q_n$. All force-field parameters

are kept fixed, except the rest value of the potential term belonging to $q_n$, which is subsequently fitted.

All steps are separated to avoid fitting deficiencies due to the correlations between the force constants and rest values. This fitting procedure leads to the generation of a harmonic covalent force field where no cross terms are required to obtain accurate results by construction. Other force field fitting procedures typically rely on the reproduction of a Hessian in internal coordinate space, which is obtained after a non-uniquely defined transformation from the ab initio Cartesian Hessian. Another advantage of this method, where the ab initio Cartesian Hessian is directly used, is thus the elimination of this ambiguous transformation.

**Dihedral potential energy term**

In some special occasions, the description of the dihedral potential energy term according to Eq. 2.5 is not sufficient. However, QuickFF is designed in such a way that more advanced potentials can easily be introduced in the third step, while the first and second step can be carried out without any adjustments. The perturbation trajectories generated with QuickFF for the harmonic ICs can still be used to estimate a first value for the force constants and rest values. Then one can add the extra dihedrals, such that they are included in the refinement steps.

Three cases where QuickFF fails in obtaining a reliable dihedral energy term are shown here. The first example occurs when studying a triphenyldicarboxylate (TPDC) organic linker in e.g. IRMOF-16. In Figure 2.2 the cluster model with the relevant atom types is shown. The problem arises from the fact that multiple minima cannot be described by a single cosine term. The dihedral pattern $C_2$-$C_3$-$C_4$-$C_5$ in this cluster has multiple minima at $\phi_0$, $-\phi_0$, $\pi - \phi_0$ and $\phi_0 - \pi$ with $\phi_0$ approximately 38°.

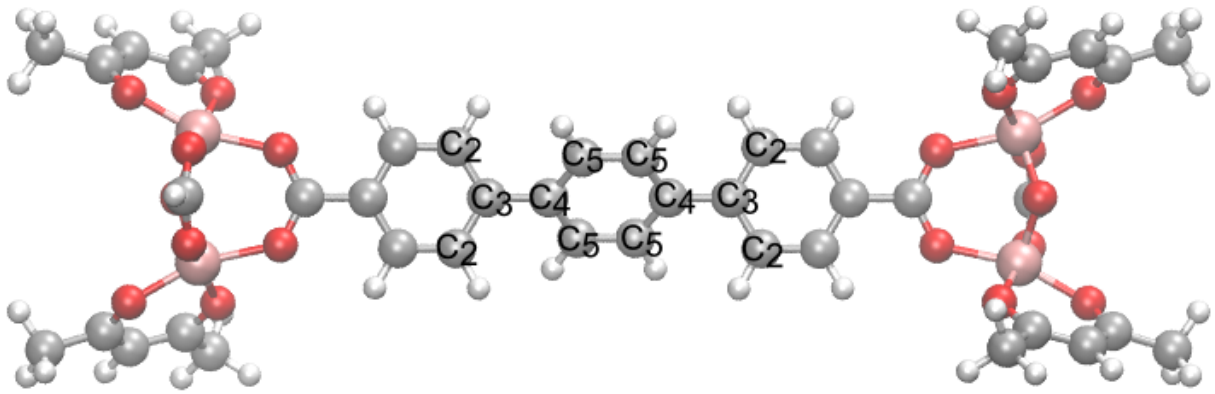


**Figure 2.2:** Cluster model for a triphenyldicarboxylate (TPDC) linker of MIL-53. The problematic dihedral pattern $C_2$-$C_3$-$C_4$-$C_5$ has multiple local energy minima that cannot be described using the single cosine term shown in Eq. 2.5.

To describe these minima, an ab initio scan over the dihedral angle was performed and a series of

cosines (see Eq. 2.13) was fitted to these data to obtain a good reproduction. In this equation it was found that $N$ had to be minimally three. The energy scale shown in Figure 2.3 is for one such dihedral pattern relative to the minimum at 38°. Along one TPDC linker, there are eight of them present. Note that to be consistent, the energy related to the electrostatic interactions has been subtracted before performing the fit.

$$V_{dih}^{FF}(\phi) = \sum_{i=1}^{N} [A_i \cos(2i(\phi - \phi_0)) + B_i \cos(2i(\phi - (\pi - \phi_0)))] \tag{2.13}$$

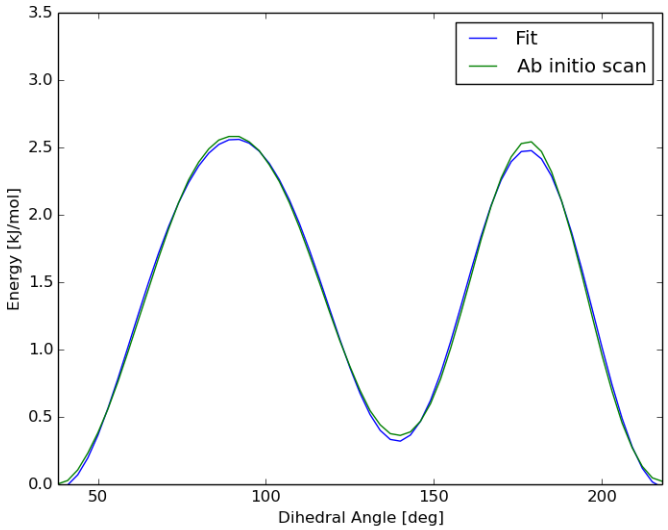


**Figure 2.3:** The ab initio scan and potential energy term for the dihedral pattern $C_2$-$C_3$-$C_4$-$C_5$ in MIL-53(Al).

In the literature other force field dihedral terms are available to describe such dihedral patterns and more elaborate schemes exist for fitting an accurate energy barrier [66, 70]. This ab initio scan has been performed for this cluster model (with inorganic part of MIL-53(Al)), but it can be expected that this rotational barrier is nearly independent of the inorganic metal node attached to this linker. For that reason, the force-field parameters were directly transferred to all other TPDC linkers studied in this work.

A second problem encountered with the dihedral fitting by QuickFF, is when no unique rest value emerges from the geometry-based procedure. This problem arises for some functionalized linkers where due to steric effects a rotation of the inorganic part around the $C_{ca}$-$C_{pc}$ axis is visible. This is illustrated in Figure 2.4 for a MIL-53 cluster model functionalized with a bromine atom. This rotation is a finite-cluster effect. Due to the lack of framework constraints, one end of the cluster can rotate around the $C_{ca}$-$C_{pc}$ axis, while the other end does not, lowering the energy as the Pauli interactions between the larger bromine electron cloud and the inorganic part can be minimized by this twist.

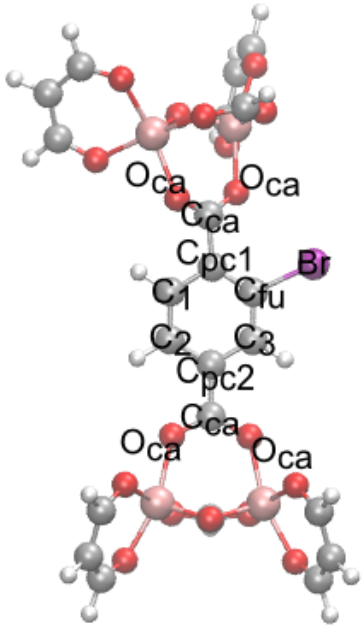


**Figure 2.4:** Rotation around the $C_{ca}$-$C_{pc}$ axis due to steric effects.

The dihedral patterns $C_2$-$C_{pc2}$-$C_{ca}$-$O_{ca}$ and $C_3$-$C_{pc2}$-$C_{ca}$-$O_{ca}$ are correctly determined with QuickFF. A multiplicity of 2 and rest value of 0° is detected. However, QuickFF does not succeed in detecting a unique pattern for $C_1$-$C_{pc1}$-$C_{ca}$-$O_{ca}$ and $C_{fu}$-$C_{pc1}$-$C_{ca}$-$O_{ca}$. Here, the ab initio equilibrium geometry predicts a dihedral angle of 38°. This can easily be described with the single cosine energy term (Eq. 2.5) using a rest value of 38° and multiplicity 2. By adding it in the third step of the fitting procedure, a force constant of e.g. 5.25 kJ/mol in MIL-53(Al) with a bromine functional group is found.

In the third problem, QuickFF gives a zero potential energy barrier. This is the case for the linker illustrated in Figure 2.5 for the dihedral $C_2$-$C_3$-$C_4$-N. The system can be described with a single cosine term with rest value 0° and multiplicity 2. In the periodic structure, using the parameters derived from this cluster for the organic linker, a dihedral angle is measured in the force field optimized structure between 40° and 50° for different inorganic clusters, which is due to noncovalent electrostatic and van der Waals interactions.

This problem, the underestimation of so-called soft dihedral patterns, was also noted in Ref. [67], when QuickFF was validated on an extensive set of organic molecules. The problem was explained by the fact that these dihedrals typically correspond to anharmonic motions. They are not well described as the fitting procedure is based on the Hessian and thus harmonic motions. To obtain an accurate parametrization, a scan is performed of the potential energy surface along this dihedral motion. The simulated result and the corresponding fitted potential term are shown in Figure 2.6. The deviation between both is to be expected, as a single cosine term is not able to accurately describe the whole dihedral motion.

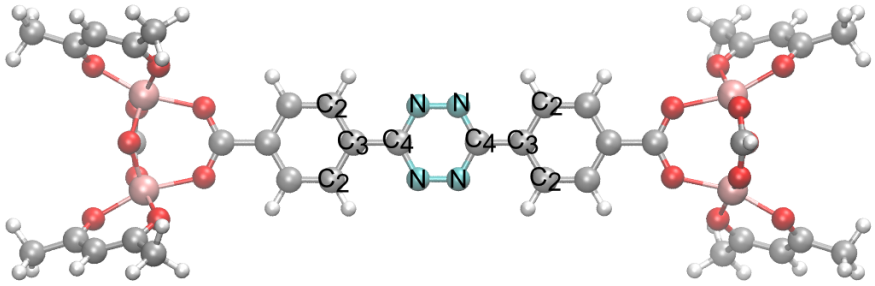


**Figure 2.5:** Organic linker where QuickFF gives a zero potential energy barrier for the dihedral $C_2$-$C_3$-$C_4$-N.

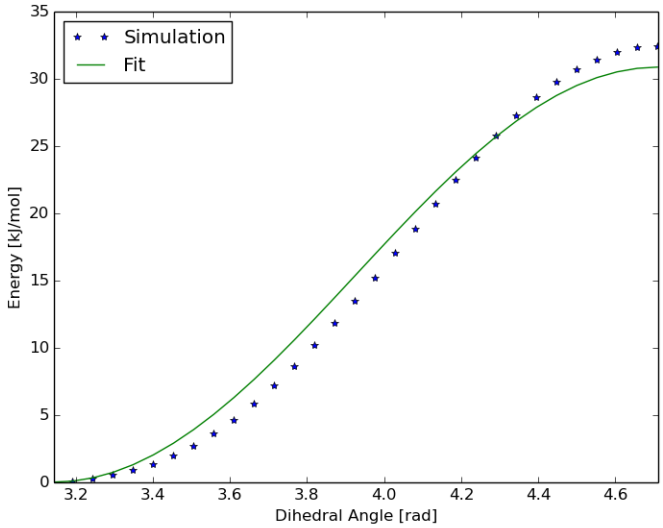


**Figure 2.6:** Scan of the potential energy surface along the dihedral angle of $C_2$-$C_3$-$C_4$-N over 90°.

Finally, by default, QuickFF attempts to estimate dihedral force-field parameters for every dihedral pattern present in the molecular system. As such, it also tries to determine them in the highly coordinated environments of the inorganic clusters (e.g. the octahedrally coordinated metal ions in MIL-53). However, QuickFF typically neglects these terms as no unique patterns are detected. The covalent energy terms such as the bonds and bends are sufficient to accurately describe these rigid parts, such that no reparametrization of the neglected dihedrals is required.

### Anharmonic terms

In Chapter 3, the influence of anharmonic contributions to bond and bend terms is evaluated for the calculation of the intrinsic anharmonic thermal expansion behavior. It was opted to use the anharmonic contributions as proposed in the MM3 force-field energy expression [50]. They result in a quartic potential term for the bonds

$$V_{bond} = \frac{K_r}{2}(r - r_0)^2 \left[1 - 2.55(r - r_0) + \frac{7}{12}(2.55(r - r_0))^2\right] \tag{2.14}$$

and a sixth-order polynomial for the bends.

$$V_{bend} = \frac{K_\theta}{2}(\theta - \theta_0)^2 \left[1 - 0.14(\theta - \theta_0) + 5.6 \cdot 10^{-5}(\theta - \theta_0)^2 - 7 \cdot 10^{-7}(\theta - \theta_0)^3 + 2.2 \cdot 10^{-8}(\theta - \theta_0)^4\right] \tag{2.15}$$

This has also been used in MOF-FF. The estimated force constants and rest values with QuickFF can be recuperated in these expressions, as the fixed anharmonic contributions are higher-order correction terms of the harmonic potential. As illustrated in Figure 2.7, these small contributions have a large influence on the potential energy further away from the equilibrium.

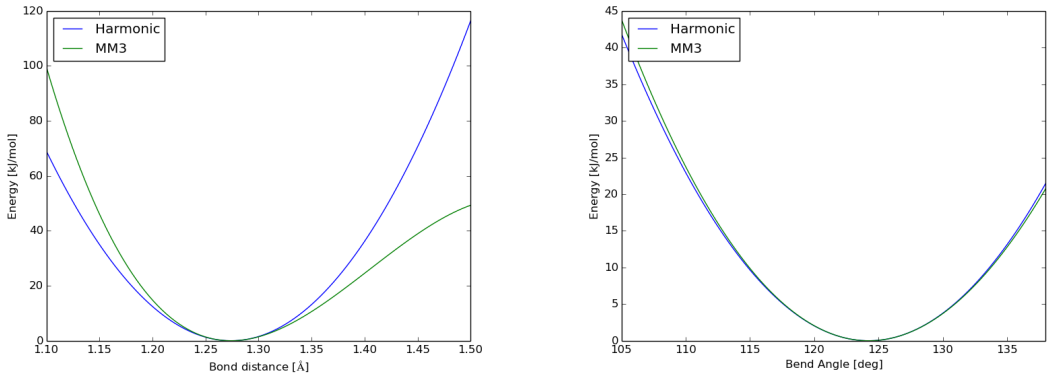


**Figure 2.7:** Comparison of standard harmonic potential and potential with fixed anharmonic contributions for a bond (left) and bend (right).

### 2.2.4 Electrostatic interaction

In force fields, the electrostatic interaction is typically described as a pairwise Coulombic interaction between point charges. This is a simplified description that is not always sufficiently accurate. As the cluster models are only finite representations of the periodic structure and the electrostatic interaction is a long-range interaction, a good set of charges is required for an accurate model of the periodic crystal. The atomic charges used in the force fields should be able to accurately describe the molecular electrostatic potential. However, one would also like transferable charges such that charges of various atoms in similar molecular environments are approximately the same, and still give a good representation of the electrostatic potential. Especially force field investigations of guest-framework interactions require a precise tuning of the charges as the only interactions between guest and host are the electrostatic and van der Waals interaction. Hamad *et al.* [71] recently illustrated that the chosen charges can also have an influence on structural properties such as the negative thermal expansion behavior of MOF-5.

In general, two distinct routes are available for obtaining atomic charges. The most popular methods used in force field development for MOFs are the electrostatic potential (ESP) fitting schemes. Here, the charges are directly fitted to reproduce the ab initio ESP. Opposed to these ESP fitting methods

are the population analysis schemes or atom-in-molecules (AIMs) schemes. In these schemes, one starts from the idea that the molecular electron density can be partitioned in contributions of the different atoms, hence the name atom-in-molecule. Examples are the Iterative Hirshfeld scheme and the Minimum Basis Iterative Stockholder scheme. More details on other methods that have been used to derive atomic charges in MOFs can be found in Ref. [71].

**Electrostatic potential (ESP) fitting**

Charges derived from such a scheme succeed in reproducing the ESP quite well outside the molecule, which is desired for a good force field. The basic idea of these methods is always the same, i.e. fitting the charges to reproduce the electrostatic potential at chosen grid points. These methods differ in the choice of weight function $W(\overrightarrow{r})$ and/or grid points. If only atomic charges are used and not higher-order multipoles, the cost function can basically be represented by:

$$\begin{aligned} f(q_1, q_2, ..., q_N) &= \sum_{j=1}^{n} \left[V_j^{ESP}(q_1, q_2, ..., q_N) - V_j^{AI}\right]^2 W_j \\ &= \frac{1}{4\pi\epsilon_0} \sum_{j=1}^{n} \left[\sum_{i=1}^{N} \frac{q_i}{r_{ij}} - V_j^{AI}\right]^2 W_j \end{aligned} \tag{2.16}$$

where $r_{ij}$ is the distance between atom $i$ and grid point $j$ with $n$ the number of grid points. One typically adds the fixed total charge constraint using a Lagrange multiplier, i.e. one forces the sum of the charges to be equal to the total charge of the molecular system. Important here is that an accurate description of the ESP in the near-atom space is less desired. This can be understood from the fact that most contributions to the short-range interactions between the atoms are represented by the covalent terms such as the bond stretch. Very distant points, where the electrostatic potential is only sensitive to the total charge of the system and not the contribution, are neglected in the fit to avoid an ill-conditioned system of equations. These considerations lead to a cost function dominated by the mid-range space in the fitting procedure.

Two schemes were considered, but other methods are available and have been used on MOFs. The first method is the popular scheme known as the Merz-Kollman (MK) scheme [62]. The ab initio electrostatic potential is evaluated at a number of grid points located on several layers with a fixed density of grid points around the molecule. Each atom is assigned an atomic radius and the layers are constructed as an overlay of the spheres with scaled radii. Near-atom space is not considered as the volume within the envelope of the spheres is discarded in the fitting procedure. A discontinuous weight function is used that is zero at short and long distance and one in the medium range. Another scheme is the one proposed by Hu *et al.* [72]. A weight function was introduced weights points within the medium range of the atoms more heavily. The aim was to improve the numerical accuracy of existing ESP fitting methods and solve problems with the overestimation of charges. However, an important problem that remains with these ESP methods, is the transferability of the

charges in different molecules. The charges show a strong dependence on the molecular geometry. A solution that reduces this effect to some extent, is the restrained ESP (RESP) method. Here, a regularization term is added in the cost function, mainly to solve the buried charges problem, i.e. the weak dependence of the ESP on the charges of atoms buried in layers of other atoms, which can result in chemically nonintuitive values. This method was also tested, but did not seem to give meaningful results.

In this work, most MOFs were based on the connection of a metal node to the organic linker by a dicarboxylate group. As this group is present in the inorganic and organic cluster model, it is logical to demand that on the connection between both parts the charges should be very similar in both clusters. In Figure 2.8, charges derived on various cluster models considered in this work via different charge schemes are shown. On the horizontal axis the charges obtained in the inorganic cluster are shown, while the charges derived on the organic linker are shown on the vertical axis. Robust charges lie on the bisector. It can immediately be seen that the ESP charges strongly deviate from the bisector, implicating that these charges are not robust with respect to molecular environment. What is not shown in this figure, is the standard deviation of the charges for each atom type in the cluster itself, which is also significantly worse for ESP charges. The ESP fitted charges will, due to this behavior, not be considered for constructing the force fields, but the reproduction of the electrostatic potential will be measured for other schemes through the cost function (see Eq. 2.16), intuitively validate the quality of the charges.

**Iterative Hirshfeld (HI) partitioning scheme**

A first AIM scheme considered in this work is the HI partitioning scheme [73], which is an extension of the original Hirshfeld method [74]. The electron density in each point is distributed among all atoms. The atomic electron density $\rho_A(\overrightarrow{r})$ is determined by the product of a weight function $w_A(\overrightarrow{r})$ and the ab initio molecular density $\rho(\overrightarrow{r})$:

$$\rho_A(\overrightarrow{r}) = w_A(\overrightarrow{r})\rho(\overrightarrow{r}) \tag{2.17}$$

The weight function of atom $A$ is defined by the ratio of the ab initio electron density calculated for the isolated atom $A$ and the so-called pro-molecular density, which is the superposition of the electron densities of the isolated atoms.

$$w_A(\overrightarrow{r}) = \frac{\rho_A^0(\overrightarrow{r})}{\rho_0(\overrightarrow{r})} \text{ with } \rho_0(\overrightarrow{r}) = \sum_A \rho_A^0(\overrightarrow{r}) \tag{2.18}$$

A problem with the original Hirshfeld scheme was the strong dependency of the atomic charges on the chosen $\rho_A^0(\overrightarrow{r})$. This is solved by imposing an iterative scheme (HI), where this density is updated every iteration. The weight function is defined based on the electron density of the previous

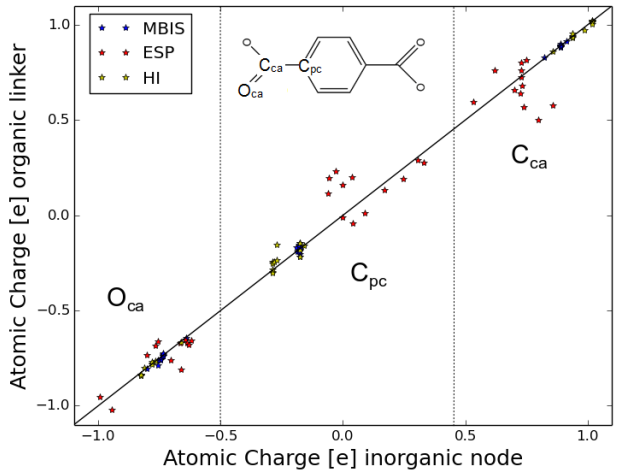


**Figure 2.8:** Evaluation of the transferability of ESP, HI and MBIS charges. On the horizontal axis the charges obtained in the inorganic cluster are shown, while the charges derived in the organic linker are shown on the vertical axis. Robust charges lie on the bisector.

step, so that Eq. 2.17 can be rewritten to yield

$$w_A^i(\overrightarrow{r}) = \frac{\rho_A^{i-1}(\overrightarrow{r})}{\rho^{i-1}(\overrightarrow{r})} \tag{2.19}$$

The atomic charges have converged when the electron population of the atoms does not longer change or

$$\Delta_A^i = |N_A^i - N_A^{i-1}| \tag{2.20}$$

is zero for each atom. The atomic populations obtained in each step are usually fractional numbers. To obtain a suitable isolated electron density to describe the pro-molecular density in each step, one uses linear interpolations of the electron densities of the neutral atom and different charged states. In other words, one needs a database of electron densities of different charge states for the atoms under study. The atomic charge is then given by the difference of the atomic number and the electron population of atom $A$ in the last step

$$q_A = Z_A - N_A \tag{2.21}$$

Different studies have shown that this approach combines ESP accuracy with transferability. However, the problem with HI is the overestimation of the charges in a strong ionic environment [75]. An example is the charge on an oxygen atom chemically bonded to an atom with low electronegativity. This results in oxygen charges between -1e and -2e. As a consequence, the scheme as presented above requires the density of an artificial unstable oxygen dianion to describe the pro-molecular density. A new scheme was proposed to solve some of the problems related to this: Extended Hirshfeld [76]. Early tests showed that this scheme strongly underestimates the atomic charges in the inorganic part of the MOFs. For this reason, this scheme was not applied in this thesis.

**Minimal Basis Iterative Stockholder (MBIS) partitioning scheme**

Currently, a new atom-in-molecules scheme is being developed at the CMM. It will be shown in Section 2.3, that the charges obtained in this way are superior to the ones obtained with Hirshfeld-I. They provide a better reproduction of the electrostatic potential as measured via the ESP cost and are more robust and transferable than the ESP fitted charges.

In this partitioning scheme, the molecular electron density is again split up into atomic contributions. The pro-molecular density is expanded in a sum of 1s-Slater functions:

$$\rho_0(\overrightarrow{r}) = \sum_{i=1}^{N} \sum_{\alpha=1}^{n_i} \frac{N_{i_\alpha}}{8\pi\sigma_{i_\alpha}^3} e^{-\frac{|\overrightarrow{r}-\overrightarrow{R_i}|}{\sigma_{i_\alpha}}} \tag{2.22}$$

This sum runs over all atoms $N$ and over all electron shells $n_i$ of atom $i$. The unknowns in this expression are the electron population $N_{i_\alpha}$ and the slope $\sigma_{i_\alpha}$ of the Slater function. These are fitted by minimizing the Kullback-Leibler divergence $D_{KL}$ of $\rho_0(\overrightarrow{r})$ with respect to the ab initio electron density $\rho(\overrightarrow{r})$:

$$D_{KL} = \int \mathrm{d}\overrightarrow{r}\, \rho(\overrightarrow{r}) \ln\left(\frac{\rho(\overrightarrow{r})}{\rho_0(\overrightarrow{r})}\right) \tag{2.23}$$

This objective function is used in information theory and is a measure of the information lost when $\rho_0(\overrightarrow{r})$ is used to approximate $\rho(\overrightarrow{r})$. By using this as a cost, as much information as possible from the ab initio density is contained in the pro-molecular density.

The atomic charge is then obtained by the difference of the atomic number $Z_i$ and the integration of the electron shells assigned to atom $i$ over the entire volume:

$$\begin{aligned} q_i &= Z_i - \sum_{\alpha=1}^{n_i} \frac{N_{i_\alpha}}{8\pi\sigma_{i_\alpha}^3} \int \mathrm{d}\overrightarrow{r}\, e^{-\frac{|\overrightarrow{r}-\overrightarrow{R_i}|}{\sigma_{i_\alpha}}} \\ &= Z_i - \sum_{\alpha=1}^{n_i} N_{i_\alpha} \end{aligned} \tag{2.24}$$

**Gaussian charge distributions**

The atomic charges were determined for every atom using one of the schemes as discussed previously. In the force field, these atomic charge distributions were described using a spherical Gaussian charge distribution. A spherical Gaussian charge is described by its total charge $q_i$ and the distribution width $d_i$. These parameters were determined with the method proposed by Chen and Martinéz [77]. In this method, the orbital exponents from s-type Gaussian orbitals are fitted to reproduce two-electron Coulomb integrals of s-type Slater orbitals. It was shown that these integrals, which actually represent the electrostatic interaction, can be reproduced with a small error by inexpensive Gaussian orbitals. This Gaussian orbital exponent can then be linked with an atomic

charge radius $d_i$.

The use of these charge distributions in force fields for MOFs was introduced in MOF-FF [64]. The Coulombic interaction between Gaussian charge distributions is given in Eq. 2.25. This approach has the advantage that the electrostatic interactions for high charges are damped at close distances, which is beneficial for the description of the inorganic part.

$$V_{EI}^{FF} = \frac{1}{4\pi\epsilon_0}\frac{q_i q_j}{r_{ij}}\mathrm{erf}\left(\frac{r_{ij}}{d_{ij}}\right) \text{ with } d_{ij} = \sqrt{d_i^2 + d_j^2} \tag{2.25}$$

A comparison of the Coulombic interaction between Gaussian charge distributions and point charges is made in Figure 2.9. The error functions damps the $r^{-1}$ behavior at short distances ($r \leq d_{ij}$). At larger distances ($r \geq d_{ij}$) both potentials give the same result as the error function is then equal to one.

In the fitting procedure of QuickFF, the energy related to the electrostatic interaction is subtracted from the ab initio energy before the covalent part is fitted. This means that the effect of this damping is accounted for in the covalent parameters. Moreover, due to this damping effect, it now makes more sense to include the 1-2 and 1-3 electrostatic interactions as was done in MOF-FF [64].

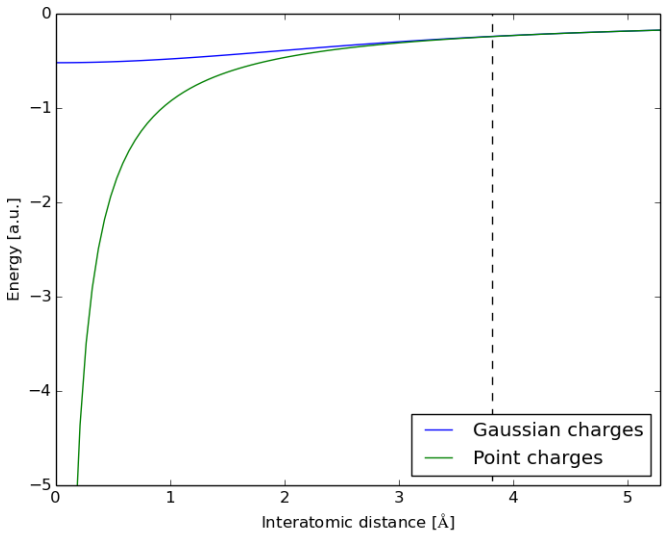


**Figure 2.9:** Comparison of Coulombic interaction between Gaussian charge distributions and point charges for an Al-$O_{ca}$ pair in MIL-53(Al). The black dotted line indicates an interatomic distance of $\sigma_{ij}$.

#### 2.2.4.1 Periodic charges via bond charge increments

Typically, the force fields are constructed using ab initio reference data generated on two different finite clusters. If the derived charges are directly transferred to the periodic crystal, no neutral unit

cell is found. To this end, the atomic charges are transformed into bond charge increments [78], which can be interpreted as a charge transfer from one atom to the other. This approach was previously used in the development of the force field of MIL-53(Al) by Vanduyfhuys *et al.* in Ref. [14].

The atomic charge $q_i$ is rewritten as the sum of a precharge $q_{i,0}$ and all bond charge increments $p_{ij}$. Here the summation runs over all atoms $j$ bonded to atom $i$.

$$q_i = q_{i,0} + \sum_j p_{ij} \tag{2.26}$$

Some of the cluster models were not neutral themselves. The precharge of all atoms in such a cluster was fixed to the total charge of the cluster divided by the number of atoms. This precharge was neglected in the transfer from the isolated clusters to the periodic structure. The bond charge increments were then fitted in a least-squares way to the atomic charge minus the fixed precharge.

### 2.2.5 van der Waals interaction

The van der Waals interactions are long-range attractive forces which stem from many-particle effects and play an important role in MOFs [79]. Standard DFT functionals do not capture these effects. Several solutions are available for the inclusion of these effects, such as specifically designed functionals or adding an empirical dispersion term to the energy. This last solution is the most popular method for including dispersion in calculations without much effort.

An advantage of force fields is the possibility to easily include these effects. Quantum mechanically one can derive a potential energy expression at large distance with a $r^{-6}$ dependence between two atoms separated with a distance $r$. This term describes the dipole-dipole interactions due to electron correlation. Repulsive interactions, resulting from the Pauli exclusion principle, are less straightforward to describe analytically, but they only play a role at short distances. A common approximation has a $r^{-12}$ dependence. This has no physical basis, but is chosen for the ease of calculation as the square of the attractive contribution. Both contributions lead to the well-known Lennard-Jones potential which approximates the interatomic potential:

$$V(r) = 4\epsilon \left[ \left(\frac{\sigma}{r}\right)^{12} - \left(\frac{\sigma}{r}\right)^{6} \right] \tag{2.27}$$

In this potential, $\sigma$ and $\epsilon$ are the equilibrium radius and well depth of the minimum. Another approximation for the repulsive part is the Buckingham potential, which is less repulsive than the Lennard-Jones potential and has an exponential dependence on the interatomic distance. This is inspired by the fact that electron-electron repulsions are well represented by exponential Slater-type functions. The potential is given by

$$V(r) = A \exp\left(-\frac{B}{r}\right) - \frac{C}{r^6} \tag{2.28}$$

where $A$, $B$ and $C$ are constants depending on the molecular situation. A problem with this potential is the incorrect limit for $r$ going to zero and the fact that it reaches a maximum at very short distances. This is due to the specific form of the potential, where the attractive interaction dominates at small separations ($r^{-6}$).

In most force fields, the van der Waals interactions are described with the Lennard-Jones potential. In the MM3 force field [50], the Buckingham potential was modified such that it only depends on two parameters. This form introduces a fixed steepness of the repulsive part. This is the so-called MM3 Buckingham potential:

$$V(r) = \epsilon_{ij} \left[ 1.84 \times 10^5 \exp\left( -12 \frac{r}{\sigma_{ij}} \right) - 2.25 \left( \frac{\sigma_{ij}}{r} \right)^6 \right] \tag{2.29}$$

The two parameters $\sigma_{ij}$ and $\epsilon_{ij}$ are, similarly as in the Lennard-Jones potential, the equilibrium distance and well depth of the potential. These parameters are typically determined with empirical mixing rules for the interaction between atom $i$ and atom $j$:

$$\sigma_{ij} = \sigma_i + \sigma_j \text{ and } \epsilon_{ij} = \sqrt{\epsilon_i \epsilon_j} \tag{2.30}$$

and these parameters were estimated in the MM3 force field for every atom and are tabulated in Ref. [80]. In MM3, the 1-2 and 1-3 interactions are discarded to avoid a strong overestimation of the repulsion terms. A comparison between the MM3 Buckingham potential and Lennard-Jones potential for MOFs was made by the authors of MOF-FF [64, 65]. They showed that the Lennard-Jones potential is too repulsive, which is why the authors of MOF-FF opted for the MM3 Buckingham potential. In this work, it was also chosen to use the MM3 Buckingham potential with the parameters of Ref. [80]. The MM3 van der Waals form has, however, several known problems in general and for the application on MOFs.

A first problem with the parameters of the MM3 force field is the accuracy of the repulsion between apolar hydrogen atoms. However, as was stated by Vanduyfhuys *et al.* [14] and the authors of MOF-FF, the effects are only minor. A second problem, as mentioned above, is the incorrect limit at short distances due to the functional form. In MOF-FF, this problem was solved by adding a damping term, but this artifact should have no influence due to the very high barrier, which is not thermally accessible at regular temperatures in MD simulations. The most important problem with the MM3 Buckingham term for the application on MOFs is that it is too repulsive, especially in the inorganic coordination environment. This leads to deviations of the correct unit cell shape. While the parameters in MM3 are designed to include the 1-4 interactions, one should note that these were not estimated for complex metal clusters that are present in MOFs.

In that regard, a slight modification of the exclusion rule and the parameters itself is justified. In Ref. [14], it was shown that for a more realistic description of the breathing behavior of MIL-53(Al),

the MM3 $\epsilon_i$ should be uniformly rescaled for all atoms with a factor 0.86. This study also illustrates the sensitivity of the force field towards its van der Waals parameters. With this in mind, the van der Waals parameters are regarded as a term that needs refinement in this work, with which a better reproduction of experimental and theoretical results can be obtained. A big part of the difficulty of optimizing the van der Waals interaction parameters lies in the limitation of standard ab initio techniques in treating these effects. Therefore, highly accurate parametrization of the van der Waals part requires experimental results to estimate the unknowns, which are not available for hypothetical MOFs.

It is clear that a better description of the nonconvalent terms, both the electrostatic and the van der Waals interactions, is highly desirable, but definitely not trivial. A potential improvement was very recently introduced by Grimme in the Quantum Mechanically Derived Force Field (QMDFF) [66], where the Pauli repulsion and London dispersion interactions were separated. The advantage of the separation of these effects is that the effects of Pauli repulsion could be included in the QuickFF fitting procedure, which is not an option for the Lennard-Jones or Buckingham potential as the two terms in the interaction energy cannot be strictly separated in repulsion and dispersion. For the dispersion interactions, QMDFF uses a potential energy term similar to the well-established and very succesful empirical dispersion correction term [81, 82] in DFT, while the Pauli repulsion is described by an exponential term, depending on various empirical and fitted parameters. More details can be found in Ref. [66].

### 2.2.6 Computational details

The ab initio DFT cluster calculations were carried out with Gaussian09 [83]. The clusters were build with Zeobuilder [84]. The popular hybrid Becke, 3-parameter, Lee-Yang-Parr (B3LYP) functional [85] was used for all calculations, with the 6-311G(d,p) Pople basis sets [86] unless otherwise stated. Extra polarization functions were added for a better description of the metal oxygen bonds. The first step was the optimization of the cluster model. A tighter convergence criterium (opt=tight) was used when necessary to obtain a true minimum on the potential energy landscape and a finer grid for the numerical integration was used in all calculations with the keyword int=ultrafine. The required ab initio Hessian was obtained with the keyword freq, with which the vibrational frequencies were analytically determined. In some occasions, the default convergence criterium of this method had to be reduced with a factor ten to obtain a converged result. It has previously been shown by Furche and Perdew [87] that the B3LYP functional tends to overestimate bond distances in $3d$ transition metal compounds. Here, it was chosen not to correct for this and therefore, the force field was directly fitted to reproduce ab initio data, which allows for a systematic approach.

The HI and MBIS charges were derived using Horton [88] and the force fields were all generated with QuickFF [67]. The force field simulations were performed with Yaff [89]. The real space cutoff used for the electrostatic interactions is 15 Å and the longe-range interactions were handled using

the Ewald summation technique. A cutoff radius for the van der Waals interactions of 15 Å is used.

## 2.3 Development of force fields for well-known MOFs

In this section, the force fields derived in this thesis for well-known and experimentally characterized MOFs are discussed. The selected MOFs display different molecular environments, to illustrate the general applicability of the methodology. The test set contains MOF-5, MIL-53, MIL-47, HKUST-1, DMOF-1 and ZIF-8.

### 2.3.1 MOF-5

MOF-5 was the first metal-organic framework, synthesized by the group of Yaghi [10] in 1999 and it has received much attention in theoretical and experimental studies. The crystal has a cubic unit cell and space group F$m\bar{3}$m. The framework consists of a $Zn_4O(CO_2)_6$ inorganic node connected through 1,4-benzenedicarboxylate (BDC) linkers (see Figure 2.10).

Several authors have developed an ab initio parametrized force field for MOF-5 using the cluster model approach [47, 64]. In this work, the zinc benzoate cluster model (see Figure 2.11 on page 32) as proposed by Tafipolsky and Schmid in Ref. [56] is used to describe the $Zn_4O(CO_2)_6$ building unit of the IRMOF series. The organic linker cluster model was also inspired by Tafipolsky and Schmid in Ref. [56]. The ab initio calculations were carried with extra diffuse basis functions (6-311++G(d,p)), which was deemed necessary for an accurate description of the inorganic coordination environment. Some ab initio reference data are tabulated in Table 2.1. In this table the bond lengths obtained with two different force fields are compared with the DFT values.

In the third and fourth column, the data obtained after relaxing the zinc benzoate cluster with the force field is presented. To compare with the ab initio reference data, the van der Waals interactions were excluded. The bond distance $O_{ce}$-Zn shows the largest deviation. From this table, one could conclude that the force field with MBIS charges is a better choice as the deviation of this distance is smaller. While the DFT reference cluster predicts a slightly shorter bond distance for $O_{ca}$-Zn than for $O_{ce}$-Zn, the opposite is true for the derived force fields. When these parameters are transferred to the periodic structure and the van der Waals interactions are added to mimic the experimental behavior, the results in the last column are obtained. The experimental $O_{ca}$-Zn and $O_{ce}$-Zn distances are 1.94 Å and 1.95 Å respectively [10]. The periodic structure optimized with the force field shows a better correspondence than the DFT cluster.

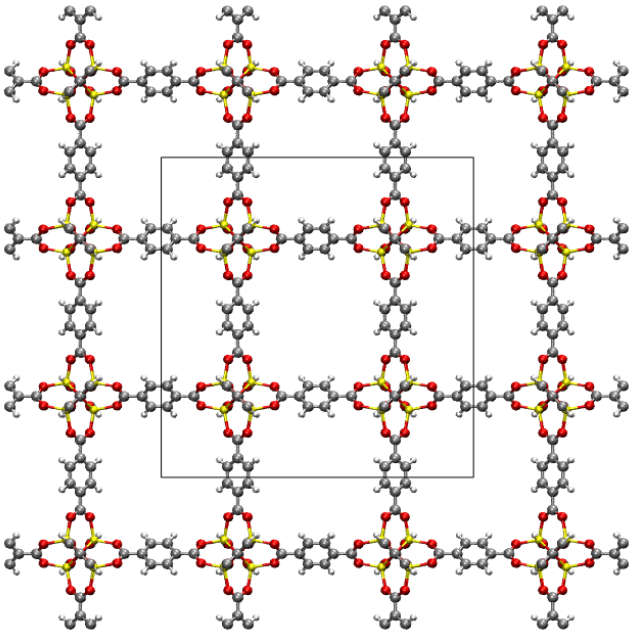

**Figure 2.10:** View along the [100] direction of MOF-5. The conventional unit cell is indicated on the figure.

**Table 2.1:** Comparison of bond lengths in the zinc benzoate cluster. In the last two column the bond lengths of the periodic structure are given, obtained with the final force field.

| Atom types | DFT cluster | FF (HI, excl. vdW) cluster | FF (MBIS, excl. vdW) cluster | FF (MBIS, incl. vdW) periodic |
|---|---|---|---|---|
| $C_{ca}$-$C_{pc}$ | 1.496 | 1.495 | 1.494 | 1.501 |
| $C_{ca}$-$O_{ca}$ | 1.267 | 1.266 | 1.266 | 1.265 |
| $C_{pc}$-$C_{ph}$ | 1.399 | 1.400 | 1.400 | 1.401 |
| $C_{ph}$-$C_{ph}$ | 1.391 | 1.392 | 1.392 | 1.387 |
| $C_{ph}$-$H_{ph}$ | 1.082 | 1.082 | 1.083 | 1.081 |
| $O_{ca}$-Zn | 1.977 | 1.980 | 1.980 | 1.974 |
| $O_{ce}$-Zn | 1.979 | 1.960 | 1.972 | 1.964 |

**Table 2.2:** Comparison of ESP cost for MK and Hu ESP cost function for different schemes.

| Charge scheme | MK Cost | Hu Cost |
|---|---|---|
| MK | 0.00585 | 0.00584 |
| Hu | 0.00647 | 0.00549 |
| HI | 0.02633 | 0.02830 |
| MBIS | 0.01943 | 0.01768 |

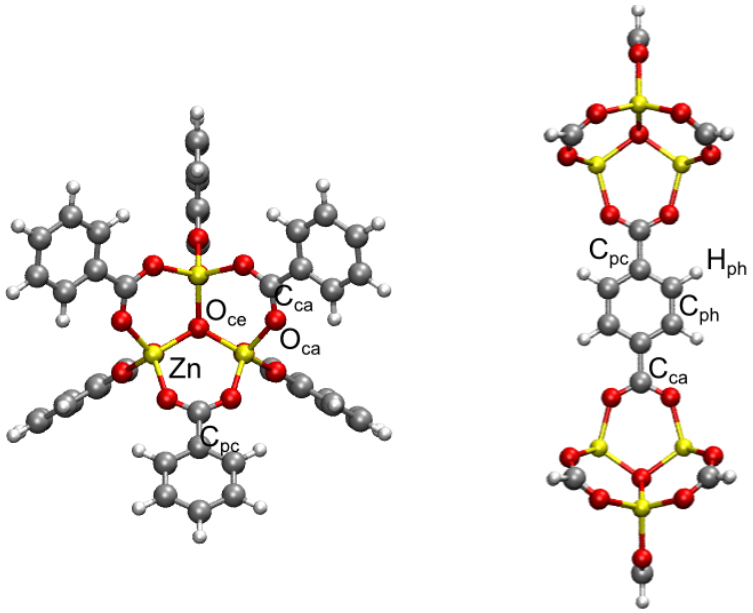


**Figure 2.11:** Cluster models for the parametrization of MOF-5 as proposed by Tafipolsky *et al.* [56] In the left pane, the zinc benzoate model for the inorganic building block is shown. In the right pane, the cluster model for the organic linker is displayed.

In MOF-5, Zn has an oxidation number of +II. The HI estimated charge for Zn in the zinc benzoate cluster is +1.427 and with MBIS this is +1.275, indicating that the charge on the Zn atom is rather high with HI. This is even more pronounced for the charge of $O_{ce}$, where the value obtained with HI is -1.721, while the MBIS scheme predicts -1.357. In Table 2.2 on the previous page a comparison of the ESP cost is shown. The MK and Hu ESP cost functions are evaluated with the HI and MBIS derived charges and it can be seen that the MK-fitted charges have the lowest MK cost. The same is true for the Hu-fitted charges and the Hu cost function. This is normal as these charges are specifically fit to minimize the corresponding cost functions. More interestingly, it can be seen that MBIS performs better than the HI charges in reproducing the ESP according to both cost functions. This result, together with the slightly better correspondence of the QuickFF bond distances with the ab initio reference data, justifies the choice for the MBIS charges for MOF-5 in the remainder of this work.

In Table 2.3, the lattice parameter of the cubic MOF-5 is shown as optimized with the final force field. The lattice parameter is slightly ($\approx 1\%$) overestimated compared to the experimental result, but is in agreement with other theoretical results. The MM3 van der Waals parameters are directly added to the estimated force field, but 1-4 interactions are excluded. When including these interactions, an increased lattice parameter of 26.304 Å is observed, which is due to the overestimation of the Pauli repulsion in the inorganic metal node. Civalleri *et al.* [90] performed periodic DFT calculations with the B3LYP functional and obtained a lattice parameter of 26.088 Å. The force field shows a good agreement with this value.

**Table 2.3:** Comparison of lattice parameter of MOF-5 with literature data.

| | Exp. [10] | This work | MOF-FF [64] | DFT [91] LDA | DFT [91] GGA | DFT [90] B3LYP |
|---|---|---|---|---|---|---|
| $a$ [Å] | 25.885 | 26.134 | 26.080 | 25.56 | 26.04 | 26.088 |

### 2.3.2 MIL-53

The MIL-53 family (MIL = Matériaux de l'Institut Lavoisier) is known for its breathing behavior. Starting from the first experimental synthesis in 2002 of MIL-53(Cr) by Férey and co-workers [12], these materials have been the subject of many experimental and theoretical investigations. The framework consists of 1,4-benzenedicarboxylate (BDC) organic linkers connecting one dimensional $M^{3+}$(OH) chains (see Figure 2.12).

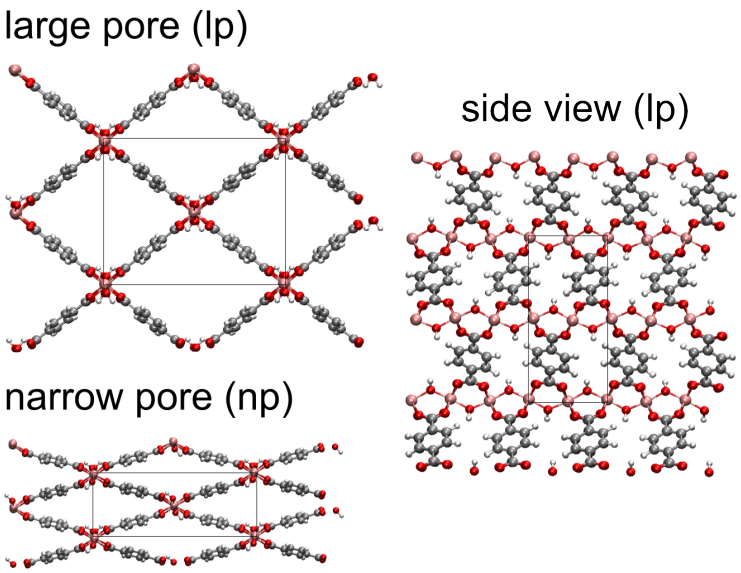


**Figure 2.12:** Illustration of MIL-53(Al). The unit cell is indicated on the figure.

There have been some attempts in obtaining force fields for this flexible material. Salles *et al.* [1] developed a force field for MIL-53(Cr) that is able to describe the transformation between the large-pore and narrow-pore state. An accurate description of this framework flexibility is a difficult task. It is, however, very important to understand the microscopic underlying features. Since experimental techniques are not able to elucidate on these mechanisms due to the fast transition speed, one needs to resort to computer simulations to gain insight in these mechanisms. The force field developed by Salles *et al.* contains bonded and nonbonded potential terms. The organic linker is described using parameters from the CVFF [52], and the inorganic covalent part (e.g. Cr-O bond) is adopted from DREIDING [49], but adjusted to reproduce structural features of the narrow pore and large pore. The connection between both parts (angles and torsions) is also fitted to reproduce

both phases. A Coulombic point charge interaction and a Lennard-Jones potential are used for the nonbonded interactions. This force field is able to reproduce the crystal structure of MIL-53(Cr) in both the large pore and narrow pore as well as to describe the guest-induced transitions. This approach, where the parameters for the organic linker are taken from generic force fields and the inorganic part and the connection are adjusted to reproduce structural data, has shown to be succesful in later studies [92].

However, such an approach is inherently limited by the available amount of experimental data. It offers no possibility to study hypothetical structures and it is not capable to predict such transformations without experimental signs hinting towards it. A next step in the development of flexible force fields for MOFs is hence to derive force fields without experimental input, but starting only from ab initio data. The force field derived from quantum mechanical data by Vanduyfhuys *et al.* [14] was able to describe the energy profile along the breathing mode of the empty MIL-53(Al) material. It has also been shown that QuickFF is able to generate an accurate force field for these flexible materials [67]. Structural transitions of the empty framework, i.e. breathing without the presence of guest molecules, was observed for the first time experimentally by Liu *et al.* [93] and later confirmed by means of DFT calculations by Walker *et al.* [79]. The novelty of the force field of Vanduyhuys *et al.* lies in the possibility to describe this with a force field derived only from quantum mechanical data. A critical remark that must be made concerns the strong sensitivity of the breathing profile on the van der Waals parameters. These parameters are usually not refitted to ab initio data, but taken from other force fields and some problems still remain, as will be shown in this section.

MIL-53 has been synthesized for different metal centers such as Cr [12], Al [93], Sc [94], Ga [95], In [96] and Fe [97]. In this work, force fields are derived for several of these metals and their influence on the structural and mechanical properties is investigated. With QuickFF, it has become possible to derive in an easy way force fields for the MIL-53 family. The model systems used for MIL-53 are shown in Figure 2.13. A segment of the 1D metal chain consisting of four metal atoms is considered, where the core region is made up of the two central metal atoms. The oxygen atoms along the chain are terminated with a hydrogen atom, while the linkers at both sides are terminated with an acetylacetone (ACAC) molecule. The total charge of the inorganic cluster model is -1. The parameters of the organic linker are estimated from the second cluster. The hydrogen atom is removed from the bridging OH ligand to obtain a symmetric charge-neutral system. The metal atoms are terminated at each side with a water molecule and the organic linkers again with the ACAC molecule. Similar clusters have succesfully been used by Vanduyhuys *et al.* [14] for the derivation of the MIL-53(Al) force field. The calculations were carried out using the B3LYP functional and a 6-311G(d,p) Pople basis set for all atoms (including the row 3 metal atoms), except for In and Y, for which LANL2DZ [98] pseudopotentials were used. Ab initio calculations were performed on cluster models with metal centers Al, Sc, Ti, V, Cr, Ga, In and Y. Some of these have not yet been synthesized. All DFT calculations were carried out with maximal spin (e.g. Cr has three unpaired

electrons, resulting in a maximum spin of 6 for the inorganic cluster with four metal atoms).

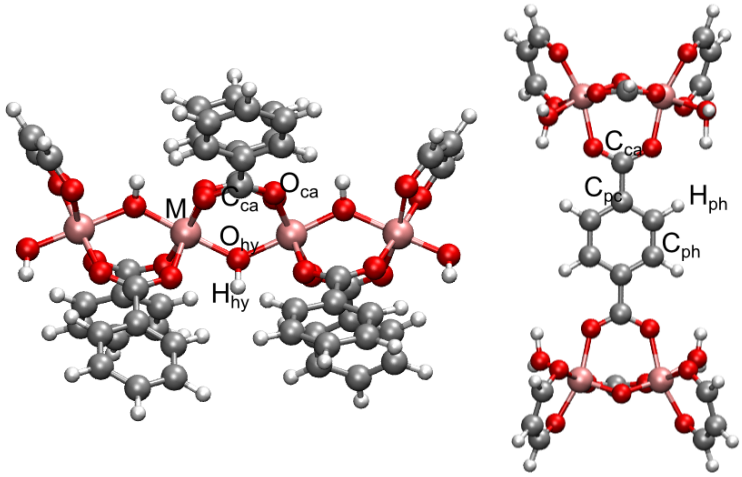


**Figure 2.13:** Cluster models used for MIL-53: metal chain (left) and organic linker (right).

For Al and the row 3 metal atoms, charges were derived using the HI and MBIS scheme. Despite its deficiencies, the MK ESP fitting method was used for In and Y, as no all-electron calculations were performed with these metal centers. The use of atoms-in-molecules schemes is not advised in this situation. In Table 2.4, the ESP cost from both MK and Hu methods is tabulated for the MK, MBIS and HI charges of metal centers Al, Cr and Ga, but the conclusions remain the same for the others. Similar as was noted for MOF-5, the MBIS charges have a lower ESP cost than the HI charges, indicating that they provide a better reproduction of the electrostatic potential.

**Table 2.4:** A comparison of the ESP cost of the MBIS and HI scheme for various metal centers in the inorganic model system of MIL-53.

| | Al | | Cr | | Ga | |
|---|---|---|---|---|---|---|
| | ESP MK | ESP Hu | ESP MK | ESP Hu | ESP MK | ESP Hu |
| MK | 0.00523 | 0.12661 | 0.00552 | 0.00530 | 0.00598 | 0.00555 |
| MBIS | 0.03281 | 0.15806 | 0.02439 | 0.02104 | 0.03916 | 0.03608 |
| HI | 0.08110 | 0.16869 | 0.08984 | 0.08554 | 0.07964 | 0.08034 |

In Table 2.5, some structural parameters are compared between the DFT cluster and the force field optimized periodic structure, with and without the inclusion of the van der Waals terms. To validate the covalent parameters, one should compare the first two as DFT lacks dispersion interactions. Instead of repeating this for every metal center, the focus lies on MIL-53(Al) to illustrate the performance of QuickFF. The agreement is very good. The largest deviations are the overestimation of the Al-$O_{hy}$-Al and Al-$O_{ca}$-$C_{ca}$ angles with approximately 1.7%. When the van der Waals interactions are included to mimic the experimental situation more closely, some structural

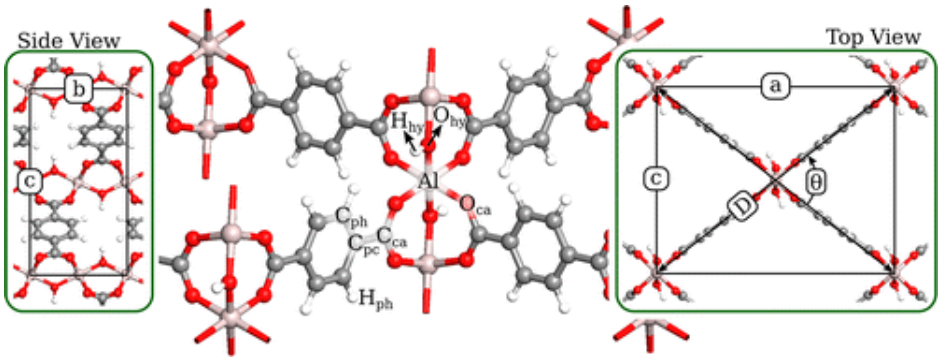


**Figure 2.14:** Definition of the diagonal $D$ and interdiagonal angle $\theta$. Figure taken from Ref. [14].

changes can be noted. The Al-Al distance decreases with 0.05 Å while the bond distances remain mostly the same. This decrease can be attributed to the decrease of the Al-$O_{hy}$-Al along the chain with 2.6°. The experimental Al-Al distance is the $b$ lattice parameter divided by 2 and gives 3.31 Å (77 K, Liu *et al.* [93]), which is clearly better represented with the inclusion of the van der Waals interactions. Another effect is the increase of the diagonal $D$ (see Figure 2.14). This in fact measures the distance along the BDC linkers. By including the dispersion interactions, the $O_{ca}$-$C_{ca}$-$O_{ca}$ and $C_{ca}$-$C_{pc}$-$C_{ph}$ angles decrease resulting in an elongation along the linker.

**Table 2.5:** Comparison of structural parameters of MIL-53(Al). The DFT cluster is compared with the force field optimized periodic structures. The symbol * indicates that it is taken from the organic linker cluster model.

| Atom types | DFT Cluster cluster | FF (excl. vdW) periodic | FF (incl. vdW) periodic |
|---|---|---|---|
| Al-Al [Å] | 3.38 | 3.39 | 3.34 |
| Al-$O_{ca}$ [Å] | 1.95 | 1.95 | 1.94 |
| Al-$O_{hy}$ [Å] | 1.87 | 1.86 | 1.86 |
| $C_{ca}$-$O_{ca}$ [Å] | 1.26 | 1.26 | 1.26 |
| $C_{ca}$-$C_{pc}$ [Å] | 1.50* | 1.50 | 1.51 |
| $C_{pc}$-$C_{ph}$ [Å] | 1.40* | 1.40 | 1.40 |
| $C_{ph}$-$C_{ph}$ [Å] | 1.39* | 1.39 | 1.39 |
| Al-$O_{hy}$-Al [°] | 129.0 | 130.6 | 127.6 |
| Al-$O_{ca}$-$C_{ca}$ [°] | 133.3 | 135.6 | 133.0 |
| $O_{ca}$-$C_{ca}$-$O_{ca}$ [°] | 125.6 | 125.9 | 124.6 |
| $C_{ca}$-$C_{pc}$-$C_{ph}$ [°] | 120.4* | 120.3 | 120.8 |

**Influence of the metal center**

MIL-53 has been the subject of a number of theoretical and experimental investigations. In this

paragraph, some experimental observations are listed briefly, mainly to indicate what already is known about the flexibility and stable forms of various guest-free MIL-53 frameworks.

As mentioned previously, the guest-free MIL-53(Al) displays breathing under influence of temperature. This was experimentally demonstrated by Liu *et al.* [93]. The transition from the narrow pore to the large pore occurs at approximately 325 to 375 K, while the reverse transition is found at temperatures around 125 to 150 K. At room temperature the large pore is the most stable form. In a transition from the large pore to narrow pore, a decrease in unit cell volume of 40% is found. While at room temperature the large pore is the stable form of MIL-53(Cr), the narrow pore can be obtained by applying mechanical pressure with a transition pressure of 55 MPa [99, 100]. The reverse transition is at approximately 10 MPa indicating that there is no stable narrow-pore minimum. On the contrary, MIL-53(Ga) displays a narrow-pore form at room temperature [95] and only at high temperatures around 500 K the structure goes to a large pore. Mowat *et al.* [94, 101] observed different phases for the MIL-53(Sc) case and none of them really resembles the MIL-53(Al) or MIL-53(Cr). The authors refer to it as a highly flexible framework that adopts many different forms depending on the amount and type of the adsorbate included. A comparison is made in the supporting information between the different MIL-53 variants synthesized at that time. They find that the Sc-O-Sc angle is smaller than in other MIL-53 frameworks, which can be explained by the larger ionic radius of $Sc^{3+}$. $NH_2$-MIL-53(In) was synthesized by Serra-Crespo *et al.* [96]. It was found that it does not behave as MIL-53(Al) or MIL-53(Cr). Instead, it goes to a very narrow-pore state with a volume of 980 Å$^3$ at ambient temperature after thermal activation. Leclerc *et al.* [102] reported a hydrated MIL-47 with V in the +III oxidation state. This strongly resembles the MIL-53 case. It is found that this structure is much more flexible than the rigid MIL-47($V^{+IV}$), which is discussed in the next section.

A first step in evaluating the influence of the metal center is by comparing the charges of the atoms in close proximity of the metal ion. This gives an idea of the electronical structure. It can be assumed that the charges are all approximately equal, as all metals have the same formal charge +III. The metal centers are ordered along the horizontal axis according to atomic number and charges derived via different schemes are shown in Figure 2.15 for the atom types $O_{ca}$, $O_{hy}$ and the metal ion. The MBIS charges for the row 3 metals show a decreasing trend from Sc to Ga. They vary between +2.1 and +1.9. This can be explained by an increasing electronegativity. Al has the largest charge, even though its electronegativity is comparable with Cr, which is probably due to the decreased ionic radius that increases the attraction of the oxygen atoms. The $O_{ca}$ charges are quite constant, illustrating that overall the same charge transfer from the metal ion to the organic linkers takes place. The $O_{hy}$ have a similar trend as the metal atoms, indicating that especially the electronic structure along the chain differs. The HI charges are always larger than the MBIS charges, which illustrates the fact that in a strongly ionic environment, these charges tend to be overestimated. The ESP fitted charges do not display a trend, but were added to compare the In and Y charges with the rest. These ESP charges are in fact somewhat larger for the metal, $O_{ca}$ and

$O_{hy}$ compared with MIL-53(Al,Sc,Ti,V,Cr,Ga).

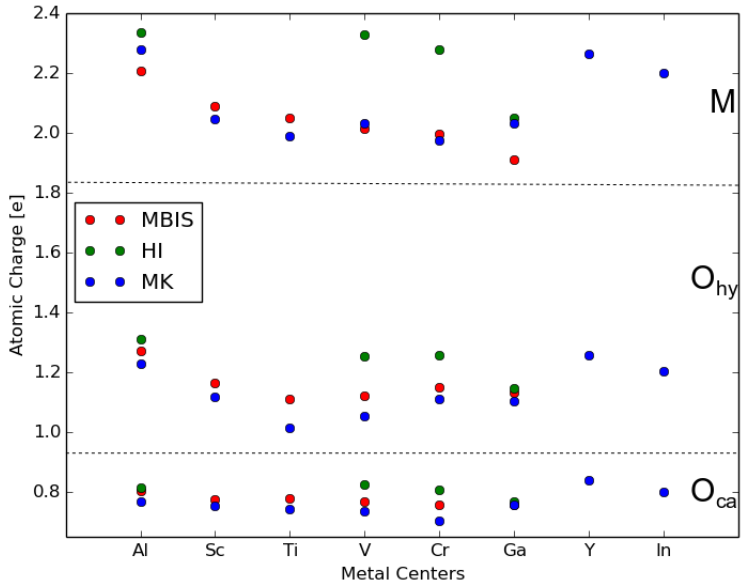


**Figure 2.15:** Absolute value of the atomic charges derived on the inorganic cluster model. The black dotted line separates the metal, $O_{ca}$ and $O_{hy}$ charges.

Two important terms in the force field for the MIL-53 framework are the dihedral force constants for the patterns M-$O_{ca}$-$C_{ca}$-$C_{pc}$ and M-$O_{ca}$-$C_{ca}$-$O_{ca}$. The motions corresponding with it were nicely illustrated in Figure 4 of Ref. [14]. The first term determines the rotation of the linker about the two $O_{ca}$-$O_{ca}$ axes, while the second determines the tilting of the plane of the linker around the $C_{ca}$-$C_{pc}$-$C_{pc}$-$C_{ca}$ axis. For instance, Salles *et al.* [1] and Yot *et al.* [92] explicitly fitted these constants for a better reproduction of the experimental data. Vanduyhuys *et al.* [14] performed an extra ab initio DFT scan of the periodic structure to obtain a better estimate. These terms are important as they strongly influence the breathing motion. The force constants corresponding to them can be seen as a measure for the ease with which the material can undergo the transition from large pore to narrow pore or vice versa. The larger the sum of these force constants, the more energy it costs to stay in the narrow pore and thus the more stable the large pore. In Figure 2.16, the force constants estimated with QuickFF on the inorganic cluster model are shown for several sets of a priori estimated atomic charges.

Some interesting trends are revealed in this figure. First, it can be seen that the dihedral force constant estimated with MK ESP charges is systematically lower. The MBIS force constant of MIL-53(V) coincides with the MK value. MIL-53(Y), which has not been synthesized, shows a very small energy barrier for deformation. The result is that in the periodic structure, it always contracts to a very narrow pore. It can be seen that MIL-53(Cr) has the same force constants as the rigid MIL-47, which is 5 kJ/mol larger than for MIL-53(Al). MIL-53(Cr) is a flexible material,

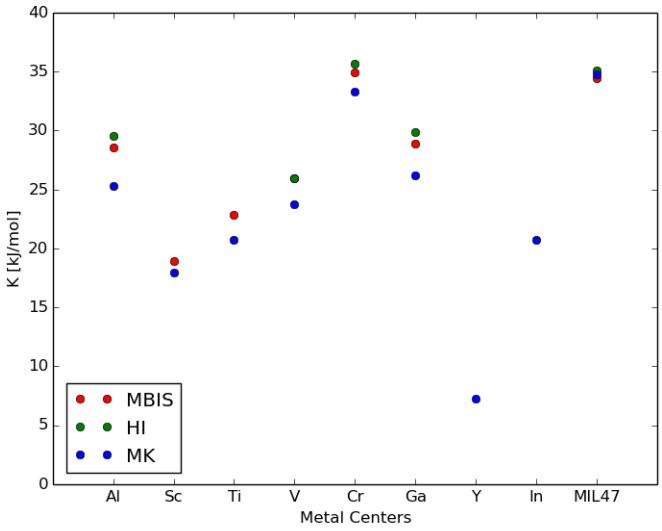


**Figure 2.16:** Sum of the force constants $K$ for the dihedral patterns M-$O_{ca}$-$C_{ca}$-$C_{pc}$ and M-$O_{ca}$-$C_{ca}$-$O_{ca}$, which strongly determine the breathing behavior.

but at room temperature it does not show a narrow-pore minimum. An external pressure has to be applied to push it into the narrow-pore phase. MIL-53(Ga) has a similar force constant as the Al case, but it undergoes a transition to the large pore at rather large temperatures. Boutin *et al.* [103] analyzed this by DFT calculations and showed that the entropic stabilization of the large pore is smaller than for Al and thus the transition temperature increases. MIL-53(In) has been synthesized with an amine functional group, such that it is not known how the empty form behaves, but only a very narrow pore was found. The obtained force constant on the ab initio cluster, which is rather low, suggests that one can expect a flexible system with a stable narrow pore. A low force constant is also found for MIL-53(Sc), where Mowat *et al.* [94] reported a highly flexible structure that is easy to deform, consistent with the lower dihedral force constant.

One can argue that the metal center will have a large influence on the structural parameters along the metal chain. In Table 2.6, the most important parameters are shown and compared among various methods. The DFT cluster values are taken from the inorganic cluster models. The $b$ lattice parameter is estimated as two times the distance between the metal atoms in the core region. The force field values are obtained after optimizing the periodic structure. This table again illustrates the good performance of QuickFF. The bond distances are nearly perfectly reproduced. The $b$ lattice parameter is underestimated for all metal centers except for Al, which is mainly due to the M-$O_{hy}$-M angle as the bond distances are the same as the DFT cluster. When the van der Waals interactions are added, the M-$O_{ca}$ bond length typically increases and the bend angle along the chain decreases.

Two different trends can be detected when looking at the M-O bond distances. When going to the

right in the periodic table along the row 3 transition metals, this distance decreases (Sc,Ti,V,Cr) due to the larger effective core charge. When descending in column 3 of the periodic table (Al,Ga,In), the bond length increases due to the occupation of more and more shells. The force fields succeed in reproducing this. The bend angle follows approximately the same trend in the DFT cluster for (Al,Ga,In), but disappears in the force field. It can, however, be noted that Mowat *et al.* [94] indicated that the angle along the chain in MIL-53(Sc), is lower than for other metal centers (values between 118° and 120°). The same is true with the force field.

**Table 2.6:** A comparison of the MBIS and HI scheme for various metal centers in the inorganic model system of MIL-53.

| | Method | Al | Sc | Ti | V | Cr | Ga | In |
|---|---|---|---|---|---|---|---|---|
| M-$O_{ca}$ [Å] | DFT cluster | 1.95 | 2.14 | 2.08 | 2.05 | 2.00 | 2.04 | 2.15 |
| | FF (excl. vdW) | 1.95 | 2.14 | 2.08 | 2.04 | 2.00 | 2.05 | 2.17 |
| | FF (incl. vdW) | 1.95 | 2.14 | 2.08 | 2.05 | 2.01 | 2.05 | / |
| M-$O_{hy}$ [Å] | DFT cluster | 1.87 | 2.10 | 2.03 | 1.98 | 1.97 | 1.94 | 2.07 |
| | FF (excl. vdW) | 1.86 | 2.10 | 2.03 | 1.97 | 1.97 | 1.94 | 2.08 |
| | FF (incl. vdW) | 1.88 | 2.11 | 2.05 | 1.99 | 1.98 | 1.96 | / |
| M-$O_{hy}$-M [°] | DFT cluster | 129.0 | 125.7 | 128.0 | 126.6 | 124.8 | 125.6 | 124.6 |
| | FF (excl. vdW) | 130.6 | 120.9 | 122.9 | 124.9 | 124.3 | 122.3 | 117.9 |
| | FF (incl. vdW) | 129.3 | 119.9 | 121.5 | 124.2 | 123.3 | 122.9 | / |
| $b$ [Å] | DFT cluster | 6.76 | 7.47 | 7.30 | 7.06 | 6.97 | 6.91 | 7.33 |
| | FF (excl. vdW) | 6.77 | 7.30 | 7.13 | 7.00 | 6.95 | 6.78 | 7.11 |
| | FF (incl. vdW) | 6.81 | 7.29 | 7.13 | 7.02 | 6.97 | 6.88 | / |
| $\Delta E_{lp\text{-}np}$ | FF (incl. vdW) | -11.2 | 77.3 | 51.2 | 44.5 | 26.3 | 46.4 | / |

In the last row, the energy difference between the large pore and narrow pore at 0 K is shown, obtained with the standard MM3 van der Waals parameters. From these results one could suggest that the narrow pore becomes more stable relative to the large pore when increasing the ionic radius (along the row 3 transition elements or downward along the column 3 elements). It should, however, be stressed that this value and trend is very sensitive to the van der Waals parameters. Rescaling $\epsilon$, while keeping the exclusion rule and $\sigma$ the same, results in the same trend. Changing $\sigma$ on the other hand, results in other trends. In the next paragraph, the breathing profile, and thus relative stability of lp versus np, is discussed for MIL-53(Al).

Finally, some periodic lattice parameters are compared with published results for the narrow pore and large pore in Tables 2.7 and 2.8. There are not many accurate experimental data available on low temperature guest-free frameworks. In fact, only for MIL-53(Al) there are data on both phases at a low temperature of 77 K. Comparing the values of MIL-53(Al) of Loiseau *et al.* [104] and Liu *et al.* [93] already shows that there are deviations between different experiments and different

temperatures. However, it can be seen that there is a reasonable agreement with periodic DFT calculations on MIL-53(Al) and MIL-53(Ga). The diagonal $D$ is typically overestimated in the large pore compared to the experiment. This overestimation along the BDC linker is noted in all our force fields on various MOFs. The interdiagonal angle $\theta$ is overestimated in both large pore and narrow pore MIL-53(Al). In other cases, such as narrow pore MIL-53(Cr), $\theta$ is slightly underestimated. It does not seem that there is a systematic trend in the deviations from experiment.

**Table 2.7:** A comparison of the cell shape for the large pore MIL-53. The symbol * indicates that the van der Waals parameters had to be modified to find a minimum at 0 K. The high-temperature (ht) experimental form of Al, Cr and Ga is given.

| Metal | Method | $a$ [Å] | $b$ [Å] | $c$ [Å] | $V$ [Å$^3$] | $\theta$ [°] | $D$ [Å] |
|---|---|---|---|---|---|---|---|
| Al | This work (0 K) | 16.40 | 6.66 | 13.78 | 1505 | 80.0 | 21.42 |
| | FF (0 K) [14] | 17.05 | 6.59 | 12.90 | 1449 | 74.3 | 21.38 |
| | DFT, B3LYP (0 K) [105] | 16.48 | 6.68 | 13.24 | 1458 | 77.6 | 21.14 |
| | Exp. (77 K) [93] | 16.91 | 6.62 | 12.67 | 1418 | 73.7 | 21.13 |
| | Exp. ht [104] | 16.68 | 6.61 | 12.81 | 1412 | 75.0 | 21.03 |
| Cr | This work (0 K)* | 16.87 | 6.89 | 13.37 | 1552 | 76.8 | 21.53 |
| | Exp. ht [12] | 16.73 | 6.81 | 13.04 | 1486 | 75.9 | 21.21 |
| Ga | This work (0 K)* | 17.98 | 6.62 | 12.28 | 1462 | 68.7 | 21.77 |
| | DFT, B3LYP (0 K) [103] | 17.65 | 6.84 | 12.03 | 1453 | 68.6 | 21.36 |
| | Exp. ht [95] | 16.68 | 6.75 | 13.35 | 1480 | 77.3 | 21.36 |

**Table 2.8:** A comparison of the cell shape for the narrow pore MIL-53. The low-temperature (lt) form of Al, Cr and Ga is given.

| Metal | Method | $a$ [Å] | $b$ [Å] | $c$ [Å] | $\gamma$ [°] | $\theta$ [°] | $D$ [Å] |
|---|---|---|---|---|---|---|---|
| Al | This work (0 K) | 19.70 | 6.56 | 7.83 | 90.2 | 43.3 | 21.20 |
| | FF (0 K) [14] | 19.57 | 6.53 | 6.24 | 97.2 | 35.4 | 20.54 |
| | Exp. (77 K) [93] | 20.82 | 6.61 | 6.87 | 113.9 | 36.5 | 21.93 |
| | Exp. lt + $H_2O$ [104] | 19.51 | 6.57 | 7.61 | 104.2 | 42.6 | 20.94 |
| Cr | This work (0 K) | 20.15 | 6.71 | 7.31 | 90.0 | 39.8 | 21.44 |
| | Exp. lt + $H_2O$ [12] | 19.69 | 6.78 | 7.85 | 104.9 | 43.5 | 21.20 |
| Ga | This work (0 K) | 20.33 | 6.52 | 7.52 | 90.0 | 40.6 | 21.68 |
| | DFT, B3LYP (0 K) [103] | 21.61 | 6.68 | 7.03 | 117.57 | 36.0 | 22.72 |
| | Exp. lt [95] | 19.83 | 6.86 | 6.71 | 103.9 | 37.4 | 20.93 |

**Influence of the van der Waals parameters on the breathing behavior: MIL-53(Al)**

It is opted to study the influence of the force field van der Waals parameters by focusing on MIL-53(Al). For this structure a reversible transition between the guest-free narrow pore and large pore induced by temperature was detected by Liu *et al.* [93]. At low temperatures, the narrow

pore is found, while at higher temperatures the large pore is the stable state. Using dispersion corrected DFT (DFT-D3 [82]) as well as the vdW-DF functional, Walker *et al.* estimated the energy difference between the lp and np in the range of 34-72 kJ/mol per unit cell, depending on the exchange-correlation functional used. In case of B3LYP+D3, they found 42 kJ/mol per unit cell. Dispersion interactions were proven to be necessary to obtain a narrow pore state. Vanduyfhuys *et al.* [14] studied the sensitivity of the energy profile on the van der Waals parameters during breathing at 0 K. By uniformly rescaling the $\epsilon$ and $\sigma$ parameters, both the cell shape as well as the relative stability of the large pore and narrow pore can be changed.

Detailed information about the relative stability is not available for the other metal centers and it is hard to obtain a good idea in which range the parameters should be. The sensitivity of these parameters on the breathing profile was investigated and the effects are found to be the same for all metal centers. For this reason, the main ideas are illustrated with the example of MIL-53(Al) in Figure 2.17. Here a scan is made over the interdiagonal angle $\theta$ (see Figure 2.14 on page 36), the angle defining the opening of the pores. The experimentally measured values of the interdiagonal angles of the narrow pore (36.5°) and large pore (73.5°) at 77 K [93] are indicated by the black vertical lines. As the initial results showed that the inclusion of the 1-4 van der Waals interactions did not result in a good performance of the force field, it was opted to leave them out. The $\sigma$ and $\epsilon$ parameters used in the simulation are indicated in the legend. There are some effects that can be mentioned. By increasing $\sigma$, or thus the van der Waals radii of the atoms, the narrow-pore minimum shifts towards larger interdiagonal angles and the large-pore minimum shifts towards smaller interdiagonal angles. Increasing $\epsilon$ results in a stabilization of the narrow pore relative to an interdiagonal angle of 90°. The large-pore minimum dissapears for $\sigma$=1.1 when $\epsilon$ is increased from 0.8 to 0.9. The energy difference is of the order of 1 kJ/mol and thus much smaller than the DFT result by Walker *et al.* [79]. A more recent investigation reported an energy difference of 35.7 kJ/mol [103]. However, one could argue that the energy difference found by them is rather large as the large-pore structure is already the absolute minimum at room temperature. This means that the narrow-pore structure should shift with more than 35 kJ/mol upwards with respect to the large pore. To conclude, it does not seem that it is possible to obtain the same energy difference as Walker and the same experimental structure as Liu. As a trade-off between sufficiently large lp-np energy difference and a large pore bound at $\theta \approx 74°$, we choose to work with $\sigma$=1.10 and $\epsilon$=0.85. The narrow pore is then 9 kJ/mol per unit cell more stable than the large pore at 0 K.

As there are not sufficient experimental or theoretical data available for the other metal centers, it is opted to use the same set of parameters. These materials tend to have a more stable narrow pore at 0 K and no large pore is detected for this set of van der Waals parameters. In Chapter 3, the influence of these parameters on mechanical properties such as the elastic constants will be discussed.

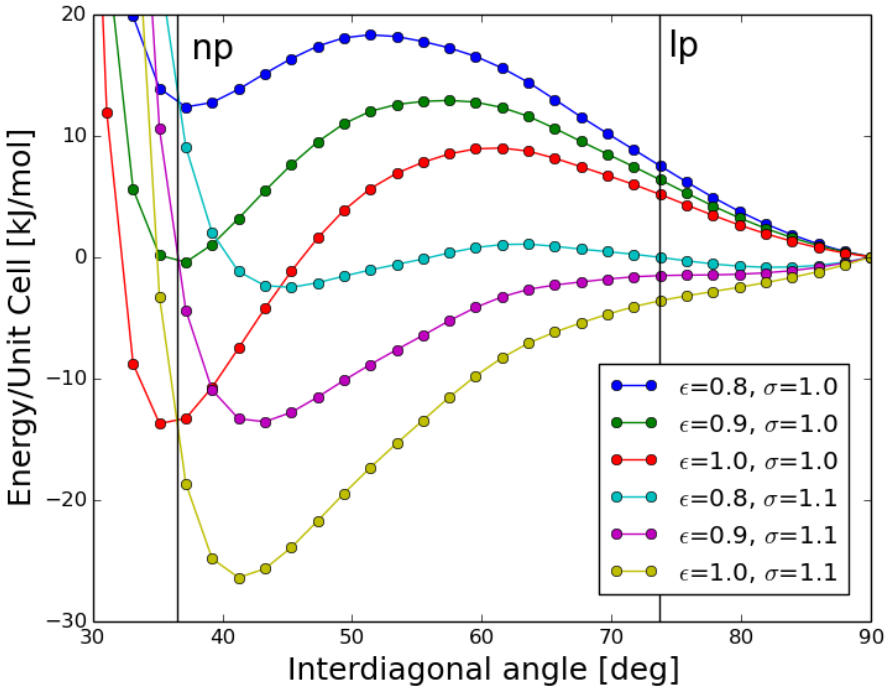


**Figure 2.17:** Influence of van der Waals scale on breathing profile. The black vertical lines indicate the experimental results of Liu *et al.* [93] at 77 K.

### 2.3.3 MIL-47

Another material from the MIL series is the MIL-47($V^{IV}$). Similarly to MIL-53, it is built from VO chains connected by BDC linkers. The main differences with MIL-53 are the oxidation number of the metal ion, which is now +IV instead of +III, and the absence of the hydrogen atom on the bridging ligand along the 1D metal chain. Each vanadium atom contains one unpaired d-electron. The periodic structure is shown in Figure 2.18. This material was synthesized for the first time by Barthelet *et al.* in 2002 and is considered to be rigid as it does not show signifact modifications upon adsorption of guest molecules (see e.g. Ref. [106]).

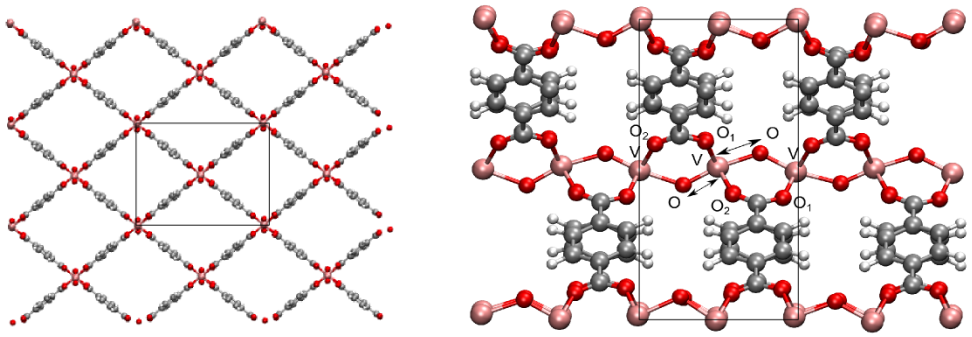


**Figure 2.18:** IIllustrations of the periodic structure of MIL-47. The unit cell is indicated on the figure.

However, Yot *et al.* [92] demonstrated a pressure-induced breathing motion. They experimentally observed a decrease of 38% of the volume when increasing the pressure above 85-125 MPa, which was assigned to the contraction of the large pore ($\approx$ 1530 Å$^3$) to a narrow pore ($\approx$ 950 Å$^3$). Moreover, it was shown that this transition can be reversed with a hysteresis of about 50 MPa. With another experimental techniques, a transition pressure between the large pore and narrow pore was found around 150 MPa. The differences in transition pressure between the experimental techniques was ascribed to differences between the samples and the experimental conditions. When the pressure is lowered beneath a value of around 60 MPa, the narrow pore opens and transforms back to the large pore. Another experimental finding was the continuously decreasing volume of the narrow pore, instead of collapsing under higher pressure.

Yot *et al.* succeeded also in reproducing this hysteresis behavior with force field MD simulations in the $N\sigma T$ ensemble using a hydrostatic pressure. To this end, they made a new flexible force-field model. The partial charges were derived from a periodic DFT calculation using the Mulliken partitioning method [107]. The bonds and bends were described using a harmonic potential and the dihedrals with a single cosine term. The parameters were taken from CVFF [52] for the organic linker and from UFF [48] for the metal chain. The bend forming the connection between the inorganic and organic building unit was described with parameters from the succesful force field by Salles *et al.* [1] for MIL-53(Cr) and the important torsion term V-$O_{ca}$-$C_{ca}$-$C_{pc}$ was manually adjusted to reproduce key structural characteristics of MIL-47(V). A Lennard-Jones potential and the 1-4 exclusion rule was used for the van der Waals interactions. The force field was validated by comparing experimental and simulated vibrational frequencies for which a good agreement was found. $N\sigma T$ MD simulations were carried out at 300 K using the Berendsen barostat and thermostat on a simulation box consisting of 32 unit cells and production runs of 2 ns were considered. They obtained a $PV$ hysteresis loop with transition pressures of 66 MPa and 137 MPa, which is a good agreement with the experimental results. Furthermore, they observed the same continuous decrease of the unit cell volume in the narrow pore under increasing pressure as was suggested by the experiment.

In this work, the aim was to generate the first ab initio derived force field able in reproducing this breathing behavior under pressure. Due to the structural similarities between the MIL-53 and MIL-47 frameworks, the same cluster models were used at first. This first attempt did, however, not succeed, as the asymetrical V-O bond distance was not well described. The chemical structure of MIL-53 along the 1D metal channel is different and these cluster models did not result in a good representation of the periodic structure.

The final cluster models, together with the definitions of the atom types, are shown in Figure 2.19. These model systems are quite similar to the ones used for MIL-53 as still four metal atoms are considered, but the termination along the metal chain is now different. Here, explicitly an asymetric pattern was obtained by adding only at one of the two ending vanadium atoms an oxygen atom.

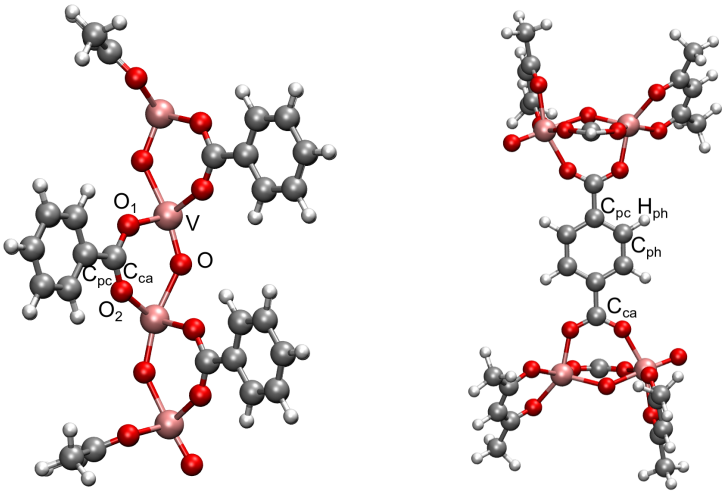


**Figure 2.19:** Cluster models used for MIL-47.

This oxygen atom is not terminated by a hydrogen atom, such that it forms a strong chemical bond with the metal atom, representing the short V-O bond distance. The cluster model for the inorganic part is neutral with the maximum spin of 2 (four vanadium atoms with one unpaired d-electron). For the organic linker a similar approach was used. The periodic MIL-47 has, however, a complex spin structure as was illustrated by Vanpoucke *et al.* [108] using periodic DFT calculations. The ground state, according to these calculations, consists of a system containing antiferromagnetic chains in an antiferromagnetic configuration. This effect can naturally not be included in a finite cluster model, which is a limitation. Furthermore, the authors showed a rather large influence of the spin state on the bulk modulus and transition pressure. The precise influence on the force-field parameters is hard to predict and was not investigated.

**Table 2.9:** Atomic charges calculated on the nonperiodic cluster compared with the charges published by Biswas *et al.* [109]. The symbol * indicates that these charges were taken from the linker cluster.

| Atom type | MBIS | HI | HI [109] |
|---|---|---|---|
| V | 2.067 | 2.443 | 2.426 |
| O | -0.783 | -0.932 | -1.012 |
| $O_1$ | -0.745 | -0.827 | / |
| $O_2$ | -0.746 | -0.819 | / |
| $C_{ca}$ | 0.888 | 1.017 | / |
| $C_{pc}$ | -0.152* | -0.286 | / |
| $C_{ph}$ | -0.100* | -0.041* | / |
| $H_{ph}$ | 0.153* | 0.096* | / |

The charges were derived from the ab initio data, using only the MBIS and HI schemes (see Table 2.9 on the preceding page), and a qualitative comparison was made by looking at the cost of the ESP fitting methods. The HI charges are larger in absolute value, especially the charges along the chain, V and O, differ widely from MBIS. Biswas *et al.* [109] derived these charges on the periodic electron density with HI. In Table 2.9 on the previous page, it can be seen that the HI charges derived on the periodic and finite structures are similar. The ESP cost (see Table 2.10) of the MBIS charges is one order of magnitude smaller than the ESP cost of HI charges. According to the Hu and MK measures, the reproduction of the electrostatic potential is better for the MBIS charges and they were used in the force field.

**Table 2.10:** Comparison of cost for MK and Hu ESP cost function for different schemes.

| Charge scheme | MK Cost | Hu Cost |
|---|---|---|
| MK | 0.00485 | 0.00461 |
| Hu | 0.00511 | 0.00438 |
| HI | 0.13729 | 0.12406 |
| MBIS | 0.02416 | 0.02161 |

The next step was the generation of the force fields with QuickFF. The core region of the inorganic cluster model consists of the two central vanadium atoms, such that one short and one long V-O bond distance are included. These different bonds are approximated with a harmonic bond term in the fitting procedure and the force constant corresponding with the long V-O bond was found to be zero (with or without the inclusion of charges), indicating a very weak bond, which cannot be described by a harmonic term. Only one atom type was used for vanadium and one for the bridging oxygen along the chain. A harmonic bond term does not suffice to capture the asymetry in the periodic structure with a force field, as the potential term related to the V-O bond distance internal coordinate has two distinct minima and a polynomial double well potential was proposed to model this. The harmonic force constants and equilibrium distances for the short and long distances were determined on the inorganic cluster model with QuickFF. The double well potential should satisfy the following conditions:

- The potential energy has a local minimum in the equilibrium distances $r_1$ (short) and $r_2$ (long).
- The second-order derivative of the potential energy towards the bond distance in $r_1$ and $r_2$ corresponds with the determined force constants or curvature.

This leads to four conditions, such that the lowest possible degree is 4. However, with the estimated parameters, it was found that this did not result in a good potential energy term (see Figure 2.20a). With this choice, the structure would contract and only the short distance would be found. A

sixth order polynomial was required to obtain a reasonable - but artificial - barrier between the two equilibrium distances. The term used is given by

$$U(r) = \frac{K}{2(r_1 - r_2)^4}(r - r_1)^2(r - r_2)^4 \tag{2.31}$$

In this equation $K$ represents the force constant for the short distance as the force constant of the long distance was determined to be zero. By inserting the obtained force constant $K$ and equilibrium distances $r_1$ and $r_2$, a barrier of approximately 25 kJ/mol (see Figure 2.20b on the next page) was found independent of the charges used in the fitting procedure. Two different atom types for the carboxyl oxygen atoms ($O_{ca}$) of the BDC linker were deemed necessary as the force constants and rest values of the bonds and bends with the two different $O_{ca}$ were strongly different. $O_1$ is the atom type, when the projection of the V-$O_{ca}$ distance on the 1D chain is closest to a short V-O bond distance, while $O_2$ is the atom type when it is closest to the large V-O distance. A straightforward averaging did not deliver good results. More specifically, the structure relaxed to a symmetric V-O bond distance. The asymetry along the chain is translated in an alternating assignment of $O_1$ and $O_2$ (see Figure 2.18 on page 43). Some force-field parameters to illustrate this asymetry are tabulated in Table 2.11.

**Table 2.11:** Force-field parameters showing the asymetry in the structure.

| | Force constant | Rest value |
|---|---|---|
| $O_1$ - $C_{ca}$ | 807.7 kJ/(mol · Å) | 1.940 Å |
| $O_2$ - $C_{ca}$ | 667.9 kJ/(mol · Å) | 1.985 Å |
| V - $O_1$ - $C_{ca}$ | 225.2 kJ/(mol · rad) | 131.0° |
| V - $O_2$ - $C_{ca}$ | 147.3 kJ/(mol · rad) | 143.2° |

Some important structural parameters are compared between the ground state obtained by periodic calculations [108], the finite cluster model, the experimental structure [110] and the structures relaxed with the force field (excluding and including vdW) in Table 2.27 on page 67. The DFT cluster model overestimates the asymetry along the metal chain: the short V-O bond distance is smaller than in the experimental and periodic DFT structure, while the long distance is larger. The V-O-V bend angle is underestimated in comparison with the experiment and both effects compensate to some extent, resulting in a good approximation of the V-V distance. The bond distances in the organic linker model are in good agreement with the experiment. Overall, the finite cluster models capture the most important features of the periodic framework. To validate the parameters obtained from the fitting procedure, the DFT cluster values should be compared to the periodic structure, relaxed with the force field without van der Waals interactions (see also Table 2.27 on page 67). The largest difference is the underestimation of the long V-O distance with 0.06 Å. The force field derived with QuickFF succeeds in reproducing the ab initio results.

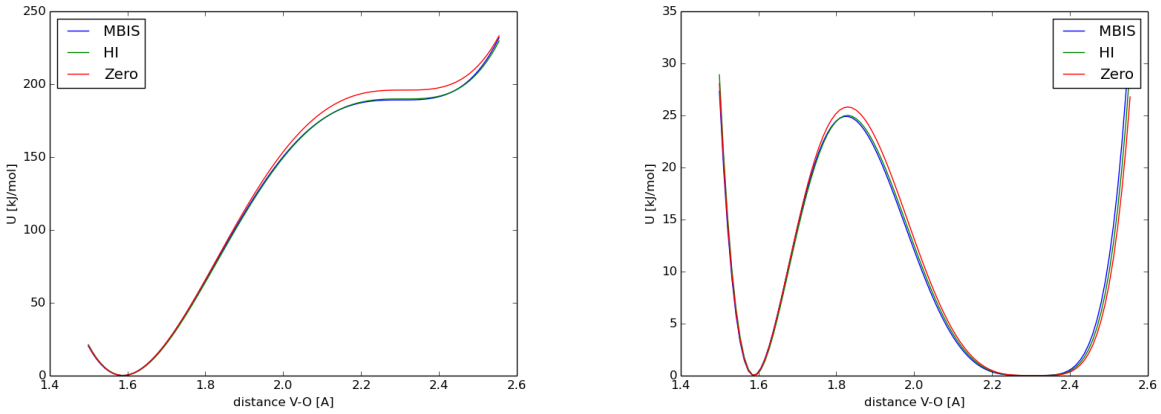


**(a)** Double well potential with a polynomial of degree 4. **(b)** Double well potential with a polynomial of degree 6.

**Figure 2.20:** Covalent energy term used to describe the bond distance V-O along the chain in MIL-47. A comparison is made between the estimated force constants resulting from a fit with (MBIS or HI) and without (Zero) the inclusion of the electrostatic interaction.

Finally, the van der Waals interactions are added and these results are shown in the last column. Similarly to what was done for MIL-53(Al), the $\epsilon$ and $\sigma$ values were rescaled to obtain a better reproduction of a certain property. One of the key characteristics of the MIL-47 guest-free framework is the pressure-induced breathing behavior as described by Yot *et al.* [92]. To obtain a good set of van der Waals parameters, such that the force field is able to reproduce the experimental behavior, the transition pressure from lp-to-np and from np-to-lp should be calculated at 300 K. This is, however, a computationally expensive procedure. A study at 0 K was performed by carrying out geometry optimizations (atomic positions and cell shape), while applying a fixed hydrostatic pressure. Repeating this for different pressures, starting from the lp or np, the pressure-dependent volume behavior was determined and the $PV$-profile of such a series of calculations (for a fixed $\epsilon$ and $\sigma$) is shown in Figure 2.21 on the next page. A hysteresis loop of about 150 MPa is observed. The dependence of the transition pressure on $\sigma$ and $\epsilon$ is shown in Figure 2.22 on page 50. The $\epsilon$ scale is varied on the horizontal axis between 0.5 and 0.8 and for $\sigma$ 1.0 and 1.1 were considered (see legend). Outside this range of parameters, no discrete transitions were found. This property is very sensitive to the van der Waals parameters. The transition pressure decrease, when the magnitude of the van der Waals interactions is increased (increasing $\epsilon$) and a nearly linear dependence can be observed. The precise influence of the $\sigma$ scale is less clear, as only two situations were plotted, but increasing $\sigma$ results in a smaller range of hysteresis. Including the 1-4 interactions results in an upward shift for both transition pressures.

At 300 K, Yot *et al.* [92] experimentally demonstrated a transition from the narrow pore to large pore at approximately 60 MPa, and between 120-170 MPa from the large pore to narrow pore. Their simulated values were 66 MPa and 137 MPa. As the temperature dependence of the transition pressure is difficult to predict, it still remains more or less a guess which set of parameters

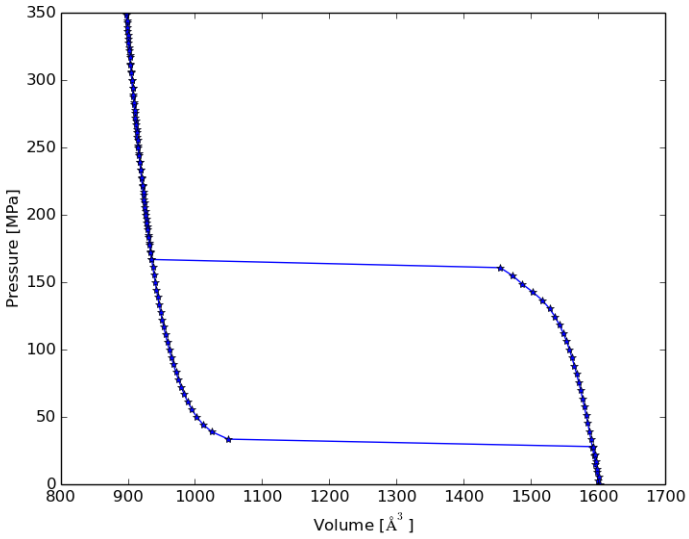


**Figure 2.21:** $PV$ profile showing hysteresis at 0 K ($\epsilon$=0.7, $\sigma$=1.1).

should be considered. It can, however, be seen in Figure 2.22 on the next page that the transition pressures at ($\epsilon$=0.7, $\sigma$=1.1) without the 1-4 interactions approach the experimental values best. The $PV$-profile at 0 K with these parameters can be found in Figure 2.21.

The transition pressures were determined at 300 K to validate this set of parameters. These calculations were performed by S.M.J. Rogge, who has recently developed a scheme for the accurate determination of the free energy profile at finite temperatures. The simulations were carried out in the ($N$, $V$, $\boldsymbol{\sigma}_a$=**0**, $T$)-ensemble. In this ensemble, the cell shape and instantaneous isotropic pressure can fluctuate freely, while the volume is kept fixed and the anisotropic contribution ($\boldsymbol{\sigma}_a$) to the stress tensor is controlled by a barostat. Within this ensemble, the cell shape can be fully sampled under the fixed volume constraint. In conventional $NVT$ MD simulations, the cell shape is kept fixed, such that only the atomic positions are sampled. The ensemble-averaged isotropic pressure $\langle P \rangle$ can be extracted from a simulation in the ($N$, $V$, $\boldsymbol{\sigma}_a$=**0**, $T$)-ensemble. This is the pressure exerted by the material on its environment. By performing calculations at different volumes, the $PV$-profile was determined at 300 K. The final result is shown in Figure 2.23 on page 51. An eleventh-order polynomial is then fitted to the $\langle P(V) \rangle$ data. The lp-to-np transition pressure is defined as the maximum pressure that can be applied to the material before the volume contraction takes place and is found as the local maximum of the $PV$ fit around the lp volume. Similarly, the np-to-lp transition pressure is the local minimum pressure around the narrow pore volume. The transition pressures obtained in this way (131.35 MPa and 55.42 MPa) show a good correspondence with the experiments of Yot *et al.* [92]. The experimental lp volume is 1530 Å$^3$, while the equilibrium volume at 300 K predicted with the force field is 1592 Å$^3$. The simulated np volume at the transition pressure is 980 Å$^3$ and the experimental volume at 178.1 MPa was determined to be 944 Å$^3$. The np and lp volumes are slightly overestimated compared to the experiment. From the

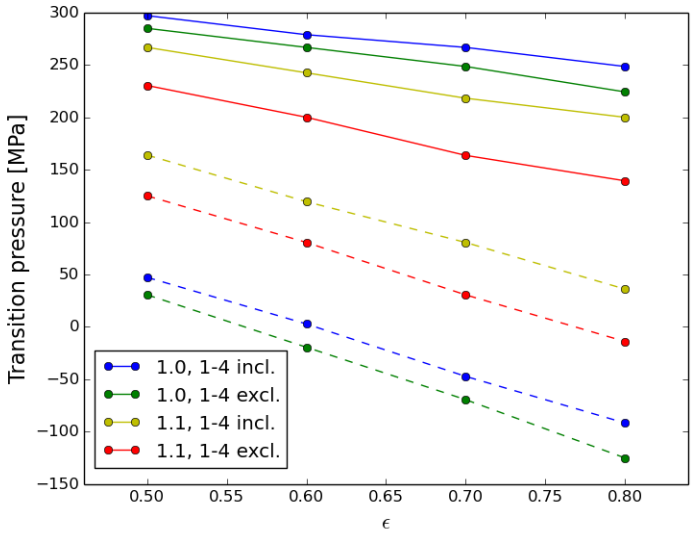


**Figure 2.22:** Influence of the van der Waals parameters on the transition pressure from lp to np and from np to lp at 0 K. The value of $\sigma$ is given in the legend. The full line represents the lp-to-np transition pressure, while the dotted line is the np-to-lp transition pressure.

results presented in this section, one can conclude that the force field is able to correctly mimic the pressure-induced breathing motion.

In Table 2.12, the lattice parameters are listed. The structure relaxed with the force field (at 0 K), with the modified van der Waals parameters, correctly describes the unit cell shape.

**Table 2.12:** Lattice parameters of MIL-47.

| | Exp. [110] | DFT, PBE [108] | FF (excl. vdW) | FF (incl. vdW) |
|---|---|---|---|---|
| $a$ [Å] | 16.143 | 16.231 | 15.944 | 16.492 |
| $b$ [Å] | 6.818 | 6.854 | 7.091 | 6.980 |
| $c$ [Å] | 13.939 | 13.975 | 14.354 | 13.910 |
| $\theta$ [°] | 81.6 | 81.5 | 84.0 | 80.3 |
| $D$ [Å] | 21.3 | 21.5 | 21.5 | 21.6 |
| $V$ [Å$^3$] | 1534 | 1555 | 1623 | 1601 |

### 2.3.4 HKUST-1

HKUST-1, synthesized for the first time at the Hong Kong University of Science and Technology (HKUST) by Chui *et al.* [111], is a paddle wheel MOF with metal center Cu. Paddle wheel MOFs are build from two divalent metal centers bridged by four carboxylate groups. These metal ions are in a square planar coordination. The organic linker in HKUST-1 is the 1,3,5-benzenetricarboxylate

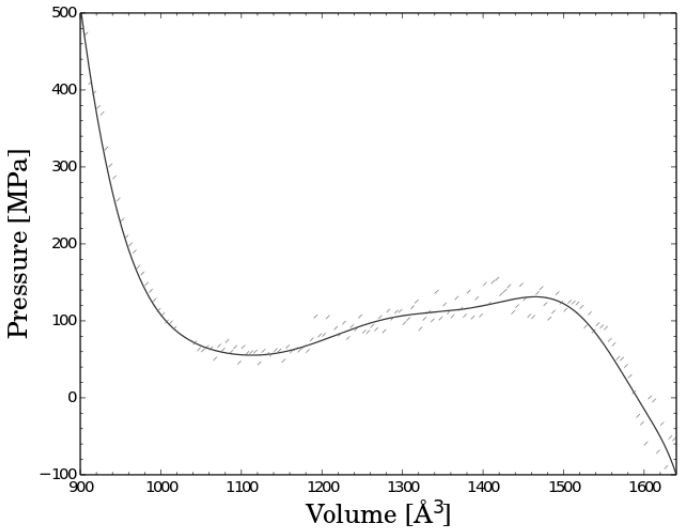


**Figure 2.23:** Simulated volume dependence of the pressure of MIL-47. The crosses represent the simulated data on a volume grid and the solid line is a polynomial fit of order 11.

(BTC). Each metal center has an additional water coordination in vertical alignment with the metal-metal interaction, resulting in a pseudo-octahedral coordination for the hydrated HKUST-1. In this work, only the dehydrated structure $[Cu_3(BTC)_2]$ was considered and the periodic structure is shown in Figure 2.24. It has a cubic crystal symmetry with space group $Fm\bar{3}m$. This structure was also synthesized with Zn and Ni as divalent metal centers [112, 113].

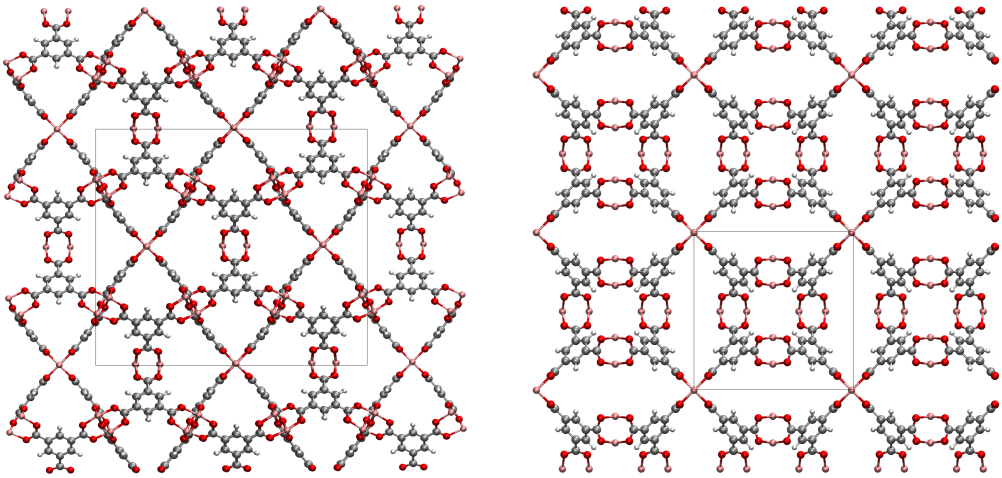

**Figure 2.24:** HKUST-1 along the [110] direction, with Cu paddle wheel in tbo topology (left). Cu paddle wheel in pto topology (right). The unit cells are indicated on the figure.

Tafipolsky *et al.* [63] derived a first-principles based force field for Cu-HKUST-1 and was later added in the MOF-FF [64] database. Force-field parameters were also derived in BTW-FF [59] and UFF4MOF [58]. The latter spent some effort in obtaining accurate parameters for the description

of paddle wheel MOFs with different metal centers. They included Ti, V, Cr, Mn, Fe, Co, Ni, Cu and Zn in their test set as all of these were previously used in paddle wheel MOFs (for Refs. see UFF4MOF). In this work, some of these metals were studied in the HKUST framework.

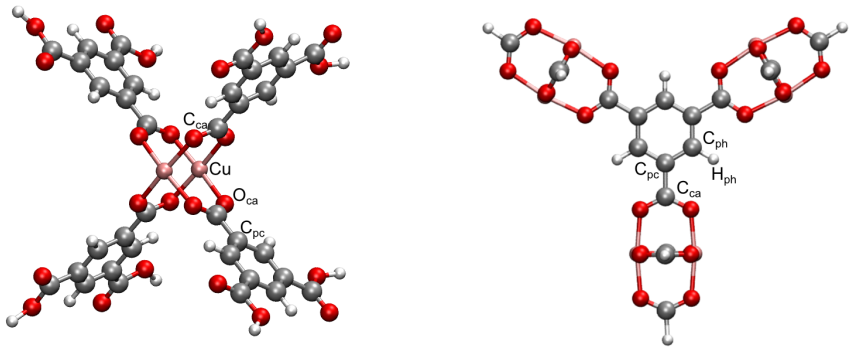


**Figure 2.25:** Cluster models for HKUST-1.

Two cluster models were used for HKUST-1 and these are shown in Figure 2.25 together with the relevant atom types. The calculations were performed using a 6-311++G(d,p) basis set and the hybrid B3LYP functional. Tafipolsky *et al.* [63] terminated the carboxyl group with a hydrogen atom, while Ryan *et al.* [114] used a methyl group. In this work, a larger cluster was used for the inorganic unit, similar to the one of Lukose *et al.* [115] (left pane of Figure 2.25) and the parameters of the BTC linker were derived from the second model system (right pane of Figure 2.25).

The copper paddle wheel displays an antiferromagnetic character. The ground electronic state of the periodic structure is an open-shell singlet, where the unpaired electrons on neighboring Cu atoms have opposite spin [114]. Tafipolsky *et al.* [63] investigated into more detail the electronic structure of their cluster model. They found that the open shell antiferromagnetic state is slightly lower in energy than the triplet state. They used, however, the triplet state data for the development of their force field, as the open-shell ground state with lower energy showed a large spin contamination. They noted that the closed-shell singlet lies far above the triplet and suggested not to use it as reference data. The ab initio calculations performed here, indicated the same result with an energy difference of 1 eV between the triplet (obtained with unrestricted DFT) and the singlet (obtained with restricted DFT) for the inorganic cluster model. However, for the triplet state, the frequency calculations did not converge. Decreasing the convergence criteria in this step, did not work and therefore it was decided to use the singlet data. Similarly as was mentioned for MIL-47 and MIL-53, it is hard to predict the influence on the final force field. In Table 2.13, some structural data is compared between the singlet and triplet state and the results obtained by Tafipolsky *et al.* [63]. They used the aug-cc-pVDZ-PP basis with the B3LYP functional. The Cu-Cu distance is found to be the same with both spin multiplicities, but the value obtained by Tafipolsky (with a different basis set) is 0.01 Å larger. The Cu-$O_{ca}$ distance, however, is larger in the triplet state, but the value

of Tafipolsky lies in between. This table shows some differences, but there is as much deviation between the singlet and triplet stated obtained in this work, as between the result of Tafipolsky and the triplet state here, such that no conclusions can be drawn from this.

**Table 2.13:** Comparison of some key distances and angles in the DFT reference clusters.

| | Singlet (RB3LYP) | Triplet (UB3LYP) | Triplet (UB3LYP) Tafipolsky *et al.* [63] |
|---|---|---|---|
| Cu-Cu | 2.507 | 2.507 | 2.518 |
| Cu-$O_{ca}$ | 1.960 | 1.972 | 1.967 |
| $C_{ca}$-$O_{ca}$ | 1.265 | 1.267 | 1.265 |
| $O_{ca}$-$C_{ca}$-$O_{ca}$ | 126.5 | 125.3 | 127.8 |

Despite the limitations of the ab initio data, this input is used to derive the force field. The charges derived via HI and MBIS are presented in Table 2.14. A comparison of the ESP cost for the MK and Hu cost function shows that the MBIS and HI charges have approximately the same cost, with a slight preference for the MBIS charges (see Table 2.15). The charges itself are quite similar (see Table 2.14). It was opted to work with the MBIS charges to remain consistent with previous sections. In the final force field, the 1-4 van der Waals parameters interactions are excluded and the parameters were not rescaled in analogy with the rigid MOF-5.

**Table 2.14:** Atomic charges derived on the nonperiodic cluster model with the MBIS and HI scheme. The symbol * indicates that it is derived from the linker cluster.

| Atom type | MBIS | HI |
|---|---|---|
| Cu | 0.989 | 1.003 |
| $O_{ca}$ | -0.640 | -0.662 |
| $C_{ca}$ | 0.822 | 0.859 |
| $C_{pc}$* | -0.188 | -0.158 |
| $C_{ph}$* | -0.017 | -0.020 |
| $H_{ph}$* | 0.169 | 0.142 |

One important aspect of the force field is the Cu-Cu bond. As was argued by Tafipolsky *et al.* [63], it is necessary to include this bond. It is just an articial bond that has nothing to do with a potential chemical bond in between, but they required this as the strong electrostatic repulsion between the two metal point charges would result in an overestimation of the bond and bend force constants of the atoms in the neighborhood to compensate this effect. In this work, Gaussian charges were used, such that this effect should be damped. QuickFF estimated the force constant with and without in-

clusion of the electrostatic interactions in the fitting procedure on approximately 300 kJ/(mol · Å$^2$). Compared to typical bond force constants, this is a rather weak connection (a factor ten lower), but still not negligible. The fact that the same force constant was obtained without the electrostatic interactions indicates that there is some kind of force working in between.

**Table 2.15:** Comparison of cost for MK and Hu ESP cost function for different schemes on inorganic cluster.

| Charge scheme | MK Cost | Hu Cost |
|---|---|---|
| MK | 0.00385 | 0.00510 |
| Hu | 0.00392 | 0.00501 |
| HI | 0.02594 | 0.02683 |
| MBIS | 0.02379 | 0.02372 |

In paddle wheel MOFs, the metal centers are in a square planar coordination. The $O_{ca}$-Cu-$O_{ca}$ bend potential term has two minima (at 90° and at 180°). A harmonic potential term is not able to describe this, as it has only one minimum. Just leaving this term out, as was done in the octahedral coordination environment of MIL-53 and MIL-47, did not result in a good relaxed structure. Tafipolsky *et al.* [63] used a so-called improved Fourier bending term to model this. Here, it was opted to use the same term:

$$V(\theta) = \frac{K}{2}\left[1 + \cos(\theta)\right]\left[1 + \cos(2\theta)\right] \tag{2.32}$$

The only unknown parameter is the force constant $K$. Similarly as was discussed in the case of the special dihedrals, this potential term can be added in the refinement step in the fitting procedure of QuickFF. Here the force constants of the potential energy terms are estimated via the minimization of a cost function based on the Cartesian Hessian. In Table 2.16 the structural parameters are listed. The largest deviations are found around the Cu-Cu paddle wheel. The Cu-Cu distance is overestimated with the force field and the $O_{ca}$-Cu-$O_{ca}$ angle is somewhat underestimated, but overall a good correspondence between the DFT cluster and force field structures (excluding and including van der Waals interactions) is found. The experimental lattice parameter of the fully desolvated HKUST-1 is 26.3046 Å [116] (77 K), which was well reproduced by Tafipolsky *et al* [117] with a lattice parameter of 26.38 Å. With our force field, a value of 26.631 Å is found.

**Exploring network topologies of Cu paddle wheel MOFs**

Amirjalayer *et al.* [117] investigated the relative stability of network topologies of copper paddle wheel MOFs using their ab initio derived force fields. Two different organic linkers were considered (the organic linker of HKUST-1 (BTC) and benzene-1,3,5-tribenzoate (BTB)) and two different topologies: tbo (HKUST-1) and pto, which is shown in Figure 2.24 on page 51. They studied an interpenetrated form (int) for each topology and linker (see Figures in Ref. [117]). In Table 2.17

and Table 2.18, their results are shown.

**Table 2.16:** Structural parameters of HKUST-1. The symbol * indicates that it was taken from the organic linker cluster.

| | DFT cluster | FF (excl. vdW) periodic | FF (incl. vdW) periodic |
|---|---|---|---|
| $Cu\text{-}O_{ca}$ [Å] | 1.96 | 1.99 | 1.99 |
| Cu-Cu [Å] | 2.51 | 2.59 | 2.59 |
| $O_{ca}\text{-}C_{ca}$ [Å] | 1.27 | 1.26 | 1.26 |
| $C_{ca}\text{-}C_{pc}$ [Å] | 1.50* | 1.50 | 1.51 |
| $C_{pc}\text{-}C_{ph}$ [Å] | 1.40* | 1.40 | 1.40 |
| $Cu\text{-}Cu\text{-}O_{ca}$ [°] | 86.5 | 85.1 | 85.1 |
| $O_{ca}\text{-}Cu\text{-}O_{ca}$ [°] | 89.9 | 86.1 | 85.9 |
| $Cu\text{-}O_{ca}\text{-}C_{ca}$ [°] | 120.2 | 121.6 | 121.9 |
| $O_{ca}\text{-}C_{ca}\text{-}C_{pc}$ [°] | 116.8 | 116.7 | 117.0 |
| $C_{ca}\text{-}C_{pc}\text{-}C_{ph}$ [°] | 120.0* | 119.9 | 120.0 |

To illustrate the general applicability of the force fields derived with QuickFF, a similar analysis was made. The parameters for the BTB linker were derived from a different cluster model shown in Figure 2.26. The initial structures were taken from the supporting information of Ref. [117] and were fully relaxed (atomic positions and cell shape). The relative energies per formula unit $S_3T_4$ (S stands for the square planar coordination plane and T for the BTB or BTC linker) and unit cell parameters are shown in Tables 2.17 and 2.18. These energies can be compared as all structures have the same connectivity (no different chemical bonds) and are build from the same formula unit. The only difference is their topology. The conventional unit cell of HKUST-1 contains 8 of these formula units, but the pto unit cell only 2. This number is multiplied by two in the interpenetrated case.

**Table 2.17:** Relative energies per formula unit $S_3T_4$ for the investigated network topologies of Cu-BTC. The value between brackets gives the procentual difference with the optimized structure of Amirjalayer *et al.* [117], determined as $(X\text{-}X_{ref})/X_{ref}$.

| | tbo (HKUST-1) | pto | tbo (int) | pto (int) |
|---|---|---|---|---|
| $a$ [Å], This work | 26.631 (0.9) | 15.406 (0.8) | 26.577 (0.8) | 15.139 (0.5) |
| $\Delta\ E$ [kJ/mol], This work | 0.0 | 87.5 | -155.5 | 150.0 |
| $a$ [Å] [117] | 26.383 | 15.281 | 26.362 | 15.063 |
| $\Delta\ E$ [kJ/mol] [117] | 0.0 | 49.8 | -167.8 | 749.8 |

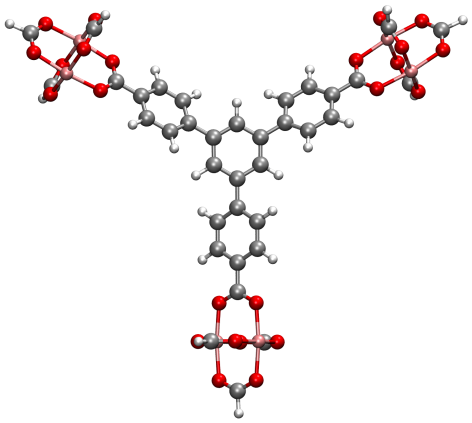

**Figure 2.26:** Cluster model for BTB-linker in Cu paddle wheel MOFs.

**Table 2.18:** Relative energies per formula unit $S_3T_4$ for the investigated network topologies of Cu-BTB. The value between brackets gives the procentual difference with the optimized structure of Amirjalayer *et al.* [117], determined as $(X\text{-}X_{ref})/X_{ref}$.

| | tbo | pto | tbo (int) | pto (int) |
|---|---|---|---|---|
| $a$ [Å], This work | 47.747 (0.7) | 27.685 (0.8) | 47.721 (0.7) | 27.217 (0.8) |
| $\Delta$ $E$ [kJ/mol], This work | 160.4 | 0.0 | 76.2 | -94.25 |
| $a$ [Å] [117] | 47.409 | 27.463 | 47.344 | 26.994 |
| $\Delta$ $E$ [kJ/mol] [117] | 64.0 | 0.0 | -31.8 | -133.1 |

All lattice parameters are well reproduced with a maximal overestimation of 0.9% for HKUST-1. The absolute energies do not fully agree, but this can be expected when comparing force field energies. A slightly different parametrization can lead to large differences, but it is however satisfying that the same trends were found with the newly developed force fields. From Table 2.17, one can understand why Cu-BTC (both int and non-int) crystallizes in the tbo network topology and not in the pto topology. MOF-14, a Cu-BTB paddle wheel structure with a complex interpenetrated unit cell, is observed experimentally in a pto topology. In the second table, it can be seen that indeed the pto topology for Cu-BTB is energetically preferable according to the force field. The non-interpenetrated form of Cu-BTB has not been detected experimentally, however, this table suggests a pto-topology.

**Table 2.19:** Overview of studied metal centers.

| | V | Fe | Co | Ni | Cu |
|---|---|---|---|---|---|
| Charge metal | 1.103 | 1.007 | 1.049 | 0.905 | 0.989 |
| Charge $O_{ca}$ | -0.681 | -0.637 | -0.649 | -0.612 | -0.640 |
| Charge $C_{ca}$ | 0.840 | 0.790 | 0.811 | 0.808 | 0.822 |
| Spin (DFT Cluster) | 0 | 2 | 0 | 0 | 0 |

**Influence of metal center on structural parameters of HKUST-1**

Force-field parameters were determined for different metal centers using the inorganic cluster model as presented in Figure 2.25 on page 52. These are all row 3 elements. This was previously done by the authors of UFF4MOF [58] for the guest-free HKUST-1 framework. In Table 2.19, some charges derived with the MBIS scheme are listed. The charges are approximately the same, indicating that the electronic-structure is similar. The last row indicates the spin used for the DFT calculations. For V, Fe and Co the same spin was considered as in the DFT cluster calculations performed by the authors of UFF4MOF. In UFF4MOF, the spin of the Ni cluster was 1, but the same problems arised as with Cu. The geometry optimization using unrestricted B3LYP (S=1) converged and was lower in energy than the restricted singlet case, but again the frequencies could not be calculated. Instead, the energetically less favorable spin 0 was used.

**Table 2.20:** Bond distances, bend angles and lattice parameter of HKUST-1 with different metal centra.

| | Method | V | Fe | Co | Ni | Cu |
|---|---|---|---|---|---|---|
| M-$O_{ca}$ [Å] | DFT | 2.05 | 1.93 | 1.91 | 1.90 | 1.96 |
| | Force Field | 2.03 | 1.92 | 1.90 | 1.89 | 1.99 |
| M-M [Å] | DFT | 2.02 | 2.12 | 2.20 | 2.44 | 2.51 |
| | Force Field | 1.93 | 2.14 | 2.20 | 2.42 | 2.59 |
| $O_{ca}$-M-$O_{ca}$ [°] | DFT | 89.9 | 90.0 | 90.0 | 89.9 | 89.8 |
| | Force Field | 88.9 | 89.1 | 89.0 | 88.8 | 85.9 |
| M-M-$O_{ca}$ [°] | DFT | 92.5 | 91.6 | 90.6 | 87.3 | 86.5 |
| | Force Field | 94.1 | 91.3 | 90.4 | 87.4 | 85.1 |
| M-$O_{ca}$-$C_{ca}$ [°] | DFT | 117.7 | 117.3 | 117.7 | 119.9 | 120.2 |
| | Force Field | 114.4 | 117.4 | 117.8 | 119.95 | 121.9 |
| $a$ [Å] | Force Field | 26.91 | 26.45 | 26.30 | 26.18 | 26.63 |

In Table 2.20, some structural characteristics are compared to study the influence of the metal center. When moving to the right in the periodic table (V, Fe, Co, Ni, Cu), the metal-metal distance increases from 2.0 Å to 2.5 Å in the DFT cluster. Except for V, where this value is 0.1 Å underestimated, the force field succeeds in reproducing this distance correctly. In all cases,

the metal-metal bond was added in the fitting procedure as proposed by Tafipolsky *et al.* [63]. The V-HKUST-1 framework is predicted to have the largest unit cell, while Ni-HKUST-1 has the smallest and no clear connection between the lattice parameter and metal-metal distance is detected. However, it seems that the lattice parameter is correlated to the $O_{ca}$-M distance. These values are also well reproduced by the force field. For the bend angles, $O_{ca}$-M-$O_{ca}$ is the most difficult one to reproduce, but overall a good agreement is found between the DFT cluster and the force field optimized periodic structure. As explained above, this was modeled using an improved Fourier bend. If this term is neglected, an underestimation of 10° is found (not shown), illustrating the importance of this term. It can be concluded that the force field succeeds in reproducing the most important structural parameters. The trends observed when comparing the DFT clusters, are reproduced in the periodic force field. A more comprehensive study on the differences in properties will be made in Chapter 4.

### 2.3.5 DMOF-1

DMOF-1 [$Zn_2$(1,4-BDC)$_2$(DABCO)] is a flexible MOF that shows breathing behavior. It was synthesized for the first time by Dybtsev *et al.* [118]. The framework is composed of $Zn_2$ units with a paddle wheel structure, which are bridged with 1,4-BDC linkers to form a 2D square-grid. The axial sites of the paddle wheels are occupied by 1,4-diazabicyclo[2.2.2]octane (DABCO) and in this way the $Zn_2$ units are connected. The 3D structure has a tetragonal unit cell with space group P4/mmm and is shown in Figure 2.27. Experimental lattice parameters can be found in Table 2.22.

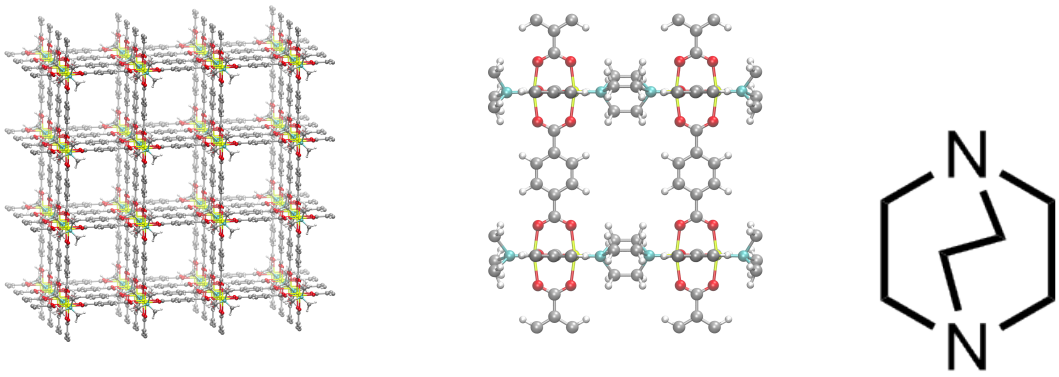


**(a)** 3D view of paddle wheel MOF. **(b)** Unit cell along the *a*- or *c*-direction. **(c)** DABCO

**Figure 2.27**

A flexible force field was made for this structure by Grosch and Paesani [68] based on ab initio calculations and parameters from an extension of the AMBER force field [51]. This structure is available in the parameter set of MOF-FF [64] and extra parameters were determined by Addicoat *et al.* in UFF4MOF [58].

In this work, three different clusters were used to estimate the force-field parameters. The first model system (Figure 2.28 (left)) has previously been used in MOF-FF, while the other two clusters (Figure 2.28 (center, right)) were suggested by Grosch and Paesani. The last two represent the organic linkers (BDC and DABCO) and the parameters related to the inorganic part (containing Zn) were derived from the first cluster. The axial positions in the second cluster (Figure 2.28 (center)) were capped with -$NH_3$ groups to mimic the electrostatic environment present in DMOF-1. Grosch and Paesani found that calculations with the M062X functional more accurately reproduce the experimental structure than the B3LYP functional used here, however to remain consistent with the previous sections we decided to use B3LYP. The relevant force field atom types are indicated in the figure.

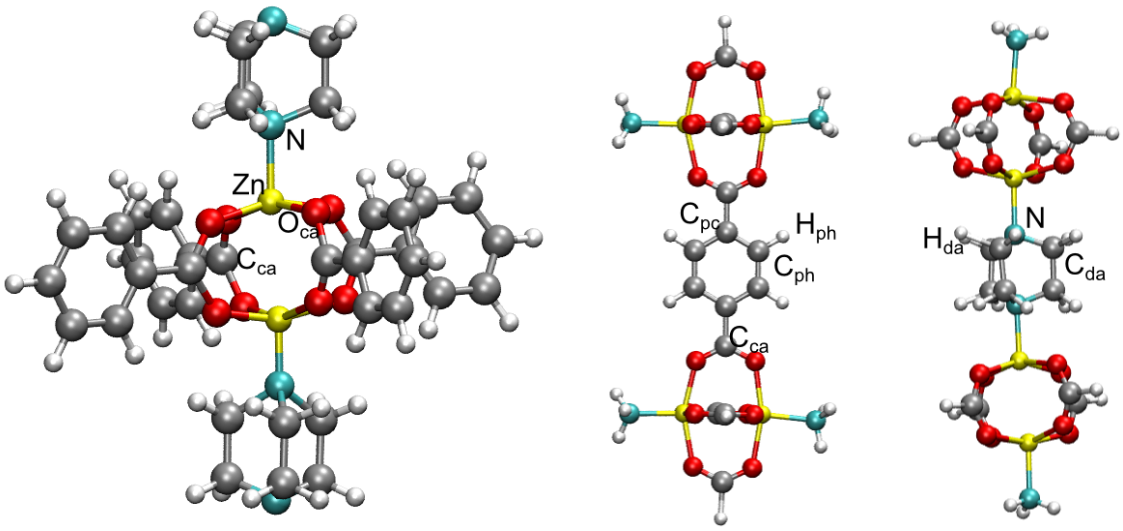


**Figure 2.28:** Cluster models for the parametrization of DMOF-1.

The resulting ESP costs were compared for different schemes (results not shown) and the MBIS charges again performed better than the HI charges. In Table 2.21, structural parameters of all three clusters are compared between the experimental structure, the DFT clusters and the force field optimized periodic structure. It can be seen that there is an overall good agreement between the DFT clusters and the force field structures. The largest deviations situate around the metal centers. The force field strongly underestimates the Zn-Zn DFT distance (with and without van der Waals interactions). In contrast to what one might think, there is a better reproduction of the DFT values when including the van der Waals interactions. The values related to the organic linkers are well reproduced. Similarly to the other paddle wheel MOFs, the metal-metal bond was explicitly included, which was also done by Grosch and Paesani [68]. The improved Fourier bending term was again used for the square planar metal coordination environment as discussed in Section 2.3.4.

The obtained lattice parameters are listed in Table 2.22. An overestimation (at 0 K) of is found for the $a$ and $c$ lattice parameters along the BDC linker (compared to MOF-FF and the experimental value). This is a similar overestimation as the distance along the BDC linkers of MOF-5 and

MIL-53. The lattice parameter $b$ (DABCO linker) is well reproduced, which is due to a cancellation of errors (Zn-N distance overestimated, Zn-Zn distance underestimated). The force field optimized structure is not perfectly tetragonal, as the angle $\beta$ between the major crystal axes $a$ and $c$ is not 90°, but 88.2°. Overall, the unit cell shape is in excellent agreement with other published values.

**Table 2.21:** Structural parameters of DMOF-1. The symbol * indicates that it was averaged over two clusters.

| | Exp. (223 K) [118] periodic | DFT cluster | FF (excl. vdW) periodic | FF (incl. vdW) periodic |
|---|---|---|---|---|
| Zn-N [Å] | 2.07 | 2.07* | 2.04 | 2.14 |
| Zn-$O_{ca}$ [Å] | 2.03 | 2.06 | 2.06 | 2.05 |
| Zn-Zn [Å] | 2.88 | 3.04 | 2.58 | 2.74 |
| N-$C_{da}$ [Å] | 1.44 | 1.49 | 1.49 | 1.50 |
| $C_{da}$-$C_{da}$ [Å] | 1.54 | 1.55 | 1.55 | 1.55 |
| $O_{ca}$-$C_{ca}$ [Å] | 1.26 | 1.26* | 1.26 | 1.26 |
| $C_{ca}$-$C_{pc}$ [Å] | 1.50 | 1.50 | 1.50 | 1.51 |
| $C_{pc}$-$C_{ph}$ [Å] | 1.37 | 1.40 | 1.40 | 1.40 |
| $C_{ph}$-$C_{ph}$ [Å] | 1.38 | 1.39 | 1.39 | 1.39 |
| Zn-Zn-$O_{ca}$ [°] | 80.6 | 78.6 | 85.0 | 83.1 |
| Zn-N-$O_{ca}$ [°] | 111.2 | 110.1 | 109.8 | 110.4 |
| Zn-$O_{ca}$-$C_{ca}$ [°] | 125.5 | 127.9 | 123.0 | 125.0 |
| $O_{ca}$-$C_{ca}$-$C_{pc}$ [°] | 117.2 | 117.3* | 118.1 | 118.0 |

**Table 2.22:** Lattice parameters of DMOF-1.

| | Method | $a$ [Å] | $b$ [Å] | $c$ [Å] |
|---|---|---|---|---|
| This work | FF (0 K) | 11.11 | 9.64 | 11.11 |
| Dybtsev *et al.* [118] | Exp. (223 K) | 10.93 | 9.61 | 10.93 |
| Grosch and Paesani [68] | FF, MD at 223 K | 11.0±0.1 | 9.6±0.1 | 11.0±0.1 |
| MOF-FF [64] | FF (0 K) | 11.01 | 9.75 | 11.01 |
| UFF4MOF [58] | FF (0 K) | 11.31 | 9.20 | 11.31 |
| Ortiz [105] | DFT (0 K) | 11.04 | 9.61 | 11.04 |

DMOF-1 shows guest-dependent breathing behavior. The structure remains e.g. rigid upon adsorption of $H_2$, but contracts and forms a diamond-shaped pore under the influence of benzene [68,118]. An experimental interdiagonal angle (definition analogous to MIL-53, Figure 2.14) of approximately

77° is found [118], which is comparable to the large-pore phase of the MIL-53 family. No reversible transitions upon pressure or temperature stimuli of the guest-free framework have been reported.

In Figure 2.29, potential energy scans over the interdiagonal angle are shown at 0 K. Similarly as with MIL-53, a study was made of the influence of the $\epsilon$ and $\sigma$ scale of the van der Waals parameters. Overall, the influence on the energy profile is rather small compared to the large variations in the MIL-53 family. A narrow pore local minimum was found (see Figure 2.29 (left)), but only at a relatively high $\epsilon$ scale. It can be assumed that this is not a real minima, but only results from the artificially high interactions between the BDC linkers. The absolute minima is always the open form, which is clearly more stable with an energy difference of minimal 5 kJ/mol per Zn atom. In both figures, a broad minimum is revealed around 90°. A small reparametrization of the covalent part could probably lead to a perfect tetragonal unit cell.

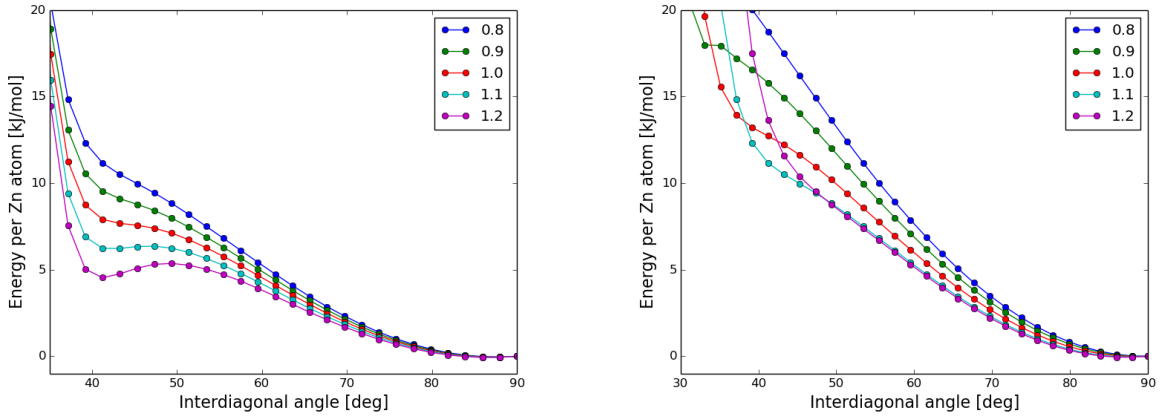


**Figure 2.29:** A potential energy scan over the interdiagonal angle. Rescaling of $\epsilon$ ($\sigma = 1.1$) in the left pane. Rescaling of $\sigma$ ($\epsilon = 0.8$) in the right pane.

### 2.3.6 ZIF-8

The zeolitic imidazolate frameworks (ZIFs) are a class of MOFs that are topologically isomorphic with zeolites. ZIFs have drawn attention due to the attractive combination of thermal, chemical and mechanical stability comparable with zeolites and rich topological diversity, pore size tunability and structural flexibility as in MOFs. ZIF-8 [$Zn(MeIM)_2$] is a prototypical example of this class and has been synthesized by the group of Yaghi [13]. It has a sodalite zeolite-like topology with a cubic space group I-43m and is composed of $Zn^{2+}$ ions tetragonally linked with 2-methylimidazole (MeIM), which can be seen in Figure 2.30.

There have been some attempts to derive flexible force fields for the ZIFs and to the best of my knowledge no first-principles parametrized force fields have been published. Hu *et al.* [57] made an all-atom flexible force field for ZIF-8 based on experimental results and parameters from the

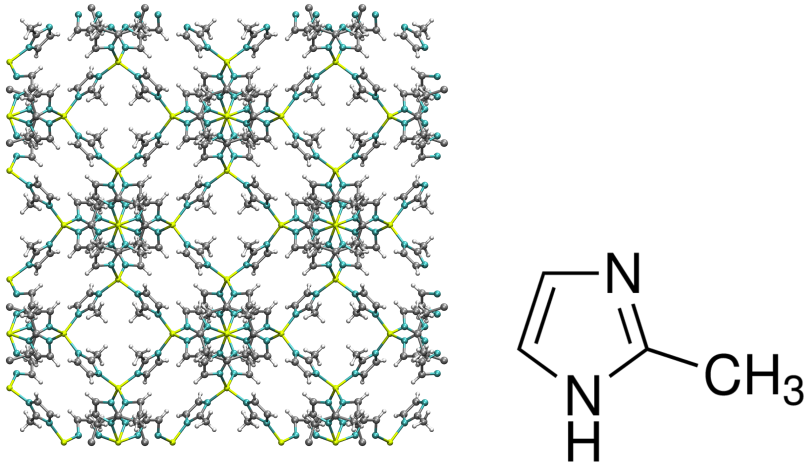


**Figure 2.30:** View along the [100] direction in ZIF-8 in the left pane. In the right pane, the organic linker (DABCO) is illustrated.

AMBER [51] force field for the organic linker. The functional form of the AMBER force field is also adopted to describe the inorganic part. The covalent terms include harmonic bonds and bends and single cosine torsional terms. The noncovalent part consists of a Coulombic point charge potential and a Lennard-Jones potential to describe the dispersion interacctions. Terms related to the inorganic part were fitted to reproduce experimental crystallographic data.

In this work, a single cage-like cluster model is proposed for the estimation of all force-field parameters. It is shown in Figure 2.31. The Zn atoms at the corners of a square are connected via MeIM linkers. It is the repeating unit in ZIF-8 as can be seen in Figure 2.30. Each Zn-atom is still tetrahedrally surrounded by methylimidazole groups, but only two of these are connected with other metal centers. The termination of the other two groups is inspired by a recent study of Wang *et al.* [69], who used a cluster model of ZIF-8 with only one tetrahedrally coordinated Zn atom (see Figure 2.31 (right)). The 4 methylimidazolate groups were terminated by a proton (or hydrogen) resulting in a total charge +2. In this way, the metal-nitrogen bonds are equivalent between the four linkers and the central metal ion. In the cage cluster, 8 groups need to be terminated and similarly it was opted for proton saturation. The cluster has then a total charge of +4.

A comparison between different charge schemes is made in Table 2.23. The same trends as in the previous sections are visible. The ESP fitted charges (Hu) have the lowest ESP cost and the MBIS charges perform better than the HI charges. The MBIS charges used in the force field are shown in Table 2.24 on page 64.

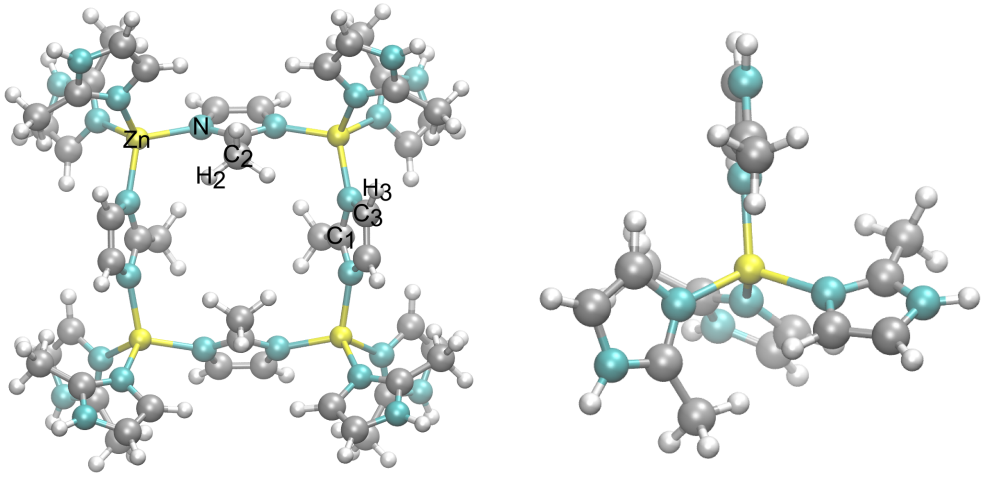


**Figure 2.31:** Cluster model for ZIF-8 used to parametrize the force field (left) and cluster model used by Wang *et al.* [69] (right).

**Table 2.23:** Comparison of ESP cost for ZIF-8.

| Charge scheme | MK Cost | Hu Cost |
|---|---|---|
| Hu | 0.00633 | 0.00605 |
| HI | 0.05621 | 0.05478 |
| MBIS | 0.03378 | 0.02961 |

The force field generated with QuickFF resulted in an unstable structure. The material collapses during a geometry optimization of the unit cell at 0 K. This is due to the strong underestimation of the force constant of the N-Zn-N bend. After the second step in the QuickFF fitting method, a large force constant of 785.693 kJ/(mol · rad$^2$) is found. This is averaged over all perturbation trajectories generated for the same atom types with a standard deviation of only 1.406 kJ/(mol · rad$^2$). However, as was explained in Section 2.2.3, this is a strong overestimation. In the third step, the refinement of the force constants, this force constant is put to zero. It could be that the electrostatic interactions alone are enough to reproduce the tetrahedal coordination environment, such that there is no need for a covalent term.

To gain a better understanding of this force constant, a smaller cluster model was investigated. This is the one used by Wang *et al.* [69] (Figure 2.31 (right)). All surrounding groups of the Zn ion are the same. In Table 2.25 the estimated force constants after the different steps of the QuickFF fitting procedure are shown. The estimated force constant in the cage cluster is a factor two larger than in the small cluster after fitting it to the perturbation trajectories. The MeIM groups are relatively free to bend in the smaller cluster and therefore this motion is more decoupled from the other internal degrees of freedom than in the cage cluster. This results in a less overestimated force constant. It can also be seen that the electrostatic interactions play a rather large role, as the force

constant is 25% larger when these interactions are neglected (fourth column). However, in both situations, with and without the electrostatic interactions, this force constant is put to zero in the refinement step. To test if this is not due to the harmonic description of the bend in a tetrahedral coordination environment, a force field was generated for methane. In Table 2.25 is shown that the force constant of the H-C-H bend is not zero. This indicates that it should be possible to obtain a reliable estimate of the bend in such an environment. Hu *et al.* [57] noted that the lattice parameters of ZIF-8 are rather insensitive to this N-Zn-N force constant. They obtain through fitting their unknown parameters to experimental structures a force constant of 100 kJ/(mol $\cdot$ rad$^2$).

**Table 2.24:** Atomic charges derived via MBIS scheme.

| Atom Type | Charge |
|---|---|
| Zn | 1.290 |
| N | -0.692 |
| $C_1$ | 0.623 |
| $C_2$ | -0.604 |
| $H_2$ | 0.180 |
| $C_3$ | -0.050 |
| $H_3$ | 0.154 |

**Table 2.25:** Force constant of the harmonic N-Zn-N bend in kJ/mol/rad$^2$. In the last column the H-C-H force constant for methane is shown.

| QuickFF step | Cage (incl. EI) | Small (incl. EI) | Small (excl. EI) | $CH_4$ (incl. EI) |
|---|---|---|---|---|
| Perturbation trajectories | 786.693 $\pm$ 1.406 | 306.256 $\pm$ 2.061 | 380.250 $\pm$ 12.223 | 416.479 $\pm$ 0.002 |
| Refine force constant | 0.0 $\pm$ 0.0 | 0.0 $\pm$ 0.0 | 0.0 $\pm$ 0.0 | 248.13 $\pm$ 0.000 |

In Figure 2.32 on page 66, the dependence of the lattice parameters and angles is shown on this constant. At the same time, the $\epsilon$ and $\sigma$ scale are varied to obtain a good set of parameters. All these calculations have been done with the 1-4 interactions turned off. In Figure 2.32a, the dependence of the lattice parameter on $\sigma$ and the force constant of the N-Zn-N bend is shown. The missing points, e.g. for the curve without van der Waals part, indicate that the structure collapses. It can be seen that there is relatively no influence of the force constant if the value is large enough, while the $\sigma$ scale has a large influence. A decrease of $\sigma$ with 20% results in a nearly perfect reproduction of the experimental lattice parameter. However, this in fact means that the radii of the atoms are decreased with 20%, which is a rather large deviation of the original MM3 parameters. Therefore it is chosen to work with a $\sigma$ parameter of 0.9, which results in overestimation of approximately 1% of the lattice parameter. This is comparable with the accuracy obtained in previous sections.

In Figure 2.32b, the $\epsilon$ parameter is varied. It has clearly no influence on the lattice parameters. Finally, the unit cell angle is plotted in Figure 2.32c. For a cubic unit cell, this should be 90°. The area within the black dotted lines indicates a precision of one decimal. It is chosen here to work with $\epsilon$ equal to 1, as this is the standard parameter in MM3. To conclude, the van der Waals scale chosen from these calculations is ($\epsilon$=1, $\sigma$=0.9) and 1-4 interactions are turned off. All these plots show that the force constant of the N-Zn-N bend has no influence on the unit cell parameters, when chosen large enough. Values larger than 60 kJ/(mol $\cdot$ rad$^2$) produce a correct shape for the chosen van der Waals parameters. From now on, this value will be fixed at 100 kJ/(mol $\cdot$ rad$^2$), which is also the value used by Hu *et al.* [57].

In Table 2.26, structural parameters are compared between the experimental structure [13], the DFT cluster and the force field optimized structures. The lattice parameter obtained with the final force field is 17.13 Å, which is within 1% of the experimental lattice parameter of 16.992 Å(295 K) and is a better reproduction than a periodic DFT calculation by Tan *et al.* [119] (17.35 Å) with the B3LYP functional. It can be seen that the DFT cluster overestimates the experimental Zn-Zn distance, but the force field (with and without dispersion interactions) reproduces it exactly. Overall, there is a very good reproduction of the structural parameters by the final force field. The largest procentual error is only 0.7% (Zn-N-$C_1$) compared to the experiment. It can be concluded that the ab initio developed force field results in an excellent reproduction of the experimental structure.

**Table 2.26:** Structural parameters of ZIF-8. Comparison between experiment, DFT cluster and force field.

| | Exp. [13] periodic | DFT cluster | FF (excl. vdW) periodic | FF (incl. vdW) periodic |
|---|---|---|---|---|
| Zn-Zn [Å] | 6.01 | 6.10 | 6.01 | 6.01 |
| Zn-N [Å] | 1.99 | 2.01 | 2.01 | 2.00 |
| N-$C_1$ [Å] | 1.34 | 1.35 | 1.34 | 1.34 |
| N-$C_3$ [Å] | 1.37 | 1.38 | 1.38 | 1.38 |
| $C_1$-$C_2$ [Å] | 1.49 | 1.50 | 1.50 | 1.50 |
| N-Zn-N [°] | 109.8 | 111.0 | 108.7 | 109.1 |
| Zn-N-$C_1$ [°] | 128.3 | 130.0 | 127.4 | 127.3 |
| Zn-N-$C_3$ [°] | 126.4 | 124.1 | 126.1 | 126.3 |
| N-$C_1$-$C_2$ [°] | 123.9 | 124.1 | 124.1 | 124.1 |

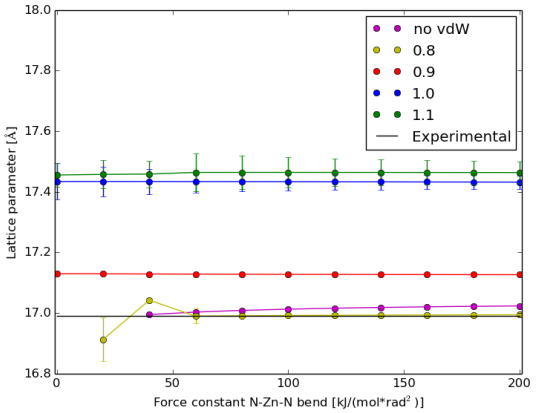


**(a)** Influence of $\sigma$ and force constant on the lattice parameter of ZIF-8 ($\epsilon$=1). Error bars indicate standard deviation. In most cases the error bars are smaller than the dot.

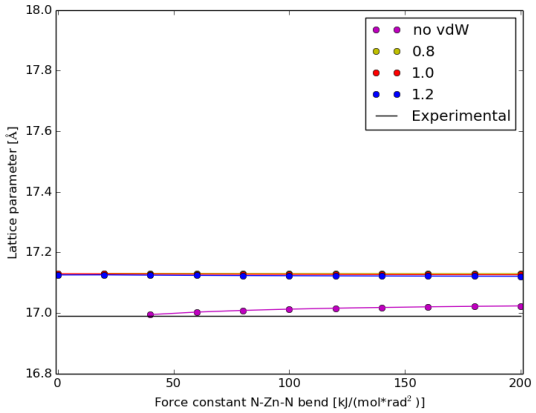


**(b)** Influence of $\epsilon$ and force constant on the lattice parameter ($a$=$b$=$c$) of ZIF-8 ($\sigma$=0.9). In all cases the error bars are smaller than the dot.

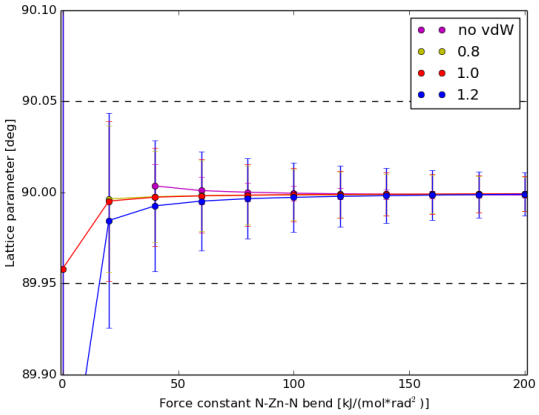


**(c)** Influence of $\epsilon$ and force constant on the unit cell angle ($\alpha$=$\beta$=$\gamma$) of ZIF-8 ($\sigma$=0.9). Area within black dotted lines indicates an angle of 90.0°. Error bars indicate standard deviation.

**Figure 2.32**

**Table 2.27:** Structural parameters of the equilibrium structure. The symbol * indicates that these distances are taken from the linker cluster.

| | Exp. [110] periodic | DFT (PBE) [108] periodic | DFT cluster | FF (excl. vdW) periodic | FF (incl. vdW) periodic |
|---|---|---|---|---|---|
| V - O (short) [Å] | 1.672 | 1.654 | 1.588 | 1.593 | 1.593 |
| V - O (long) [Å] | 2.108 | 2.097 | 2.311 | 2.252 | 2.346 |
| V - $O_1$ [Å] | 1.970 | 1.990 | 1.977 | 1.984 | 1.980 |
| V - $O_2$ [Å] | 1.976 | 1.976 | 2.033 | 2.042 | 2.040 |
| V - V [Å] | 3.422 | 3.440 | 3.531 | 3.496 | 3.550 |
| $O_1$ - $C_{ca}$ [Å] | 1.277 | 1.281 | 1.275 | 1.272 | 1.273 |
| $O_2$ - $C_{ca}$ [Å] | 1.252 | 1.278 | 1.255 | 1.254 | 1.255 |
| $C_{ca}$ - $C_{pc}$ [Å] | 1.501 | 1.487 | 1.494* | 1.491 | 1.496 |
| $C_{pc}$ - $C_{ph}$ [Å] | 1.372 | 1.404 | 1.399* | 1.400 | 1.400 |
| V - O - V [°] | 129.4 | 132.7 | 128.8 | 130.0 | 127.7 |
| $O_1$ - V - $O_1$ [°] | 91.5 | | 91.3 | 91.1 | 90.3 |
| $O_2$ - V - $O_2$ [°] | 90.4 | | 87.7 | 89.9 | 88.9 |
| $O_1$ - $C_{ca}$ - $O_2$ [°] | 126.0 | 125.2 | 125.3 | 125.6 | 126.7 |

# Chapter 3

# Calculating properties on MOFs

## 3.1 Introduction

In a high-throughput characterization of MOFs, one should try to determine as many characteristics as possible in an efficient way. In this section, procedures to obtain different properties are presented. The focus lies on the textural, thermal and mechanical properties.

First the textural properties are discussed in Section 3.2. Knowledge of these properties, such as pore diameters and accessible volume areas, can for instance be used to narrow down the search space of a set of MOFs for the gas separation of $CO_2$ and $N_2$ [33]. Textural properties are also employed to identify structure-property relations. Secondly, some thermal properties are studied in Section 3.3. First, the heat capacity is discussed. It is shown that an accurate determination of the heat capacity of MOFs is not possible using classical MD simulations or normal mode analysis (NMA). Advanced methods should be used to include nuclear quantum effects, but are beyond the scope of this work. The other thermal property under investigation is the thermal expansion, describing how the volume of the structure depends on the temperature. It is seen that MOFs often show anomalous negative thermal expansion. Finally, the mechanical characterization of MOFs is studied in Section 3.4. In contrast to the aforementioned properties, few efforts have been performed to calculate the elastic properties, and the limited results available in literature are presented. In this work, the elastic constants are determined at 0 K and are then used to study the elastic anisotropy and other properties. As was shown recently by Ortiz *et al.* [42], such an investigation can give a lot of information to predict framework flexibility.

## 3.2 Textural properties

Because of their nanoporous structure, a textural characterization of MOFs is a prerequisite in a thorough investigation of these materials. Examples of textural properties are surface area, void fraction, pore diameters and pore size distribution. Since these properties can be calculated geo-

metrically, they are computationally cheap, while being extremely useful. This can be illustrated with the study of Watanabe and Sholl [33]. They narrowed down a large set of MOFs for the gas separation of $CO_2$ and $N_2$ based on the pore diameters of the MOFs. By comparing the kinetic diameters of $CO_2$ and $N_2$ to the pore limiting diameter (PLD), i.e. the largest probe diameter that can pass through the MOF, and the largest cavity diameter (LCD), i.e. the largest probe diameter that fits in the structure, it becomes possible to select only those MOFs which can adsorb one of these molecules, but not the other. The definition of the PLD and LCD is illustrated in Figure 3.1. The kinetic diameter is a measure for the size of the gas molecules. This selected subset was then used as a basis to determine the diffusion and adsorption properties which passed the first screening. Simular studies are available in the literature when investigating diffusion and adsorption. An extensive review on the computational methodologies used to study these properties in MOFs is written by Yang *et al.* [45].

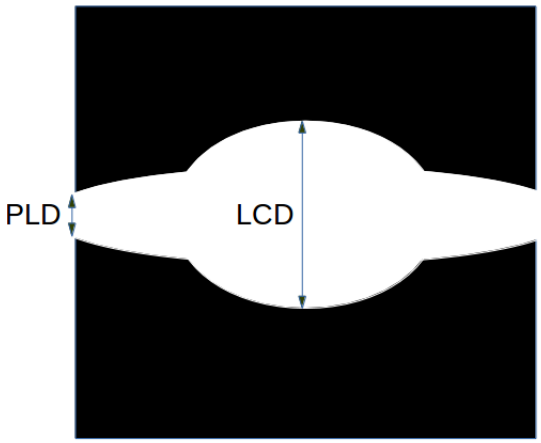


**Figure 3.1:** Illustration of the definition of the pore diameters: PLD and LCD.

Several high-throughput tools for a textural characterization are already available. The basic idea is always more or less the same. The properties are calculated in a geometrical fashion, only based on structural information such as the unit cell and the atomic positions, without performing ab initio calculations. Moreover, atoms are considered as solid spheres with a certain radius. This is definitely not the most accurate way to determine these properties since necessary chemical information is not included. However, it gives an acceptable measure for high-throughput screening. To calculate the accessible surface area (ASA) or accessible volume (AV), one simply fits a probe, represented by a solid sphere, into the crystal structure and measures the surface or volume accessible for this probe. In a recent review by Sarkisov and Kim, an overview of available tools is given [120]. These tools mainly differ in the algorithms to efficiently sample the volume. In this work, Zeo++, developed by Haranczyk and co-workers, has been used. It is a freely available C++ package specifically designed for the high-throughput analysis of porous materials [121–123]. The default radii of the atoms are the ones provided by the Cambridge Crystallographic Data Center (CCDC) [30].

The main interest to calculate textural properties in this work does not lie in the detailed study of the pores, but just as a tool in the identification of potential structure-property relations. This has been used e.g. by Wilmer *et al.* [32]. After building the Hypothetical MOF database, the authors determined surface area and pore diameters and plotted this with respect to absolute $CH_4$ adsorption. In this way they could conclude that maximizing gravimetric surface area only worsens the $CH_4$ adsorption after an optimal point around ∼2500-3000 $m^2g^{-1}$ (see also Figure 1.3 on page 5). The textural properties of the total HMOF database have been characterized by Sikora *et al.* [40]. An example which is not related to diffusion or adsorption is given by Tan *et al.* [124]. The authors presented a good correlation between the density or porosity and the Young's modulus of some ZIFs. Identification of such features may allow for a more rationalized design of high-performance MOFs.

In Table 3.1 results obtained with Zeo++ are shown. The equilibrium structures used for the different MOFs are the ones obtained after a geometry optimization with the force fields developed in the previous chapter. It can be seen that MOF-5 has a very large accessible surface area per mass of the material. ZIF-8 has a very large pore inside the framework, but the PLD is smaller than the other MOFs in this table. The MIL-53 and MIL-47 topology show a large 1D channel, which is approximately equally large along the channel (PLD ≈ LCD).

**Table 3.1:** Textural properties determined with Zeo++. The accessible surface area, the accessible volume and the void fraction were determined with a $CO_2$ probe (radius ≈ 1.5 Å).

| Property | MOF-5 | HKUST-1 | MIL-53(Al) | MIL-47 | ZIF-8 | DMOF-1 |
|---|---|---|---|---|---|---|
| $\rho$ [g/cm$^3$] | 0.57 | 0.85 | 0.92 | 0.96 | 0.90 | 0.80 |
| PLD [Å] | 8.1 | 6.9 | 7.1 | 7.0 | 3.5 | 7.8 |
| LCD [Å] | 15.3 | 13.4 | 7.4 | 7.6 | 11.5 | 9.7 |
| ASA [m$^2$/g] | 3917 | 2606 | 2019 | 1985 | 1826 | 2789 |
| AV [cm$^3$/g] | 0.84 | 0.40 | 0.20 | 0.21 | 0.23 | 0.34 |
| Void fraction [%] | 48 | 34 | 19 | 20 | 21 | 27 |

One can expect a strong dependence on the probe radius of properties such as the void fraction, the ASA and the AV. This is illustrated for the void fraction of MIL-53(Al) and MOF-5 in Figure 3.2. The void fraction is monotonically decreasing as it should be. In the remainder of this work, the probe radius is fixed at 1.5 Å, which is approximately the radius of a $CO_2$ molecule.

## 3.3 Thermal Properties

Unlike for textural properties, tools for a complete thermal characterization of MOFs are not yet available. In this work, the objective is to determine properties in a computationally efficient way. A full thermal characterization requires very demanding simulations which are not feasible in a

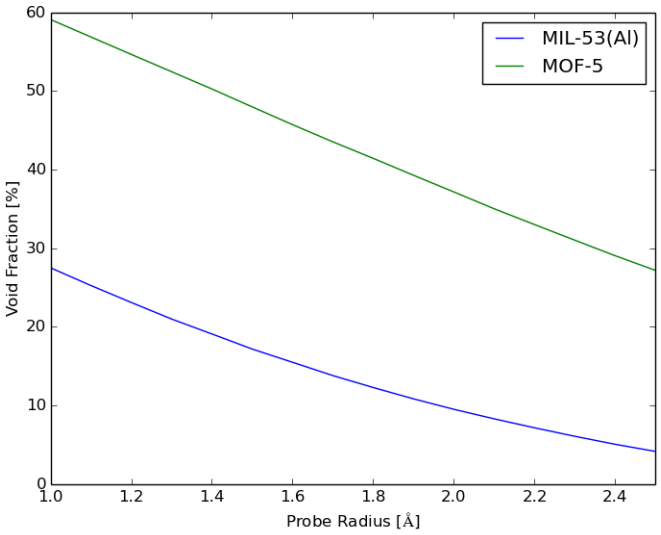


**Figure 3.2:** Dependence of the void fraction of MOF-5 and MIL-53(Al) on the probe radius.

high-throughput search. In practice very few experimental results are available in the literature, which makes it hard to validate the obtained results. One of the most general thermal properties is the heat capacity. While easy in definition, it poses many problems to acquire a reliable result. The second thermal property that will be explored in this work is the thermal expansion coefficient, which determines the relative volume change of the material with temperature. This property shows one of the many extraordinary properties of MOFs. For most solids, this coefficient is positive, but there exist several MOFs showing a negative thermal expansion.

### 3.3.1 Heat Capacity

**Definition**

The heat capacity $C$ of a system is defined as the heat $Q$ required to increase the temperature $T$ with one kelvin.

$$C = \frac{\delta Q}{\mathrm{d}T} \tag{3.1}$$

The heat capacity is an extensive property and is thus proportional to the size of the system. For crystalline materials such as MOFs, it is typically expressed per unit cell. Since heat is not a state function, the heat capacity depends on the way the heat is added to the system.

If the heat is added at a constant volume $V$, one obtains the isochoric heat capacity $C_V$, which is, according to the first law of thermodynamics, related to changes in the internal energy $E$:

$$C_V = \left(\frac{\partial Q}{\partial T}\right)_V = \left(\frac{\partial E}{\partial T}\right)_V \tag{3.2}$$

When the heat is added at constant pressure $P$, one obtains the isobaric heat capacity $C_P$.

$$C_P = \left(\frac{\partial Q}{\partial T}\right)_P = \left(\frac{\partial H}{\partial T}\right)_P \tag{3.3}$$

Here, the changes in heat are related to changes in the enthalpy $H$ given by

$$H = E + PV \tag{3.4}$$

A thermodynamic relation exists between these two heat capacities (proof can be found in textbooks such as Ref. [125]):

$$C_P - C_V = VT\frac{\alpha_V^2}{\beta_T} \tag{3.5}$$

where $\alpha_V$ is the volumetric thermal expansion coefficient and $\beta_T$ the isotropic compressibility, which is the inverse of the bulk modulus. By directly calculating both heat capacities on MOFs, this relation can in principle be checked.

**Methods to determine the heat capacity**

*Method 1: molecular dynamics simulation(s)*
A first method to determine the heat capacity per unit cell directly follows from statistical mechanics. The values of the internal energy per unit cell $E$ and the enthalpy per unit cell $H$ are replaced by the values $\langle E \rangle$ and $\langle H \rangle$ averaged over a large amount of microstates. This can be obtained with a MD simulation over a long interval of time, assuming ergodicity. The ergodic principle states that the time-averaged properties of a system are the same as when these properties are averaged over the system in its different microstates.

When performing a MD simulation in the canonical ensemble, the specific heat capacity at constant volume can be determined from the fluctuations of the energy of the unit cell. In the canonical or $NVT$ ensemble, the averaged internal energy is determined by

$$\langle E \rangle_{NVT} = \sum_r p_r E_r = \frac{1}{Z}\sum_r E_r e^{-\beta E_r} \text{ with } \beta = \frac{1}{k_B T} \tag{3.6}$$

where $E_r$ is the energy of microstate $r$ and $p_r$ the probability of encountering this microstate. This probability is given by

$$p_r = \frac{1}{Z}e^{-\beta E_r} \tag{3.7}$$

where $Z$ is the partition function

$$Z = \sum_r e^{-\beta E_r} \tag{3.8}$$

such that the total probability of all microstates is normalized to one. From Eq. 3.6 and Eq. 3.8, it

is clear that the energy can also be written as

$$\langle E\rangle_{NVT} = -\frac{\partial \ln(Z)}{\partial \beta} \tag{3.9}$$

The specific heat capacity in the canonical ensemble is then determined by

$$C_V(T) = \frac{\partial \langle E\rangle_{NVT}}{\partial T} = -\frac{\partial^2 \ln(Z)}{\partial \beta^2}\frac{\partial \beta}{\partial T} = \frac{1}{k_B T^2}\frac{\partial^2 \ln(Z)}{\partial \beta^2} \tag{3.10}$$

where Eq. 3.9 and the chain rule have been used. Carrying out this derivative explicitly yields:

$$\begin{aligned}
C_V(T) &= \frac{\partial}{\partial T}\left[\frac{1}{Z}\sum_r E_r e^{-\beta E_r}\right] \\
&= -\frac{1}{k_B T^2}\frac{\partial}{\partial \beta}\left[\frac{1}{Z}\sum_r E_r e^{-\beta E_r}\right] \\
&= -\frac{1}{k_B T^2}\left[\left(-\frac{1}{Z^2}\right)\frac{\partial Z}{\partial \beta}\sum_r E_r e^{-\beta E_r} + \frac{1}{Z}\frac{\partial}{\partial \beta}\left(\sum_r E_r e^{-\beta E_r}\right)\right] \\
&= -\frac{1}{k_B T^2}\left[\left(-\frac{1}{Z}\frac{\partial Z}{\partial \beta}\right)\left(\frac{1}{Z}\sum_r E_r e^{-\beta E_r}\right) + \frac{1}{Z}\sum_r (-E_r^2) e^{-\beta E_r}\right] \\
&= \frac{1}{k_B T^2}\left[\frac{1}{Z}\sum_r E_r^2 e^{-\beta E_r} - \left(-\frac{\partial \ln(Z)}{\partial \beta}\right)\langle E\rangle_{NVT}\right] \\
&= \frac{1}{k_B T^2}\left[\langle E^2\rangle_{NVT} - \langle E\rangle_{NVT}^2\right] = \frac{\sigma_E^2}{k_B T^2}
\end{aligned} \tag{3.11}$$

Repeating the same steps in the isobaric-isothermal ensemble or $NPT$ ensemble, where the pressure is kept constant, using Eq. 3.3 and the isobaric-isothermal partition function,

$$Z = \sum_r e^{-\beta(E_r + PV_r)} = \sum_r e^{-\beta H_r} \tag{3.12}$$

results in

$$C_P(T) = \frac{1}{k_B T^2}\left[\langle H^2\rangle_{NPT} - \langle H\rangle_{NPT}^2\right] = \frac{\sigma_H^2}{k_B T^2} \tag{3.13}$$

The heat capacity in both ensembles can be obtained from the fluctuations of the energy or the enthalpy. By carrying out a sufficiently long MD simulation, a large set of the accessible phase space can be sampled and many microstates can be reached. One can select the energy at different time steps or the enthalpy and average over these values according to Eq. 3.11 and Eq. 3.13 under the assumption of ergodicity.

In this way, one can obtain from a single $NVT$ or $NPT$ MD simulation the heat capacity at the given temperature. Performing multiple $NVT$ or $NPT$ MD simulations, the heat capacity can also

be approximated in a finite-differences approach:

$$C_V\left(\frac{T_1+T_2}{2}\right) = \frac{\langle E\rangle_{NVT_2} - \langle E\rangle_{NVT_1}}{T_2 - T_1} \tag{3.14}$$

*Method 2: Harmonic approximation*
A second method to determine the heat capacity in a practical way follows from the equipartition theorem in classical statistical mechanics. In a crystalline solid, the $N$ atoms can oscillate in three directions and one could approximate the solid as $3N$ independent simple harmonic oscillators. Every harmonic oscillator has, according to the equipartition theorem, an average energy of $k_BT$, which by applying Eq. 3.2, results in a specific heat capacity of $3Nk_B$ for the metal. This is the Dulong-Petit law which is only valid at high temperatures.

The Dulong-Petit law is a classical theory where the energy levels are assumed to be continuous. At lower temperatures, the discretisation of the energy becomes more and more important due to the dominant occupancy of the lowest energy levels of the system. This deviation of the Dulong-Petit law arises when $\hbar\omega$, with $\omega$ the vibrational frequency of the oscillators, becomes larger than $k_BT$. An improvement of this theory is the harmonic approximation, where the harmonic oscillators are treated quantum mechanically.

The energy of one quantum harmonic oscillator (HO) with frequency $\omega$ is given by

$$E_n = \left(n + \frac{1}{2}\right)\hbar\omega \tag{3.15}$$

with $n$ the occupation number of the oscillator and $\frac{\hbar\omega}{2}$ the zero-point vibrational energy. In the canonical ensemble the quantum mechanical partition function can be determined for this single oscillator:

$$\begin{aligned} Z^{HO} &= \sum_{n=0}^{\infty} e^{-\beta E_n} \\ &= \sum_{n=0}^{\infty} e^{-\beta\left(n+\frac{1}{2}\right)\hbar\omega} \\ &= e^{-\beta\frac{1}{2}\hbar\omega}\sum_{n=0}^{\infty} e^{-\beta n\hbar\omega} \\ &= e^{-\beta\frac{1}{2}\hbar\omega}\frac{1}{1-e^{-\beta\hbar\omega}} \\ &= \frac{1}{e^{\beta\frac{1}{2}\hbar\omega} - e^{-\beta\frac{1}{2}\hbar\omega}} \\ &= \frac{1}{2\sinh(\frac{1}{2}\beta\hbar\omega)} \end{aligned} \tag{3.16}$$

The average energy of this single harmonic oscillator can be found using Eq. 3.9

$$\begin{aligned}\langle E\rangle_{HO} &= -\frac{\partial \ln(Z^{HO})}{\partial\beta} = -\frac{1}{Z^{HO}}\frac{\partial Z^{HO}}{\partial\beta} \\ &= \left[-2\sinh\left(\frac{1}{2}\beta\hbar\omega\right)\right](-1)\left[\frac{1}{2\sinh\left(\frac{1}{2}\beta\hbar\omega\right)}\right]^2\left[2\cosh\left(\frac{1}{2}\beta\hbar\omega\right)\right]\left(\frac{1}{2}\hbar\omega\right) \\ &= \frac{1}{2}\hbar\omega\coth\left(\frac{1}{2}\beta\hbar\omega\right)\end{aligned} \tag{3.17}$$

The specific heat capacity of a single harmonic oscillator in the canonical ensemble is, then, using Eq. 3.10, given by

$$\begin{aligned}C_{V,HO}(T) &= -\frac{1}{k_BT^2}\frac{\partial\langle E\rangle_{HO}}{\partial\beta} \\ &= -\frac{1}{k_BT^2}\left(\frac{1}{2}\hbar\omega\right)\left(-\frac{1}{\sinh^2(\beta\frac{1}{2}\hbar\omega)}\right)\left(\frac{1}{2}\hbar\omega\right) \\ &= \frac{1}{k_BT^2}\left(\frac{\hbar\omega}{2}\right)^2\frac{1}{\sinh^2(\frac{\beta\hbar\omega}{2})} \\ &= \frac{1}{k_BT^2}\left(\frac{\hbar\omega}{2}\right)^2\left(\frac{2}{e^{\frac{1}{2}\beta\hbar\omega}-e^{-\beta\frac{1}{2}\hbar\omega}}\right)^2 \\ &= \frac{1}{k_BT^2}(\hbar\omega)^2\frac{e^{-\frac{\hbar\omega}{k_BT}}}{\left(1-e^{-\frac{\hbar\omega}{k_BT}}\right)^2}\end{aligned} \tag{3.18}$$

This is the contribution of the collective vibration of the atoms at frequency $\omega$ to the heat capacity. In a crystal the vibrations of the atoms can be decoupled into independent harmonic oscillators or normal modes with frequencies $\omega_k$ for which the quanta are called the phonons. In the assumption of complete independent harmonic oscillators, the total partition function $Z^{HO}$ of the system will be the product of the partition functions corresponding to each harmonic oscillator $Z_k^{HO}$.

$$Z^{HO} = \prod_k Z_k^{HO} = \prod_{\omega_k}\frac{1}{2\sinh(\frac{1}{2}\beta\hbar\omega_k)} \tag{3.19}$$

Using Eq. 3.10, it can be seen that every oscillator leads to a contribution to the heat capacity corresponding to Eq. 3.18. The total heat capacity per unit cell of the crystal is then the summation over the normal modes:

$$C_{V,HO}(T) = \frac{1}{k_BT^2}\sum_{\omega_k}(\hbar\omega_k)^2\frac{e^{-\frac{\hbar\omega_k}{k_BT^2}}}{\left(1-e^{-\frac{\hbar\omega_k}{k_BT^2}}\right)^2} \tag{3.20}$$

To determine the heat capacity one has to calculate these normal modes. The frequencies can be

determined by solving the normal mode equations

$$H\nu = \omega^2 M\nu \tag{3.21}$$

where $H$ is the Cartesian Hessian of the system and $M$ the mass matrix containing the masses of all $N$ atoms of the unit cell. Solving this equation yields $3N$ eigenmodes with corresponding eigenfrequencies.

This second method has been applied by Bristow *et al.* [59] on several MOFs (MOF-5, IRMOF-10, IRMOF-14, UiO-66, UiO-67 and HKUST-1). Their results could not be validated due to the lack of experimental data. Canepa *et al.* [126] have also used this approach in a combined theoretical-experimental research. The influence of molecular adsorption in MOF-74(Zn) on the isochoric heat capacity was studied. They compared the isochoric heat capacity obtained from ab initio calculated phonons and from experimentally determined IR frequencies. They concluded that the changes in heat capacacity upon loading are substantial and specific for each adsorbate.

**Case study on MOF-5**

In this section a comparison of the results obtained with both methods is made on MOF-5. The MD simulations and the calculation of the Hessian are carried out with Yaff [89], while NMA is performed with TAMkin [127]. A time step of 1 fs is used and averages are taken over a simulation length of 600 ps after an equilibration of 150 ps. Samples were taken every 100 steps to minimize the correlations between consecutive samples. $NVT$ and $NPT$ simulations were performed to determine the isochoric and isobaric heat capacity. The unit cell at finite temperature for the $NVT$ simulations was determined as the ensemble-averaged unit cell of the $NPT$ simulation at the corresponding temperature at 1 bar. Different thermostats (Nose-Hoover chain [128–130] (NHC) and Langevin [131]) and barostats (Martyna-Tuckerman-Tobias-Klein [132], Berendsen [133], Langevin [134]) were tested, but the results and conclusions are independent of this choice. In Figure 3.3 the values determined with the NHC thermostat for different temperatures are presented. One experimental result [135] is also added.

A large difference is noted between the harmonic approximation and the results obtained with MD simulations. In contrast, the results obtained with the MD simulations correspond with the high-temperature limit represented by the Dulong-Petit law even at low temperatures. It is important to understand that the obtained results will not be improved by longer simulations lengths. Some properties require large simulation lengths, but the results of the MD simulations are inherently wrong due to the classical approximation of the nuclei in classical MD, as used here. MOF-5 contains C-H bonds with vibrational frequencies around 3200 $cm^{-1}$, which corresponds to a Debye temperature higher than 4000 K. This vibrational mode should thus only be populated at temperatures much higher than 4000 K. In contrast, when using classical MD, all nuclear quantum effects are neglected and all modes are activated at low temperatures. Consequently, the MD results correspond to the

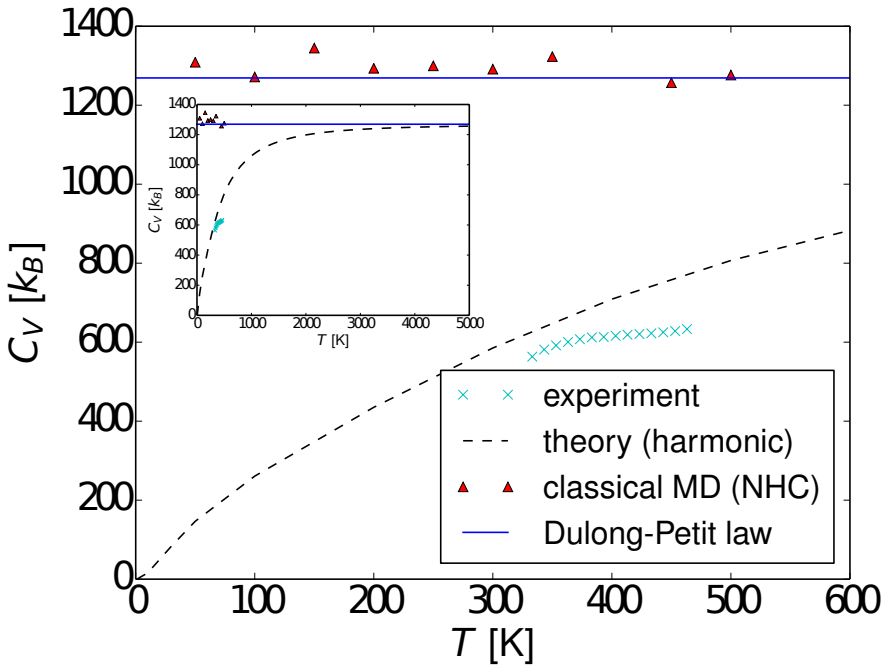


**Figure 3.3:** Comparison of different methods for the calculation of the heat capacity of MOF-5. Experimental data for MOF-5 are taken from Ref. [135].

high-temperature limit, in which all modes are fully activated. In contrast, nuclear quantum effects are present in the second method. However, in this approximation only harmonic contributions are accounted for, neglecting anharmonic effects. This is in contrast with the first method, utilizing MD, where anharmonic effects are included. Deviations between both methods are hence to be expected.

In this case the experimental results [135] (see Figure 3.3) are better approximated by the harmonic approximation, but still a deviation is visible. For MOFs which have a more flexible framework than MOF-5, such as MIL-53(Al), it can be expected that the anharmonic effects are more important. However, this statement cannot be validated because no experimental results are available for the heat capacity of MIL-53(Al).

Improvements of classical MD exist, namely Path Integral Molecular Dynamics (PIMD) [136, 137], that could allow a better description of nuclear quantum effects. Especially the work of Ceriotti and co-workers is promising [138, 139], but this has not yet been explored for MOFs.

### 3.3.2 Thermal expansion coefficients

**Definition**

The thermal expansion coefficient $\alpha$ gives information about the relative change in volume $V$ or lattice parameter $a$ when increasing or decreasing the temperature at constant pressure. The volumetric thermal expansion coefficient is given by following formula:

$$\alpha_V = \frac{1}{V}\left(\frac{\partial V}{\partial T}\right)_P = \left(\frac{\partial \ln(V)}{\partial T}\right)_P \tag{3.22}$$

The lattice expansion coefficient of the lattice parameter $a$ is defined analogously:

$$\alpha_a = \frac{1}{a}\left(\frac{\partial a}{\partial T}\right)_P = \left(\frac{\partial \ln(a)}{\partial T}\right)_P \tag{3.23}$$

The relation between both coefficients for isotropic expansion is given by $\alpha_V = 3\alpha_a$.

**Overview of literature**

Most solids expand with increasing temperature. Some MOFs, however, show negative thermal expansion (NTE). Their volume decreases when heating, similar to ice. An extensive review by Barrera *et al.* [140] presents a survey of NTE behavior over a wide range of solid materials, highlighting the thermodynamics and the diverse mechanisms operating at the atomic level. Although NTE has been investigated extensively in different materials during recent decades, the underlying physics remains poorly understood. However, the understanding is crucial for the tailoring of materials possessing specific expansion properties. A review that describes the progress in the field of NTE is written by Lind [141].

Thermal expansion is determined by the phonons or the lattice vibrations. The expansion is typically ascribed to the anharmonicity of the vibrational modes. NTE materials find applications in electronics and optics, sensors and actuators, and in the design of new materials, e.g. dental filling materials [55]. MOFs provide a framework onto which other materials might blend to form composites with negligible volume change with temperature [142].

NTE in MOFs was first observed in 2005 by Rowsell *et al.* [143] for MOF-5. Last decade, some experimental [144–146] and theoretical studies [55,142,144] have been made specifically on this MOF to explain this strange behavior. Several authors have reported thermal expansion coefficients, such that a validation of the results obtained in this work is possible. The calculation of the thermal expansion of this MOF has previously been used to verify force fields [47,54,59,61].

A detailed computational study on the thermal expansion of MOFs was made by Dubbeldam *et al.* [55] for isoreticular MOFs (IRMOFs) such as MOF-5. They used a force field made of existing models (DREIDING [49], CVFF [52]) for the organic linker and the $Zn_4O$ metal oxide cluster was described using only nonbonded interactions. This was then further calibrated with experimental data. The thermal expansion coefficients were determined using long $NPT$ MD simulation of 15 ns with two different methods. The first method was a spline fit of the unit cell length as a function of temperature and the second method was via a fluctuation formula (see Eq. 3.25 on page 80), but the results of both methods agree well. In this way, they obtain a temperature dependent thermal expansion coefficient for MOF-5 and other IRMOFs. They conclude from their simulations that the observed NTE behavior is the result of two competing effects. First, there is a local

effect where all bond lengths increase with temperature, which is the regular behavior resulting from the anharmonicity of the vibrational modes, and which could lead to an expansion of the material. However, a second long-range effect, the thermally activated hinging around the metal oxide nodes of the linkers, leads to a shorter average distance between the corners with increasing temperature. Associated with this, the material also gets softer with increasing length of the linkers.

Han and Goddard [142] investigated the thermal expansion of five NTE IRMOFs using the DREIDING [49] force field. By fitting the temperature dependent lattice constants, obtained by MD simulations, the thermal expansion coefficient is calculated. The results are in agreement with the second effect postulated by Dubbeldam *et al.* [55]. The theoretical studies performed by Han and Goddard [142], Dubbeldam *et al.* [55] and Zhou *et al.* [144] do not fully agree on the mechanism responsible for the NTE in MOF-5. A more recent experimental study made by Lock *et al.* [145] tried to determine which model gives the best description. Their in-depth crystallographic characterization combined with a theoretical model for the linker suggested a mechanism in which a transverse vibration of the linear linker together with a local carboxylate motion is responsible. This is only an example to illustrate the high complexity of the mechanisms of the thermal expansion. In a high-throughput search, the objective is not to make such detailed investigations, but only to hint towards potential large thermal expansion coefficients.

An experimental article by Henke *et al.* [147] is an example illustrating the importance of the building block design of MOFs. The authors demonstrate extreme thermal expansion (positive and negative), which can be tuned utilizing functionalized linkers. Another remarkable example of thermal expansion behavior is given by Lama *et al.* [148]. The authors have synthesized a MOF with very rare anisotropic thermal expansion behavior. The linear expansion coefficients along the major crystal axes are respectively negative, positive and zero, which is a result of a combined stretching-tilting mechanism.

One critical remark must be made on the fact that the thermal expansion can be strongly influenced by guest molecules. Several experimental studies have focused on this topic. For example, the experimental study of Wei *et al.* [149] showed that the thermal expansion profile can be tuned by guest molecules, showing extremely large coefficients of $430 \cdot 10^{-6}$ $K^{-1}$. Grobler *et al.* [150] have developed a tunable MOF showing unusual anisotropic thermal expansion properties. Their study claims the establishment of guest-tunable thermal expansion. In this work, the focus lies on the pure materials without guest molecules inside the framework. Nevertheless, if exceptional thermal expansion can be detected for pure materials, it could be a good starting point for a more case-specific study of these materials under influence of guest molecules.

**Methods to determine the thermal expansion coefficients**

There are several ways to obtain the thermal expansion coefficients from MD simulations in the isobaric-isothermal ensemble.

*Method 1: Fluctuation formula*

The volumetric thermal expansion coefficient can be determined from a single $NPT$ MD simulation assuming ergodicity. Using the isobaric-isothermal partition function (see Eq. 3.12), the average volume of the system is given by

$$\langle V \rangle_{NPT} = \frac{1}{Z} \sum_r V_r e^{-\beta H_r} = \frac{\sum_r V_r e^{-\beta H_r}}{\sum_r e^{-\beta H_r}} \tag{3.24}$$

with $V_r$ the volume of microstate $r$. Inserting Eq. 3.24 in the definition of the volumetric thermal expansion coefficient, Eq. 3.22, results in:

$$\begin{aligned}
\alpha_V(T) &= \frac{1}{\langle V \rangle_{NPT}} \frac{\partial}{\partial T} \langle V \rangle_{NPT} \\
&= \frac{1}{\langle V \rangle_{NPT}} \left( -\frac{1}{k_B T^2} \right) \frac{\partial}{\partial \beta} \left( \frac{1}{Z} \sum_r V_r e^{-\beta H_r} \right) \\
&= \frac{1}{\langle V \rangle_{NPT}} \left( -\frac{1}{k_B T^2} \right) \left[ \frac{\partial}{\partial \beta} \left( \frac{1}{Z} \right) Z \langle V \rangle_{NPT} + \frac{1}{Z} \frac{\partial}{\partial \beta} \left( \sum_r V_r e^{-\beta H_r} \right) \right] \\
&= \frac{1}{\langle V \rangle_{NPT}} \left( -\frac{1}{k_B T^2} \right) \left[ -\frac{1}{Z^2} \left( \sum_r (-H_r) e^{-\beta H_r} \right) Z \langle V \rangle_{NPT} + \frac{1}{Z} \left( \sum_r V_r (-H_r) e^{-\beta H_r} \right) \right] \\
&= \frac{\langle HV \rangle_{NPT} - \langle V \rangle_{NPT} \langle H \rangle_{NPT}}{\langle V \rangle_{NPT} k_B T^2} \\
&= \frac{1}{k_B T^2} \left[ \frac{\langle HV \rangle_{NPT}}{\langle V \rangle_{NPT}} - \langle H \rangle_{NPT} \right]
\end{aligned} \tag{3.25}$$

By averaging over the samples taken at discrete time steps, one can determine the volumetric thermal expansion from a single MD run with this equation, assuming ergodicity. This approach was used by Dubbeldam *et al.* [55].

*Method 2: Fitting the lattice parameter/volume over a temperature range*

The coefficients obtained by Dubbeldam *et al.* show a strong dependence on the temperature. However, the experimental studies of Rowsell *et al.* [143], Zhou *et al.* [144] and Lock *et al.* [145] show a near linear NTE behavior, meaning that the thermal expansion coefficient is approximately independent of temperature in the interval between 0 K and 600 K for MOF-5.
These observations suggest a linear fit of:

1. $\ln(V)$ versus $T$, where the volumetric thermal expansion coefficient is given by the slope
2. $V$ versus $T$, where the volumetric expansion coefficient is given by the slope divided by a $V_0$ at a certain temperature

This approach is used by Han and Goddard [142], Greathouse and Allendorf [54], Tafipolsky and Schmid [61], Bristow *et al.* [59], and Sun and Sun [47]. In this work, it is opted to work with the more correct $\ln(V)$ versus T fit.

*Method 3: Finite-differences approximation*
Similarly as for the heat capacity, one could approximate the derivative of Eq. 3.22 with intervals:

$$\alpha_V \left( \frac{T_1 + T_2}{2} \right) = \frac{1}{T_2 - T_1} \ln \left( \frac{\langle V \rangle_{NPT_2}}{\langle V \rangle_{NPT_1}} \right) \tag{3.26}$$

The last two methods can also be used for the linear thermal expansion coefficient by replacing the volume $V$ by the lattice parameter $a$.

**Validation of the methodology**
The number of MOFs for which theoretical and/or experimental thermal expansion coefficients are available is very limited. In this section, a comparison is made between the proposed methods and other published results. All MD simulations are carried out with Yaff [89]. The NHC thermostat [128–130] and MTTK barostat [132] are used for every $NPT$ simulation at 1 bar. The samples are taken after an equilibration time of 150 ps and the time step is 0.5 fs or 1 fs. The latter is used when there are no O-H bonds in the MOF (e.g. in the case of MOF-5).

*Fluctuation formula*
Dubbeldam *et al.* [55] showed that the thermal expansion coefficient of MOF-5 follows a trend, when simulating for a sufficient long time of 15 ns at 1 atm with the MTTK barostat [132]. In Figure 3.4, our results for MOF-5 are shown. The black line indicates the thermal expansion coefficient obtained by performing a linear fit of $\ln(V)$ versus $T$ (method 2). With both methods, the same order of magnitude is found, however, with the fluctuation formula a downward trend is observed. This is in fact the opposite of the behavior observed by Dubbeldam *et al.* [55]. To obtain this trend, at least five simulations of 750 ps were needed. Reducing the number of simulations at each temperature to one, resulted in a thermal expansion coefficient that fluctuated around the fitted result. It can be expected that longer and/or more simulations converge to a smoother curve. The blue squares in Figure 3.4 are determined using the finite-differences approximation (method 3). With this approach a good measure for the thermal expansion coefficient is found, as it results in qualitatively the same trend as the fluctuation formula. To determine whether this fluctuation formula converges to a smooth line, six simulations of 1.75 ns were carried out with DMOF-1 at each temperature. This gives a total simulation length of 10.5 ns. In Figure 3.5 on page 83 the result is shown. An extreme NTE behavior is found at low temperatures and converges to a high-temperature value of $-33 \cdot 10^{-6}$ $K^{-1}$. In fact, when the second method is employed, this high-temperature limit is found (black line). This result proves that it is possible to obtain a measure for the temperature dependence, but that lengthy simulations are required.

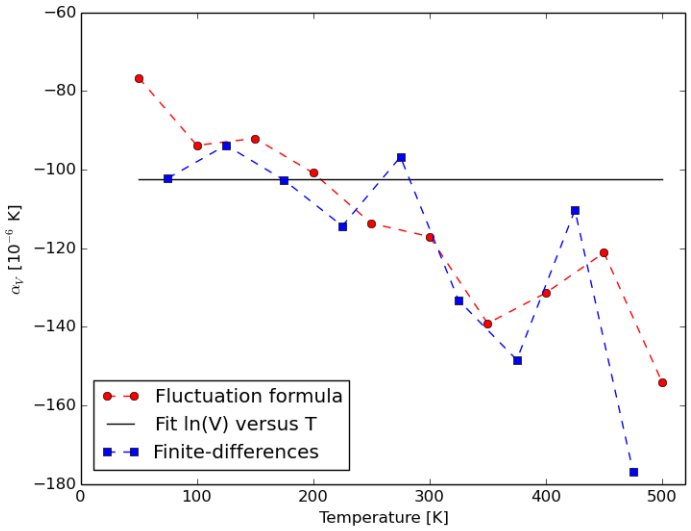


**Figure 3.4:** Temperature dependence of the thermal expansion coefficient of MOF-5.

To conclude, while the fluctuation formula gives a temperature dependent thermal expansion coefficient, the fit of $\ln(V)$ versus $T$ gives a value with the same order of magnitude. Moreover, this result can already be obtained after only one simulation at each temperature, while the fluctuation formula requires many more samples. In the remainder of this work, only the second method was applied.

*MOF-5*

The thermal expansion coefficient of MOF-5 has previously been calculated to validate a new force field. $NPT$ MD simulations of 1 ns were performed by Greathouse and Allendorf [54] and the expansion coefficient was determined by fitting the volume to the temperature. Tafipolsky and Schmid [61] did also use MD simulations to validate their force field for MOF-5. Thermal expansion data were obtained from $NPT$ MD simulations with a duration of 1 ns. The Berendsen bath coupling method was used as thermostat/barostat [133]. They conclude that longer simulations (10 ns) gave statistically indistinguishable results. Simulations were performed at temperatures between 10 K and 600 K and the average volumes were then fitted to the temperature. More recently, Bristow *et al.* [59] have calculated thermal expansion coefficients for MOF-5, but also for HKUST-1, IRMOF-10, IRMOF-14, UiO-66 and UiO-67. They calculated this property with a series of $NPT$ MD simulations of only 250 ps using the Berendsen bath coupling method as thermostat/barostat [133]. To determine the thermal expansion coefficient, they fitted their averaged lattice parameters to the temperature. According to their results all these MOFs show NTE. The same conclusion as for the IRMOF series of Dubbeldam *et al.* [55] could be drawn: the larger the linker, the more negative the thermal expansion.

In Table 3.3, the simulated results available in the literature are shown. All these results were

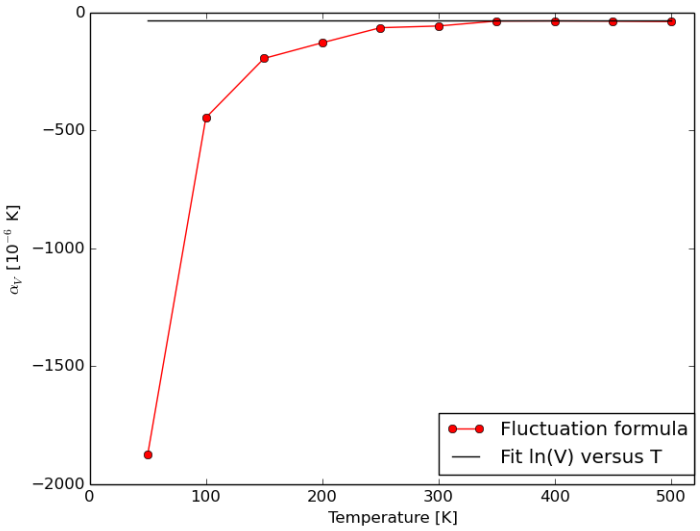


**Figure 3.5:** Temperature dependence of the thermal expansion coefficient of DMOF-1.

**Table 3.2:** Experimental thermal expansion coefficient of the lattice parameter of MOF-5.

| | $\alpha_a$ [$10^{-6}$ $K^{-1}$] | Temperature range [K] |
|---|---|---|
| Rowsell *et al.* [143] | -13.3 | 0-600 |
| Zhou *et al.* [144] | -16 | 4-600 |
| Lock *et al.* [145] | -13.1(1) | 80-500 |

calculated with force fields and MD simulations. The published values range between -5.3 · $10^{-6}$ $K^{-1}$and -13.3 · $10^{-6}$ $K^{-1}$, while the experimental results (see Table 3.2) range between -13.1 · $10^{-6}$ $K^{-1}$and -16 · $10^{-6}$ $K^{-1}$. The value obtained in this thesis is -34.1 · $10^{-6}$ $K^{-1}$. This is clearly an overestimation of the thermal expansion behavior.

Thermal expansion behavior is an anharmonic effect due to the crystal vibrations. A potential improvement of the force field derived with QuickFF is the addition of anharmonic contributions, as discussed in Section 2.2.3. Instead of using harmonic potentials for the bends and bonds, now a fixed anharmonic contribution is added, which was determined for the MM3 force field. The result obtained with these extra terms is shown in the third row (with symbol *) of Table 3.3. With this force field, a simulation of 1.5 ns was carried out, which should be sufficiently long for a good estimate. Adding these terms results in an expansion coefficient of -14.8 · $10^{-6}$ $K^{-1}$, which is in the range of the experimental values. In Figure 3.6, the simulated temperature dependence of the volume is shown. Finally, in Table 3.4 on page 85, our results for the IRMOF series are listed (without anharmonic contributions). Except for IRMOF-8, an overestimation with roughly a factor three of the negative thermal expansion is found.

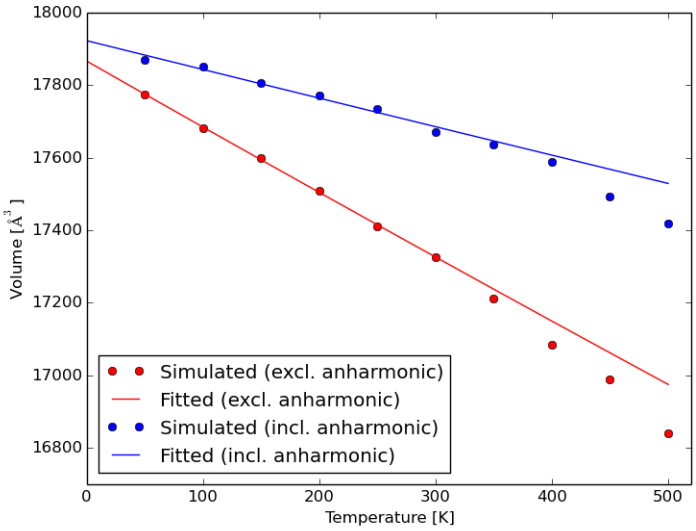


**Figure 3.6:** Thermal expansion behavior of MOF-5. A comparison between the force field with/without fixed anharmonic contributions.

**Table 3.3:** Thermal expansion coefficient of the lattice parameter of MOF-5 at 300 K via force field MD simulations. The symbol * indicates extra fixed anharmonic contributions.

| | $\alpha_a$ [$10^{-6}$ $K^{-1}$] |
|---|---|
| This work | -34.1 |
| This work* | -14.8 |
| Dubbeldam *et al.* [55] | -13.3 |
| Han and Goddard [142] | -8 |
| Greathouse and Allendorf [54] | -13 |
| Tafipolsky and Schmid [61] | -7.3 |
| Bristow *et al.* [59] | -5.27 |
| Sun and Sun [47] | -10.1 |

*HKUST-1*

In Figure 3.7 the simulated thermal expansion behavior of HKUST-1 is shown. Here, a nearly perfect agreement between the fit and the simulation is found. In Table 3.5, it can be seen that again an overestimation with a factor three compared to other force fields and to the experiment is found in this work.

*Conclusion*

The thermal expansion coefficient obtained via the fluctuation formula displays a downward trend at low temperatures for MOF-5. It seems to converge to a smooth line with longer simulation times,

however, more and longer calculations should be carried out to validate this statement. DMOF-1, which has less atoms in the unit cell, was considered as a second test case. Here, a smooth temperature dependence is found, where the thermal expansion coefficient converges at high temperature to the fitted coefficient with method 2. The second method is much more efficient as it is only based on the ensemble-averaged volume, which converges faster.

**Table 3.4:** Simulated thermal expansion coefficient $\alpha_a$ [$10^{-6}$ $K^{-1}$] of the lattice parameter of the IRMOF series.

| IRMOF | This work | Dubbeldam [55] | Han [142] | Bristow [59] | Sun [47] |
|---|---|---|---|---|---|
| IRMOF-1 (MOF-5) | -34.1 | -13.3 | -8 | -5.27 | -10.1 |
| IRMOF-6 | -44.4 | / | / | / | -11.2 |
| IRMOF-8 | -36.2 | / | -10.8 | / | -6.9 |
| IRMOF-10 | -53.4 | ≈17 | / | -8.11 | -13.7 |
| IRMOF-14 | -37.1 | / | -8.1 | -4.95 | -10.0 |

**Table 3.5:** Thermal expansion coefficient $\alpha_a$ [$10^{-6}$ $K^{-1}$] of the lattice parameter of HKUST-1.

| | This work | Tafipolsky [63] | Bristow [59] | Peterson [151] |
|---|---|---|---|---|
| $\alpha_a$ [$10^{-6}$ $K^{-1}$] | -13.4 | -3.4 | -3.2 | -4.9 (Exp.) |

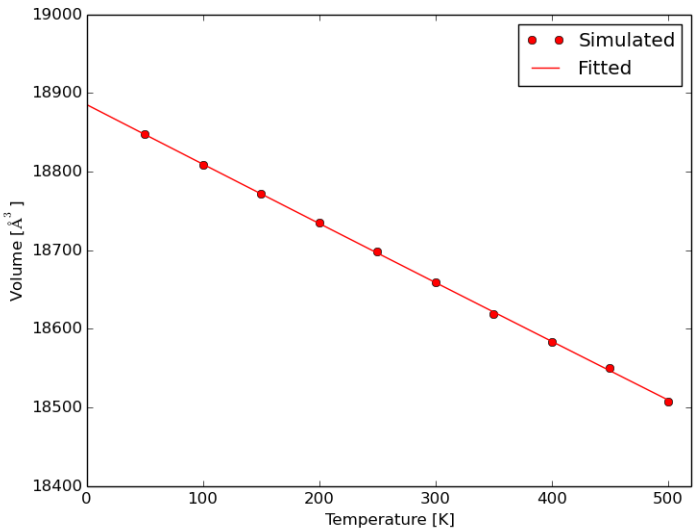


**Figure 3.7:** Thermal expansion behavior of HKUST-1.

A comparison with the literature for HKUST-1 and the IRMOFs showed that the new force fields tend to overestimate the negative thermal expansion. The values are systematically overestimated

by a factor three. However, adding anharmonic contributions to the bond and bend terms seems to solve this.

## 3.4 Mechanical Properties

Studies have shown that MOFs become amorphous or collapse under low mechanical loading, which remains a bottleneck for the industrialization of MOFs [152,153]. Often high porosity and mechanical stability are two competing factors. However, especially those MOFs with high porosity are interesting for industrial applications. A detailed understanding of the response to mechanical stress is needed for technological applications, requiring a characterization of mechanical properties. For example, Wu *et al.* [154] showed that the highly-porous framework UiO-66 has a remarkable mechanical stability which can be explained by the network topology. Understanding of such features, responsible for exceptional mechanical properties, could lead to new high-performance MOFs. It is now known that the mechanical properties of a MOF are predominantly determined by its framework topology and geometry. Obtaining a better understanding of the chemical effects on the mechanical behavior, then allows for a further fine-tuning of the desired properties [155].

The basic mechanical property under consideration are the elastic constants. They can be used to calculate other mechanical properties such as the bulk modulus, Young's modulus, Poisson's ratio, shear modulus and structural stability (Section 3.4.4). These quantities provide a link between the mechanical and dynamic behavior of a crystal. In general, they provide information on the elastic behavior or the response under low mechanical stress. In this work, the behavior in the elastic region as illustrated in Figure 3.11 is described. In this region, the material returns to its original shape after the mechanical stress is removed. In the plastic region, the material undergoes non-reversible changes of shape in response to the applied forces.

There is a major lack of data, both computational and experimental, about these properties for MOFs. The well-known MOF-5 has been the subject of some computational studies where the stiffness tensor has been determined. However, only limited experimental data are available on its mechanical properties. A critical review by Tan and Cheetham [153] offers an overview of theoretical and experimental results for various mechanical properties of MOFs. During the past few years some computational studies have focused on the anisotropic elastic behavior of MOFs [42,119,156]. After obtaining the stiffness tensor, the directional dependence of properties such as the Young's modulus and shear modulus can be investigated. Ortiz *et al.* [42] have suggested that these anisotropic properties can be indicators of framework flexibility. This interesting insight is further explored in this work.

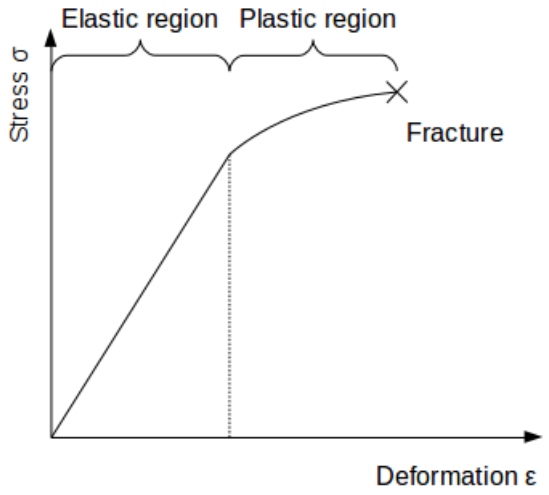


**Figure 3.8:** Illustration of the mechanical behavior of a deformed material.

### 3.4.1 Definition of the elastic constants

The elastic properties of a crystal are typically introduced by focusing on a continuous medium [157,158]. Strain and stress are considered on an infinitesimal volume element of this material that is described by the orthonormal Cartesian vectors $\overrightarrow{1_x}$, $\overrightarrow{1_y}$ and $\overrightarrow{1_z}$ .

The orthonormal vectors will be distorted in orientation and length if an infinitesimal strain is applied. If the strain is uniform, the distortion of these vectors is the same for every point of the material. This is described by the deformation tensor **d**:

$$\begin{cases} \overrightarrow{1_{x'}} = (1+d_{xx})\overrightarrow{1_x} + d_{xy}\overrightarrow{1_y} + d_{xz}\overrightarrow{1_z} \\ \overrightarrow{1_{y'}} = d_{yx}\overrightarrow{1_x} + (1+d_{yy})\overrightarrow{1_y} + d_{yz}\overrightarrow{1_z} \\ \overrightarrow{1_{z'}} = d_{zx}\overrightarrow{1_x} + d_{zy}\overrightarrow{1_y} + (1+d_{zz})\overrightarrow{1_z} \end{cases} \tag{3.27}$$

The deformation $d_{ij}$ is dimensionless. A point in the material, described by a Cartesian position vector $\overrightarrow{r}$, is after deformation described by $\overrightarrow{r}'$.

$$\overrightarrow{r} = x\overrightarrow{1_x} + y\overrightarrow{1_y} + z\overrightarrow{1_z} \tag{3.28}$$

$$\overrightarrow{r}' = x\overrightarrow{1_x'} + y\overrightarrow{1_y'} + z\overrightarrow{1_z'} \tag{3.29}$$

The displacement vector is described by $\overrightarrow{R} = \overrightarrow{r}' - \overrightarrow{r}$ or thus:

$$\begin{aligned} \overrightarrow{R} &= (x\ d_{xx} + y\ d_{yx} + z\ d_{zx})\overrightarrow{1_x} + (x\ d_{xy} + y\ d_{yy} + z\ d_{zy})\overrightarrow{1_y} + (x\ d_{xz} + y\ d_{yz} + z\ d_{zz})\overrightarrow{1_z} \\ &= u_x(x,y,z)\overrightarrow{1_x} + u_y(x,y,z)\overrightarrow{1_y} + u_z(x,y,z)\overrightarrow{1_z} \end{aligned} \tag{3.30}$$

Typically, the deformation tensor is then split into a symmetric and an antisymmetric part: **d**=

$\nabla \overrightarrow{u} = \boldsymbol{\omega} + \boldsymbol{\epsilon}$. In this section the indices $i$ and $j$ represent the orthonormal directions $\overrightarrow{1_x}$, $\overrightarrow{1_y}$ and $\overrightarrow{1_z}$, with

$$\omega_{ij} = \frac{1}{2}\left(\frac{\partial u_i}{\partial j} - \frac{\partial u_j}{\partial i}\right) \tag{3.31}$$

The antisymmetric rotation tensor describes a global rotation of the volume element. This does not contribute to the stress on the material as the relative positions of the particles remain the same. Moreover, an infinitesimal global rotation described by $\boldsymbol{\omega}$ does not change the energy of the system. $\boldsymbol{\omega}$ is a tensor of rank 2 with three independent elements:

$$\boldsymbol{\omega} = \frac{1}{2}\left(\nabla \overrightarrow{u} - (\nabla \overrightarrow{u})^T\right) = \frac{1}{2}\nabla \times \overrightarrow{u} = \begin{pmatrix} 0 & \omega_{xy} & \omega_{xz} \\ -\omega_{xy} & 0 & \omega_{yz} \\ -\omega_{xz} & -\omega_{yz} & 0 \end{pmatrix} \tag{3.32}$$

The second contribution to $\mathbf{d}$ is the infinitesimal strain tensor $\boldsymbol{\epsilon}$, and its elements are given by:

$$\epsilon_{ij} = \frac{1}{2}\left(\frac{\partial u_i}{\partial j} + \frac{\partial u_j}{\partial i}\right) \tag{3.33}$$

$\boldsymbol{\epsilon}$ is a symmetric rank 2 tensor with six independent elements. As the deformation $d_{ij}$ is dimensionless, so is the strain $\epsilon_{ij}$.

$$\boldsymbol{\epsilon} = \frac{1}{2}\left(\nabla \overrightarrow{u} + (\nabla \overrightarrow{u})^T\right) = \begin{pmatrix} \epsilon_{xx} & \epsilon_{xy} & \epsilon_{xz} \\ & \epsilon_{yy} & \epsilon_{yz} \\ & & \epsilon_{zz} \end{pmatrix} \triangleq \begin{pmatrix} \epsilon_{xx} & \epsilon_{xy} & \epsilon_{xz} \\ \epsilon_{xy} & \epsilon_{yy} & \epsilon_{yz} \\ \epsilon_{xz} & \epsilon_{yz} & \epsilon_{zz} \end{pmatrix} \tag{3.34}$$

As a strain does not keep the relative positions of the atoms intact, it gives rise to stresses.

The stress $\sigma_{ij}$ represents the force in the $i$-direction along the unit area of a plane whose normal lies in the $j$-direction. The nine stresses form the components of the second-order stress tensor. The dimension of stress is force per unit area or energy per volume. A 2D example is given in Figure 3.9 to illustrate this. To obtain a static equilibrium, the angular acceleration must vanish and this implies $\sigma_{ij} = \sigma_{ji}\ \forall i, j$. In the three dimensional case, this results in six independent stress components which can be represented by a 3×3 symmetric matrix.

$$\boldsymbol{\sigma} = \begin{pmatrix} \sigma_{xx} & \sigma_{xy} & \sigma_{xz} \\ & \sigma_{yy} & \sigma_{yz} \\ & & \sigma_{zz} \end{pmatrix} \tag{3.35}$$

The generalized Hooke's law states that under the assumption of small strain, the stress is directly proportional to it. If the strain is applied and the stress is the response, both are related through the stiffness tensor $\mathbf{C}$

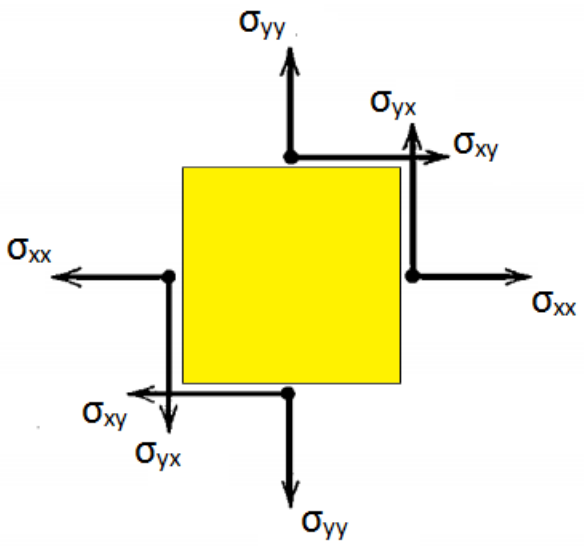


**Figure 3.9:** Graphical representation of the stress tensor components for a 2D volume element. Force and torque equilibrium are required to obtain a static equilibrium. The torque caused by $\sigma_{xy}$ must be equal to the torque following from $\sigma_{yx}$. This results in $\sigma_{xy} = \sigma_{yx}$. The normal stresses $\sigma_{ii}$ at opposite sides must be equal in magnitude to obtain force equilibrium.

$$\boldsymbol{\sigma} = \mathbf{C} \cdot \boldsymbol{\epsilon} \iff \sigma_{ij} = \sum_{k,l} C_{ijkl}\ \epsilon_{kl} \text{ with } i,j,k \text{ and } l = x,y,z \tag{3.36}$$

This quantity is a tensor of rank 4 and its elements are given by the elastic constants. They have the dimension of an energy per volume or a force per unit area. The matrix notation of the stiffness tensor can be simplified using the Voigt notation: ($xx \to 1$, $yy \to 2$, $zz \to 3$, $yz = zy \to 4$, $xz = zx \to 5$, $xy = yx \to 6$). $\mathbf{C}$ can then be represented by a symmetric $6 \times 6$ matrix with at most 21 independent elements:

$$\mathbf{C} = \begin{pmatrix} C_{11} & C_{12} & C_{13} & C_{14} & C_{15} & C_{16} \\ & C_{22} & C_{23} & C_{24} & C_{25} & C_{26} \\ & & C_{33} & C_{34} & C_{35} & C_{36} \\ & & & C_{44} & C_{45} & C_{46} \\ & & & & C_{55} & C_{56} \\ & & & & & C_{66} \end{pmatrix} \tag{3.37}$$

The number of independent elements can be further reduced using the symmetry of the crystal structure. The different crystal systems and their independent elastic constants can be found in Ref. [159].

Using the Voigt notation, the strain and stress matrices can be represented as six-dimensional vectors,

$$\begin{pmatrix} \epsilon_{xx} & \epsilon_{xy} & \epsilon_{xz} \\ & \epsilon_{yy} & \epsilon_{yz} \\ & & \epsilon_{zz} \end{pmatrix} \Longleftrightarrow \begin{pmatrix} \epsilon_1 \\ \epsilon_2 \\ \epsilon_3 \\ \epsilon_4 \\ \epsilon_5 \\ \epsilon_6 \end{pmatrix} = \begin{pmatrix} \epsilon_{xx} \\ \epsilon_{yy} \\ \epsilon_{zz} \\ 2\epsilon_{yz} \\ 2\epsilon_{xz} \\ 2\epsilon_{xy} \end{pmatrix}, \begin{pmatrix} \sigma_{xx} & \sigma_{xy} & \sigma_{xz} \\ & \sigma_{yy} & \sigma_{yz} \\ & & \sigma_{zz} \end{pmatrix} \Longleftrightarrow \begin{pmatrix} \sigma_1 \\ \sigma_2 \\ \sigma_3 \\ \sigma_4 \\ \sigma_5 \\ \sigma_6 \end{pmatrix} = \begin{pmatrix} \sigma_{xx} \\ \sigma_{yy} \\ \sigma_{zz} \\ \sigma_{yz} \\ \sigma_{xz} \\ \sigma_{xy} \end{pmatrix}, \tag{3.38}$$

where a factor two is added at certain elements of the strain vector. The generalized Hooke's law can then be written as a matrix equation:

$$\begin{pmatrix} \sigma_1 \\ \sigma_2 \\ \sigma_3 \\ \sigma_4 \\ \sigma_5 \\ \sigma_6 \end{pmatrix} = \begin{pmatrix} C_{11} & C_{12} & C_{13} & C_{14} & C_{15} & C_{16} \\ & C_{22} & C_{23} & C_{24} & C_{25} & C_{26} \\ & & C_{33} & C_{34} & C_{35} & C_{36} \\ & & & C_{44} & C_{45} & C_{46} \\ & & & & C_{55} & C_{56} \\ & & & & & C_{66} \end{pmatrix} \begin{pmatrix} \epsilon_1 \\ \epsilon_2 \\ \epsilon_3 \\ \epsilon_4 \\ \epsilon_5 \\ \epsilon_6 \end{pmatrix} \tag{3.39}$$

With an elastic deformation corresponds a strain energy. Just as in the case of a 1D Hookean spring, this energy is stored as potential energy. The strain energy density is the reversible work per unit volume that has been done to produce the strain. As $\sigma_i$ is the stress or force per unit area corresponding with the applied strain, it is the derivative of the strain energy density to the strain $\epsilon_i$ or

$$\begin{aligned} U(\boldsymbol{\epsilon}) &= \int \boldsymbol{\sigma} \cdot \mathrm{d}\boldsymbol{\epsilon} = \frac{1}{2} \boldsymbol{\epsilon}^T \cdot \mathbf{C} \cdot \boldsymbol{\epsilon} \\ &= \frac{1}{2} \begin{pmatrix} \epsilon_1 & \epsilon_2 & \epsilon_3 & \epsilon_4 & \epsilon_5 & \epsilon_6 \end{pmatrix} \begin{pmatrix} C_{11} & C_{12} & C_{13} & C_{14} & C_{15} & C_{16} \\ & C_{22} & C_{23} & C_{24} & C_{25} & C_{26} \\ & & C_{33} & C_{34} & C_{35} & C_{36} \\ & & & C_{44} & C_{45} & C_{46} \\ & & & & C_{55} & C_{56} \\ & & & & & C_{66} \end{pmatrix} \begin{pmatrix} \epsilon_1 \\ \epsilon_2 \\ \epsilon_3 \\ \epsilon_4 \\ \epsilon_5 \\ \epsilon_6 \end{pmatrix} \end{aligned} \tag{3.40}$$

One could thus also define the elastic constants as

$$C_{ij} = \frac{\partial^2 U}{\partial \epsilon_i \partial \epsilon_j} = \frac{1}{V_0} \frac{\partial^2 E}{\partial \epsilon_i \partial \epsilon_j}, \tag{3.41}$$

a formula used in some codes [160, 161].

While most of these definitions originate from continuum mechanics, they are also applicable to crystals, composed of unit cells. The unit cell of a crystal is characterized by its lattice vectors $\overrightarrow{a}$,

$\overrightarrow{b}$ and $\overrightarrow{c}$. The lattice parameters are given by the norms of these vectors. The relation between the lattice vectors and the orthonormal vectors is given by the unit cell tensor $\mathbf{h}_0$:

$$\begin{cases} \overrightarrow{a} = a_x\overrightarrow{1_x} + a_y\overrightarrow{1_y} + a_z\overrightarrow{1_z} \\ \overrightarrow{b} = b_x\overrightarrow{1_x} + b_y\overrightarrow{1_y} + b_z\overrightarrow{1_z} \\ \overrightarrow{c} = c_x\overrightarrow{1_x} + c_y\overrightarrow{1_y} + c_z\overrightarrow{1_z} \end{cases} \iff \mathbf{h}_0 = \begin{pmatrix} a_x & a_y & a_z \\ b_x & b_y & b_z \\ c_x & c_y & c_z \end{pmatrix} \tag{3.42}$$

The position of atom $\alpha$ in this unit cell ($\alpha$ = 1, 2, ..., $N$ with $N$ the number of atoms) can be represented by its fractional coordinates ($s_{\alpha a}\ s_{\alpha b}\ s_{\alpha c}$) along the lattice vectors or by its Cartesian coordinates ($x_\alpha\ y_\alpha\ z_\alpha$) along the orthonormal vectors $\overrightarrow{1_x}$, $\overrightarrow{1_y}$ and $\overrightarrow{1_z}$. The relation between the fractional coordinates and the Cartesian coordinates of the atom can be found by looking at the Cartesian coordinate vector $\overrightarrow{r_\alpha}$.

$$\overrightarrow{r_\alpha} = x_\alpha\overrightarrow{1_x} + y_\alpha\overrightarrow{1_y} + z_\alpha\overrightarrow{1_z} = s_{\alpha a}\overrightarrow{a} + s_{\alpha b}\overrightarrow{b} + s_{\alpha c}\overrightarrow{c} = (s_{\alpha a}\ s_{\alpha b}\ s_{\alpha z})_{abc} = \overrightarrow{s_\alpha}\ \mathbf{h}_0 \tag{3.43}$$

After a deformation, the Cartesian coordinate vector of atom $\alpha$, $\overrightarrow{r_\alpha}$, becomes $\overrightarrow{r_\alpha}'$, where the deformed orthonormal vectors are given in Eq. 3.27. This also deforms the unit cell tensor $\mathbf{h}_0$ to $\mathbf{h}$:

$$\overrightarrow{r_\alpha} \Rightarrow \overrightarrow{r_\alpha}' = x_\alpha\overrightarrow{1_{x'}} + y_\alpha\overrightarrow{1_{y'}} + z_\alpha\overrightarrow{1_{z'}} = s_{\alpha a}\overrightarrow{a}' + s_{\alpha b}\overrightarrow{b}' + s_{\alpha c}\overrightarrow{c}' = (s_{\alpha a}\ s_{\alpha b}\ s_{\alpha z})_{abc} = \overrightarrow{s_\alpha}\ \mathbf{h} \tag{3.44}$$

An infinitesimally deformed lattice vector can be written as

$$\overrightarrow{a}' = a_x\overrightarrow{1_{x'}} + a_y\overrightarrow{1_{y'}} + a_z\overrightarrow{1_{z'}} \tag{3.45}$$

or also

$$\overrightarrow{a}' = a'_x\overrightarrow{1_x} + a'_y\overrightarrow{1_y} + a'_z\overrightarrow{1_z} \tag{3.46}$$

Inserting the strained base vectors of Eq. 3.27 allows to determine $a'_x$, $a'_y$ and $a'_z$ in terms of $a_x$, $a_y$ and $a_z$ and the strains $\epsilon_{ij}$. This can be written in matrix form:

$$\overrightarrow{a}'^T = (a'_x\ a'_y\ a'_z) = (a_x\ a_y\ a_z)\begin{pmatrix} 1+\epsilon_{xx} & \epsilon_{xy} & \epsilon_{xz} \\ \epsilon_{xy} & 1+\epsilon_{yy} & \epsilon_{yz} \\ \epsilon_{xz} & \epsilon_{yz} & 1+\epsilon_{zz} \end{pmatrix} \tag{3.47}$$

The same can be done for lattice vectors $\overrightarrow{b}'$ and $\overrightarrow{c}'$. In this way the strained unit cell tensor can be related to the undeformed unit cell tensor:

$$\mathbf{h} = \begin{pmatrix} a'_x & a'_y & a'_z \\ b'_x & b'_y & b'_z \\ c'_x & c'_y & c'_z \end{pmatrix} = \begin{pmatrix} a_x & a_y & a_z \\ b_x & b_y & b_z \\ c_x & c_y & c_z \end{pmatrix}\begin{pmatrix} 1+\epsilon_{xx} & \epsilon_{xy} & \epsilon_{xz} \\ \epsilon_{xy} & 1+\epsilon_{yy} & \epsilon_{yz} \\ \epsilon_{xz} & \epsilon_{yz} & 1+\epsilon_{zz} \end{pmatrix} \tag{3.48}$$

$$= \mathbf{h}_0 \begin{pmatrix} 1+\epsilon_1 & \frac{1}{2}\epsilon_6 & \frac{1}{2}\epsilon_5 \\ & 1+\epsilon_2 & \frac{1}{2}\epsilon_4 \\ & & 1+\epsilon_3 \end{pmatrix} \tag{3.49}$$

### 3.4.2 Overview of literature

Several works have focused on the mechanical behavior of MOF-5. One of the first works on its mechanical stability was a combined theoretical-experimental study by Zhou and Yildirim [162]. By looking at the three independent elastic constants of this cubic structure, the structural stability was evaluated. These constants were determined by fitting ab initio total energies to well-chosen applied strains. A low $C_{44}$ of 1 GPa was found, while the other two moduli ($C_{11}$ and $C_{12}$) are at least one order of magnitude larger (Table 3.11 on page 110). This indicates that the structure is close to structural instability. By experimentally measuring of the neutron inelastic scattering spectrum and the ab initio determination of the phonon spectrum, the authors could determine that the twisting of the organic linkers gives rise to the softest modes and that it is responsible for the low $C_{44}$. Several other authors have published ab initio elastic constants for MOF-5 [91, 163–165], but they are all very similar, as can be seen in Table 3.11 on page 110 in Section 3.4.5.

The mechanical properties of MOF-5 have also been studied with force fields. Han and Goddard [142] have calculated the temperature dependence of the elastic constants with a DREIDING [49] force field. This was done with a series of $NVT$ MD simulations, where different strains were applied to the unit cell. By fitting the ensemble-averaged energy to the applied strain, the independent elastic constants were determined. $C_{11}$, $C_{44}$ and the shear modulus of MOF-5 were shown to decrease with increasing temperature. This is, however, remarkable if one takes the anomalous negative thermal expansion into account. If the volume decreases, a material typically stiffens, which results in higher elastic constants. For MOF-5 this is not the case. According to the authors, the flexibility of the metal-linker-metal bond is responsible for this behavior.

Because published values are available for the elastic constants and other mechanical properties of MOF-5, force fields are often validated based on these properties. Greathouse and Allendorf [54] determined the bulk modulus and Young's modulus at 0 K by fitting the energy to strain and at finite temperatures via MD simulations. The authors obtained a strong softening of these elastic properties with increasing temperature, similar to Han and Goddard [142]. Tafipolsky and Schmid [61] also calculated the elastic constants, bulk modulus and Young's modulus as a validation of their ab initio parametrized force field. The elastic constants were determined from energy versus strain fitting. The strain versus stress approach was also applied and both methods gave comparable results according to the authors. MD simulations were performed to obtain elastic properties at 300 K. Bristow *et al.* [59] determined bulk moduli to verify their force fields for MOF-5, IRMOF-10, IRMOF-14, HKUST-1, UiO-66 and UiO-67. To this end, a series of $NVT$ simulations at 1 K was employed for different volumes around the equilibrium structure. The ensemble-averaged pressure was then fitted as a function of the volume with an equation of state (EOS) (Eq. 3.53). Sun and

Sun [47] have also studied the mechanical properties of several IRMOFs. The bulk modulus and Young's modulus were determined at finite temperatures using $NVT$ MD simulations.

Ortiz *et al.* [42] published elastic constants for several MOFs such as MIL-47 and MIL-53(Al). The elastic constants were calculated by fitting total energy versus strain curves. The ab initio calculations were performed using the hybrid B3LYP functional with a localized basis set. The influence of the widely used Grimme dispersion correction [81] on the elastic constants was shown to be negligible. This is probably because the elastic constants are more strongly determined by the chemical bond properties than by van der Waals forces. The authors also pointed out that flexible MOFs have, in contrast to rigid MOFs, very anisotropic elastic properties, an idea that subsequently has been used in other publications [166–168] In Section 3.4.4 the connection between the framework flexibility and the elastic anisotropy is discussed more extensively.

The ZIFs have drawn some attention due to the attractive combination of thermal, chemical and mechanical stability comparable with the zeolites, and rich topological diversity, pore size tunability and structural flexibility like in MOFs. Several experimental [124, 169, 170] and computational studies [119, 156] are available on the mechanical properties for this subclass of MOFs. For ZIF-8, Tan *et al.* [119] found an exceptionally low shear modulus of about 1 GPa. The elastic constants were determined both experimentally and theoretically. The ab initio elastic constants are obtained using the procedure developed by Perger *et al.* with the hybrid B3LYP functional [160]. Using such an approach, Tan *et al.* found the elastic constants to be overestimated by 15-20% compared to the experiment. This was, according to the authors, due to the calculation at 0 K instead of 300 K and due to the neglect of zero-point vibrations [171]. A full tensorial analysis was performed after obtaining the elastic constants, indicating that the shear modulus is much smaller than the bulk modulus. This implies a vulnerability for shear-induced plasticity, amorphization and rupture. According to the authors this also raises questions about the practical use of flexible MOFs with an even lower shear modulus [42]. A similar ab initio study was carried out on ZIF-4 and ZIF-zni by Tan *et al.* [156].

Tan *et al.* [124] also experimentally studied the influence of network topology and porosity on the mechanical properties of various ZIFs. An excellent correlation was found between the density of the material and the Young's modulus, despite the diverse chemical structures studied. A good inverse correlation was also found between the porosity (determined by the accessible surface area) and the Young's modulus. Sun and Sun [47] also made a connection between the density or free volume and the elastic moduli for IRMOFs. This raises the question whether such structure-property relations can be generalized to other classes of MOFs. In contrast, such correlations were not observed in a recent study on a larger subset of ZIFs [172]. High-throughput screenings could shed light on this.

Wu *et al.* [154] investigated the mechanical stability of UiO-66(Zr). The elastic constants were extracted from ab initio calculations using the method of Le Page and Saxe [173]. The semi-

empirical dispersion correction by Grimme [81] was found to have a negligible influence on the elastic constants, consistent with Ortiz *et al.* [42]. By comparison with previously calculated elastic constants and properties of MOFs such as MOF-5, ZIF-8 and HKUST-1, the authors concluded that UiO-66 shows exceptional mechanical properties. A detailed study of the deformation mechanism in the MOFs under study suggested that the main reason for the mechanical stability is the high organic-inorganic coordination number. In highly coordinated structures, mechanical deformation requires changes in bond length, because flexible bending of the framework is made more difficult. Changes in bond length are energetically more costly than bending, which explains the more rigid UiO-66 framework. Figure 3.10 illustrates the idea that more interconnections (higher coordination number) increase the mechanical rigidity. Wu *et al.* suggest that it is possible, just by looking at the crystal structure and topology, and by empirically judging whether shear deformations might lead to bond length changes, to get a qualitative idea of the mechanical stability.

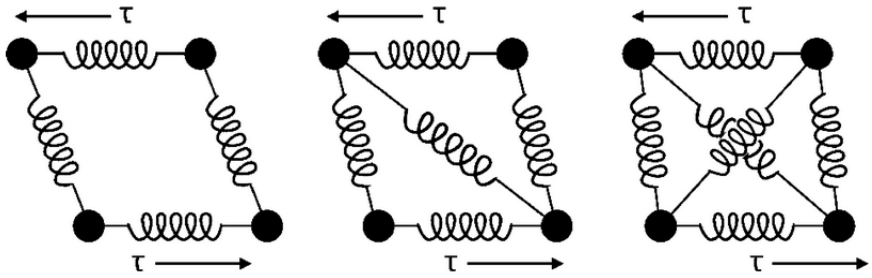


**Figure 3.10:** Behavior under shear stresses $\tau$ of simple 2D lattices of nodes connected by springs. The lattice shear stability (or rigidity) improves significantly with an increasing number of network connections. Figure taken from Ref. [154].

Recently, Canepa *et al.* [126] investigated, among other things, the elastic behavior of MOF-74(Zn) and the influence of loading it with $H_2$, $CO_2$, $CH_4$ and $H_2O$. Canepa *et al.* concluded, from both the theoretical and the experimental results, that the molecular adsorption causes an overall stiffening of the MOF. A similar investigation was also carried out by Ortiz *et al.* [174], where the influence of methane loading on the elastic constants of ZIF-8 was studied. In Ref. [175], Henke *et al.* experimentally investigated the anisotropic elastic behavior of MOFs as a function of guest adsorption. They demonstrated very large changes of the elastic modulus and hardness depending on the crystal direction. The authors explain this behavior by the guest-induced changes of the network geometry. Other studies, on the less flexible ZIFs, indicated a rather small influence of pore occupancy [124]. In summary, it has now been accepted that mechanical properties of MOFs are strongly determined by the framework topology, i.e. the motive of connectivity within a framework, and the framework geometry, i.e. the geometry of the connections depending on the nature of the individual building units, as was shown for different types of MOFs: the UiO family [154], ZIFs [119] and wine-rack frameworks [166]. In a review written by Li *et al.* [155] this idea was confirmed, but they also discussed the influence of chemical effects. As the authors point out, insight in these chemical effects is highly desirable for the development of materials with targeted response and for a better understanding of framework flexibility. That chemical effects do matter, was illustrated

e.g. by an experimental study of Tan *et al.* [176]. While mechanical properties are dominated by the network topology, their study illustrates the possibility of fine-tuning the stiffness of the MOF if the chemical effects are well understood.

Calculations of elastic constants at finite temperatures have not received much attention for MOFs, but they have been studied several times for other materials. An example is the study by Shang *et al.* [177], where the temperature dependence of the elastic constants was determined for $Al_2O_3$ using a quasiharmonic approach. Using force fields, different authors [47,54,61,142] have predicted widely varying temperature dependences for the elastic properties of MOF-5 and other IRMOFs. However, the material definitely gets softer with increasing temperature. In a study of Ortiz *et al.* [174] something similar was done, but instead of the temperature dependence, the pressure dependence of the elastic constants was investigated to gain insight into the pressure-induced amorphization of ZIF-8. A good agreement between the experimental and the simulated transition pressure was found. The temperature and/or pressure dependence of the elastic constants is not explored in this work, where the focus lies on the characterization of the elastic behavior at 0 K. However, with the flexible force fields developed in this work, it is in principle possible to determine the elastic properties at finite temperatures and various pressures.

### 3.4.3 Methods to determine the elastic constants

In the following subsections, two different methods to determine the elastic constants are discussed. Both methods are based on the mathematical relations derived in Section 3.4.1.

**Method 1: Fitting stress to strain**

In the first method, the unknown elastic constants are determined from Eq. 3.39. Many papers have focused on the efficient determination of the elastic constants for cubic crystals. However, MOFs also occur in less symmetric crystal systems [178, 179]. MIL-53(Al) in the narrow pore phase is triclinic, while MOF-5 is cubic, to give some examples. A symmetry-general method to determine the elastic constants is required. In this work, the principles of Le Page and Saxe [180] are adopted.

By applying different well-chosen strains and calculating the corresponding stresses, an overdetermined system of equations can be obtained for the unknown elements of the stiffness matrix. The elastic constants are then extracted in a least-squares way. The strains chosen in this work are similar to the independent strains $\overrightarrow{\epsilon}^{(a)}$ of Shang *et al.* [181]:

$$\epsilon_b^{(a)} = x\ \delta_{ab} \text{ with } a, b = 1,\ 2,\ 3,\ 4,\ 5,\ 6 \tag{3.50}$$

In this work, 48 strains are applied, using $x = \pm\ 0.003$, $\pm\ 0.006$, $\pm\ 0.009$ and $\pm\ 0.012$. An overdetermined system of 48 equations for 21 elastic constants is obtained in this way. The calculation of the stresses corresponding to these strains is facilitated by the fact that working with force fields is computationally less expensive than working with ab initio calculations using DFT. An approach

where as few strains as possible are applied, such as proposed by Yu *et al.* [182], is not necessary here. Yu *et al.* mentioned that the independent strains are perhaps not the best choice. The strains are linearly independent in the strain space, but sample only limited parts of the stress space. For instance, in an orthorhombic crystal system $C_{14}$, $C_{15}$ and $C_{16}$ are zero. When applying a strain ($x$ 0 0 0 0 0), the response would only sample three out of six stress components ($\sigma_1$ $\sigma_2$ $\sigma_3$ 0 0 0) (see Eq. 3.39), and only three nonzero elastic constants ($C_{11}$, $C_{12}$, $C_{13}$) of the in total nine independent constants would enter the equation. The authors proposed a new set of strains: the universal linear-independent coupling strains (ULIC) (*sic*), where these problems are solved. However, by chosing a sufficiently large number of strains following Shang *et al.* [181], this problem is circumvented as well.

In summary, the procedure is thus:

- Choose a strain $\overrightarrow{\epsilon}^{(a)}$
- Deform the unit cell of the crystal according to Eq. 3.49
- Relax the atomic positions while holding the unit cell fixed
- Determine the stress $\overrightarrow{\sigma}^{(a)}$
- Link $\overrightarrow{\sigma}^{(a)}$ and $\overrightarrow{\epsilon}^{(a)}$ with Hooke's law in Eq. 3.39
- Repeat this, obtain a set of equations and extract the elastic constants in a least-squares way

The third step, relaxation of the atomic positions, is necessary. In continuum mechanics, the elastic constants are defined to link the stress and strain on an infinitesimal continuous volume element. The strain is hence directly related to the deformation of this element. The volume element here is a unit cell containing atoms. To minimize the stress resulting from interactions inside the cell, the atomic positions are relaxed, such that the link between the strain defined as a deformation of the unit cell and the stress resulting from this deformation is as closely related to the definition of the continuously deformed element as possible. In practice, when deforming a material, the atoms will also relax after a certain time (on the order of the period of the atomic vibrations). Here, static calculations are performed to mimic the behavior of the deformed crystal cell after this relaxation time. Dynamical behavior is not necessary.

In this work, force fields are used to model the metal-organic frameworks and atom relaxations are carried out with Yaff [89]. The Cauchy stress tensor

$$\boldsymbol{\sigma}_{\text{cauchy}} = \frac{1}{2V} \sum_{i,j \neq i} \overrightarrow{r_{ij}} \otimes \overrightarrow{f_{ij}} - \frac{1}{V} \sum_{i} m_i \overrightarrow{v_i} \otimes \overrightarrow{v_j} \tag{3.51}$$

is a measure of the mechanical stress at the atomistic scale. It is widely used in atomistic simulations as the counterpart of the continuum stress. Here $i$ and $j$ are the indices of the atoms with mass $m_i$ in the volume $V$ of the material. $\overrightarrow{r_{ij}}$ is the position vector pointing from atom $i$ towards atom $j$. $\overrightarrow{f_{ij}}$

is the interatomic force exerted on atom $i$ by atom $j$. In this work, static calculations are performed at 0 K. Therefore only the first part contributes to the stress because the atomic velocities $\overrightarrow{v_i}$ are identically zero.

**Method 2: Fitting strain energy density to strain**
A second method is fitting the strain energy density to strain in the harmonic approximation (i.e. Hooke's law). The elastic constants are the second-order coefficients of the expansion of the energy density $U$ in the strain $\epsilon$, as shown in Eq. 3.40.

The procedure is very similar as in method 1:

- Choose a strain $\overrightarrow{\epsilon}^{(a)}$
- Deform the unit cell of the crystal according to Eq. 3.49
- Relax the atomic positions while holding the unit cell fixed
- Determine the total energy and divide this by the equilibrium volume
- Link $U^{(a)}$ and $\overrightarrow{\epsilon}^{(a)}$ to the potential energy corresponding with Hooke's law in Eq. 3.40
- Repeat this, obtain a set of equations and extract the elastic constants in a least-squares way

The stress-based method is more efficient as each static calculation results in six equations, instead of only one with the energy approach. The energy method is particularly interesting for highly symmetric crystal structures, such as cubic [183] and tetragonal [184] ones, where only a limited number of strains have to be applied. However, the energy method is more robust than the stress-strain method, i.e. it is less prone to numerical errors. There exist schemes to extract the elastic constants from total energy calculations [173], but they were not considered in this work.

### 3.4.4 Derived characteristics

Several other mechanical properties are based on the elastic constants. These properties characterize the elastic behavior of the material and it is much easier to extract them experimentally, which allows for a direct validation of the computational results. Some of these results are compared in Section 3.4.5.

The averaged or polycrystalline elastic properties such as the bulk modulus can be directly obtained from the single-crystal elastic constants. Different averaging schemes are available. In the Voigt scheme [185] the properties are calculated based on the stiffness tensor and assuming a uniform strain. In the Reuss scheme [186] the compliance tensor $\mathbf{S}$ is used, i.e. the inverse of the stiffness tensor, and uniform stress is assumed. The Hill scheme [187] works with the arithmetic mean of the Voigt and Reuss values. Due to the often anisotropic elastic behavior of MOFs, the different schemes can give very different values. The Voigt scheme presents an upper bound and the Reuss

scheme a lower bound for the stiffness of a material.

In this work, the anisotropic elastic behavior is investigated as well. The anisotropic behavior can be calculated using the Elastic Anisotropy Measures (ElAM) code developed by Marmier *et al.* [188]. This program only requires the elastic constants of the crystal structure. Several properties can be calculated: Young's modulus, linear compressibility, shear modulus and Poisson's ratio. In addition, the averaged values of these properties using the Voigt, Reuss and Hill scheme can be determined and the directional dependence of the Young's modulus, linear compressibility, shear modulus and Poisson's ratio can be visualized. The directional dependence of these properties is determined in terms of the compliance tensor **S**. The formulas used for the tensorial analysis can be found in the article by Marmier *et al.* [188].

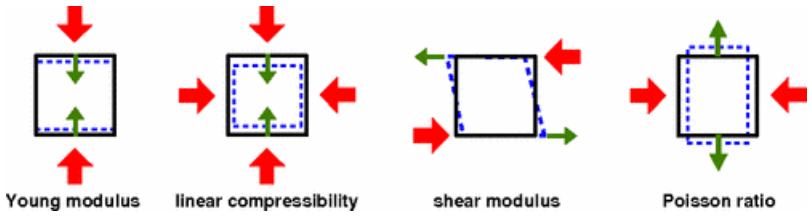


**Figure 3.11:** Scheme of the directional elastic properties calculated in this work. Figure taken from Ref. [42].

### Bulk modulus

The bulk modulus $K$ is a measure of the material's resistance to uniform compression or expansion. It has the dimension of a pressure and can be seen as the pressure change required to realize a relative volume change. It is formally defined as

$$K = -V\frac{\mathrm{d}P}{\mathrm{d}V} = V\frac{\mathrm{d}^2F}{\mathrm{d}V^2} \tag{3.52}$$

with $F$ the free energy.

A first method to directly estimate the value of the bulk modulus is to perform a series of calculations where the volume is increased isotropically. Several equations of state (EOS) are available to obtain a good fit from pressure versus volume or energy versus volume curves. Two examples are the Birch-Murnaghan EOS (Eq. 3.53) [189]

$$P(V) = \frac{3B_0}{2}\left[\left(\frac{V_0}{V}\right)^{7/3} - \left(\frac{V_0}{V}\right)^{2/3}\right]\left[1 + \frac{3}{4}\left(B_1 - 4\right)\left[\left(\frac{V_0}{V}\right)^{2/3} - 1\right]\right] \tag{3.53}$$

and the Rose-Vinet EOS (Eq. 3.54) [190]

$$P(V) = 3B_0\left[\frac{1 - \left(\frac{V}{V_0}\right)^{\frac{1}{3}}}{\left(\frac{V}{V_0}\right)^{\frac{2}{3}}}\right] e^{\frac{3}{2}(B_1-1)\left(1-\left(\frac{V}{V_0}\right)^{\frac{1}{3}}\right)} \tag{3.54}$$

$V_0$ is the equilibrium volume and $B_0$ and $B_1$ represent the bulk modulus and its first derivative with respect to the pressure. For a cubic isotropic material such as MOF-5, one can straightforwardly increase the volume of the unit cell and determine the pressure or energy for several volumes around the equilibrium volume and fit it to an EOS. For an anisotropic material such as MIL-53, it is not always clear how the volume changes. The lattice parameters could change in different ways such that a static approach where one linearly increases the lattice parameters is not reliable. To solve this one could instead apply a hydrostatic pressure and fully optimize the cell (both cell tensor and atomic positions). In this way a pressure or energy versus volume fit can be obtained. With canonical MD simulations at different volumes, it is possible to determine the bulk modulus at a finite temperature by fitting the ensemble-averaged pressure or energy to the volume via an EOS.

The bulk modulus can also be determined from the elastic constants by assuming an isotropic deformation in Hooke's law 3.39. In the Voigt scheme it is defined as:

$$K_V = \sum_{i,j=1}^{3} \frac{C_{ij}}{9} \tag{3.55}$$

with $C_{ij}$ the elements of the stiffness tensor. In the Reuss scheme, the following formula can be obtained:

$$K_R = \sum_{i,j=1}^{3} \frac{1}{S_{ij}} \tag{3.56}$$

with $S_{ij}$ the elements of the compliance tensor. In this work, the bulk modulus is calculated with both approaches at 0 K.

In general, the direct approach ($PV$-fitting) is more accurate than using an averaging scheme with the elastic constants, which is numerically less stable. As the bulk modulus is considered to be one of the most important mechanical properties for practical applications of MOFs, the direct approach is adopted here.

**Linear compressibility**

The linear compressibility $\beta(\overrightarrow{u})$ is a measure for the deformation in the $\overrightarrow{u}$-direction under hydrostatic pressure. Ortiz *et al.* [42] showed extreme negative linear compressibility in certain directions for flexible MOFs. When the material is subject to a positive hydrostatic pressure, it expands in this direction.

**Shear modulus**

The shear modulus $G$ describes the material's response to shear stress and is one of the many aspects related to the resistance to plastic deformation. Hydrostatic compressions and shear forces are the two most common mechanical loadings on MOF powders in industrial applications [154]. The bulk modulus and shear modulus are considered to be the most important mechanical properties

representing the stability for applications. The averaged or polycrystalline shear modulus in the Voigt scheme is given by:

$$G_V = \frac{C_{11} + C_{22} + C_{33} - (C_{12} + C_{13} + C_{23}) + 3\,(C_{44} + C_{55} + C_{66})}{15} \tag{3.57}$$

and in the Reuss scheme:

$$G_R = \frac{15}{4\,(S_{11} + S_{22} + S_{33} - S_{12} - S_{13} - S_{23}) + 3\,(S_{44} + S_{55} + S_{66})} \tag{3.58}$$

In general, the shear modulus is anisotropic for a single crystal.

**Young's modulus**

The Young's modulus $E$ is a measure of the uniaxial stiffness. It is defined as the ratio of the normal stress to normal strain under unidirectional loading. The averaged or polycrystalline Young's modulus is given in both the Voigt and Reuss schemes by:

$$E = \left(\frac{1}{3G} + \frac{1}{9K}\right)^{-1} \tag{3.59}$$

The reciprocal Young's modulus is a measure of the uniaxial compliance of the material. In general, this property is anisotropic for a single crystal.

**Poisson's ratio**

When a material is compressed in one direction, it tends to expand in the two directions perpendicular to the direction of compression. The Poisson's ratio $\nu$ is a measure of this effect.

In the Voigt and Reuss schemes its polycrystalline value is given by

$$\nu = \frac{1}{2}\left(1 - \frac{3G}{3K + G}\right) \tag{3.60}$$

An isotropic material has a value around $\frac{1}{3}$. For systems dominated by central interatomic interactions (e.g. ionic and van der Waals crystals) the Poisson's ratio is close to 0.25. The numerical limits are set by -1 and 0.5 for the isotropic Poisson's ratio [191]. The anisotropic Poisson ratio $\nu(\overrightarrow{u}, \overrightarrow{v})$ is defined as the ratio of the transverse strain in direction $\overrightarrow{v}$ to the axial strain in direction $\overrightarrow{u}$, when uniaxial stress in the $\overrightarrow{u}$ direction is applied.

In some materials, when stretched in a certain direction, an expansion in the transverse direction is observed. This counterintuitive behavior results in a negative Poisson's ratio and is called auxetic behavior. Looking at the anisotropic behavior of the Poisson ratio one can detect these special directions. The link between Poisson's ratio and the mechanical behavior of materials is extensively described in a review by Greaves *et al.* [191].

**Born stability criterion**

The Born stability criterion is equivalent to the condition that the elastic energy of Eq. 3.40 is always positive for an infinitesimal strain different from zero. Mathematically, this is fulfilled when all eigenvalues of the stiffness matrix **C** are positive, or equivalently, the stiffness matrix is positive definite. This condition is always checked for the materials in this work. The necessary and sufficient conditions for elastic stability in the harmonic approximation in all crystal classes can be found in a recent article by Mouhat and Coudert [159].

For a material with a cubic crystal structure, simple explicit formulas can be obtained for the Born stability criterion:

$$C_{11} - C_{12} > 0,\ C_{44} > 0 \text{ and } C_{11} + 2C_{12} > 0 \tag{3.61}$$

One important remark about the stability must be made here. A recent study of the ZIFs by du Bourg *et al.* [172] showed that many structures that were stable at 0 K were unstable even at low temperatures like 77 K. The energy minima obtained at 0 K using DFT or force fields were often so shallow that thermal motion at low temperatures allowed the system to escape. It was also shown that by loading the framework with molecules, it could be stabilized and that this effect is due to generic pore filling (even without interaction between the guest molecules and the framework). In this work the mechanical stability is studied at 0 K and its predictive power is thus inevitably limited.

**Indicator of framework flexibility**

Framework flexibility is one of the most important features of MOFs. It has received much attention during the past years. It is therefore interesting to develop a procedure for the computational prediction of flexible MOFs. In-depth investigations of the mechanism of flexibility for certain MOFs are already available in the literature, but methods to perform a rapid screening of flexible MOFs are rather rare.

A possible method was proposed by Sarkisov *et al.* [192], which is solely based on the crystal topology. The approach of Sarkisov *et al.* simplifies a MOF to two relatively rigid elements, the metal oxide cluster and the organic linker, connected with each other through hinges. To determine flexibility in a reliable manner, the connection between both components must be well described. An accurate determination of the dihedral force constants corresponding with the movements between linker and metal oxide cluster is hence a prerequisite in this thesis to obtain a reliable force field. Sarkisov *et al.* validated their method by comparing with the flexible or rigid character of experimentally known structures. Many flexible MOFs were also identified by looking at a small subset of the hypothetical MOF database constructed by Wilmer *et al.* [32].

In this work, the ideas of Ortiz *et al.* [42] will be adopted. Ortiz *et al.* suggested to look at

the anisotropic elastic properties obtainable from the stiffness tensor as a predictor for framework flexibility. The anisotropy factor $A_X$ of property $X$ (such as the Young's modulus and shear modulus)

$$A_X = \frac{X_{max}}{X_{min}} \tag{3.62}$$

is two orders of magnitude larger for known flexible materials than for known rigid materials.

The framework flexibility of MIL-53 is already well-known [12, 104], but only very recently the predicted anomalous negative linear compressibility was experimentally observed by Serra-Crespo *et al.* [193]. MIL-47 was experimentally shown to exhibit breathing behavior under mechanical pressure [92] and DMOF-1 is also known to be flexible [118]. Ortiz *et al.* [42] showed that in these flexible MOFs, the stiff directions with high Young's modulus correspond to the organic linkers or inorganic chains. However, this is not always the case, as demonstrated experimentally by Tan *et al.* [194]. The direction with relatively low Young's modulus corresponded to the breathing mode of the flexible MOF. These MOFs thus had a high $A_E$ factor $\sim$100 compared with $\sim$1 for ZIF-8 and MOF-5. Moreover, these flexible MOFs not only had a high anisotropy factor; their absolute minimal value for the Young's modulus was also much lower than for rigid MOFs. The authors therefore concluded that the Young's modulus is a good indicator for framework flexibility. Analogous conclusions could be drawn for the shear modulus. Here too, a vast difference between the flexible and nonflexible MOFs with respect to their absolute minimal shear modulus and $A_G$ value exists. The anisotropy of the linear compressibility was also investigated. Ortiz *et al.* [42] showed that negative linear compressibility, expansion along a certain direction under isostatic pressure, is sometimes present in flexible MOFs. However, that this is not always the case, was shown for the flexible DMOF-1 framework. This is due to symmetry reasons; isostatic pressure cannot trigger the breathing of the framework in this case. The conclusion then was that an extreme negative linear compressibility is a sufficient condition for framework flexibility, but not a necessary one.

In a further study by the same authors [166] the results obtained for MIL-53(Al) and MIL-47 were discussed into more detail. From the values of the directional dependent Young's modulus, it could be seen that the Al-O-Al chain (61 GPa) in MIL-53(Al) was stiffer than the V-O-V chain (38 GPa) in MIL-47, while the Young's modulus along the organic linkers (in both MOFs 1,4-benzenedicarboxylate (BDC)) was approximately the same (94.7 GPa versus 96.6 GPa). According to the authors this indicated that the metal-organic coordination played little role in this direction. All together, the elastic properties and directional dependence were very similar for both MOFs, indicating that the framework topology rather than the chemical properties determines the mechanical properties as was stated before.

Ortiz and co-workers repeated their detailed study of anisotropic elastic properties for several other MOFs [166–168]. These studies prove that the anisotropic elastic properties are good predictors for framework flexibility. Further validation is then required by experimental and/or theoretical

studies. This, however, is not the aim of this work. Here, possible flexible materials are identified by the determination of the anisotropic elastic behavior as well, but further in-depth investigations are beyond the scope of this thesis. Nevertheless, the force fields generated in the context of this work can be used to perform these more detailed studies.

In contrast with the method developed by Sarkisov *et al.* [192] this work does not test the flexibility of MOFs with an automated procedure. Instead, after obtaining the stiffness tensor, ElAM [188] is used for further analysis. The anisotropy factors $A_X$ of the shear modulus and the Young's modulus are determined and rare properties such as a negative Poisson ratio or linear compressibility will be highlighted.

### 3.4.5 Validation of the methodology

To validate our methodology, several case studies were carried out. The values obtained with the newly derived force fields are compared to published results, and the different methodologies to derive elastic constants (stress versus strain and energy versus strain) are evaluated. The sensitivity on the choice of force field, the van der Waals parameters and the rigidity of the materials are studied as well and finally, the accuracy of the predictor of framework flexibility is discussed.

**Sensitivity on the method to calculate elastic constants**

Two methods for the calculation of the elastic constants are used in this work, which ideally should give the same results. This is verified for two different materials, MOF-5 and MIL-53(Al). MOF-5 has a cubic symmetry with only three independent elastic constants, while the second MOF is the flexible MIL-53(Al). This last material has a tetragonal crystal structure in the large pore with nine independent elastic constants. The different strains applied in the energy-strain method are those proposed by Ravindran *et al.* [184] for a tetragonal crystal structure. Each strain is varied in 21 steps between -0.02 and 0.02. The stress-strain method uses the linearly independent strains in the strain space, as discussed in Section 3.4.3, and no symmetry constraints were applied in the fitting procedure. This is justified as all other elastic constants, which should be zero due to symmetry reasons, are found to be $< 0.1$.

In Table 3.6 the results are listed. All results in this table were obtained using the force fields of Ref. [67]. The results obtained with the two methodologies are in good agreement and it can be concluded that both are equally applicable for the determination of the elastic constants. From now on, only the stress-strain method will be used, as this method allows to easily calculate the stiffness tensor for low-symmetry crystals.

In Section 3.4.4, the calculation of the bulk modulus was discussed. The Voigt, Reuss and Hill values are calculated with the elastic constants obtained via the stress-strain method and are shown in Table 3.7. In the direct approach, the simulated pressure versus volume data are fitted via an EOS (Eqs. 3.53, 3.54). This data is obtained by performing a series of calculations at 0 K where a

hydrostatic pressure is applied. For each applied pressure, the equilibrium volume is obtained. Two examples of $P(V)$ fits are shown in Figure 3.12 for MOF-5 and IRMOF-8. In Figure 3.12 (left) can be seen that both EOS are able to reproduce the simulated behavior of MOF-5. This is not the case for IRMOF-8, for which only the Rose-Vinet fit shows a good agreement with the simulation as is illustrated in Figure 3.12 (right). These examples show that the Rose-Vinet EOS is better for describing strongly anharmonic behavior, which is common in MOFs.

**Table 3.6:** Comparison of the $C_{ij}$ [GPa] for MOF-5 and MIL-53(Al) obtained via both methods. The relative difference is calculated as $(C_{ss} - C_{es})/C_{es}$ ($ss$ = stress-strain, $es$ = energy-strain).

| | Method | $C_{11}$ | $C_{22}$ | $C_{33}$ | $C_{12}$ | $C_{13}$ | $C_{23}$ | $C_{44}$ | $C_{55}$ | $C_{66}$ |
|---|---|---|---|---|---|---|---|---|---|---|
| MOF-5 | Stress-Strain | 18.18 | | | 7.65 | | | 0.47 | | |
| | Energy-Strain | 18.18 | | | 7.70 | | | 0.48 | | |
| | Difference [%] | 0.0 | | | -0.6 | | | -1.9 | | |
| MIL-53(Al) | Stress-Strain | 39.92 | 32.64 | 20.29 | 7.26 | 28.07 | 5.25 | 4.28 | 29.57 | 5.55 |
| | Energy-Strain | 39.46 | 32.24 | 20.15 | 6.80 | 28.87 | 4.95 | 4.12 | 29.45 | 5.46 |
| | Difference [%] | 1.1 | 1.2 | 0.7 | 6.8 | -2.8 | 6.1 | 3.9 | 0.4 | 1.6 |

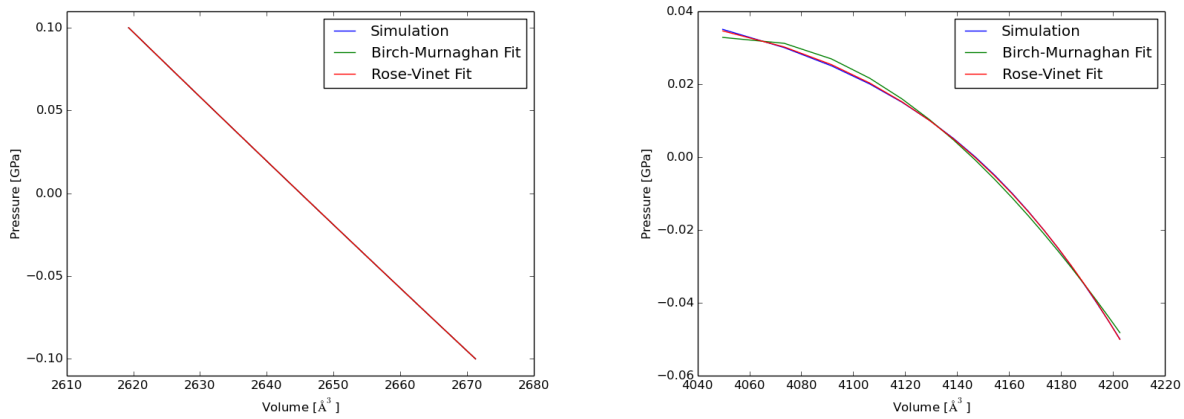


**Figure 3.12:** $P(V)$ fit to simulation results for two MOFs.

**Table 3.7:** Bulk moduli of MOF-5 at 0 K: comparison of methodologies.

| Method | Detail | $K$ [GPa] |
|---|---|---|
| This work | Fitting pressure to volume | 10.19 |
| This work | Voigt | 10.19 |
| This work | Reuss | 0.01 |
| This work | Hill | 5.10 |

When calculating the bulk modulus $K$ from the elastic constants, large fluctuations can be observed among the different averaging schemes, as shown in Table 3.7. In this case, rather coincidental, the Voigt modulus is the same as via the direct approach. In contrast, the Reuss bulk modulus is practically zero. The Hill bulk modulus is in between both results, as it is the arithmetic mean. In general, the direct approach ($PV$-fitting) is more accurate and will be used in the remainder of this work.

**Sensitivity on the choice of force field**

*MOF-5*

The elastic constants obtained via the force fields derived by the group of Schmid [61, 64] and force fields generated with QuickFF are compared. The results are tabulated in Table 3.8. The published elastic constants by Tafipolsky *et al.* [61] are shown on the first row. In the second row the MOF-FF force field [64] is used to calculate the elastic constants with the developed stress-strain method. The last rows show results obtained via force fields derived with QuickFF. The MOF-FF and QuickFF [67] force field (fourth row) are derived on the same ab initio input data and the nonbonded interactions are exactly the same.

**Table 3.8:** A comparison of the elastic constants of MOF-5 obtained via force fields generated by the group of Schmid [61, 64] and force fields generated with QuickFF.

| Force field | $C_{11}$ [GPa] | $C_{12}$ [GPa] | $C_{44}$ [GPa] |
|---|---|---|---|
| Tafipolsky *et al.* [61] | 25.3 | 8.9 | 2.3 |
| Bureekaew *et al.* [64] (MOF-FF) | 28.1 | 6.8 | 0.9 |
| Vanduyfhuys *et al.* [67] (QuickFF) | 18.2 | 7.6 | 0.5 |
| This work, harmonic | 17.5 | 6.5 | 0.4 |
| This work, anharmonic | 16.5 | 6.0 | 0.4 |

A difference in $C_{11}$ is observed. In MOF-5, this elastic constant is a measure of the bond strength along the organic linker, which thus seems to be lower for the QuickFF force field. The bond strength is mainly determined by the covalent bond and bend potential terms and there are some differences between the MOF-FF and QuickFF force fields. A first difference is that QuickFF describes these covalent interactions with harmonic terms, while MOF-FF contains anharmonic contributions. However, when the same contributions are added in the QuickFF force field, the results in the last row are obtained, indicating a further softening of the material. Another difference is the fitting procedure, which in QuickFF is designed to minimize the correlations between the different terms, while this is not the case for MOF-FF. That is why the latter requires cross-terms, which are not included in QuickFF. The absolute differences are smaller for the other two elastic constants, but the low $C_{44}$ is also significantly underestimated with QuickFF, as compared to MOF-FF. As this quantity is responsible for the weak resistance against shear deformation of MOF-5, it can be expected that the structure is much less rigid with the QuickFF force field.

Note that the differences between the elastic constants derived via the energy-strain and stress-strain relations are much smaller than the differences between the QuickFF and MOF-FF force field.

*MIL-53(Al)*

For MIL-53(Al), two ab initio force fields were derived by Vanduyfhuys *et al.* [14, 67], where the second force field was derived using QuickFF. In this work, a third force field is added, also derived via QuickFF, but with different ab initio input data. The two force fields generated with QuickFF result in the same values, as can be seen in Table 3.9. Negative values for $C_{12}$ and $C_{23}$ are revealed with the force field of Ref. [14]. To make sure that this is not due to a fitting deficiency in the stress-strain method, the calculations were repeated via the energy-strain method. However, the same results were obtained. Overall there is a reasonable agreement between the values obtained with the different force fields, especially between the two QuickFF force fields. The largest difference is $C_{22}$, which represents the strength along the metal oxide chain. This is strongly correlated with the force constant of the Al-$O_{hy}$ bond stretch, which is shown in Table 3.10. The Born criterion is checked to determine whether this material is mechanically stable, according to these force fields. In Table 3.10 the six eigenvalues of the stiffness tensor are shown for the three force fields. All these eigenvalues are positive implying that the material is stable. It is thus no problem that there are some negative elastic constants.

**Table 3.9:** Comparison of the $C_{ij}$ [GPa] for MIL-53(Al) calculated with different force fields.

| Force field | $C_{11}$ | $C_{22}$ | $C_{33}$ | $C_{12}$ | $C_{13}$ | $C_{23}$ | $C_{44}$ | $C_{55}$ | $C_{66}$ |
|---|---|---|---|---|---|---|---|---|---|
| Vanduyfhuys *et al.* [14] | 44.6 | 25.2 | 17.1 | -0.5 | 27.0 | -1.3 | 2.7 | 30.7 | 4.7 |
| Vanduyfhuys *et al.* [67] (QuickFF) | 39.9 | 32.6 | 20.3 | 7.3 | 28.1 | 5.2 | 4.3 | 29.6 | 5.5 |
| This work | 42.5 | 19.1 | 20.1 | 5.7 | 29.0 | 2.5 | 3.9 | 26.6 | 5.3 |

**Table 3.10:** Force constant $K$ of Al-$O_{hy}$ bond stretch and eigenvalues of the stiffness tensor of MIL-53(Al) according to three different force fields.

| Force field | $K$ [kJ/(mol · Å$^2$)] | $\lambda_1$ | $\lambda_2$ | $\lambda_3$ | $\lambda_4$ | $\lambda_5$ | $\lambda_6$ |
|---|---|---|---|---|---|---|---|
| Vanduyfhuys *et al.* [14] | 1738 | 61.2 | 30.7 | 25.2 | 4.7 | 2.7 | 0.4 |
| Vanduyfhuys *et al.* [67] (QuickFF) | 2073 | 62.5 | 30.0 | 29.6 | 5.5 | 4.3 | 0.4 |
| This work | 876 | 63.3 | 29.6 | 18.3 | 5.3 | 3.8 | 0.1 |

**Sensitivity on the van der Waals parameters**

Ortiz *et al.* [42] and Tan *et al.* [119] found that the dispersion correction in DFT has a negligible influence on the elastic constants obtained via ab initio calculations. In Chapter 2 it was shown

that a uniform rescaling of the van der Waals parameters, the depth $\epsilon$ and the van der Waals radius $\sigma$, has a large influence on the energy along the breathing profile. One could wonder how much influence these force-field parameters have on the elastic constants. In many cases it is not clear what these rescaling parameters have to be as there is no experimental information available. It would be a serious limitation if a large sensitivity is detected. To comment on this, a case study is made on three different materials: the rigid MOF-5, the large pore MIL-47 and the narrow pore MIL-53(Al).

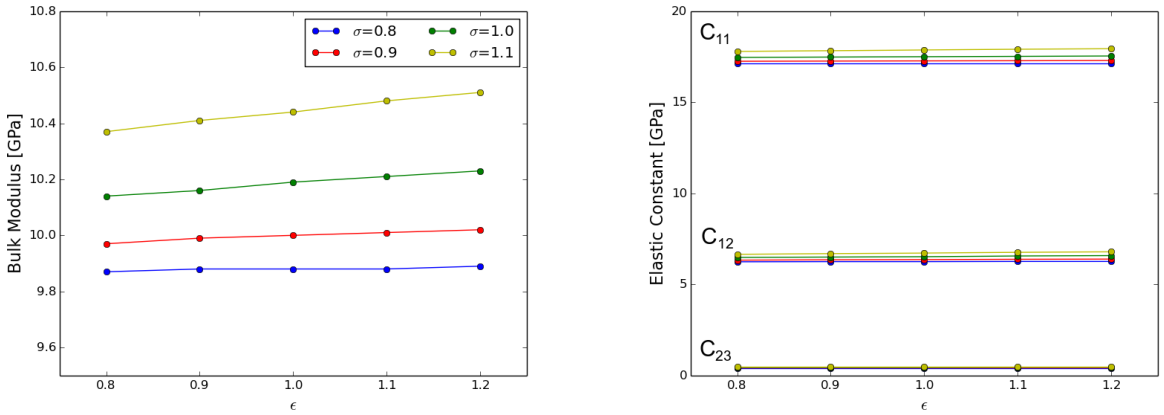


**(a)** **(b)**

**Figure 3.13:** Influence of the rescaling of the van der Waals parameters on the bulk modulus (left) and the elastic constants (right) of MOF-5 at 0 K. $\epsilon$ rescaling parameter is varied along the horizontal axis, while the $\sigma$ rescaling parameter is indicated in the legend (only shown in the left pane).

*MOF-5*

In Figure 3.13, the simulated values for the bulk modulus and elastic constants are presented. The $\epsilon$ rescaling parameter is varied along the horizontal axis and the $\sigma$ rescaling parameter is indicated in the legend. It is quite satisfying to see that both properties are relatively independent of the van der Waals parameters. Increasing the $\sigma$ rescaling parameter from 0.8 to 1.2 results in an increase of the bulk modulus of less than 1 GPa, while the lattice parameters vary between 26.08 Å ($\sigma = 0.8$) and 26.33 Å ($\sigma = 1.2$). This is small compared to the range of values that has been published in the literature (see further in Table 3.12 on page 110). That there is some influence does not need to surprise as by increasing $\sigma$, the van der Waals radius of the atom is increased, making it harder to compress the material. In Figure 3.13b the elastic constants are shown. MOF-5 has only three independent elastic constants. It can be seen that the elastic constants are rather insensitive to the van der Waals parameters (e.g. $C_{11}$ varies in a range of 0.8 GPa). From these results it can be concluded that for a rigid MOF such as MOF-5, the mechanical properties are rather insensitive towards the van der Waals parameters.

*MIL-47 and MIL-53 np*

In Chapter 2 the influence of the van der Waals parameters on the breathing profile was shown

for the flexible MIL-53(Al). The relative stability and shape was found to be strongly sensitive on these parameters. As the bulk modulus is the second derivative of the energy to the volume divided through the equilibrium volume, one can expect that especially this property will vary a lot. This is indeed verified in Figure 3.14 for the lp structure of the flexible MIL-47, for which the bulk modulus varies between 1-10 GPa. The experimental bulk modulus has not been published for MIL-47, but for the isostructural large pore MIL-53(Cr) a value of 2.0 GPa at 300 K was found [100]. The bulk modulus of MIL-47 can be extracted from the simulated $P(V)$-profile at 300 K, which was discussed in Chapter 2 (see Figure 2.23). The obtained value is 2.75 GPa, which is in a good agreement with the experimental value for MIL-53(Cr).

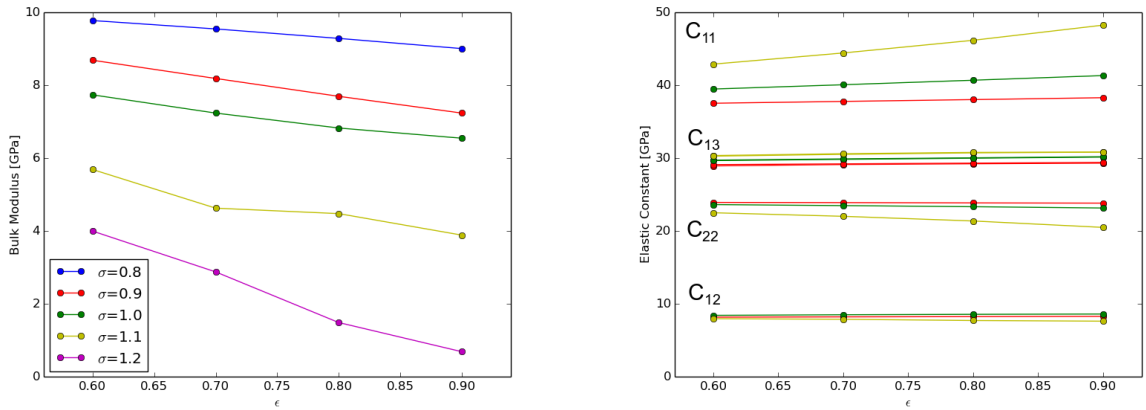


**(a)** **(b)**

**Figure 3.14:** Influence of the rescaling of the van der Waals parameters on the bulk modulus (left) and the elastic constants (right) of MIL-47 at 0 K. $\epsilon$ rescaling parameter is varied along the horizontal axis, while the $\sigma$ rescaling parameter is indicated in the legend (only shown in the left pane).

In Figure 3.14b the sensitivity of the elastic constants is shown. MIL-47 has an orthorhombic symmetry, with nine independent elastic constants. Here only four of them are shown, although the conclusions stay the same. The $C_{11}$ and $C_{33}$ values change much more than the others. This can be explained by looking at the unit cell shape and the influence of the van der Waals interactions. By rescaling the van der Waals parameters, the interdiagonal angle $\theta$ of the unit cell varies and the shape of the pore changes. When the pore contracts ($\theta$ decreases), it becomes harder to change the long diagonal, i.e. the $a$-axis ($C_{11}$ increases) and easier to change the short diagonal, i.e. the $c$-axis ($C_{33}$ decreases). Increasing the $\epsilon$ and $\sigma$ rescaling parameters in the range shown in the figure results in a decrease of the interdiagonal angle (or thus contraction of the pore) from 84° to 78°. The elastic constants are mainly a measure of the chemical bond strength and in a force field this is mostly covered by the bond distance potential terms. When the interdiagonal angle decreases, the organic linkers become more and more aligned along the $a$-axis. The effect on the bond distances when elongating (or straining) the material along this axis becomes increasingly larger when the interdiagonal angle is smaller and thus it will cost more energy. The result is an increase of $C_{11}$ (and a corresponding decrease of $C_{33}$). Off course, the bend $O_{ca}$-M-$O_{ca}$ will also play a role, but

the force constant of this term is a factor 10 lower than the force constants of the bonds.

The observed sensitivity of the bulk modulus of MIL-53(Al) np (not shown) is less than is the case for MIL-47. A smaller range of bulk moduli between 2.1 GPa and 4.5 GPa is found, but the values are less predictable. While the bulk modulus of MIL-47 shows clear trends in function of $\epsilon$ and $\sigma$, this is not the case for the narrow pore of MIL-53(Al). This can be explained by the fact that while the interdiagonal angle and relative stability of the narrow pore change drastically under influence of the van der Waals parameters, the curvature of the energy profile in this np remains more or less the same (see Figure 2.17 in Chapter 2). The narrow pore of MIL-53(Al) is described by a triclinic crystal system with 21 independent elastic constants. The results are not shown, but also here the conclusions remain the same as for MIL-47. Especially $C_{11}$ varies a lot in function of the $\sigma$ scale (values in the range of 115-160 GPa when decreasing the $\sigma$ scale), while the constants are insensitive to the $\epsilon$ scale. As was noted in Chapter 2 (see Figure 2.17), the influence of increasing $\sigma$ on the breathing profile is an increase of the interdiagonal angle of the narrow pore and a decrease of the interdiagonal angle of the large pore. As the interdiagonal angle increases, the pore opens and the organic linkers are less aligned with the $a$-axis, hence decreasing $C_{11}$. The large value of $C_{11}$ of the narrow pore compared to the large pore of MIL-47 is a further confirmation of this idea; in the narrow pore the $a$-axis lies nearly parallel with the BDC-linker, so that a strain along this axis results in a direct increase of the bond distances.

The conclusion is that the chemical bond strength itself is insensitive to the long-range van der Waals interactions (see MOF-5), but as the cell shape changes, the effect of certain strains on the bond distances grows larger. As this is the most energetically costly term in the force field, the elastic constants change due to the way they are defined and measured. The problem with this sensitivity is the limited predictive power of our simulated values. For the set of different linkers, no experimental or theoretical data is available for a fine-tuning of the van der Waals scale. As the calculated bulk modulus varies in a range of 1-10 GPa such as for MIL-47, this is the accuracy that one can expect from the force field.

**Sensitivity on the rigidity of the materials**

*Rigid MOFs: MOF-5, HKUST-1 and ZIF-8*

In Table 3.11, an overview is presented of the elastic constants of MOF-5 as found in literature. As was mentioned in Section 3.4.2, a low $C_{44}$ compared to the other independent elastic constants is in general found. The twisting of the organic linkers is responsible for this [162]. Tafipolsky and Schmid [61] produce with their force field comparable values to the ab initio elastic constants, while Han and Goddard [142] deviate a lot from the others. This is probably due to the fact that they use a generic force field (DREIDING [49]), which is not ideally suited to describe MOFs. The values obtained with the newly derived force field in this work clearly differ from the other published results. The three elastic constants are underestimated. On the one hand, Tafipolsky *et al.* [61] illustrated that it is possible to obtain similar values as the DFT results with an ab initio force field.

On the other hand, Bahr *et al.* [91] showed that the $C_{44}$ is sensitive to the used theoretical method (LDA versus GGA). However, the $C_{44}$ obtained in this work is a factor 3-4 smaller. The $C_{11}$ of MOF-5 is a direct measure for the bond strength along the organic linker. Compared to MOF-FF, an underestimation was found. In Table 3.11, it can be seen that the DFT values are even higher than the force field values. An underestimation on the order of 35% is found.

**Table 3.11:** Comparison of the $C_{ij}$ [GPa] for MOF-5 at 0 K.

| | Theoretical | $C_{11}$ [GPa] | $C_{12}$ [GPa] | $C_{44}$ [GPa] | $a_0$ [Å] |
|---|---|---|---|---|---|
| This work | FF | 17.50 | 6.53 | 0.45 | 26.13 |
| Mattesini *et al.* [163] | DFT, LDA | 21.52 | 14.77 | 7.54 | 25.89 |
| Zhou and Yildirim [162] | DFT, LDA | 29.42 | 12.56 | 1.16 | 25.58 |
| Samanta *et al.* [164] | DFT, LDA | 29.2 | 13.1 | 1.4 | 25.64 |
| Bahr *et al.* [91] | DFT, LDA | 28.5 | 12.1 | 1.7 | 25.59 |
| Bahr *et al.* [91] | DFT, GGA | 27.8 | 10.6 | 3.6 | 26.04 |
| Han and Goddard [142] | FF (MD, 10 K) | 44.53 | 6.79 | 1.82 | / |
| Tafipolsky and Schmid [61] | FF | 25.3 | 8.9 | 2.3 | 26.04 |

**Table 3.12:** Bulk moduli of MOF-5 at 0 K: overview of results.

| | Method | $K$ [GPa] |
|---|---|---|
| This work | FF | 10.19 |
| Zhou and Yildirim [162] | DFT, LDA | 18.2 |
| Mattesini *et al.* [163] | DFT, LDA | 17.02 |
| Samanta *et al.* [164] | DFT, LDA | 18.5 |
| Bahr *et al.* [91] | DFT, LDA | 17.6 |
| Bahr *et al.* [91] | DFT, GGA | 16.3 |
| Kuc *et al.* [165] | DFTB | 8.70 |
| Han and Goddard [142] | FF, MD at 10 K | 19.37 |
| Greathouse and Allendorf [54] | FF | 20 |
| Tafipolsky and Schmid [61] | FF | 14.4 |
| Bristow *et al.* [59] | FF | 11.95 |

In Table 3.12, the published bulk moduli are listed. The DFT values are quite consistent with values ranging between 16.3 GPa and 18.2 GPa. The range of the force field results is larger (11.95-20 GPa). The value obtained in this work is again underestimated. Only the value obtained by Kuc *et*

*al.* [165] with Density-Functional-based Tight-Binding (DFTB) is lower. From all the results shown for MOF-5 (elastic constants and bulk moduli), it can only be concluded that the bond strength obtained with the new force field is lower than for other theoretical methods.

The same results are obtained for HKUST-1. However, not as much data is available as is the case for MOF-5. In Table 3.13, some results are shown. The experimental bulk modulus obtained by Chapman *et al.* [195] is well reproduced by the force fields of Tafipolsky and Schmid [61] and Bristow *et al.* [59]. The ab initio calculations of Wu *et al.* [154] also show a good agreement. In contrast, the bulk modulus obtained in this work is almost 10 to 15 GPa lower. HKUST-1 has a cubic crystal structure and hence only three independent elastic constants. Wu *et al.* [154] obtained a rather small $C_{44}$, compared to the other elastic constants, which is not the case for Tafipolsky *et al.* The values determined in this work are definitely lower than the force field by Tafipolsky *et al.*, comparable to the trend seen when comparing the MOF-FF force field [64] with our results for MOF-5.

**Table 3.13:** Comparison of the $C_{ij}$ [GPa] for HKUST-1.

| | Method | $C_{11}$ [GPa] | $C_{12}$ [GPa] | $C_{44}$ [GPa] | $K$ [GPa] |
|---|---|---|---|---|---|
| This work | FF | 15.80 | 13.21 | 5.09 | 14.26 |
| Wu *et al.* [154] | DFT, PBE | 25.92 | 23.84 | 4.41 | 24.53 |
| Tafipolsky *et al.* [63] | FF | $\approx 19$ | $\approx 15$ | 13 | 25 |
| Chapman *et al.* [195] | Exp. | / | / | / | 30.7(5) |
| Bristow *et al.* [59] | FF, MD at 1 K | / | / | / | 25.05 |

Another rigid MOF is ZIF-8. It has a cubic crystal structure and thus only three independent elastic constants. For this structure, experimental and theoretical elastic constants have been published by Tan *et al.* [119]. In this case, the force field shows a good agreement with the theoretical and experimental results, as seen in Table 3.14.

*Flexible MOFs: MIL-53(Al), MIL-53(Ga), MIL-47 and DMOF-1*

To date, there is not much data available on the elastic constants of flexible MOFs. Ortiz *et al.* [42] published some results obtained using periodic DFT calculations and these values are tabulated in Table 3.15. The considered structures were MIL-53(Al), MIL-53(Ga), MIL-47 and DMOF-1. For all these MOFs ab initio force fields were derived in this work. One can immediately see that the values obtained with the force field differ a lot from the DFT values. The procentual differences are indicated in the table. In previous sections, it was shown that the elastic constants and bulk modulus of MOF-5 and HKUST-1 are underestimated compared to other published results. Here the same trend is observed, but an even larger deviation is noted.

**Table 3.14:** Comparison of the $C_{ij}$ [GPa] for ZIF-8.

| | Method | $C_{11}$ [GPa] | $C_{12}$ [GPa] | $C_{44}$ [GPa] | $a_0$ [Å] |
|---|---|---|---|---|---|
| This work | FF (0 K) | 9.38 | 7.34 | 0.74 | 17.128 |
| Tan [119] | B3LYP (0 K) | 11.04 | 8.33 | 0.94 | 17.348 |
| Tan [119] | B3LYP-D (0 K) | 11.03 | 8.43 | 0.73 | 17.063 |
| Tan [119] | PBE (0 K) | 10.14 | 8.00 | 0.78 | 17.261 |
| Tan [119] | HF (0 K) | 10.17 | 9.29 | 1.36 | 17.455 |
| Tan [119] | Exp. (295 K) | 9.52 | 6.86 | 0.97 | 16.992 |

**Table 3.15:** Comparison of the elastic constants $C_{ij}$ [GPa] with the results obtained by Ortiz *et al.* [42]. The procentual error, determined as $(X - X_{ortiz})/X_{ortiz}$, is also given.

| | $C_{11}$ | $C_{22}$ | $C_{33}$ | $C_{12}$ | $C_{13}$ | $C_{23}$ | $C_{44}$ | $C_{55}$ | $C_{66}$ |
|---|---|---|---|---|---|---|---|---|---|
| MIL-53(Al) lp | 42.53 | 19.06 | 20.13 | 5.74 | 29.04 | 2.53 | 3.85 | 26.64 | 5.33 |
| MIL-53(Al) lp [42] | 90.85 | 65.56 | 33.33 | 20.41 | 54.28 | 12.36 | 7.24 | 39.52 | 8.27 |
| MIL-53(Al) lp [%] | -53.1 | -71.2 | -39.6 | -71.9 | -46.5 | -79.5 | -46.8 | -32.6 | -35.6 |
| MIL-53(Ga) lp | 43.30 | 16.04 | 15.10 | 5.88 | 24.36 | 2.36 | 3.22 | 25.11 | 5.29 |
| MIL-53(Ga) lp [42] | 112.32 | 56.66 | 18.52 | 22.87 | 45.35 | 10.86 | 5.48 | 21.71 | 6.64 |
| MIL-53(Ga) lp [%] | -61.4 | -71.7 | -18.5 | -74.3 | -46.3 | -78.3 | -41.2 | +15.7 | -20.3 |
| MIL-47 | 44.40 | 9.87 | 21.98 | 7.85 | 30.49 | 5.42 | 3.64 | 30.57 | 5.08 |
| MIL-47 [42] | 62.60 | 40.69 | 36.15 | 12.58 | 46.98 | 9.28 | 7.76 | 50.83 | 9.30 |
| MIL-47 [%] | -29.1 | -75.7 | -39.2 | -37.6 | -35.1 | -41.6 | -53.1 | -39.9 | -45.8 |
| DMOF-1 | 39.23 | 23.40 | 39.96 | 3.75 | 1.01 | 3.80 | 2.15 | 0.37 | 2.16 |
| DMOF-1 [42] | 58.20 | 35.33 | 58.45 | 7.32 | 11.68 | 7.55 | 0.444 | 0.112 | 0.284 |
| DMOF-1 [%] | -32.6 | -33.8 | -31.6 | -48.8 | -91.4 | -71.5 | +384.2 | +70.0 | +660.5 |

The elastic constants are strongly determined by the chemical bonds and less by the long-range interactions. As the covalent interactions model the chemical bonds in the force field, these could be seen as the main reason for the large deviations. In an orthorhombic unit cell, the $C_{ii}$ represents the curvature of the energy versus strain along the $i$-th crystallographic axis ($i = 1, 2, 3$) or thus the ease with which it can be deformed along this axis. The largest underestimation ($\approx 70\%$) compared to the values of Ortiz *et al.* [42] is found for the $C_{22}$ parameter in the case of MIL-53(Al), MIL-53(Ga) and MIL-47. This is not a surprise considering the unit cell and the idea that the chemical bond strength is underestimated. $C_{22}$ is calculated along the 1D chain ($b$-axis) and it is thus nearly a direct measure for the chemical bond strength of M-$O_{ca}$. In the case of MIL-47 a double well potential was proposed to describe the asymmetric V-O bond distance along the chain. It is in some way reassuring that the underestimation of the strength along the metal chain is similar to the one of MIL-53, indicating that the same relative strength is included in the framework. The deviations of $C_{11}$ and $C_{33}$ are hard to interpret as they strongly dependend on the unit cell shape as

mentioned in the paragraph on the sensitivity of the van der Waals parameters. DMOF-1 breathes upon guest adsorption, but does not show flexibility without guests [118]. The crystal axes of the unit cell lay along the organic linkers (BDC, DABCO). In other words, the $C_{ii}$ (i=1,2,3) are again a measure for the chemical bond strength. Compared to the values of Ortiz *et al.* an underestimation of 30% is found in all cases. This is comparable with the underestimation of $\approx 35\%$ of $C_{11}$ along the BDC linker in MOF-5. Large deviations for DMOF-1 are also found for $C_{jj}$ ($j = 4, 5, 6$), where the values of Ortiz *et al.* are very small.

Overall, it can be concluded that there is an underestimation of the force constants of flexible MOFs. The values obtained for $C_{22}$ for MIL-53 and MIL-47, and the $C_{ii}$ ($i = 1, 2, 3$) of DMOF-1 seem to point towards a systematic underestimation. It is, however, hard to detect the origin solely based on the elastic constants. The elastic constants different from the $C_{ii}$ were not discussed, as here a complex interplay from various covalent terms is responsible for the difference.

**Table 3.16:** Comparison of the anisotropic elastic behavior of well-known MOFs.

| | $E_{min}$ [GPa] | $E_{max}$ [GPa] | $A_E$ | $G_{min}$ [GPa] | $G_{max}$ [GPa] | $A_G$ |
|---|---|---|---|---|---|---|
| MIL-53(Al) lp | 0.21 | 59.89 | 285 | 0.07 | 29.64 | 423 |
| MIL-53(Al) lp [42] | 0.90 | 94.7 | 105 | 0.35 | 39.5 | 112 |
| MIL-53(Ga) lp | 1.33 | 52.61 | 40 | 0.53 | 25.11 | 47 |
| MIL-53(Ga) lp [42] | 0.16 | 69.7 | 444 | 0.08 | 21.7 | 270 |
| MIL-47 | 1.03 | 58.99 | 57 | 0.36 | 30.56 | 85 |
| MIL-47 [42] | 0.9 | 96.6 | 108 | 0.29 | 50.8 | 175 |
| DMOF-1 | 1.22 | 39.34 | 32 | 0.33 | 19.30 | 58 |
| DMOF-1 [42] | 0.45 | 55 | 123 | 0.11 | 18.4 | 165 |
| MOF-5 | 1.32 | 13.94 | 11 | 0.45 | 5.48 | 12 |
| MOF-5 [42, 91] | 9.5 | 19.7 | 2.1 | 3.4 | 7.5 | 2.2 |
| ZIF-8 | 2.15 | 2.93 | 1.36 | 0.74 | 1.02 | 1.38 |
| ZIF-8 [42, 119] | 2.7 | 3.9 | 1.4 | 0.94 | 1.4 | 1.4 |
| HKUST-1 | 3.77 | 13.62 | 3.62 | 1.00 | 5.09 | 5.09 |

**Accuracy of the framework flexibility predictors**

In the previous paragraphs, a large underestimation of the elastic constants was noted, but the question is whether this has as large influence on the derived characteristics such as framework flexibility. In this paragraph, a comparison is made of the anisotropic elastic behavior of the well-known MOFs with the results obtained by Ortiz *et al.* [42] by considering the anisotropy factors of Eq. 3.62. The minimal, maximal and anisotropy factors of the Young modulus and shear modulus are shown in Table 3.16. It is obvious that the minimal and maximal values strongly differ from the values obtained by Ortiz *et al.* This is not a surprise since these quantities are strongly sensitive on the elastic constants, which were also strongly different. However, a trend, pointing towards

a systematic deviation, seems to be absent. The anisotropy factors are somewhat more similar. The rigid materials HKUST-1 and ZIF-8 have anisotropy factors of at most 5, while the flexible materials have values larger than 30. MOF-5 on the other hand, has anisotropy factors of 10, which can be explained by the very low $C_{44}$ predicted with the force field.

In Table 3.17, the two other properties considered by Ortiz *et al.* are compared. Ortiz *et al.* only published the linear compressibilities along the crystal axes, instead of the maximum and minimum values displayed in this work. These results look much more promising. There is a very clear difference in $\Delta\beta = \beta_{max} - \beta_{min}$ between the rigid and flexible MOFs. Ortiz *et al.* also pointed out that especially the extreme negative linear compressibility indicates flexibility. However, due to symmetry reasons, this is sometimes not present. In a cubic crystal symmetry (MOF-5, ZIF-8, HKUST-1) the linear compressibility is isotropic. A large range in linear compressibility is hence a sufficient condition for flexibility, but not a necessary one. A clear separation of the Poisson ratio is not found between flexible and rigid materials. For example, while HKUST-1 shows low anisotropy factors, it displays an anomalous negative Poisson ratio. The Poisson ratio is thus not a good predictor for framework flexibility.

In Table 3.18, the smallest eigenvalue of the stiffness tensor of each MOF is listed. Ortiz *et al.* [166] suggested that this also could be a good predictor. This is not the case for the results obtained in this work. For example, ZIF-8, which reproduced very well the ab initio and experimental elastic constants of Tan *et al.* [119], has a smaller eigenvalue than MIL-53(Ga), which is supposed to be very flexible.

**Table 3.17:** Comparison of the anisotropic elastic behavior of the linear compressibility $\beta$ and Poisson's ratio $\nu$ for some well-known MOFs.

| | $\beta_{min}$ [TP$a^{-1}$] | $\beta_{max}$ [TP$a^{-1}$] | $\Delta\beta$ [TP$a^{-1}$] | $\nu_{min}$ | $\nu_{max}$ |
|---|---|---|---|---|---|
| MIL-53(Al) lp | -1255 | 1836 | 3091 | -4.43 | 4.31 |
| MIL-53(Al) lp [42] | / | / | / | -2.4 | 1.9 |
| MIL-53(Ga) lp | -196 | 370 | 566 | -0.86 | 1.90 |
| MIL-53(Ga) lp [42] | / | / | / | -6.2 | 2.9 |
| MIL-47 | -201 | 303 | 504 | -0.87 | 1.79 |
| MIL-47 [42] | / | / | / | -1.5 | 2.2 |
| DMOF-1 | -40 | 87 | 127 | -0.43 | 1.29 |
| DMOF-1 [42] | / | / | / | 0.00 | 1.0 |
| MOF-5 | 32.72 | 32.72 | 0.00 | 0.03 | 0.91 |
| MOF-5 [42, 91] | / | / | / | 0.03 | 0.67 |
| ZIF-8 | 41.04 | 42.18 | 1.14 | 0.35 | 0.56 |
| ZIF-8 [42, 119] | / | / | / | 0.33 | 0.57 |
| HKUST-1 | 23.68 | 23.69 | 0.01 | -0.19 | 1.00 |

**Table 3.18:** Smallest eigenvalue of the stiffness tensor of well-known MOFs.

| MIL-53(Al) | MIL-53(Ga) | MIL-47 | DMOF-1 | MOF-5 | ZIF-8 | HKUST-1 |
|---|---|---|---|---|---|---|
| 0.14 | 0.99 | 0.70 | 0.33 | 0.45 | 0.74 | 2.59 |

**Conclusion**

In this section, the methodology was validated. First, a direct comparison was made between the elastic constants obtained with the stress versus strain method and the energy versus strain method. The results indicated that both methods produce the same elastic constants, however, the stress-strain method is easier applicable in the case of low-symmetry crystals. For the remainder of this work, this method is used.

Second, the sensitivity of the elastic constants on the force field was tested. While the elastic constants obtained with the QuickFF force fields were quite similar, some differences were noted with MOF-FF [64]. When comparing the elastic constants and bulk moduli of rigid and flexible MOFs with theoretical and experimental results, it can only be concluded that the new ab initio derived force fields underestimate these quantities. This indicates that the covalent interactions, representing the chemical bonds, are weaker than in other theoretical results. This was also noted in the comparison of the values of the thermal expansion coefficients. Here, an overestimation of roughly a factor three was found compared to the literature. The materials are thus more easily deformed under mechanical and thermal stress.

The underestimation is however not systematic for the elastic constants. For the rigid MOFs, HKUST-1 and MOF-5, there is a clear underestimation of both bulk moduli and elastic constants compared to DFT and other force field results. ZIF-8 on the other hand, shows a very good agreement with the experimental and theoretical results. A remarkable result is the underestimation of the elastic constants along the BDC organic linker for MOF-5 ($C_{11}$) and DMOF-1 ($C_{11}$, $C_{33}$) with 30%, while a 70% underestimation is found along the 1D metal chain in MIL-53(Al), MIL-53(Ga) and MIL-47. The other elastic constants are more difficult to interpret as they are strongly sensitive to various covalent interactions. To understand these effects, a more systematic study should be carried out. In this work, it is an inevitable limitation.

The numerical values of the framework flexibility indicators deviate from the calculations of Ortiz *et al.* [42] and there does not seem to be a systematic trend. However, there is still at least a factor three difference between the rigid and the flexible MOFs in the anisotropy factors, which enables the further use of this method. The extreme negative linear compressibility for flexible materials also showed to be very different for flexible and rigid MOFs and can be used as a sufficient condition. In contrast, the Poisson ratio and smallest eigenvalue are found not to be good predictors for framework flexibility.

# Chapter 4

# Extending the search space

In Chapter 2, force fields were generated for a limited set of well-known MOFs. The validation of Chapter 3 proved that the methodology leads to good results. In this chapter, we will again apply this methodology to derive force fields for and characterize an extended set of MOFs. Parameters were derived for different organic linkers, which were subsequently combined with the validated inorganic parts of MOF-5, MIL-47 and MIL-53. The model systems used for these new linkers were inspired by the previously proposed organic linker cluster models. The organic linkers were taken from the Hypothetical Metal-Organic Frameworks database of Wilmer *et al.* [32] and those that were studied are presented in Figure 4.11 on page 129. Eight different functional groups ($CH_3$, $OCH_3$, OH, CN, $NH_2$, Br, Cl, F) were also considered and they were used to functionalize the BDC linkers. In this chapter, textural, thermal and mechanical properties are compared for an extended set containing the IRMOF series, MIL-53 family, the MIL-47 family and the HKUST-1 family.

## 4.1 The IRMOF series

In this section, the results obtained for MOF-5 with different functional groups as well as some other linkers are discussed. Eight different functionalized groups were studied as mentioned above, but only five of them gave a reliable measure for the thermal expansion coefficient. With Br, CN and $CH_3$, the framework collapsed due to the large pressure fluctuations in the $NPT$ simulations. The simulated temperature dependence of the volume (at 1 bar) is illustrated in Figure 4.2 for MOF-5, MOF-5-F and MOF-5-Cl. An increase of 30% in thermal expansion coefficient can be noted for MOF-5-F and MOF-5-OH. The values of the different properties discussed in Chapter 3, are shown in Table 4.1 on page 118.

The functional group has not much influence on the cell shape. All structures remain cubic, while the lattice parameter $a$ has a value in the range of 26.11 Å to 26.17 Å. The MOFs with functional groups Br (IRMOF-2) and $NH_2$ (IRMOF-3) were synthesized by the group of Yaghi [11]. An interesting property, wich does show some variation, is the pore limiting diameter (PLD). Using CN or Br, an increase of more than 1 Å is noted relative to MOF-5, due to the presence of open

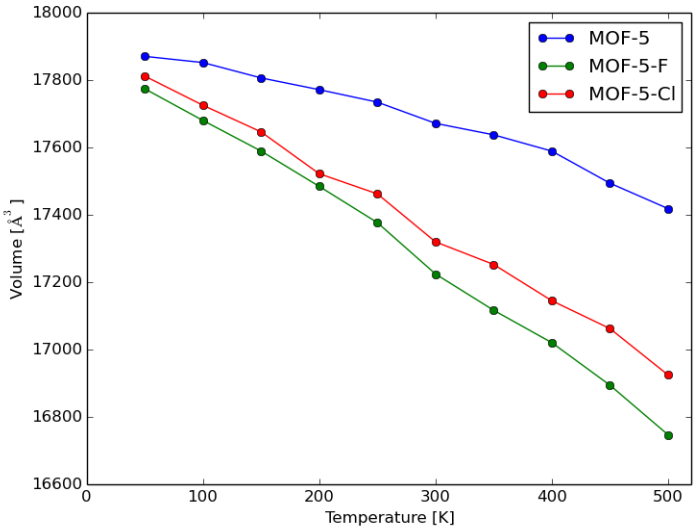


**Figure 4.1:** Thermal expansion behavior of functionalized MOF-5: volume as function of the temperature.

channels (Figure 4.8). These channels arise because of the strong electrostatic repulsion between the carboxyl oxygen and functional group, which causes the linker to twist. The accessible surface area (ASA) decreases, except for MOF-5-CH3, where a slight increase is noted. The functionalized MOFs get softer, i.e. the bulk modulus degrades, with a maximal decrease for MOF-5-OH of 40%. The anisotropy factor $A_E$ remains largely unchanged, but there are some slight deviations of the isotropic structure, when looking at the range of the linear compressibility $\Delta\beta = \beta_{max} - \beta_{min}$. For flexible MOFs, this value was found to be higher than 100 TPa$^{-1}$ based on the results of Chapter 3. Here, all functionalized MOFs remain rigid according to this criterion. Functionalizing the material does not lead to auxetic behavior, as the minimal Poisson ratio ($\nu$) remains positive in all cases. Overall, the mechanical properties are not very affected by the functional group.

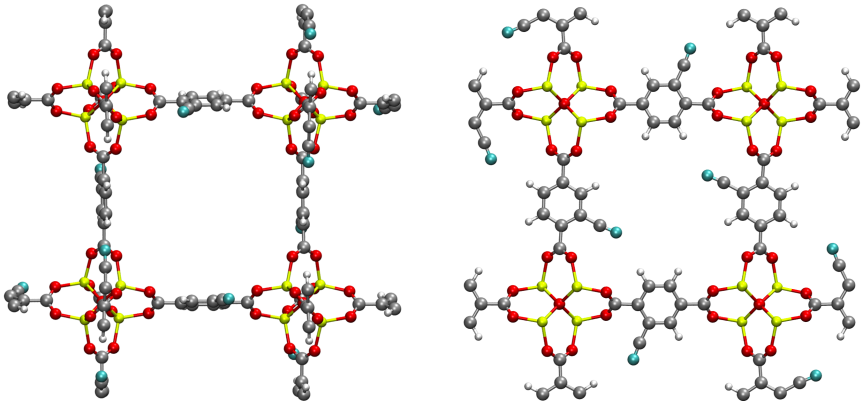

**Figure 4.2:** Open channel (left) and closed channel (right) in MOF-5-CN.

**Table 4.1:** Textural, thermal and mechanical properties for the functionalization of MOF-5.

| | PLD [Å] | ASA [$m^2g^{-1}$] | $\alpha_V$ [$10^6$ $K^{-1}$] | $K$ [GPa] | $A_E$ | $\Delta\beta$ [$TPa^{-1}$] | $\nu_{min}$ | $a$ (0 K) [Å] |
|---|---|---|---|---|---|---|---|---|
| MOF-5 | 8.06 | 3917 | -102 | 10.19 | 10.6 | 0.0 | 0.03 | 26.13 |
| MOF-5-Br | 9.54 | 2945 | / | 8.98 | 10.5 | 27.0 | 0.02 | 26.11 |
| MOF-5-Cl | 8.09 | 3568 | -112 | 8.45 | 10.6 | 22.0 | 0.02 | 26.15 |
| MOF-5-F | 8.82 | 3679 | -132 | 9.36 | 12.5 | 1.9 | 0.03 | 26.16 |
| MOF-5-$NH_2$ | 7.98 | 3759 | -104 | 9.82 | 9.2 | 5.6 | 0.03 | 26.17 |
| MOF-5-$CH_3$ | 7.51 | 3942 | / | 8.79 | 12.8 | 5.9 | 0.02 | 26.12 |
| MOF-5-$OCH_3$ | 7.04 | 3918 | -110 | 8.36 | 10.9 | 5.6 | 0.03 | 26.13 |
| MOF-5-OH | 7.12 | 3864 | -132 | 5.87 | 10.2 | 26.2 | 0.01 | 26.11 |
| MOF-5-CN | 9.28 | 3626 | / | 9.35 | 11.1 | 2.0 | 0.03 | 26.11 |

**Table 4.2:** Properties of the IRMOF series, extended with other hypothetical materials.

| | PLD [Å] | ASA [$m^2g^{-1}$] | Void [%] | $\alpha_V$ [$10^6$ $K^{-1}$] | $K$ [GPa] | $A_E$ | $A_G$ | $\lambda$ [GPa] | $a$ (0 K) [Å] |
|---|---|---|---|---|---|---|---|---|---|
| MOF-5 (BDC) | 8.06 | 3917 | 48 | -102 | 10.19 | 11 | 12 | 0.45 | 26.134 |
| IRMOF-6 (CBBDC) | 8.11 | 3566 | 41 | -133 | 9.81 | 13 | 15 | 0.36 | 26.204 |
| IRMOF-8 (2,6-NDC) | 9.17 | 4568 | 56 | -109 | 2.66 | 10 | 12 | 0.22 | 30.364 |
| IRMOF-10 (BPDC) | 11.11 | 5153 | 65 | -160 | 2.78 | 21 | 24 | 0.11 | 34.698 |
| IRMOF-14 (PDC) | 10.52 | 4953 | 61 | -111 | 6.69 | 26 | 30 | 0.13 | 34.621 |
| IRMOF-16 (TPDC) | 16.63 | 6044 | 76 | / | 3.67 | 37 | 43 | 0.05 | 43.368 |
| HMOF 1 (DPADC) | 14.62 | 5826 | 74 | -175 | 4.60 | 31 | 36 | 0.06 | 39.849 |
| HMOF 2 (HPDC) | 12.11 | 5008 | 64 | / | 6.40 | 22 | 26 | 0.12 | 34.808 |
| HMOF 3 (DPTZDC) | 16.73 | 5516 | 77 | -162 | 3.95 | 45 | 55 | 0.05 | 42.870 |

In Table 4.2, several organic linkers (Figure 4.11 on page 129) were combined with the inorganic building block of MOF-5. The linker is indicated between brackets in Table 4.2. Some of them were previously synthesized by the group of Yaghi [11]. All structures satisfy the Born stability criterion as the smallest eigenvalue $\lambda$ of the stiffness tensor remains positive. It can be noted that this eigenvalue decreases with increasing linker length. The PLD is directly related to the linker length and the largest pore diameters are therefore found in IRMOF-16, HMOF-1 (HMOF = Hypothetical MOF) and HMOF-3, while the smallest are found in MOF-5 and IRMOF-6 (see Figure 4.11 on page 129). The first have an extremely large void fraction, i.e. the empty space within the unit cel, of more than 75%. This is an increase of 25% compared with MOF-5. In Chap-

ter 3, the thermal expansion coefficients of several IRMOFs were compared with published results, which indicated an overestimation of the negative expansion with roughly a factor 3. In Table 4.2, two structures (HMOF-1 and HMOF-3) are found with an even larger thermal expansion coefficient.

With increasing linker length, the anistropy factors for Young's modulus ($A_E$) and shear modulus ($A_G$) increase up to a value of 45 and 55 for HMOF-3, which is comparable to the anisotropy factors of MIL-53(Ga) and DMOF-1. The results also show that IRMOF-10, with a BPDC linker, can be strengthened by replacing it with a PDC or HPDC linker. This results in a slight decrease of the ASA and void fraction, but more than doubles the bulk modulus.

## 4.2 The MIL-53 family

**Influence of the metal center**

The thermal expansion behavior obtained for the narrow pore of MIL-53(Sc), MIL-53(Cr) and MIL-53(Ga) is shown in Figure 4.3. In contrast with other MOFs, a positive thermal expansion is revealed, that cannot be described by a linear $\ln(V)$ versus T fit. It can, however, be observed that the temperature dependence of the volume is the lowest for MIL-53(Sc), while the volume of MIL-53(Cr) increases with nearly 10% in the temperature range 50-500 K.

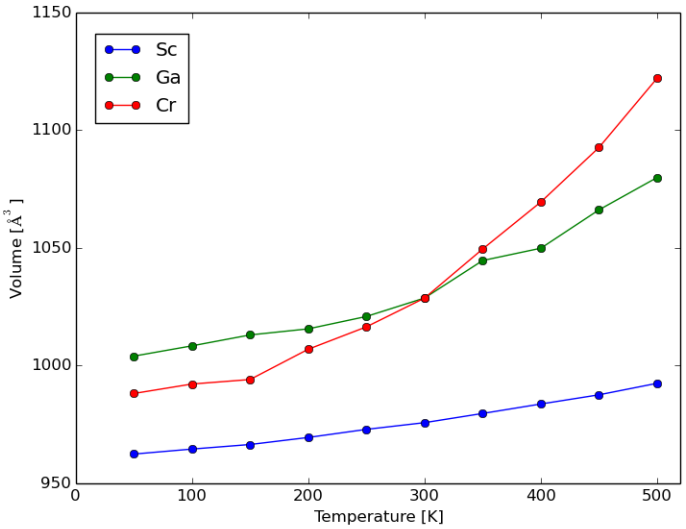


**Figure 4.3:** Thermal expansion behavior of MIL-53(Sc), MIL-53(Cr) and MIL-53(Ga) in the narrow pore: volume versus temperature.

MIL-53(Al) displays another behavior (Figure 4.4). The volume indicated on the figure is the ensemble-averaged volume of the last 150 ps of a 750 ps run, averaged over two simulations at each temperature at 1 bar. The red dots are simulations that were initially in the narrow pore, while the blue dots started in the large pore. At low temperatures, the large-pore structure collapses

towards the narrow-pore structure, while the narrow pore remains in the narrow pore. At higher temperatures, the opposite is true and the large pore is observed at the end of each simulation. A transition area in the temperature range of 200-300 K is found, where transitions between both states are observed. An example of such a simulation at 250 K is shown in Figure 4.5, where multiple transitions occur during 750 ps. This agrees with the experimental behavior demonstrated by Liu *et al.* [93]. However, more elaborate calculations should be performed to obtain better estimates for the temperatures of the lp-to-np and np-to-lp transitions since it was shown that transitions might be due to stochastic processes.

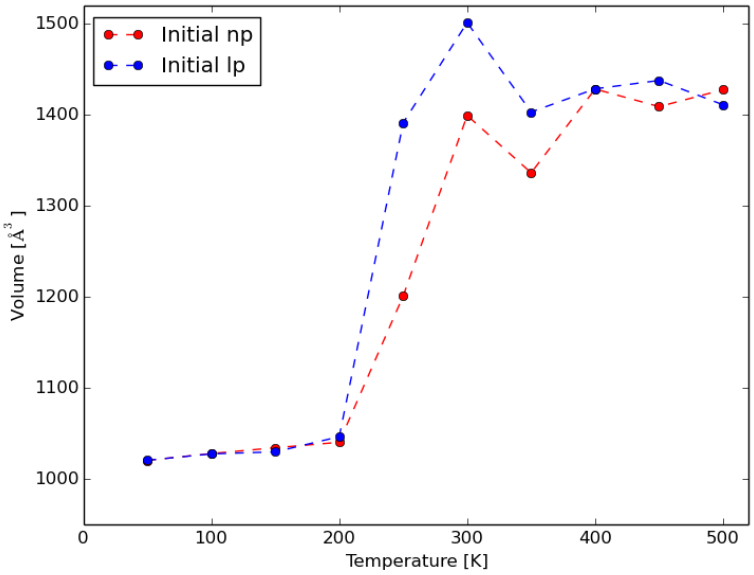


**Figure 4.4:** Thermal expansion behavior of MIL-53(Al): volume versus temperature.

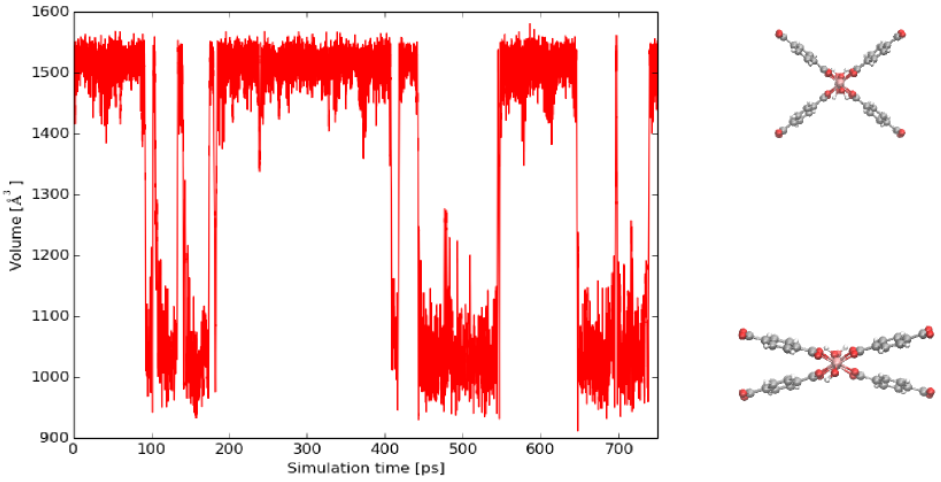


**Figure 4.5:** Evolution of the volume during a simulation of MIL-53(Al) at 250 K.

In Table 4.3, textural and mechanical properties of the stable states of these MOFs at 0 K are listed. The PLD of the np states is smaller than 3 Å (except for Al), which means that the spherical probe will not fit in, resulting in a zero ASA. The bulk modulus is correlated with the volume and interdiagonal angle $\theta$. The smaller the interdiagonal angle, the harder it becomes to compress the framework, which results in a larger bulk modulus. MIL-53(Sc), with a very narrow-pore state ($\theta = 35°$), has a bulk modulus of 5 GPa, while the other narrow pores have values beneath 2 GPa. The anisotropic elastic measures $A_E$, $A_G$ and $\Delta\beta$ are also a lot smaller than for MIL-53(Al), MIL-53(Cr) and MIL-53(Ga). Therefore, we can conclude that MIL-53(Sc) has the most rigid framework.

**Table 4.3:** Influence of the metal center on the textural and mechanical properties of MIL-53.

| | PLD [Å] | ASA [$m^2g^{-1}$] | $K$ [GPa] | $A_E$ | $A_G$ | $\Delta\beta$ [$TPa^{-1}$] | $\nu_{max}$ | $\nu_{min}$ | $V$ [Å$^3$] | $\theta$ [°] |
|---|---|---|---|---|---|---|---|---|---|---|
| Al (np) | 3.09 | 183 | 1.05 | 107 | 28 | 1241 | 5.97 | -3.42 | 1012 | 43 |
| Al (lp) | 7.07 | 1010 | 0.88 | 285 | 423 | 3091 | 4.31 | -4.43 | 1505 | 80 |
| Sc (np) | 2.11 | 0.0 | 5.27 | 35 | 19 | 184 | 1.30 | -0.67 | 960 | 35 |
| Cr (np) | 2.81 | 0.0 | 1.78 | 84 | 23 | 811 | 3.34 | -3.58 | 987 | 40 |
| Ga (np) | 2.90 | 0.0 | 1.53 | 80 | 19 | 828 | 5.2 | -2.73 | 998 | 41 |

**Influence of the functional group**

In Table 4.4, the interdiagonal angle of the stable states at 0 K is indicated. It is revealed that by adding a functional group at every BDC linker in the unit cell, the structure prefers the lp state for most functional groups. For instance, MIL-53(Al) shows no stable narrow pore with the different functional groups considered. MIL-53(Sc) is in a very narrow-pore state without functional group and for OH and $NH_2$ the system also remains in a narrow pore. For the other functionalizations, the large pore is more stable. MIL-53(Cr) and MIL-53(Ga) display some intermediate states with an interdiagonal angle $\theta$ around 65°. In Figure 4.6, the thermal expansion behavior of MIL-53(Al) with a functional group is shown. Very distinct features are revealed. On the one hand, Br, Cl and $CH_3$ functional groups lead to a clear negative expansion and $OCH_3$ to a positive expansion. On the other hand, the volume of MIL-53(Al)-CN increases when increasing the temperature at low temperature, while it decreases again starting from 250 K. MIL-53(Al)-$NH_2$ does not expand or shrink until 250 K, where a sudden decrease of nearly 80 Å$^3$ is found.

A selected number of functional groups is compared in Table 4.5 on page 123. It can be seen that the ASA is mainly determined by the metal center, while the mechanical properties are determined by the functional group. The bulk moduli of MIL-53-Cl and MIL-53-$OCH_3$ are larger than the bulk modulus of MIL-53-$NH_2$. The anisotropy factors and range of the linear compressibility are larger in the case of MIL-53-$NH_2$. The largest negative Poisson ratio is also consistently found for $NH_2$. Only MIL-53(Sc) seems to break this trend, e.g. $NH_2$ functionalization results in a np and the bulk moduli are lower.

**Table 4.4:** Interdiagonal angle $\theta$ of the MIL-53 after functionalizing it at 0 K.

| Functional group | Al | Sc | Cr | Ga |
|---|---|---|---|---|
| none | 43 | 35 | 40 | 41 |
| Br | 88 | 81 | 84 | 82 |
| Cl | 83 | 75 | 78 | 78 |
| F | 79 | 82 | 77 | 62 |
| $OCH_3$ | 78 | 72 | 75 | 74 |
| $CH_3$ | 87 | 78 | 81 | 80 |
| $NH_2$ | 80 | 44 | 71 | 71 |
| CN | 76 | / | 74 | 74 |
| OH | 81 | 49 | 61 | 67 |

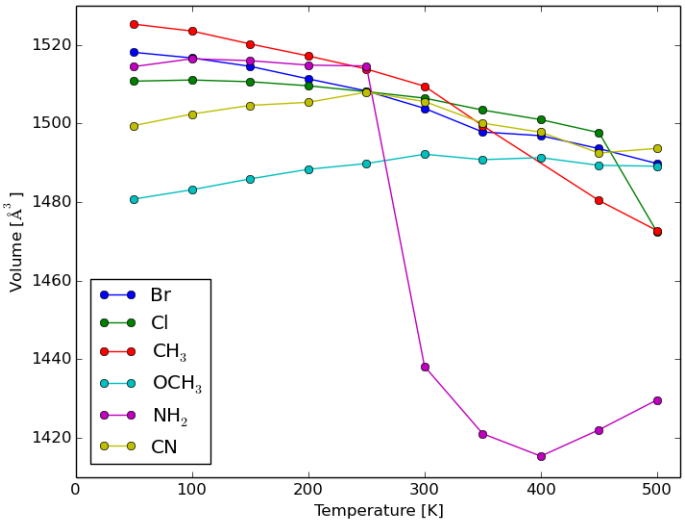


**Figure 4.6:** Thermal expansion behavior of MIL-53(Al) with a functional group: volume versus temperature.

### Influence of the organic linker

In Figure 4.7, the thermal expansion behavior of MIL-53(Al) with other organic linkers is displayed. The thermal expansion behavior of these structures shows strong deviations of the linear $\ln(V)$ versus $T$ behavior, such that it was decided not to determine a single expansion coefficient, but rather show the entire profile. Some linkers result in positive thermal expansion and others in negative thermal expansion. On the left side, structures that are stable narrow-pore states are shown, while on the right side, large-pore structures are given. These figures illustrate the wealth of possibilities one has in selecting the required thermal expansion behavior, by choosing the appropriate linker.

**Table 4.5:** Textural and mechanical properties of functionalized MIL-53(Al), MIL-53(Sc), MIL-53(Cr) and MIL-53(Ga).

| | | | PLD [Å] | ASA [$m^2g^{-1}$] | $K$ [GPa] | $A_E$ | $A_G$ | $\Delta\beta$ [$TPa^{-1}$] | $\nu_{min}$ |
|---|---|---|---|---|---|---|---|---|---|
| Al | Cl | lp | 5.48 | 1612 | 8.4 | 35 | 58 | 297 | -0.86 |
| | $NH_2$ | lp | 6.22 | 1720 | 4.81 | 80 | 115 | 735 | -1.62 |
| | $OCH_3$ | lp | 4.37 | 1507 | 7.07 | 28 | 36 | 301 | -0.61 |
| Sc | Cl | lp | 6.39 | 1677 | 4.26 | 38 | 48 | 528 | -0.86 |
| | $NH_2$ | np | 3.51 | 568 | 1.51 | 67 | 21 | 887 | -2.40 |
| | $OCH_3$ | lp | 5.09 | 1559 | 5.82 | 25 | 28 | 389 | -0.77 |
| Cr | Cl | lp | 5.81 | 1485 | 8.09 | 28 | 41 | 279 | -0.69 |
| | $NH_2$ | lp | 6.57 | 1494 | 3.05 | 64 | 68 | 758 | -1.46 |
| | $OCH_3$ | lp | 4.57 | 1364 | 6.82 | 23 | 30 | 281 | -0.59 |
| Ga | Cl | lp | 5.66 | 1359 | 6.14 | 20 | 29 | 231 | -0.39 |
| | $NH_2$ | lp | 6.48 | 1355 | 3.02 | 52 | 55 | 705 | -1.34 |
| | $OCH_3$ | lp | 4.57 | 1232 | 5.39 | 19 | 26 | 266 | -0.56 |

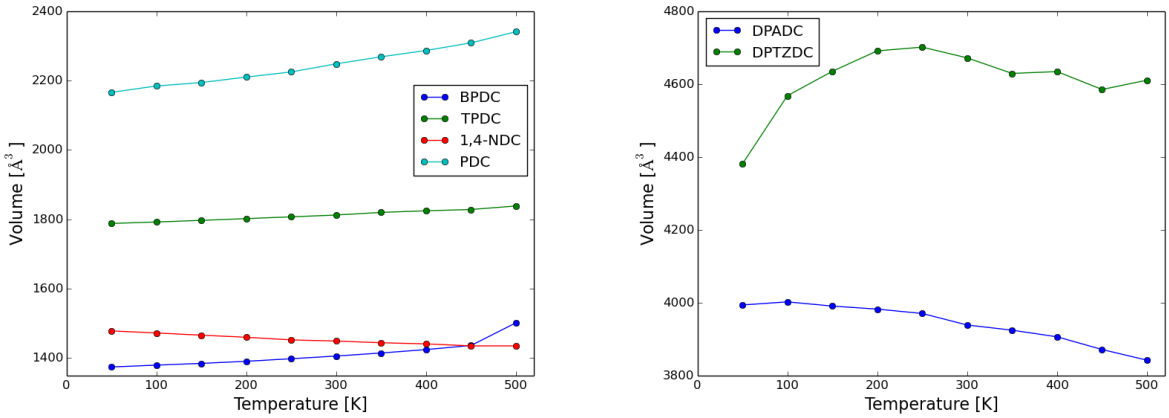


**Figure 4.7:** Influence of organic linker on thermal expansion behavior of MIL-53(Al). On the left side, the structures display a closed form, while on the right side a large pore is obtained.

In Table 4.6, a comparison is made between different linkers for the MIL-53 structures with Al and Sc as metal centers. In all cases a lower interdiagonal angle is found for scandium, consistent with the standard MIL-53 case, where MIL-53(Sc) has a very narrow-pore state. While with BPDC and TPDC linkers a narrow pore is found at 0 K, DPADC, DPTZDC and 1,4-NDC are in the large pore. The BPDC and TPDC are not surprising as the narrow pore in MIL-53(Al) is largely stabilized by the dispersion interactions between the BDC linkers. By increasing the length of the linker, this effect is increased. For PDC, which is a large planar structure, this is not possible due to the Pauli repulsion of neighboring linkers, therefore, an intermediate state is observed (Figure 4.8 (left)). The

same occurs for 1,4-NDC, where a closed disordered structure is found in which the Pauli repulsion is minimized (Figure 4.8 (right)). It is remarkable that for the extended MIL-53(Al) with DPADC and DPTZDC a large pore is detected. By replacing the middle phenyl group with a nitrogen substituted ring or by a linear C-C bond the stabilization energy is not sufficient to stabilize the narrow pore. The mechanical quantities are very similar for MIL-53(Sc) and MIL-53(Al), except for 1,4-NDC. The large-pore states with extended linkers have a very small bulk modulus and the smallest eigenvalue is almost zero, indicating a very unstable structure.

**Table 4.6:** Textural and mechanical properties of other organic linkers for MIL-53(Al) and MIL-53(Sc).

| | Linker | PLD [Å] | ASA [$m^2g^{-1}$] | $K$ [GPa] | $A_E$ | $A_G$ | $\Delta\beta$ [$TPa^{-1}$] | $\lambda$ [GPa] | $\theta$ [°] |
|---|---|---|---|---|---|---|---|---|---|
| Al | BPDC | 2.53 | 0 | 5.03 | 29 | 16 | 195 | 1.54 | 29 |
| | DPADC | 12.39 | 3532 | 0.59 | 924 | 1170 | 14564 | 0.02 | 82 |
| | TPDC | 2.41 | 0 | 8.67 | 15 | 26 | 100 | 3.20 | 22 |
| | PDC | 3.11 | 697 | 6.23 | 21 | 48 | 289 | 0.92 | 84 |
| | 1,4-NDC | 6.98 | 1295 | 1.36 | 69 | 25 | 1018 | 0.08 | 49 |
| | DPTZDC | 15.21 | 3210 | 0.53 | 275 | 478 | 4061 | 0.08 | 82 |
| Sc | BPDC | 2.16 | 0 | 5.80 | 26 | 11 | 150 | 1.18 | 27 |
| | TPDC | 2.33 | 0 | 9.16 | 16 | 15 | 79 | 2.58 | 21 |
| | 1,4-NDC | 3.79 | 1293 | 2.40 | 20 | 36 | 764 | 0.97 | 73 |
| | HPDC | 5.95 | 1214 | 1.32 | 67 | 17 | 1012 | 0.58 | 43 |

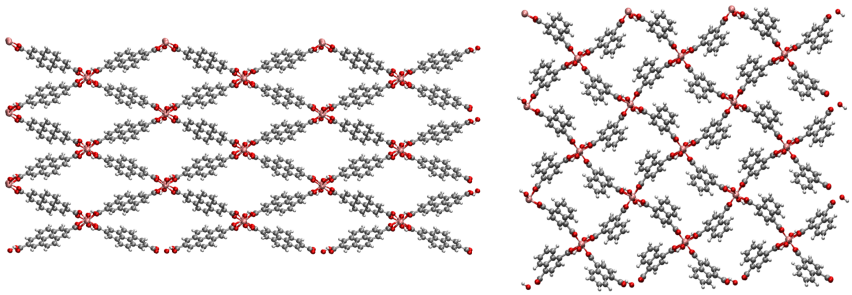

**Figure 4.8:** Periodic structures of MIL-53(Al) with PDC (left) and 1,4-NDC (right) linkers.

## 4.3 The MIL-47 family

The thermal expansion behavior of functionalized MIL-47 is shown in Figure 4.9. MIL-47 without functional group exhibits a linear decrease of the volume in the range of 50 to 250 K and for 350 to 500 K, while an increase of the volume is found for intermediate temperatures. These results were found after a total simulation length of 9 ns at 1 bar, such that the ensemble-averaged volume should be converged. The thermal expansion behavior of the the functionalized MIL-47 structures was determined from a single 2 ns run at each temperature. Different thermal expansion behaviors

are observed, similar as for MIL-53(Al). MIL-47-$NH_2$ shows a large positive expansion, while MIL-53(Al)-$NH_2$ displayed a strange temperature dependence. Functionalization with $OCH_3$, CN or Cl only leads to a slight change in volume with temperature.

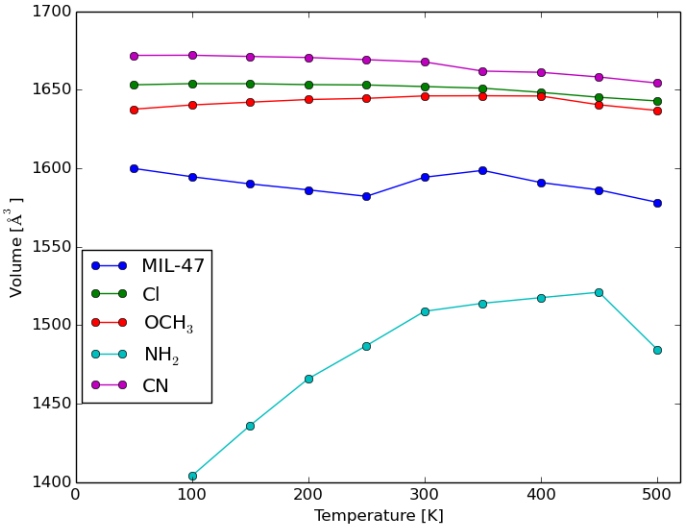


**Figure 4.9:** Thermal expansion behavior of MIL-47 with a functional group.

**Table 4.7:** Influence of the functional group on textural and mechanical properties of MIL-47.

| | PLD [Å] | ASA [$m^2g^{-1}$] | $K$ [GPa] | $A_E$ | $A_G$ | $\Delta\beta$ [$TPa^{-1}$] | $\nu_{min}$ | $\theta$ [°] |
|---|---|---|---|---|---|---|---|---|
| MIL-47 | 7.00 | 1985 | 4.63 | 57 | 85 | 503 | -0.87 | 80 |
| Br | 6.02 | 1432 | 10.43 | 26 | 39 | 196 | -0.57 | 81 |
| Cl | 6.68 | 1600 | 6.68 | 42 | 54 | 450 | -0.85 | 77 |
| F | 7.31 | 1739 | 4.44 | 65 | 93 | 581 | -0.92 | 80 |
| $OCH_3$ | 4.92 | 1743 | 6.61 | 28 | 36 | 328 | -0.62 | 76 |
| $CH_3$ | 6.33 | 1792 | 6.62 | 28 | 44 | 293 | -0.56 | 79 |
| $NH_2$ | 6.42 | 1639 | 1.26 | 116 | 117 | 1746 | -2.47 | 69 |
| OH | 6.62 | 1894 | 2.37 | 93 | 105 | 1166 | -1.83 | 74 |
| CN | 5.88 | 1666 | 8.89 | 18 | 30 | 183 | -0.38 | 80 |

In Table 4.7, some mechanical and textural properties of functionalized MIL-47 are listed. The interdiagonal angle is also given, to illustrate that a large pore is always observed. The ASA varies in the range 1432-1894 $m^2g^{-1}$ and is the lowest for MIL-47-Br. This is probably because Br is a heavier element and the ASA is normalized on the weight. By functionalizing the material with Br, Cl, CN, $CH_3$ and $OCH_3$, the material gets harder with a maximum bulk modulus of 10

GPa for MIL-47-Br. The anisotropy factors, $\Delta\beta$ and $\nu_{min}$ decrease for these materials (in absolute value) compared with the non-functionalized MIL-47, while the opposite is true for F, $NH_2$ and OH.

**Table 4.8:** Influence of other linkers on textural and mechanical properties of MIL-47.

| | PLD [Å] | Void [%] | $K$ [GPa] | $A_E$ | $A_G$ | $\Delta\beta$ [$TPa^{-1}$] | $\nu_{min}$ |
|---|---|---|---|---|---|---|---|
| MIL-47 | 7.00 | 20 | 4.63 | 57 | 85 | 503 | -0.87 |
| DPADC | 12.74 | 42 | 0.65 | 122 | 93 | 3549 | -2.13 |
| TPDC | 12.64 | 41 | 0.52 | 251 | 221 | 6669 | -3.46 |
| 1,4-NDC | 3.47 | 3 | 4.03 | 23 | 46 | 402 | -0.88 |
| PDC | 6.74 | 13 | 0.58 | 117 | 40 | 2128 | -3.52 |

The thermal expansion is not shown for different organic linkers, but the same conclusions can be drawn as for MIL-53(Al), where strongly different thermal expansion behavior was found depending on the linker. In Table 4.8, some textural and mechanical properties are listed. The void fraction doubles when changing the BDC linker to a TPDC linker. The PLD is then 12.6 Å and a very low bulk modulus of 0.5 GPa is found. This structure is very soft and close to mechanical unstability. In contrast with MIL-53(Al), the extended linker materials remain in the large pore, consistent with the more rigid behavior of MIL-47. An extremely large range of linear compressibility can also be found for the TPDC linker.

## 4.4 The HKUST-1 family

In Figure 4.10, the thermal expansion behavior is presented for HKUST-1 with metal centers V, Fe, Co, Ni and Cu. All materials show negative thermal expansion on average, but HKUST-1(V) seems to expand at low temperatures. The other four metal centra show a near linear behavior and the fitted thermal expansion coefficient is shown in Table 4.9. HKUST-1(Fe), HKUST-1(Co) and HKUST-1(Ni) display a negative thermal expansion with a coefficient of approximately $-30 \cdot 10^6$ $K^{-1}$, while HKUST-1(Cu) has a somewhat larger coefficient of $-40 \cdot 10^6$ $K^{-1}$. In previous chapter, it was shown that HKUST-1(Cu) is isotropic and rigid (compared to the other studied MOFs), but that it shows a negative Poisson ratio in certain directions. When pulling in the [110] directions, the material expands in the $[1\bar{1}0]$ directions. In Table 4.9, some mechanical properties are listed to illustrate that the elastic properties are independent of the metal centra. This supports the idea that the mechanical properties are mainly determined by the framework topology, instead of the precise chemical nature. Textural properties such as pore diameters and void fraction are all very similar. The accessible surface area is also tabulated, which in this case follows the same trend of the volume of the structure (see lattice parameter $a$ in Table 4.9).

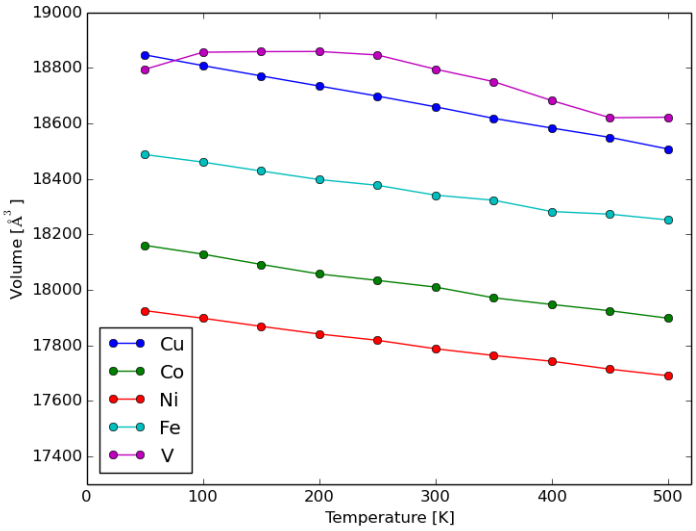


**Figure 4.10:** Thermal expansion behavior of HKUST-1 with different metal centra.

**Table 4.9:** Textural, thermal and mechanical properties of HKUST-1 with different metal centra.

| | ASA [m$^2$g$^{-1}$] | $\alpha_V$ [10$^6$ K$^{-1}$] | $K$ [GPa] | $A_E$ | $A_G$ | $\nu_{min}$ | $a$ [Å] (0 K) |
|---|---|---|---|---|---|---|---|
| V | 2839 | / | 13.5 | 3.01 | 5.35 | -0.12 | 26.907 |
| Fe | 2671 | -29 | 15.6 | 2.83 | 5.96 | -0.08 | 26.455 |
| Co | 2579 | -32 | 16.3 | 3.29 | 5.88 | -0.14 | 26.301 |
| Ni | 2530 | -29 | 16.3 | 3.13 | 6.04 | -0.12 | 26.183 |
| Cu | 2606 | -40 | 14.3 | 3.61 | 5.09 | -0.19 | 26.631 |

## 4.5 Conclusion

The final set of materials is too small to detect structure-property relations, but some interesting effects were revealed by studying the influence of the linker and/or metal center. The whole IR-MOF series displays negative thermal expansion. The structures become more flexible, but also more unstable, when the linker length is increased, which also results in a larger thermal expansion coefficient. The maximal void fraction is found for IRMOF-16 with approximately 75% empty space in the framework. IRMOF-10, with a biphenyl linker, can be strengthened with a PDC or HPDC linker, without jeopardizing the interesting properties such as a large PLD and accessible surface area. Functionalizing MOF-5 leads to softer materials, i.e. a lower bulk modulus, but overall this has not much influence on the anisotropic elastic behavior.

With functional groups and different organic linkers, it is possible to obtain a wide variety of volume dependent temperature behavior in MIL-53. By adding a functional group on the BDC linker, the bulk modulus is strongly increased, and instead of a narrow pore (at 0 K), mostly a large pore is

preferred. In contrast, extended linkers lead to very mechanically unstable structures. The same conclusions could be drawn for MIL-47.

Finally, it was shown that the metal center has not much influence on the mechanical properties in HKUST-1. This supports the idea that the mechanical properties are dominantly determined by the framework topology. All structures showed a negative linear $\ln(V)$ versus $T$ behavior.

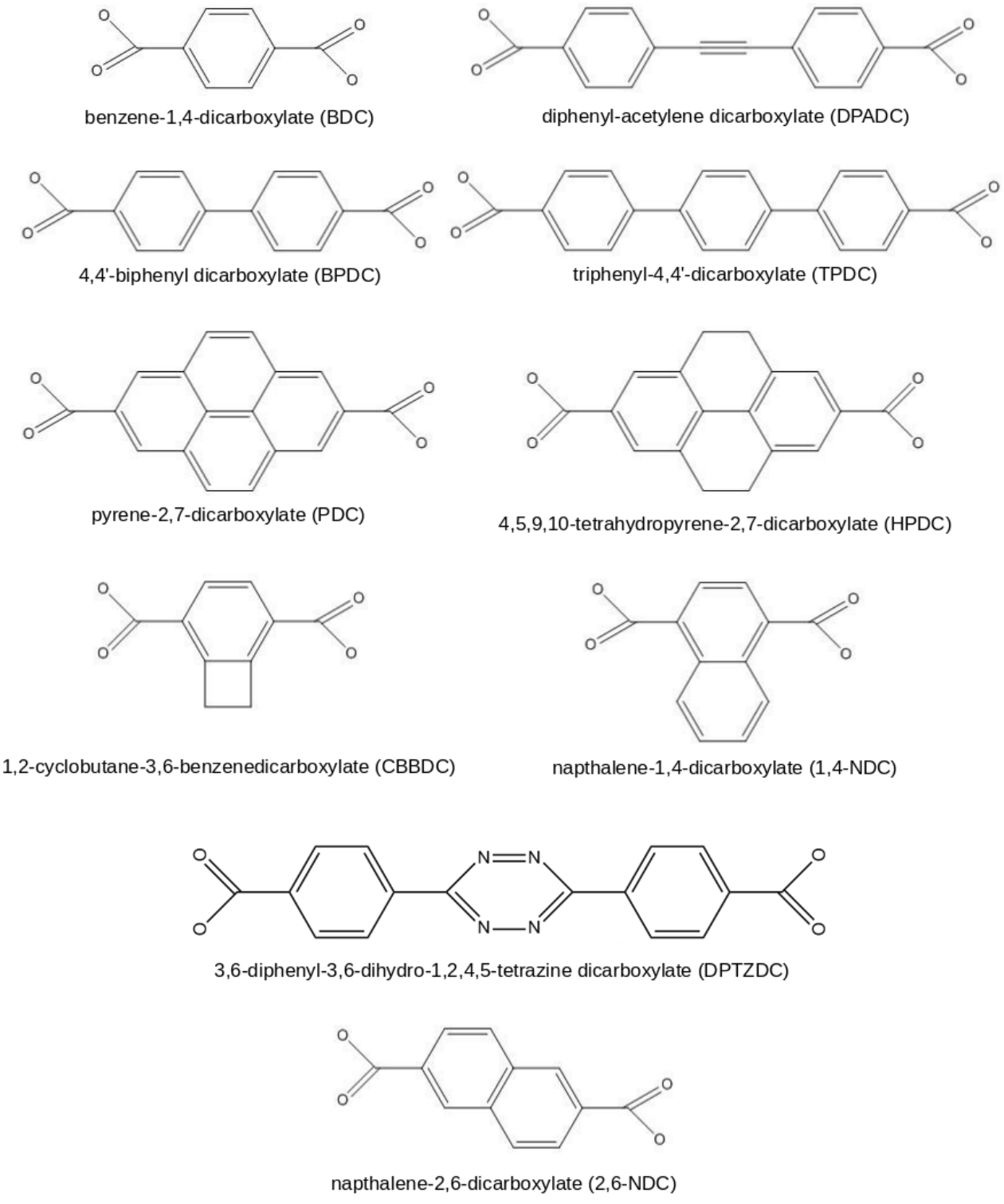


**Figure 4.11:** Overview of different organic linkers.

# Chapter 5

# Conclusion and outlook

The number of experimentally characterized metal-organic frameworks increases every day, but the great diversity of molecular building blocks, together with the various ways of combining them, leads to an unlimited number of possible structures. Computational high-throughput methods have become a new tool that offers the promise of fast and efficient materials screening. This rapidly emerging field of research aims to identify novel promising structures and to gain new physical insights such as structure-property relations. To date, a fully quantum mechanical large-scale screening of MOFs is not attainable due to the high computational cost. Other less accurate, but cheaper, simulation techniques have to be considered. Molecular mechanics and force fields offer a solution to access larger length and time scale. Until now, high-throughput studies of MOFs have mainly focused on the adsorption of small molecules such as $H_2$, $CH_4$ and $CO_2$. In these investigations, the framework is kept rigid and only the guest-host interaction is modeled, but such an approach is inherently limited. To study mechanical, thermal and dynamical behavior of the framework, intraframework interactions are required and flexible force fields must be used.

Generating accurate flexible force fields on a large scale is not a trivial task. A systematic approach consists in parametrizing the force fields with quantum mechanical data, which is possible with QuickFF [67], a software package recently developed at the CMM. Force-field parameters are derived from two different clusters, representing the inorganic metal node and organic linker, and these parameters are subsequently combined in the periodic structure. In this work, force fields were first generated for different systems with various molecular environments, to illustrate the general applicability of the applied methods. The methodology was validated in the second chapter by constructing force fields for well-known and experimentally characterized MOFs, viz. MOF-5, MIL-53, MIL-47, HKUST-1, ZIF-8 and DMOF-1. Overall, the force fields succeed in reproducing the equilibrium cell shape. A crucial term in the force-field energy expression, especially for flexible MOFs like MIL-53 and MIL-47, is the van der Waals interaction, which was added a posteriori, but fine-tuned ad hoc. These parameters were observed to strongly influence the breathing behavior and cell shape. These interactions can, however, be tuned whenever extra experimental or theoretical data are available. This was demonstrated with the force field of MIL-47, where the experimentally

observed pressure-induced breathing behavior was obtained after rescaling the standard MM3 van der Waals parameters [80].

Another very important part of a high-throughput screening is the definition of so-called descriptors, which connect the calculated microscopic parameters to macroscopic properties of the materials. For gas adsorption and separation purposes, descriptors were identified such as the pore limiting diameter and the void fraction [27]. However, to characterize mechanical and thermal behavior of MOFs, new descriptors are required. Ortiz *et al.* [42] suggested to study the anisotropic elastic behavior as a predictor of framework flexibility. This requires the calculation of the full stiffness tensor. To be feasible in a large-scale screening of MOFs, force fields must therefore be constructed that can accurately describe the elastic behavior. In this work, it was shown that the anistropic elastic behavior obtained with the force fields clearly separates the rigid from the flexible frameworks.

Furthermore, the heat capacity and thermal expansion behavior were investigated. No reliable measure of the heat capacity was found with classical molecular dynamics simulations, nor with a harmonic approximation of the phonon spectrum. Different, more advanced, techniques exist that could provide a better approximation, but they have currently not been tested on MOFs [138, 139]. The negative thermal expansion, on the other hand, tends to be overestimated by the new force fields compared to other theoretical and experimental results, but the same trends are visible. It was moreover demonstrated by means of DMOF-1 that the temperature-dependent thermal expansion coefficient could be retrieved from sufficiently long molecular dynamics simulations.

The textural properties provide a third way of characterizing the MOF, but not much time was spent on this subject, as several reliable high-throughput tools are already freely available in the literature to calculate these properties [27, 120].

In the last chapter, the search space was extended and the validated methodology of the previous chapters was applied. Different organic linkers and functional groups were now considered and with only a group of about hundred materials, already some interesting trends were revealed. For instance, the flexible MOFs - MIL-53 and MIL-47 - displayed thermal expansion behavior that was strongly dependent on the organic linker. For the mechanical properties of HKUST-1, it was found that the metal centers hardly have any influence. These two examples illustrate the wealth of information that can be obtained by increasing the search space.

In this work, some issues were detected that need to be addressed before a high-throughput search can be undertaken on the mechanical and/or thermal properties of MOFs. The cluster-based approach can be considered well-established and the newly derived force fields were found to be accurate. However, while QuickFF succeeds in accurately parametrizing the covalent interactions, the large sensitivity of the force field on the van der Waals parameters in the case of flexible frameworks is an important problem, which strongly limits the predictive power. New models for the

van der Waals interactions, and nonbonded interactions in general, are therefore highly desirable. Two other issues that must be tackled, are the deviation of the elastic constants from ab initio results and the systematic overestimation of the thermal expansion. To this end, a more in-depth investigation of these differences is required.

The final step in a high-throughput screening is the analysis of the data. In this case, a compromise between different properties often has to be made. One possible approach is to select the best performing materials with a Pareto analysis and introduce a further ranking of the Pareto elements with a scheme that was recently proposed by Lejaeghere *et al.* [9]. Although the size of the considered test set did not allow us to perform such a study yet, the methods and force fields developed in this work demonstrate that such a procedure is not only feasible, but yields unexpected insights at a computationally acceptable cost. Using the methodology outlined in this thesis, both for constructing force fields as well as for computing several properties, one now has the tools at hand to perform an extended screening of a large number of existing and hypothetical MOFs. A simple extension of this thesis to a large set of MOFs may therefore open up entire new classes of materials with a large range of fascinating properties.

# Bibliography


[1] F. Salles, A. Ghoufi, G. Maurin, R. G. Bell, C. Mellot-Draznieks, and G. Férey, "Molecular Dynamics Simulations of Breathing MOFs: Structural Transitions of MIL-53(Cr) upon Thermal Activation and $CO_2$ Adsorption," *Angew. Chem. Int. Ed.*, vol. 47, no. 44, pp. 8487–8491, 2008.

[2] S. Curtarolo, G. L. W. Hart, M. B. Nardelli, N. Mingo, S. Sanvito, and O. Levy, "The High-Throughput Highway to Computational Materials Design," *Nat. Mater.*, vol. 12, no. 3, pp. 191–201, 2013.

[3] V. Pareto, *Manuale di Economia Politica*. Societa Editrice Libraria, 1906.

[4] T. Bligaard, G. H. Jóhannesson, A. V. Ruban, H. L. Skriver, K. W. Jacobsen, and J. K. Nørskov, "Pareto-Optimal Alloys," *Appl. Phys. Lett.*, vol. 83, no. 22, pp. 4527–4529, 2003.

[5] M. P. Andersson, T. Bligaard, A. Kustov, K. E. Larsen, J. Greeley, T. Johannessen, C. H. Christensen, and J. K. J. K. Nørskov, "Toward Computational Screening in Heterogeneous Catalysis: Pareto-Optimal Methanation Catalysts," *J. Catal.*, vol. 239, no. 2, pp. 501–506, 2006.

[6] C. O'Mahony and N. Wilson, "Sorted Pareto Dominance: An Extension to Pareto Dominance and Its Application in Soft Constraints," *IEEE ICTAI*, vol. 1, pp. 798–805, 2012.

[7] O. Aguirre and H. Taboada, "A Clustering Method Based on Dynamic Self Organizing Trees for Post-Pareto Optimality Analysis," *Procedia Comput. Sci.*, vol. 6, pp. 195–200, 2011.

[8] I. Das, "A Preference Ordering among Various Pareto Optimal Alternatives," *Struct. Optim.*, vol. 18, no. 1, pp. 30–35, 1999.

[9] K. Lejaeghere, S. Cottenier, and V. V. Speybroeck, "Ranking the Stars: A Refined Pareto Approach to Computational Materials Design," *Phys. Rev. Lett.*, vol. 111, no. 7, p. 075501, 2013.

[10] H. Li, M. Eddaoudi, M. O'Keeffe, and O. M. Yaghi, "Design and Synthesis of an Exceptionally Stable and Highly Porous Metal-Organic Framework," *Nature*, vol. 402, no. 6759, pp. 276–279, 1999.

[11] M. Eddaoudi, J. Kim, N. Rosi, D. Vodak, J. Wachter, M. O'Keeffe, and O. M. Yaghi, "Systematic Design of Pore Size and Functionality in Isoreticular MOFs and Their Application in Methane Storage," *Science*, vol. 295, no. 5554, pp. 469–472, 2002.

[12] C. Serre, F. Millange, C. Thouvenot, M. Noguès, G. Marsolier, D. Louër, and G. Férey, "Very Large Breathing Effect in the First Nanoporous Chromium(III)-Based Solids: MIL-53 or CrIII(OH) $\cdot$ {$O_2$C-$C_6H_4$-$CO_2$} $\cdot$ {$HO_2$C-$C_6H_4$-$CO_2$H}x $\cdot$ $H_2$Oy," *J. Am. Chem. Soc.*, vol. 124, no. 45, pp. 13519–13526, 2002.

[13] K. S. Park, Z. Ni, A. P. Côté, J. Y. Choi, R. Huang, F. J. Uribe-Romo, H. K. Chae, M. O'Keeffe, and O. M. Yaghi, "Exceptional Chemical and Thermal Stability of Zeolitic Imidazolate Frameworks," *Proc. Natl. Acad. Sci.*, vol. 103, no. 27, pp. 10186–10191, 2006.

[14] L. Vanduyfhuys, T. Verstraelen, M. Vandichel, M. Waroquier, and V. Van Speybroeck, "Ab Initio Parametrized Force Field for the Flexible Metal-Organic Framework MIL-53(Al)," *J. Chem. Theory Comput.*, vol. 8, no. 9, pp. 3217–3231, 2012.

[15] R. E. Morris and P. S. Wheatley, "Gas Storage in Nanoporous Materials," *Angew. Chem. Int. Ed.*, vol. 47, no. 27, pp. 4966–4981, 2008.

[16] S.-L. Li and Q. Xu, "Metal-Organic Frameworks as Platforms for Clean Energy," *Energ. Environ. Sci.*, vol. 6, no. 6, pp. 1656–1683, 2013.

[17] C. Rösler and R. A. Fischer, "Metal-Organic Frameworks as Hosts for Nanoparticles," *CrystEngComm*, vol. 17, no. 2, pp. 199–217, 2014.

[18] L. E. Kreno, K. Leong, O. K. Farha, M. Allendorf, R. P. V. Duyne, and J. T. Hupp, "Metal-Organic Framework Materials as Chemical Sensors," *Chem. Rev.*, vol. 112, no. 2, pp. 1105–1125, 2012.

[19] J. Lee, O. K. Farha, J. Roberts, K. A. Scheidt, S. T. Nguyen, and J. T. Hupp, "Metal-Organic Framework Materials as Catalysts," *Chem. Soc. Rev.*, vol. 38, no. 5, p. 1450, 2009.

[20] P. Horcajada, R. Gref, T. Baati, P. K. Allan, G. Maurin, P. Couvreur, G. Férey, R. E. Morris, and C. Serre, "Metal-Organic Frameworks in Biomedicine," *Chem. Rev.*, vol. 112, no. 2, pp. 1232–1268, 2012.

[21] S. T. Meek, J. A. Greathouse, and M. D. Allendorf, "Metal-Organic Frameworks: A Rapidly Growing Class of Versatile Nanoporous Materials," *Adv. Mater.*, vol. 23, no. 2, pp. 249–267, 2011.

[22] M. Kurmoo, "Magnetic Metal-Organic Frameworks," *Chem. Soc. Rev.*, vol. 38, no. 5, p. 1353, 2009.

[23] C. G. Silva, A. Corma, and H. García, "Metal-Organic Frameworks as Semiconductors," *J. Mater. Chem.*, vol. 20, no. 16, pp. 3141–3156, 2010.

[24] S. Horike, S. Shimomura, and S. Kitagawa, "Soft Porous Crystals," *Nat. Chem.*, vol. 1, no. 9, pp. 695–704, 2009.

[25] A. Schneemann, V. Bon, I. Schwedler, I. Senkovska, S. Kaskel, and R. A. Fischer, "Flexible Metal-Organic Frameworks," *Chem. Soc. Rev.*, vol. 43, no. 16, pp. 6062–6096, 2014.

[26] C. R. Murdock, B. C. Hughes, Z. Lu, and D. M. Jenkins, "Approaches for Synthesizing Breathing MOFs by Exploiting Dimensional Rigidity," *Coord. Chem. Rev.*, vol. 258-259, pp. 119–136, 2014.

[27] Y. J. Colón and R. Q. Snurr, "High-Throughput Computational Screening of Metal-Organic Frameworks," *Chem. Soc. Rev.*, vol. 43, no. 16, pp. 5735–5749, 2014.

[28] H. Furukawa, K. E. Cordova, M. O'Keeffe, and O. M. Yaghi, "The chemistry and applications of metal-organic frameworks," *Science*, vol. 341, no. 6149, p. 1230444, 2013.

[29] M. O'Keeffe, M. A. Peskov, S. J. Ramsden, and O. M. Yaghi, "The Reticular Chemistry Structure Resource (RCSR) Database Of, and Symbols For, Crystal Nets," *Accts. Chem. Res.*, vol. 41, no. 12, pp. 1782–1789, 2008.

[30] F. H. Allen, "The Cambridge Structural Database: A Quarter of a Million Crystal Structures and Rising," *Acta Crystallogr., Sect. B: Struct. Sci.*, vol. 58, pp. 380–388, 2002.

[31] Y. G. Chung, J. Camp, M. Haranczyk, B. J. Sikora, W. Bury, V. Krungleviciute, T. Yildirim, O. K. Farha, D. S. Sholl, and R. Q. Snurr, "Computation-Ready, Experimental Metal-Organic Frameworks: A Tool To Enable High-Throughput Screening of Nanoporous Crystals," *Chem. Mat.*, vol. 26, no. 21, pp. 6185–6192, 2014.

[32] C. E. Wilmer, M. Leaf, C. Y. Lee, O. K. Farha, B. G. Hauser, J. T. Hupp, and R. Q. Snurr, "Large-Scale Screening of Hypothetical Metal-Organic Frameworks," *Nat. Chem.*, vol. 4, no. 2, pp. 83–89, 2012.

[33] T. Watanabe and D. S. Sholl, "Accelerating Applications of Metal-Organic Frameworks for Gas Adsorption and Separation by Computational Screening of Materials," *Langmuir*, vol. 28, no. 40, pp. 14114–14128, 2012.

[34] M. Fernandez, P. G. Boyd, T. D. Daff, M. Z. Aghaji, and T. K. Woo, "Rapid and Accurate Machine Learning Recognition of High Performing Metal Organic Frameworks for CO2 Capture," *J. Phys. Chem. Lett.*, vol. 5, no. 17, pp. 3056–3060, 2014.

[35] C. E. Wilmer, O. K. Farha, Y.-S. Bae, J. T. Hupp, and R. Q. Snurr, "Structure-property relationships of porous materials for carbon dioxide separation and capture," *Energ. Environ. Sci.*, vol. 5, no. 12, pp. 9849–9856, 2012.

[36] M. Fernandez, T. K. Woo, C. E. Wilmer, and R. Q. Snurr, "Large-Scale Quantitative Structure-Property Relationship (QSPR) Analysis of Methane Storage in Metal-Organic Frameworks," *J. Phys. Chem. C*, vol. 117, no. 15, pp. 7681–7689, 2013.

[37] D. A. Gomez, J. Toda, and G. Sastre, "Screening of Hypothetical Metal-Organic Frameworks for H2 Storage," *Phys. Chem. Chem. Phys.*, vol. 16, no. 35, pp. 19001–19010, 2014.

[38] Y. J. Colón, D. Fairen-Jimenez, C. E. Wilmer, and R. Q. Snurr, "High-Throughput Screening of Porous Crystalline Materials for Hydrogen Storage Capacity Room Temperature," *J. Phys. Chem. C*, vol. 118, no. 10, pp. 5383–5389, 2014.

[39] D. A. Gómez-Gualdrón, C. E. Wilmer, O. K. Farha, J. T. Hupp, and R. Q. Snurr, "Exploring the Limits of Methane Storage and Delivery in Nanoporous Materials," *J. Phys. Chem. C*, vol. 118, no. 13, pp. 6941–6951, 2014.

[40] B. J. Sikora, R. Winnegar, D. M. Proserpio, and R. Q. Snurr, "Textural Properties of a Large Collection of Computationally Constructed MOFs and Zeolites," *Microporous and Mesoporous Materials*, vol. 186, pp. 207–213, 2014.

[41] B. J. Sikora, C. E. Wilmer, M. L. Greenfield, and R. Q. Snurr, "Thermodynamic Analysis of Xe/Kr Selectivity in over 137000 Hypothetical Metalâorganic Frameworks," *Chem. Sci.*, vol. 3, no. 7, pp. 2217–2223, 2012.

[42] A. U. Ortiz, A. Boutin, A. H. Fuchs, and F.-X. Coudert, "Anisotropic Elastic Properties of Flexible Metal-Organic Frameworks: How Soft Are Soft Porous Crystals?," *Phys. Rev. Lett.*, vol. 109, no. 19, p. 195502, 2012.

[43] A. I. Skoulidas and D. S. Sholl, "Self-Diffusion and Transport Diffusion of Light Gases in Metal-Organic Framework Materials Assessed Using Molecular Dynamics simulations," *J. Phys. Chem. B*, vol. 109, no. 33, pp. 15760–15768, 2005.

[44] Q. Yang, C. Zhong, and J.-F. Chen, "Computational Study of $CO_2$ Storage in Metal-Organic Frameworks," *J. Phys. Chem. C*, vol. 112, no. 5, pp. 1562–1569, 2008.

[45] Q. Yang, D. Liu, C. Zhong, and J.-R. Li, "Development of Computational Methodologies for Metal-Organic Frameworks and Their Application in Gas Separations," *Chem. Soc. Rev.*, vol. 113, no. 10, pp. 8261–8323, 2013.

[46] S. Amirjalayer, M. Tafipolsky, and R. Schmid, "Molecular Dynamics Simulation of Benzene Diffusion in MOF-5: Importance of Lattice Dynamics," *Angew. Chem. Int. Ed.*, vol. 46, no. 3, pp. 463–466, 2007.

[47] Y. Sun and H. Sun, "An All-Atom Force Field Developed for $Zn_4O(RCO_2)_6$ Metal-Organic Frameworks," *J. Mol. Model.*, vol. 20, no. 3, p. 2146, 2014.

[48] A. K. Rappé, C. J. Casewit, K. S. Colwell, W. A. Goddard III, and W. M. Skiff, "UFF, a Full Periodic Table Force Field for Molecular Mechanics and Molecular Dynamics Simulations," *J. Am. Chem. Soc.*, vol. 114, no. 25, pp. 10024–10035, 1992.

[49] S. L. Mayo, B. D. Olafson, and W. A. Goddard III, "DREIDING: A Generic Force Field for Molecular Simulations," *J. Phys. Chem.*, vol. 94, no. 26, pp. 8897–8909, 1990.

[50] N. L. Allinger, Y. H. Yuh, and J. H. Lii, "Molecular Mechanics. The MM3 Force Field for Hydrocarbons. 1.," *J. Am. Chem. Soc.*, vol. 111, no. 23, pp. 8551–8566, 1989.

[51] W. D. Cornell, P. Cieplak, C. I. Bayly, I. R. Gould, K. M. Merz, D. M. Ferguson, D. C. Spellmeyer, T. Fox, J. W. Caldwell, and P. A. Kollman, "A Second Generation Force Field for the Simulation of Proteins, Nucleic Acids, and Organic Molecules," *J. Am. Chem. Soc.*, vol. 117, no. 19, pp. 5179–5197, 1995.

[52] P. Dauber-Osguthorpe, V. A. Roberts, D. J. Osguthorpe, J. Wolff, M. Genest, and A. T. Hagler, "Structure and Energetics of Ligand Binding to Proteins: Escherichia Coli Dihydrofolate Reductase-Trimethoprim, a Drug-Receptor System," *Proteins: Struct., Funct., Bioinf.*, vol. 4, no. 1, pp. 31–47, 1988.

[53] J. M. Wang, R. M. Wolf, J. W. Caldwell, P. A. Kollman, and D. A. Case, "Development and Testing of a General Amber Force Field," *J. Comput. Chem.*, vol. 25, no. 9, pp. 1157–1174, 2004.

[54] J. A. Greathouse and M. D. Allendorf, "Force Field Validation for Molecular Dynamics Simulations of IRMOF-1 and Other Isoreticular Zinc Carboxylate Coordination Polymers," *J. Phys. Chem. C*, vol. 112, no. 15, pp. 5795–5802, 2008.

[55] D. Dubbeldam, K. S. Walton, D. E. Ellis, and R. Q. Snurr, "Exceptional Negative Thermal Expansion in Isoreticular Metal-Organic Frameworks," *Angew. Chem. Int. Ed.*, vol. 46, no. 24, pp. 4496–4499, 2007.

[56] M. Tafipolsky, S. Amirjalayer, and R. Schmid, "Ab Initio Parameterized MM3 Force Field for the Metal-Organic Framework MOF-5," *J. Comput. Chem.*, vol. 28, no. 7, pp. 1169–1176, 2007.

[57] Z. Hu, L. Zhang, and J. Jiang, "Development of a Force Field for Zeolitic Imidazolate Framework-8 with Structural Flexibility," *J. Chem. Phys.*, vol. 136, no. 24, p. 244703, 2012.

[58] M. A. Addicoat, N. Vankova, I. F. F. Akter, and T. Heine, "Extension of the Universal Force Field to Metal-Organic Frameworks," *J. Chem. Theory Comput.*, vol. 10, no. 2, pp. 880–891, 2013.

[59] J. K. Bristow, D. Tiana, and A. Walsh, "Transferable Forcefield for Metal-Organic Frameworks from First-Principles: BTW-FF," *J. Chem. Theory Comput.*, vol. 10, no. 10, pp. 4644–4652, 2014.

[60] R. F. W. Bader, "Atoms in Molecules," *Acc. Chem. Res.*, vol. 18, no. 1, pp. 9–15, 1985.

[61] M. Tafipolsky and R. Schmid, "Systematic First Principles Parametrization of Force Fields for Metal-Organic Frameworks Using a Genetic Algorithm Approach," *J. Phys. Chem. B*, vol. 113, no. 5, pp. 1341–1352, 2009.

[62] B. H. Besler, K. M. Merz, and P. A. Kollman, "Atomic Charges Derived from Semi-Empirical Methods," *J. Comput. Chem.*, vol. 11, no. 4, pp. 431–439, 1990.

[63] M. Tafipolsky, S. Amirjalayer, and R. Schmid, "First-Principles-Derived Force Field for Copper Paddle-Wheel-Based Metal-Organic Frameworks," *J. Phys. Chem. C*, vol. 114, no. 34, pp. 14402–14409, 2010.

[64] S. Bureekaew, S. Amirjalayer, M. Tafipolsky, C. Spickermann, T. K. Roy, and R. Schmid, "MOF-FF - A Flexible First-Principles Derived Force Field for Metal-Organic Frameworks," *Phys. Status Solidi B*, vol. 250, no. 6, pp. 1128–1141, 2013.

[65] S. Amirjalayer and R. Schmid, "Adsorption of Hydrocarbons in Metal-Organic Frameworks: A Force Field Benchmark on the Example of Benzene in Metal-Organic Framework 5," *J. Phys. Chem. C*, vol. 116, no. 29, pp. 15369–15377, 2012.

[66] S. Grimme, "A General Quantum Mechanically Derived Force Field (QMDFF) for Molecules and Condensed Phase Simulations," *J. Chem. Theory Comput.*, vol. 10, no. 10, pp. 4497–4514, 2014.

[67] L. Vanduyfhuys, S. Vandenbrande, T. Verstraelen, R. Schmid, M. Waroquier, and V. Van Speybroeck, "QuickFF: A Program for a Quick and Easy Derivation of Force Fields for Metal-Organic Frameworks from Ab Initio Input," *J. Comput. Chem.*, vol. 36, no. 13, pp. 1015–1027, 2015.

[68] J. S. Grosch and F. Paesani, "Molecular-Level Characterization of the Breathing Behavior of the Jungle-Gym-Type DMOF-1 Metal-Organic Framework," *J. Am. Chem. Soc.*, vol. 134, no. 9, pp. 4207–4215, 2012.

[69] H. Wang, L. Zhao, W. Xu, S. Wang, Q. Ding, X. Lu, and W. Guo, "The Properties of the Bonding Between CO and ZIF-8 Structures: a Density Functional Theory Study," *Theor. Chem. Acc.*, vol. 134, no. 3, pp. 1–9, 2015.

[70] S. K. Burger, P. W. Ayers, and J. Schofield, "Efficient Parameterization of Torsional Terms for Force Fields," *J. Comput. Chem.*, vol. 35, no. 19, pp. 1438–1445, 2014.

[71] S. Hamad, S. R. G. Balestra, R. Bueno-Perez, S. Calero, and A. R. Ruiz-Salvador, "Atomic Charges for Modeling Metal-Organic Frameworks: Why and How," *J. Solid State Chemistry*, vol. 233, pp. 144–151, 2015.

[72] H. Hu, Z. Lu, and W. Yang, "Fitting Molecular Electrostatic Potentials from Quantum Mechanical Calculations," *J. Chem. Theory Comput.*, vol. 3, no. 3, pp. 1004–1013, 2007.

[73] P. Bultinck, C. V. Alsenoy, P. W. Ayers, and R. Carbo-Dorca, "Critical Analysis and Extension of the Hirshfeld Atoms in Molecules," *J. Chem. Phys.*, vol. 126, no. 14, p. 144111, 2007.

[74] F. L. Hirshfeld, "Bonded-Atom Fragments for Describing Molecular Charge Densities," *Theor. Chem. Acc.*, vol. 44, no. 2, pp. 129–138, 1977.

[75] T. Verstraelen, S. V. Sukhomlinov, V. Van Speybroeck, M. Waroquier, and K. S. Smirnov, "Computation of Charge Distribution and Electrostatic Potential in Silicates with the Use of Chemical Potential Equalization Models," *J. Phys. Chem. C*, vol. 116, no. 1, pp. 490–504, 2012.

[76] T. Verstraelen, P. W. Ayers, V. Van Speybroeck, and M. Waroquier, "Hirshfeld-E Partitioning: AIM Charges with an Improved Trade-off between Robustness and Accurate Electrostatics," *J. Chem. Theory Comput.*, vol. 9, no. 5, pp. 2221–2225, 2013.

[77] J. Chen and T. J. Martinéz, "The dissociation catastrophe in fluctuating-charge models and its implications for the concept of atomic electronegativity," in *Advances in the Theory of Atomic and Molecular Systems* (P. Piecuch, J. Maruani, G. Delgado-Barrio, and S. Wilson, eds.), vol. 19 of *Progress in Theoretical Chemistry and Physics*, pp. 397–415, Springer Netherlands, 2009.

[78] T. A. Halgren, "Merck Molecular Force Field. II. MMF94 van der Waals and Electrostatic Parameters for Intermolecular Interactions," *J. Comput. Chem.*, vol. 17, no. 5-6, pp. 520–552, 1996.

[79] A. M. Walker, B. Civalleri, B. Slater, C. Mellot-Draznieks, F. Corà, C. M. Zicovich-Wilson, G. Román-Pérez, J. M. Soler, and J. D. Gale, "Flexibility in a Metal-Organic Framework Material Controlled by Weak Dispersion Forces: The Bistability of MIL-53(Al)," *Angew. Chem. Int. Ed.*, vol. 49, no. 41, pp. 7501–7503, 2010.

[80] N. L. Allinger, X. Zhou, and J. Bergsma, "Molecular Mechanics Parameters," *THEOCHEM*, vol. 312, no. 1, pp. 69–83, 1994.

[81] S. Grimme, "Semi-Empirical GGA-Type Density Functional Constructed with a Long-Range Dispersion Correction," *J. Comput. Chem.*, vol. 27, no. 15, pp. 1787–1799, 2006.

[82] S. Grimme, J. Antony, S. Ehrlich, and H. Krieg, "A Consistent and Accurate Ab Initio Parametrization of Density Functional Dispersion Correction (DFT-D) for the 94 Elements H-Pu," *J. Chem. Phys.*, vol. 132, no. 15, p. 154104, 2010.

[83] M. J. Frisch, G. W. Trucks, H. B. Schlegel, G. E. Scuseria, M. A. Robb, J. R. Cheeseman, G. Scalmani, V. Barone, B. Mennucci, G. A. Petersson, H. Nakatsuji, M. Caricato, X. Li, H. P. Hratchian, A. F. Izmaylov, J. Bloino, G. Zheng, J. L. Sonnenberg, M. Hada, M. Ehara, K. Toyota, R. Fukuda, J. Hasegawa, M. Ishida, T. Nakajima, Y. Honda, O. Kitao, H. Nakai, T. Vreven, J. A. M. Jr., J. E. Peralta, F. Ogliaro, M. Bearpark, J. J. Heyd, E. Brothers, K. N. Kudin, V. N. Staroverov, R. Kobayashi, J. Normand, K. Raghavachari, A. Rendell, J. C. Burant, S. S. Iyengar, J. Tomasi, M. Cossi, N. Rega, J. M. Millam, M. Klene, J. E. Knox, J. B. Cross, V. Bakken, C. Adamo, J. Jaramillo, R. Gomperts, R. E. Stratmann, O. Yazyev, A. J. Austin, R. Cammi, C. Pomelli, J. W. Ochterski, R. L. Martin, K. Morokuma, V. G. Zakrzewski, G. A. Voth, P. Salvador, J. J. Dannenberg, S. Dapprich, A. D. Daniels, Ö. Farkas, J. B. Foresman, J. V. Ortiz, J. Cioslowski, and D. J. Fox, "Gaussian 09, Revision D.01," *Gaussian, Inc.*, 2009.

[84] T. Verstraelen, V. Van Speybroeck, and M. Waroquier, "ZEOBUILDER: A GUI Toolkit for the Construction of Complex Molecular Structures on the Nanoscale with Building Blocks," *J. Chem. Inf. Model.*, vol. 48, no. 7, pp. 1530–1541, 2008.

[85] A. Becke, "Density-Functional Thermochemistry .3. the Role of Exact Exchange," *J. Chem. Phys.*, vol. 98, no. 7, pp. 5648–5652, 1993.

[86] M. J. Frisch, M. J. Pople, and J. S. Binkley, "Self-Consistent Molecular-Orbital Methods .25. Supplementary Functions for Gaussian-Basis Sets," *J. Chem. Phys.*, vol. 80, no. 7, pp. 3265–3269, 1984.

[87] F. Furche and J. P. Perdew, "The Performance of Semilocal and Hybrid Density Functionals in 3d Transition-Metal Chemistry," *J. Chem. Phys.*, vol. 124, no. 4, p. 044103, 2006.

[88] T. Verstraelen, S. Vandenbrande, M. Chan, F. H. Zadeh, C. González, and P. A. Limacher. *Horton 1.2.1*, http://theochem.github.com/horton/.

[89] T. Verstraelen, L. Vanduyfhuys, S. Vandenbrande, and S. M. J. Rogge. *Yaff, yet another force field*, http://molmod.ugent.be/software/.

[90] B. Civalleri, F. Napoli, Y. Noël, C. Roetti, and R. Dovesi, "Ab-initio Prediction of Materials Properties with CRYSTAL: MOF-5 as a Case Study," *CrystEngComm*, vol. 8, no. 5, pp. 364–371, 2006.

[91] D. F. Bahr, J. A. Reid, W. M. Mook, C. A. Bauer, R. Stumpf, A. J. Skulan, N. R. Moody, B. A. Simmons, M. M. Shindel, and M. D. Allendorf, "Mechanical Properties of Cubic Zinc Carboxylate IRMOF-1 Metal-Organic Framework Crystals," *Phys. Rev. B*, vol. 76, no. 18, p. 184106, 2007.

[92] P. G. Yot, Q. Ma, J. Haines, Q. Yang, A. Ghoufi, T. Devic, C. Serre, V. Dimitriev, G. Férey, C. Zhong, and G. Maurin, "Large Breathing of the MOF MIL-47(V(IV)) under Mechanical

Pressure: A Joint Experimental-Modelling Exploration," *Chem. Sci.*, vol. 3, no. 2, pp. 1100–1104, 2012.

[93] Y. Liu, J.-H. Her, A. Dailly, A. J. Ramirez-Cuesta, D. A. Neumann, and C. M. Brown, "Reversible Structural Transition in MIL-53 with Large Temperature Hysteresis," *J. Am. Chem. Soc.*, vol. 130, no. 35, pp. 11813–11818, 2008.

[94] J. P. S. Mowat, S. R. Miller, A. M. Z. Slawin, V. R. Seymour, S. E. Ashbrook, and P. A. Wright, "Synthesis, Characterisation and Adsorption Properties of Microporous Scandium Carboxylates with Rigid and Flexible Frameworks," *Microporous Mesoporous Mater.*, vol. 142, no. 1, pp. 322–333, 2011.

[95] C. Volkringer, T. Loiseau, N. Guillou, G. Férey, E. Elkaïm, and A. Vimont, "XRD and IR Structural Investigations of a Particular Breathing Effect in the MOF-Type Gallium Terephtalate MIL-53(Ga)," *Dalton Trans.*, no. 12, pp. 2241–2249, 2009.

[96] P. Serra-Crespo, E. Stavitski, F. Kapteijn, and J. Gascon, "High Compressibility of a Flexible Metal-Organic Framework," *R. Soc. Chem. Adv.*, vol. 2, no. 12, pp. 5051–5053, 2012.

[97] F. Millange, N. Guillou, R. I. Walton, J.-M. Greneche, I. Margiolaki, and G. Férey, "Effect of the Nature of the Metal on the Breathing Steps in MOFs with Dynamic Frameworks," *Chem. Commun.*, no. 39, pp. 4732–4734, 2008.

[98] P. J. Hay and W. R. Wadt, "Abinitio Effective Core Potentials for Molecular Calculations - Potentials for the Transition-Metal Atoms Sc to Hg," *J. Chem. Phys.*, vol. 82, no. 1, pp. 270–283, 1985.

[99] I. Beurroies, M. Boulhout, P. L. Llewellyn, B. Kuchta, G. Férey, C. Serre, and R. Denoyel, "Using Pressure to Provoke the Structural Transition of Metal-Organic Frameworks," *Angew. Chem. Int. Ed.*, vol. 49, no. 41, pp. 7526–7529, 2010.

[100] A. V. Neimark, F.-X. Coudert, C. Triguero, A. Boutin, A. H. Fuchs, I. Beurroies, and R. Denoyel, "Structural Transitions in MIL-53(Cr): View from Outside and Inside," *Langmuir*, vol. 27, no. 8, pp. 4734–4741, 2011.

[101] J. P. S. Mowat, V. R. Seymour, J. M. Griffin, S. P. Thompson, A. M. Z. Slawin, D. Fairen-Jimenez, T. Düren, S. E. Ashbrook, and P. A. Wright, "A Novel Structural Form of MIL-53 Observed for the Scandium Analogue and Its Response to Temperature Variation and CO2 Adsorption," *Dalton Trans.*, vol. 41, no. 14, pp. 3938–3941, 2012.

[102] H. Leclerc, T. Devic, S. Devautour-Vinot, P. Bazin, N. Audebrand, G. Férey, M. Daturi, A. Vimont, and G. Clet, "Influence of the Oxidation State of the Metal Center on the Flexibility and Adsorption Properties of a Porous Metal Organic Framework," *J. Phys. Chem. C*, vol. 115, no. 40, pp. 19828–19840, 2011.

[103] A. Boutin, D. Bousquet, A. U. Ortiz, F.-X. Coudert, A. H. Fuchs, A. Ballandras, G. Weber, I. Bezverkhyy, J.-P. Bellat, G. Ortiz, G. Chaplais, J.-L. Paillaud, C. Marichal, H. Nouali, and J. Patarin, "Temperature-Induced Structural Transitions in the Gallium-Based MIL-53 Metal-Organic Framework," *J. Phys. Chem. C*, vol. 117, no. 16, pp. 8180–8188, 2013.

[104] T. Loiseau, C. Serre, C. Huguenard, G. Fink, F. Taulelle, M. Henry, T. Bataille, and G. Férey, "A Rationale for the Large Breathing of the Porous Aluminum Terephthalate (MIL-53) Upon Hydration," *Chem. Eur. J.*, vol. 10, no. 6, pp. 1373–1382, 2004.

[105] A. U. Ortiz, *Étude par simulation moléculaire de la flexibilité des matériaux nanoporeux: propriétés structurales, mécaniques et thermodynamiques.* PhD thesis, Université Pierre et Marie Curie - Paris VI, 2014.

[106] X. Wang, J. Eckert, L. Liu, and A. J. Jacobson, "Breathing and Twisting: An Investigation of Framework Deformation and Guest Packing in Single Crystals of a Microporous Vanadium Benzenedicarboxylate," *Inorg. Chem.*, vol. 50, no. 5, pp. 2028–2036, 2011.

[107] R. S. Mulliken, "Electronic Population Analysis on LCAO-MO Molecular Wave Functions. I," *J. Chem. Phys.*, vol. 23, no. 10, pp. 1833–1840, 1955.

[108] D. E. P. Vanpoucke, J. W. Jaeken, S. De Baerdemacker, K. Lejaeghere, and V. Van Speybroeck, "Quasi-1D Physics in Metal-Organic Frameworks: MIL-47(V) from First Principles," *Beilstein J. Nanotechnol.*, no. 5, pp. 1738–1748, 2014.

[109] S. Biswas, D. E. P. Vanpoucke, T. Verstraelen, M. Vandichel, S. Couck, K. Leus, Y.-Y. Liu, M. Waroquier, V. Van Speybroeck, J. F. M. Denayer, and P. V. D. Voort, "New Functionalized Metal-Organic Frameworks MIL-47-X (X = -Cl, -Br, -$CH_3$, -$CF_3$, -OH, -$OCH_3$): Synthesis, Characterization, and $CO_2$ Adsorption Properties," *J. Phys. Chem. C*, vol. 117, no. 44, pp. 22784–22796, 2013.

[110] K. Barthelet, J. Marrot, D. Riou, and G. Férey, "A Breathing Hybrid Organic-Inorganic Solid with Very Large Pores and High Magnetic Characteristics," *Angew. Chem. Int. Ed.*, vol. 41, no. 2, pp. 281–284, 2002.

[111] S. S. Y. Chui, S. M. F. Lo, J. P. H. Charmant, A. G. Orpen, and I. D. Williams, "A Chemically Functionalizable Nanoporous Material $[Cu_3(TMA)_2(H_2O)_3]_n$," *Science*, vol. 283, no. 5405, pp. 1148–1150, 1999.

[112] J. I. Feldblyum, M. Liu, D. W. Gidley, and A. J. Matzger, "Reconciling the Discrepancies between Crystallographic Porosity and Guest Access As Exemplified by Zn-HKUST-1," *J. Am. Chem. Soc.*, vol. 133, no. 45, pp. 18257–18263, 2011.

[113] P. Maniam and N. Stock, "Investigation of Porous Ni-Based Metal-Organic Frameworks Containing Paddle-Wheel Type Inorganic Building Units via High-Throughput Methods," *Inorg. Chem.*, vol. 50, no. 11, pp. 5085–5097, 2011.

[114] P. Ryan, I. Konstantinov, R. Q. Snurr, and L. J. Broadbelt, "DFT Investigation of Hydroperoxide Decomposition over Copper and Cobalt Sites within Metal-Organic Frameworks," *J. Catal.*, vol. 286, pp. 95–102, 2012.

[115] B. Lukose, B. Supronowicz, P. S. Petkov, J. Frenzel, A. B. Kuc, G. Seifert, G. N. Vayssilov, and T. Heine, "Structural properties of Metal-Organic Frameworks within the Density-Functional Based Tight-Binding Method," *Phys. Status Solidi B*, vol. 249, no. 2, pp. 335–342, 2012.

[116] V. K. Peterson, Y. Liu, C. M. Brown, and C. J. Kepert, "Neutron Powder Diffraction Study of $D_2$ Sorption in $Cu_3$(1,3,5-benzenetricarboxylate)$_2$," *J. Am. Chem. Soc.*, vol. 128, no. 49, pp. 15578–15579, 2006.

[117] S. Amirjalayer, M. Tafipolsky, and R. Schmid, "Exploring Network Topologies of Copper Paddle Wheel Based Metal-Organic Frameworks with a First-Principles Derived Force Field," *J. Phys. Chem. C*, vol. 115, no. 31, pp. 15133–15139, 2011.

[118] D. N. Dybtsev, H. Chun, and K. Kim, "Rigid and Flexible: A Highly Porous Metal-Organic Framework with Unusual Guest-Dependent Dynamic Behavior," *Angew. Chem. Int. Ed.*, vol. 43, no. 38, pp. 5033–5036, 2004.

[119] J.-C. Tan, B. Civalleri, C.-C. Lin, L. Valenzano, R. Galvelis, P.-F. Chen, T. D. Bennett, C. Mellot-Draznieks, C. M. Zicovich-Wilson, and A. K. Cheetham, "Exceptionally Low Shear Modulus in a Prototypical Imidazole-Based Metal-Organic Framework," *Phys. Rev. Lett.*, vol. 108, no. 9, p. 095502, 2012.

[120] L. Sarkisov and J. Kim, "Computational Structure Characterization Tools for the Era of Material Informatics," *Chem. Eng. Sci.*, vol. 121, pp. 322–330, 2015.

[121] R. L. Martin, B. Smit, and M. Haranczyk, "Addressing Challenges of Identifying Geometrically Diverse Sets of Crystalline Porous Materials," *J. Chem. Inf. Comput. Sci.*, vol. 52, no. 2, pp. 308–318, 2011.

[122] T. F. Willems, C. H. Rycroft, M. Kazi, J. C. Meza, and M. Haranczyk, "Algorithms and Tools for High-Throughput Geometry-Based Analysis of Crystalline Porous Materials," *Microporous Mesoporous Mater.*, vol. 149, pp. 134–141, 2012.

[123] M. Pinheiro, R. L. Martin, C. H. Rycroft, A. Jones, E. Iglesia, and M. Haranczyk, "Characterization and Comparison of Pore Landscapes in Crystalline Porous Materials," *J. Mol. Graphics Modell.*, vol. 44, pp. 208–219, 2013.

[124] J.-C. Tan, T. D. Bennett, and A. K. Cheetham, "Chemical Structure, Network Topology, and Porosity Effects on the Mechanical Properties on the Mechanical Properties of Zeolitic Imidazolate Frameworks," *Proc. Natl. Acad. Sci.*, vol. 107, no. 22, pp. 9938–9943, 2010.

[125] D. R. Gaskell, *Introduction to the thermodynamics of materials.* Tayler & Francis, 5th ed., 2008.

[126] P. Canepa, K. Tan, Y. Du, H. Lu, Y. J. Chabal, and T. Thonhauser, "Structural, Elastic, Thermal, and Electronic Response of Small-Molecule-Loaded Metal Organic Frameworks Materials," *J. Mater. Chem. A*, vol. 3, no. 3, pp. 986–995, 2015.

[127] A. Ghysels, T. Verstraelen, K. Hemelsoet, M. Waroquier, and V. Van Speybroeck, "TAMkin: A Versatile Package for Vibrational Analysis and Chemical Kinetics," *J. Chem. Inf. Model.*, vol. 50, no. 9, pp. 1736–1750, 2010.

[128] S. Nosé, "A molecular dynamics method for simulations in the canonical ensemble," *Mol. Phys.*, vol. 52, no. 2, pp. 255–268, 1984.

[129] W. G. Hoover, "Canonical Dynamics: Equilibrium Phase-Space Distributions," *Phys. Rev. A*, vol. 31, no. 3, pp. 1695–1697, 1985.

[130] G. J. Martyna, M. L. Klein, and M. Tuckerman, "Nose-Hoover Chains - the Canonical Ensemble Via Continuous Dynamics," *J. Chem. Phys*, vol. 97, no. 4, pp. 2635–2643, 1992.

[131] P. Langevin, "Sur la théorie du mouvement brownien," *C. R. Acad. Sci.*, vol. 146, pp. 530–533, 1908.

[132] G. J. Martyna, D. J. Tobias, and M. L. Klein, "Constant-Pressure Molecular-Dynamics Algorithms," *J. Chem. Phys.*, vol. 101, no. 5, pp. 4177–4189, 1994.

[133] H. J. C. Berendsen, J. P. M. Postma, W. F. van Gunsteren, A. DiNola, and J. R. Haak, "Molecular Dynamics with Coupling to an External Bath," *J. Chem. Phys.*, vol. 81, pp. 3684–3690, 1984.

[134] S. E. Feller, Y. H. Zhang, R. W. Pastor, and B. R. Brooks, "Constant-Pressure Molecular-Dynamics Simulation - the Langevin Piston Method," *J. Chem. Phys.*, vol. 103, no. 11, pp. 4613–4621, 1995.

[135] B. Mu and K. S. Walton, "Thermal Analysis and Heat Capacity of Metal-Organic Frameworks," *J. Phys. Chem. C.*, vol. 115, no. 46, pp. 22748–22754, 2011.

[136] J. Cao and G. A. Voth, "The Formulation of Quantum Statistical Mechanics Based on the Feynman Path Centroid Density. I. Equilibrium Properties," *J. Chem. Phys.*, vol. 100, no. 7, pp. 5093–5105, 1994.

[137] J. Cao and G. A. Voth, "The Formulation of Quantum Statistical Mechanics Based on the Feynman Path Centroid Density. II. Dynamical Properties," *J. Chem. Phys.*, vol. 100, no. 7, pp. 5106–5117, 1994.

[138] M. Ceriotti, D. E. Manolopoulos, and M. Parrinello, "Accelerating the convergence of path integral dynamics with a generalized Langevin equation," *J. Chem. Phys.*, vol. 134, p. 084104, 2011.

[139] M. Ceriotti, J. More, and D. E. Manolopoulos, "i-PI: A Python Interface for Ab Initio Path Integral Molecular Dynamics Simulations," *Comput. Phys. Commun.*, vol. 185, no. 3, pp. 1019–1026, 2014.

[140] G. D. Barrera, J. a. O. Bruno, T. H. K. Barron, and N. L. Allan, "Negative thermal expansion," *J. Phys.: Condens. Matter*, vol. 17, no. 4, pp. R217–R252, 2005.

[141] C. Lind, "Two Decades of Negative Thermal Expansion Research: Where Do We Stand?," *Materials*, vol. 5, pp. 1125–1154, 2012.

[142] S. S. Han and W. A. Goddard, "Metal-Organic Frameworks Provide Large Negative Thermal Expansion Behavior," *J. Phys. Chem. C*, vol. 111, no. 42, pp. 15185–15191, 2007.

[143] J. L. C. Rowsell, E. S. Spencer, J. Eckert, J. A. K. Howard, and O. M. Yaghi, "Gas Adsorption Sites in a Large-Pore Metal-Organic Framework," *Science*, vol. 309, no. 5739, pp. 1350–1354, 2005.

[144] W. Zhou, H. Wu, T. Yildirim, J. R. Simpson, and A. R. H. Walker, "Origin of the Exceptional Negative Thermal Expansion in Metal-Organic Framework-5 $Zn_4O$(1,4-benzenedicarboxylate)$_3$," *Phys. Rev. B*, vol. 78, no. 5, p. 054114, 2008.

[145] N. Lock, Y. Wu, M. Christensen, L. J. Cameron, V. K. Peterson, A. J. Bridgeman, C. J. Kepert, and B. B. Iversen, "Elucidating Negative Thermal Expansion in MOF-5," *J. Phys. Chem. C*, vol. 114, no. 39, pp. 16181–16186, 2010.

[146] L. H. N. Rimmer, M. T. Dove, A. L. Goodwin, and D. C. Palmer, "Acoustic Phonons and Negative Thermal Expansion in MOF-5," *Phys. Chem. Chem. Phys.*, vol. 16, pp. 21144–21152, 2014.

[147] S. Henke, A. Schneemann, and R. A. Fischer, "Massive Anisotropic Thermal Expansion and Thermo-Responsive Breathing in Metal-Organic Frameworks Modulated by Linker Functionalization," *Adv. Funct. Mater.*, vol. 23, pp. 5990–5996, 2013.

[148] P. Lama, R. K. Das, V. J. Smith, and L. J. Barbour, "A Combined Stretching-Tilting Mechanism Produces Negative, Zero and Positive Linear Thermal Expansion in a Semi-Flexible Cd(II)-MOF," *Chem. Commun.*, vol. 50, no. 49, pp. 6464–6467, 2014.

[149] Y.-S. Wei, K.-J. Chen, P.-Q. Liao, B.-Y. Zhu, R.-B. Lin, H.-L. Zhou, B.-Y. Wang, W. Xue, J.-P. Zhang, and X.-M. Chen, "Turning on the Flexibility of Isoreticular Porous Coordination Frameworks for Drastically Tunable Framework Breathing and Thermal Expansion," *Chem. Sci.*, vol. 4, pp. 1539–1546, 2013.

[150] I. Grobler, V. J. Smith, P. M. Bhatt, S. A. Herbert, and L. J. Barbour, "Tunable Anisotropic Thermal Expansion of a Porous Zinc(II) Metal-Organic Framework," *J. Am. Chem. Soc.*, vol. 135, no. 17, pp. 6411–6414, 2013.

[151] V. K. Peterson, G. J. Kearley, Y. Wu, A. J. Ramirez-Cuesta, E. Kemner, and C. J. Kepert, "Local Vibrational Mechanism for Negative Thermal Expansion: A Combined Neutron Scattering and First-Principles Study," *Angew. Chem. Int. Ed.*, vol. 49, no. 3, pp. 585–588, 2010.

[152] K. W. Chapman, G. J. Halder, and P. J. Chupas, "Pressure-Induced Amorphization and Porosity Modification in a Metal-Organic Framework," *J. Am. Chem. Soc.*, vol. 131, no. 48, pp. 17546–17547, 2009.

[153] J.-C. Tan and A. K. Cheetham, "Mechanical Properties of Hybrid Inorganic-Organic Framework Materials: Establishing Fundamental Structure-property Relationships," *Chem. Soc. Rev.*, vol. 40, no. 2, pp. 1059–1080, 2011.

[154] H. Wu, T. Yildirim, and W. Zhou, "Exceptional Mechanical Stability of Highly Porous Zirconium Metal-Organic Framework UiO-66 and Its Important Implications," *J. Phys. Chem. Lett.*, vol. 4, no. 6, pp. 925–930, 2013.

[155] W. Li, S. Henke, and A. K. Cheetham, "Research Update: Mechanical Properties of Metal-Organic Frameworks - Influence of Structure and Chemical Bonding," *APL Mat.*, vol. 2, no. 12, p. 123902, 2014.

[156] J.-C. Tan, B. Civalleri, A. Erba, and E. Albanese, "Quantum Mechanical Predictions to Elucidate the Anisotropic Elastic Properties of Zeolitic Imidazolate Frameworks: ZIF-4 vs. ZIF-Zni," *CrystEngComm*, vol. 17, no. 2, pp. 375–382, 2014.

[157] C. Kittel, *Introduction to Solid State Physics*. Wiley, 8th ed., 2004.

[158] J. J. Gilman, *Electronic Basis of the Strength of Materials*. Cambridge University Press, 2003.

[159] F. Mouhat and F.-X. Coudert, "Necessary and Sufficient Elastic Stability Conditions in Various Crystal Systems," *Phys. Rev. B*, vol. 90, no. 22, p. 224104, 2014.

[160] W. F. Perger, J. Criswell, B. Civalleri, and R. Dovesi, "Ab-Initio Calculation of Elastic Constants of Crystalline Systems with the CRYSTAL Code," *Comput. Phys. Commun.*, vol. 180, no. 10, pp. 1753–1759, 2009.

[161] R. Golesorkhtabar, P. Pavone, J. Spitaler, P. Puschnig, and C. Draxl, "ElaStic: A Tool for Calculating Second-Order Elastic Constants from First Principles," *Comput. Phys. Commun.*, vol. 184, no. 8, pp. 1861–1873, 2013.

[162] W. Zhou and T. Yildirim, "Lattice Dynamics of Metal-Organic Frameworks: Neutron Inelastic Scattering and First-Principles Calculations," *Phys. Rev. B*, vol. 74, no. 18, p. 180301, 2006.

[163] M. Mattesini, J. M. Soler, and F. Yndurain, "Ab Initio Study of Metal-Organic Framework-5 Zn4O(1,4-benzenedicarboxylate): An Assessment of Mechanical and Spectroscopic Properties," *Phys. Rev. B*, vol. 73, no. 9, p. 094111, 2006.

[164] A. Samanta, T. Furuta, and J. Li, "Theoretical Assessment of the Elastic Constants and Hydrogen Storage Capacity of Some Metal-Organic Framework Materials," *J. Chem. Phys.*, vol. 125, no. 8, p. 084714, 2006.

[165] A. Kuc, A. Enyashin, and G. Seifert, "Metal-Organic Frameworks: Structural, Energetic, Electronic, and Mechanical Properties," *J. Phys. Chem. B*, vol. 111, no. 28, pp. 8179–8186, 2007.

[166] A. U. Ortiz, A. Boutin, A. H. Fuchs, and F.-X. Coudert, "Metal-Organic Frameworks with Wine-Rack Motif: What Determines Their Flexibility and Elastic Properties?," *J. Chem. Phys.*, vol. 138, no. 17, p. 174703, 2013.

[167] A. U. Ortiz, A. Boutin, K. J. Gagnon, A. Clearfield, and F.-X. Coudert, "Remarkable Pressure Responses of Metal-Organic Frameworks: Proton Transfer and Linker Coiling in Zinc Alkyl Gates," *J. Am. Chem. Soc.*, vol. 136, no. 32, pp. 11540–11545, 2014.

[168] A. U. Ortiz, A. Boutin, and F.-X. Coudert, "Prediction of Flexibility of Metal-Organic Frameworks CAU-13 and NOTT-300 by First Principles Molecular Simulations," *Chem. Commun.*, vol. 50, no. 44, pp. 5867–5870, 2014.

[169] T. D. Bennett, J.-C. Tan, S. A. Moggach, R. Galvelis, C. Mellot-Draznieks, B. A. Reisner, A. Thirumurugan, D. R. Alland, and A. K. Cheetham, "Mechanical Properties of Dense Zeolitic Imidazolate Frameworks (ZIFs): A High-Pressure X-Ray Diffraction, Nanoindentation and Computational Study of the Zinc Framework $Zn(Im)_2$, and Its Lithium-Boron Analogue, $LiB(Im)_4$," *Chem. Eur. J.*, vol. 16, no. 35, pp. 10684–10690, 2010.

[170] T. D. Bennett, J. Sotelo, J.-C. Tan, and S. A. Moggach, "Mechanical Properties of Zeolitic Metal-Organic Frameworks: Mechanically Flexible Topologies and Stabilization against Structural Collapse," *CrystEngComm*, vol. 17, no. 2, pp. 286–289, 2014.

[171] H. Ledbetter, "Sound Velocities, Elastic Constants: Temperature Dependence," *Mater. Sci. Eng. A*, vol. 442, no. 1-2, pp. 31–34, 2006.

[172] L. B. du Bourg, A. U. Ortiz, A. Boutin, and F.-X. Coudert, "Thermal and Mechanical Stability of Zeolitic Imidazolate Frameworks Polymorphs," *APL Mat.*, vol. 2, no. 12, p. 124110, 2014.

[173] Y. L. Page and P. Saxe, "Symmetry-General Least-Squares Extraction of Elastic Coefficients from Ab Initio Total Energy Calculations," *Phys. Rev. B*, vol. 63, no. 17, p. 174103, 2001.

[174] A. U. Ortiz, A. Boutin, A. H. Fuchs, and F.-X. Coudert, "Investigating the Pressure-Induced Amorphization of Zeolitic Imidazolate Famework ZIF-8: Mechanical Instability Due to Shear Mode Softening," *J. Phys. Chem. Lett.*, vol. 4, no. 11, pp. 1861–1865, 2013.

[175] S. Henke, W. Li, and A. K. Cheetham, "Guest-Dependent Mechanical Anisotropy in Pillared-Layered Soft Porous Crystals - a Nanoindentation Study," *Chem. Sci.*, vol. 5, no. 6, pp. 2392–2397, 2014.

[176] J.-C. Tan, P. Jain, and A. K. Cheetham, "Influence of Ligand Field Stabilization Energy on the Elastic Properties of Multiferroic MOFs with the Perovskite Architecture," *Dalton Trans.*, vol. 41, no. 14, pp. 3949–3952, 2012.

[177] S.-L. Shang, H. Zhang, Y. Wang, and Z.-K. Liu, "Temperature-dependent elastic stiffness constants of $\alpha$-and $\theta$-$Al_2O_3$ from first-principles calculations," *J. Phys.: Condens. Matter*, vol. 22, no. 37, p. 375403, 2010.

[178] M. J. Mehl, J. E. Osburn, D. A. Papaconstantopoulos, and B. M. Klein, "Structural Properties of Ordered High-Melting-Temperature Intermetallic Alloys from First-Principles Total-Energy Calculations," *Phys. Rev. B*, vol. 41, pp. 10311–10323, 1990.

[179] M. J. Mehl, B. M. Klein, and D. A. Papaconstantopoulos, *First principles calculations of elastic properties of metals*, ch. 9, pp. 195–210. Intermetallic compounds, Chichester [etc.] Wiley & Sons 1995-2002, 1995.

[180] Y. L. Page and P. Saxe, "Symmetry-General Least-Squares Extraction of Elastic Data for Strained Materials from Ab Initio Calculations of Stress," *Phys. Rev. B*, vol. 65, no. 10, p. 104104, 2002.

[181] S. Shang, Y. Wang, and Z.-K. Liu, "First-Principles Elastic Constants of $\alpha$- and $\theta$-Al2O3," *Appl. Phys. Lett.*, vol. 90, no. 10, p. 101909, 2007.

[182] R. Yu, J. Zhu, and H. Q. Ye, "Calculations of Single-Crystal Elastic Constants Made Simple," *Comput. Phys. Commun.*, vol. 181, no. 3, pp. 671–675, 2010.

[183] M. J. Mehl, "Pressure Dependence of the Elastic Moduli in Aluminum-Rich Al-Li Compounds," *Phys. Rev. B*, vol. 47, no. 5, pp. 2493–2500, 1993.

[184] P. Ravindran, L. Fast, P. A. Korzhavyi, B. Johansson, J. Wills, and O. Eriksson, "Density Functional Theory for Calculation of Elastic Properties of Orthorhombic Crystals: Application to $TiSi_2$," *J. Appl. Phys.*, vol. 84, no. 9, pp. 4891–4904, 1998.

[185] W. Voigt, *Lehrbuch der Kristallphysik*, p. 962. Leipzig: Teubner, 2nd ed., 1928.

[186] A. Reuss, "Berechnung der Fließgrenze von Mischkristallen auf Grund der Plastizitättsbediengung für Einkristalle," *Z. Angew. Math. Mech.*, vol. 9, no. 1, pp. 49–58, 1929.

[187] R. Hill, "The Elastic Behaviour of a Crystalline Aggregate," *Proc. Phys. Soc. A*, vol. 65, no. 5, p. 349, 1952.

[188] A. Marmier, Z. A. D. Lethbridge, R. I. Walton, C. W. Smith, S. C. Parker, and K. E. Evans, "ElAM: A Computer Program for the Analysis and Representation of Anisotropic Elastic Properties," *Comput. Phys. Commun.*, vol. 181, no. 12, pp. 2012–2015, 2010.

[189] F. D. Murnaghan, "The Compressibility of Media Under Extreme Pressures," *Proc. Natl. Acad. Sci. U.S.A.*, vol. 30, no. 9, pp. 244–247, 1947.

[190] P. Vinet, J. R. Smith, J. Ferrante, and J. H. Rose, "Temperature Effects on the Universal Equation of State of Solids," *Phys. Rev. B*, vol. 35, no. 4, pp. 1945–1953, 1987.

[191] G. N. Greaves, A. L. Greer, R. S. Lakes, and T. Rouxel, "Poisson's Ratio and Modern Materials," *Nat. Mater.*, vol. 10, no. 11, pp. 823–837, 2011.

[192] L. Sarkisov, R. L. Martin, M. Haranczyk, and B. Smit, "On the Flexibility of Metal-Organic Frameworks," *J. Am. Chem. Soc.*, vol. 136, no. 6, pp. 2228–2231, 2014.

[193] P. Serra-Crespo, A. Dikhtriarenko, E. Stavitski, J. Juan-Alcaniz, F. Kapteijn, F.-X. Coudert, and J. Gascon, "Experimental Evidence of Negative Linear Compressibility in the MIL-53 Metal-Organic Framework Family," *CrystEngComm*, vol. 17, no. 2, pp. 276–280, 2015.

[194] J.-C. Tan, J. D. Furman, and A. K. Cheetham, "Relating Mechanical Properties and Chemical Bonding in an Inorganic-Organic Framework Material: A Single-Crystal Nanoindentation Study," *J. Am. Chem. Soc.*, vol. 131, no. 40, pp. 14252–14254, 2009.

[195] K. W. Chapman, G. J. Halder, and P. J. Chupas, "Guest-Dependent High Pressure Phenomena in a Nanoporous Metal-Organic Framework Material," *J. Am. Chem. Soc.*, vol. 130, no. 32, pp. 10524–10526, 2008.